# Synthesis of Microwave Assisted Transition Metal Dichalcogenides for the Catalytic Degradation of Organic Pollutants

*Thesis submitted for the award of degree of*

**Doctor of Philosophy**

*Submitted by*

**Divya Monga**

**Roll No. 901809002**

*Under the guidance of*

**Dr. Soumen Basu**

**Associate Professor**


**SCHOOL OF CHEMISTRY & BIOCHEMISTRY**

**THAPAR INSTITUTE OF ENGINEERING AND TECHNOLOGY,**

**Patiala-147004**

# *Certificate*

This is to certify that thesis entitled "**Synthesis of Microwave Assisted Transition Metal Dichalcogenides for the Catalytic Degradation of Organic Pollutants**", being submitted by Ms Divya Monga in fulfillment of the requirement for the award of the Degree of Doctor of Philosophy in the School of Chemistry and Biochemistry, Thapar Institute of Engineering and Technology, Patiala, is a record of candidate's own independent and original research work carried out by her under my supervision and guidance. The matter presented in the thesis has not been submitted in part or full for the award of any degree in any other University or Institute.

**(Supervisor)**

Dr. Soumen Basu

Associate Professor

School of Chemistry and Biochemistry

Thapar Institute of Engineering and Technology

Patiala- 147004, Punjab (India)

**(Head)**

Dr. Satnam Singh

Professor

School of Chemistry and Biochemistry

Thapar Institute of Engineering and Technology

Patiala- 147004, Punjab (India)

4/8/22

## *Candidate's Declaration*

I, hereby declare that the work presented in the thesis entitled "**Synthesis of Microwave Assisted Transition Metal Dichalcogenides for the Catalytic Degradation of Organic Pollutants**", in fulfillment of the requirement for the award of the Degree of **Doctor of Philosophy**, School of Chemistry and Biochemistry, Thapar Institute of Engineering and Technology, Patiala, is an authentic record of my own work carried out under the supervision of Dr. Soumen Basu, Associate Professor, School of Chemistry and Biochemistry, Thapar Institute of Engineering and Technology, Patiala, India. The matter embodied in this thesis has not been submitted in part or full to any other university or institute for the award of any degree in India or Abroad.

**Divya Monga**

# Dedicated

# To

# My Brother

# *Acknowledgments*

I would like to start by thanking **God** for showering his blessings and granting me the inner strength, without which it would have been impossible to successfully complete this research.

I would first like to express my heartfelt gratitude and unpayable indebtedness to my research supervisor, **Dr. Soumen Basu**, Associate Professor, School of Chemistry and Bio-chemistry, Thapar Institute of Engineering and Technology (Deemed to be University) Patiala, India, for their continuous support, skillful guidance and proficient supervision throughout my academic endeavor. From my master's project to my Ph.D. degree, my supervisor has always supported and guided me at every single step. I feel it as an obligation upon me to thank my supervisor for their availability whenever required, even during the odd hours of their jobs.

I owe sincere gratitude to **Dr. Satnam Singh**, Professor and Head, School of Chemistry and Biochemistry, TIET, Patiala. I am highly grateful to **Dr. Bonamali Pal** (Associate Professor) and **Dr. Davinder Kumar** (Assistant Professor), School of Chemistry and Biochemistry, TIET, Patiala and **Dr. Kulvir Singh** (Professor and Head), School of Physics and Material Science, TIET, Patiala, for being the esteemed members of Doctoral Committee and for providing their valuable comments and suggestions while reviewing this work. I am also thankful to **Dr. O.P. Pandey** and **Dr. Bhaskar Mohanty** for helping me in electrocatalytic studies and SAED analysis. My sincere thanks also goes to **Mr. Mayank** for all the support in documentation work. A special thanks to **Mr. Chander Kumar** and **Mr. Hemant** for their support and help during my Teaching Associateship in SCBC department.

I extend my gratitude to **Dr. Prakash Gopalan**, Honorable Director and **Dr. Rafat Siddique**, Senior Professor and Dean, Research and Sponsored Projects, TIET, Patiala, for providing all the necessary facilities to carry out this research on steady course. The help from different laborites like SAI labs, CeNS Bengaluru and Sprint Testing Solutions is highly acknowledged.

My family has always been providing the main impetus for commuting me into the person I am today. Their continuous motivation has resulted in an unconditional amelioration within me. Regardless of whether I was around them or far from them during this research

tenure, their pearls of enlightenment and counselling were always felt in furtherance of this research. Biggest thanks to my mother, **Mrs. Santosh Monga** who laughed and cried with me at every stage of my life. Who would be more than happy to see me as Dr. Divya. My father, **Mr. Ashok Monga**, always taught me this “never be afraid beta, you are right and we are always with you”. Thank you papa. My elder brother **Mr. Ishu Monga** has never let me fall till today, neither in my life nor in my career. Whatever I have achieved today, my brother has more credit in it than me. So, I would like to thank my brother, who always guided me. I also want to thank my brother, **Mr. Nishu Monga** who always looked upon me when there was no one to take care of me. A special thanks to my two nephews, **Kabeer Monga** and **Sahaj Monga,** who have always looked at me with the same love and happiness whether I have achieved something good or have failed.

I can’t thank enough to wonderful colleagues that I had during my research period. I am thankful to my seniors, **Ms. Surbhi Sharma, Dr. Aanchal Rathi and Ms. Neeraj** who always lent a helping hand whenever needed. I would like to send my heartfelt gratitude to **Aashna, Aayushi, Shelly, Mansi, Ranjeet Kumar Jha, Zaid Bin Siddiqui** for all their support. I owe deepfelt gratitude to **Rekha and Anushka** whom I met during my earliest days in TIET, and the bond between us only grew stronger. Their company turned my stay in Patiala into an amazingly wonderful experience that I will never forget. Besides this, I am thankful to the person who knowingly and unknowingly helped me during the successful completion of this work.

My memories with the **Thapar** Institute campus are simply unforgettable ones. I have enjoyed every moment of this journey from dancing on the big stage and playing badminton to relieving the stress caused by this stressful life to celebrating the failures of research with my labmates. I will surely miss the love from Thapar and its people.

**DIVYA MONGA**

# Table of Contents

# CHAPTER- 3

***Tuning the Photocatalytic Properties of $MoS_2/MoSe_2$ Heterostructures by Varying the Weight Ratios for Enhanced Wastewater Treatment***

# CHAPTER- 4

## *2D BiOCl Nanorods Decorated with 2D $MoS_2$ Nanosheets for Visible Light-driven Photocatalytic Detoxification of Organic and Inorganic Pollutants*

# CHAPTER- 5

## *Facile Assembly of 2D $MoS_2$/GO Composites with Ag Nanoparticles for Visible Light-Driven Photocatalytic Abatement of Recalcitrant Pollutants*

# *List of Figures*

## CHAPTER-1



## CHAPTER-2

**CHAPTER-3**

**CHAPTER-4**

**CHAPTER-5**

# *List of Tables*

# *List of Schemes*

## CHAPTER-2



## CHAPTER-3



## CHAPTER-4



## CHAPTER-5

# *List of Abbrevations*

| | |
|---|---|
| **a.u.** | Arbitrary unit |
| **AOP** | Advanced Oxidation Processes |
| **AOS** | Average oxidation state |
| **BET** | Brunauer Emmett Teller |
| **BJH** | Barrett-Joyner-Halenda |
| **CB/$E_{CB}$** | Conduction band/Electronic conduction band |
| **Cm** | Centi meter |
| **COD** | Chemical oxygen demand |
| **COS** | Carbon oxidation state |
| **DI** | Deionized water |
| **DRS** | Diffuse reflectance spectroscopy |
| **DMSO** | Dimethylsulfoxide |
| **EDS** | Energy dispersive X-ray spectrometer |
| **Ep** | Peak potential |
| **eV** | Electron volt |
| **FESEM** | Field emission scanning electron microscopy |
| **GO** | Graphene oxide |
| **GCE** | Glassy carbon electrode |
| **HRTEM** | High resolution transmission electron microscopy |
| **Ip** | Peak current |
| **JCPDS** | Joint committee on powder diffraction standards |
| **LC-MS** | Liquid chromatography-Mass spectroscopy |

| | |
|---|---|
| **mL** | Milli-litre |
| **mM** | Milli molar |
| **Mg** | Milli gram |
| **Mol** | Mole |
| **NHE** | Normal hydrogen electrode |
| **nm** | Nanometer |
| **NPs** | Nanoparticles |
| **PBS** | Phosphate buffer solution |
| **PL** | Photoluminescence |
| **Ppm** | Parts per million |
| **P25-$TiO_2$** | Commercially available P25-$TiO_2$ |
| **SAED** | Selected area electron diffraction |
| **SPR** | Surface plasmon resonance |
| **TEM** | Transmission electron microscopy |
| **TMDCs** | Transition metal dichalcogenides |
| **TOC** | Total organic carbon |
| **UV** | Ultraviolet |
| **VB/EVB** | Valence band/Electronic valence band |
| **Vis** | Visible |
| **VOCs** | Volatile Organic Compounds |
| **vol%** | Volume percentage |
| **wt%** | Weight percentage |
| **XPS** | X ray photoelectron spectroscopy |
| **XRD** | X-ray diffraction |
| **µL** | Micro-litre |
| **µM** | Micro molar |
| **$\lambda_{max}$** | Wavelength of maximum absorption |

# *Symbols*

| | |
|---|---|
| **e-** | Electron |
| **$h^+$** | Hole |
| **$OH^{\cdot}$** | Hydroxyl radical |
| **Ppm** | Parts per million |
| **mM** | Millimolar |
| **$O^{2.-}$** | Superoxide radical |
| **Eg** | Band gap |
| **Å** | Angstrom |
| **A** | Absorption coefficient |
| **A** | Absorbance |
| **°** | Degree |
| **Λ** | Wavelength |
| **%** | Percentage |
| **M** | Micro |
| **Min** | Minutes |
| **Ɵ** | Theta |
| **H** | Hour |
| **Φ** | Work function |
| **M** | Meter |
| **G** | Gram |
| **Mg** | Milligram |
| **V** | Volt |
| **D** | Distance |
| **S** | Second |

# *Abstracts*


**Chapter 1:**

A brief introduction about hazardous pollutants and wastewater treatment methods is given with a precise discussion on advanced oxidation processes including semiconductor photocatalysis. This section also illustrates the photocatalytic mechanism in detail using semiconductors. Furthermore, an extensive discussion on transition metal dichalcogenides (TMDCs) is provided with description of their unique photo or electrocatalytic properties like high surface-to-volume ratio, excellent charge transfer capacity, mechanical strength, and low bandgap energy. The chapter also highlights the advantages of microwave-assisted methods for synthesis of different TMDC composites and the requirement for the formation of heterojunction composites to overcome charge recombination. In addition, the research gaps, research objectives, and characterization approaches have been combined with specifications.

**Chapter 2:**

The photodegradation of toxic pollutants is a promising way to deal with water-pollution. In this regard, $MoS_2$/g-$C_3N_4$ (MSC) composites with varying weight-ratios were prepared via fast one step microwave-assisted method. The material was characterized by XRD, XPS, EDS, FESEM and HRTEM which validate the successful formation of catalyst having the flower-like and sheet-like morphologies of $MoS_2$ and g-$C_3N_4$, respectively. The PL and UV-vis DRS spectra exhibit low recombination-rate and band-gap (1.7 eV) which is appropriate for efficacious visible-light degradation. The photocatalytic performance of catalysts was then analyzed by the degradation of a model dye methylene blue and pesticide fipronil. Best results were obtained by 5:1 MSC (98.7% degradation efficacy; rate constant 0.0261 $min^{-1}$) in 80 min under sunlight. The effects of solution pH, catalyst-dose, scavengers and illumination-area were also explored. The catalyst is highly-reusable as confirmed by the characterization and degradation studies (~82% efficiency) after 5-cycles. The photocatalytic treatment of real industrial-wastewater was also conducted. The electrochemical degradation of methylene blue was also investigated using glassy carbon electrode modified with different MSC-ratios. The

electrode modified with 5:1 MSC at pH 7 manifested maximum peak current. The plausible mechanisms for photocatalytic and electrochemical degradation were proposed. The study therefore reveals that synthesized nanocomposites have a remarkable potential for wastewater treatment.

**Chapter 3:**

Two-dimensional (2D) heterojunctions with layered structures give high flexibility in varying their photocatalytic/electrocatalytic properties. Herein, 2D/2D heterostructures of $MoS_2/MoSe_2$ with different weight-ratios (1:1, 1:3, and 3:1) have been prepared by simple one-step microwave-assisted technique. The characterization studies confirm formation of crystalline $MoS_2/MoSe_2$ nanospheres with high surface area (60 $m^2/g$) and porous structure. High synergistic-effect (1.73) and narrow bandgap (~1.89 eV) of the composites shows enhanced photo-degradation efficiency towards methylene blue dye (94%) and fipronil pesticide (80%) with high rate constant (0.33 $min^{-1}$ and 0.016 $min^{-1}$ respectively) under visible light. The effect of pH, catalyst dose, and illumination area on photodegradation has been optimized. Photodegradation of real-industrial wastewater shows 65% COD and 51.5% TOC removal. Trapping experiments confirm that holes are mainly responsible for degradation. The composites were highly reusable as showing 75% degradation after 5-cycles. $MoS_2/MoSe_2$ composites show excellent electrochemical water-splitting efficacy through hydrogen-evolution-reaction (HER) exhibiting stable high current density of –19.4 $mAcm^{-2}$ after 2500 cyclic-voltammetry (CV) cycles. The CV-plots reveals high capacitance activity ($C_{dl}$ value ~607 $\mu Fcm^{-2}$) with a great % capacitance retention (>90 %). The as-prepared 2D/2D-catalysts are highly active in sunlight and beneficial for long-time physico-chemical wastewater treatment. Moreover, the electrochemical studies confirm that these composites are potential materials for HER activity and energy-storage applications.

**Chapter 4:**

Visible light-driven photocatalytic degradation is one of the promising ways to deal with the major problem of water pollution. This study involves one-step, fast, in-situ preparation of $BiOCl/MoS_2$ (2D/2D) heterostructure via microwave irradiations. The photocatalytic performance of $BiOCl/MoS_2$ composite with different weight ratios (1:1, 3:1, and 1:3) have been evaluated for degradation of organic (methylene blue dye, fipronil pesticide) and inorganic

pollutants (Cr(VI)) along with real industrial wastewater under visible light irradiation. XRD, XPS, FESEM, HRTEM, and SAED analysis indicate the formation of single-crystalline nanorods with a high aspect ratio of 1:10. The composites possess high surface area (~40$m^2$/g) with lower charge recombination and high visible light absorption tendency due to lower band gap (2.30eV) energy. The high synergistic interaction (~2.29) between BiOCl and $MoS_2$ results in enhancement of degradation activity which shows 94%, 89%, and 90% removal of MB, fipronil, and Cr(VI) metal, respectively by BiOCl/$MoS_2$ (1:3) catalyst. The optimum conditions to get maximum degradation efficiency were determined by varying different reaction parameters like pH, catalyst dose, and illumination area. Radical trapping experiments indicate that holes and hydroxyl radicals had a dominant role in the degradation process. The catalyst is highly stable and reusable as confirmed by the reusability studies. The photocatalytic treatment of industrial wastewater without any physico-chemical pretreatment showed 75% COD and 63% TOC removal under visible light, which indicates high practical efficiency of the catalyst. The current study validates that the BiOCl/$MoS_2$ composites with superior characteristic properties can be efficiently used for wastewater treatment under natural light.

**Chapter 5:**

The alarming situation of water pollution by human overuse of medications and pesticides can be efficiently dealt with by using visible-light active, efficient photocatalysts. Herein, different weight ratios (1:1, 1:3, and 3:1) of $MoS_2$/GO composites decorated with Ag nanoparticles (named as MAG) have been prepared by the microwave-assisted route. XRD and XPS investigations indicated the crystallinity of the catalyst and the oxidation states of the elements, while EDS and color mapping proved the uniform dispersion of elements in the catalyst. FESEM and HRTEM analyses revealed the presence of small $MoS_2$ nanopetals scattered on GO sheets with Ag nanoparticles dispersed on the surface whereas BET-analysis disclosed its excellent surface area (~88 $m^2$/g). The optical properties of MAG catalysts revealed that they were highly visible-light active, with a bandgap of 2.15 eV and a lower charge recombination rate. The photocatalytic performance of the as-prepared catalysts has been evaluated for degradation of antibiotic (tetracycline (TC)), pesticide (fipronil (FIP)), and real industrial wastewater. The effects of catalyst amount, pH, and effective area of illumination on degradation were investigated. Excellent efficiency was observed for TC (90.7%; 0.0186 $min^{-1}$)

and FIP-degradation (85.2%; 0.0177 $min^{-1}$) with 4mg MAG (3:1) catalyst at neutral pH under visible-light irradiation owing to the high synergistic interaction (~2.21) in the composite. The high reusable nature of the catalyst (65% (TC) and 58% (FIP) efficiency after 5 cycles) was supported by post-photocatalytic characterization studies. The scavenging experiments revealed that hydroxyl radicals and holes played an important part in the process of degradation. High COD (70.4%) and TOC (55.1%) removal rates were achieved in the photo-mineralization of real wastewater used without any pre-treatment. The current investigation, combined with comparative literature, illustrates the real-world potential of the MAG catalysts for the eradication of resistant pollutants.

# CHAPTER 1:

## *Introduction and literature review*

## 1.1 Introduction and Literature

### 1.1.1 Wastewater and pollutant

The industrial revolution accelerated the development of human civilization in the late nineteenth century. However, the progress in urbanization and industrialization has damaged environmental quality over the years.[1] Water contamination is currently one of the world's greatest concerns, owing to the uncontrolled discharge of used industrial water into the ecosystem, excessive utilization of chemical fertilizers in agricultural areas, development of roads and buildings, and so on.[2] The discharge of huge amounts of water pollutants like organic dyes, phenol, polymers, benzene-based organics, and other dangerous chemicals in natural water resources are hazardous to living beings as these are highly toxic, carcinogenic, and recalcitrant in nature.[3,4]

Among the various water pollutants, organic contaminants like dyes,[5] pesticides,[6] and pharmaceuticals[7] are the primary sources of contamination. Various chemical and textile industries dealing with dyes are responsible for the majority of dye usage and effluent discharge following the process. Every year, around 45,000 tons of organic dyes are produced worldwide; nevertheless, more than 11% of this amount is lost as effluents in water bodies.[8] Many cardiovascular and metabolic problems arise with the use of pesticides (such as fipronil (FIP)) in crops. Even their infinitesimal amount can lead to cardiovascular, reproductive, metabolic, and neurological disorders.[9] Moreover, the antibiotic (e.g., tetracycline (TC)) contamination[7] caused by human overuse of medications has sparked worldwide concern due to the long-term environmental consequences and dangers to ecosystem creatures.[10] As well as with the breakout of COVID-19, the issue of biomedical wastewater discharges has increased due to a sudden rise in the use of medications. As per recent WHO figures, approximately 3.7 million people died globally in the twenty-first century as a result of air and water pollution, and approximately 80-90% of the global population lives in locations with higher levels of water and air pollution than that of

the WHO-specified limits.[11,12] As a result, toxic waste materials must be removed from the environment.

Several studies were done to address this environmental concern, including biological, chemical, and physical methods. Some heavy and easily separable materials are separated from wastewater using physical separation methods.[13] These techniques entail filtration, adsorption, coagulation-flocculation, and ion exchange methods.[14] The biological treatment methods or bioremediation involve the use of aerobic or anaerobic microbes for the degradation of pollutants.[15] The chemical treatments are used for the degradation of non-separable or soluble contaminants such as dyes, pesticides, etc. from wastewater. These chemical methods include processes such as ozonation, Fenton's reaction, advanced oxidation processes (AOPs), etc. for the removal of pollutants.[16] AOPs have been shown to be the most beneficial for the near-complete degradation of contaminants from water. Semiconductor photocatalysis is a technology used in the AOP that has a lot of potential for degrading organic pollutants.[17]

### 1.1.2 Photocatalysis and Semiconductor Photocatalysis

Semiconductors are suitable tools for photocatalytic activity reactions because of their distinctive electronic structure that allows charge carriers to be separated spatially by photon absorption. A photocatalytic reaction, in general, comprises three main stages, as shown in fig. 1.1:[18]

1) To form electron-hole pairs, the photocatalyst captures photons with higher energy than its bandgap ($E_g$).[19]

2) These photogenerated $e^-/h^+$ split and move towards the photocatalyst surface. On the other hand, during this process, the recombination of these charge carriers can also take place either in bulk or on the surface of the photocatalyst.[20]

3) The separated $h^+$ and $e^-$ participate in the oxidation and reduction process, respectively.

The interaction of the thermodynamics and kinetics of these three essential stages determines the overall efficiency of a photocatalyst. The photocatalyst must have a broad light absorption range, rapid charge carrier separation, abundant reactive sites, and excellent redox capabilities to attain high photocatalytic effectiveness.[21]

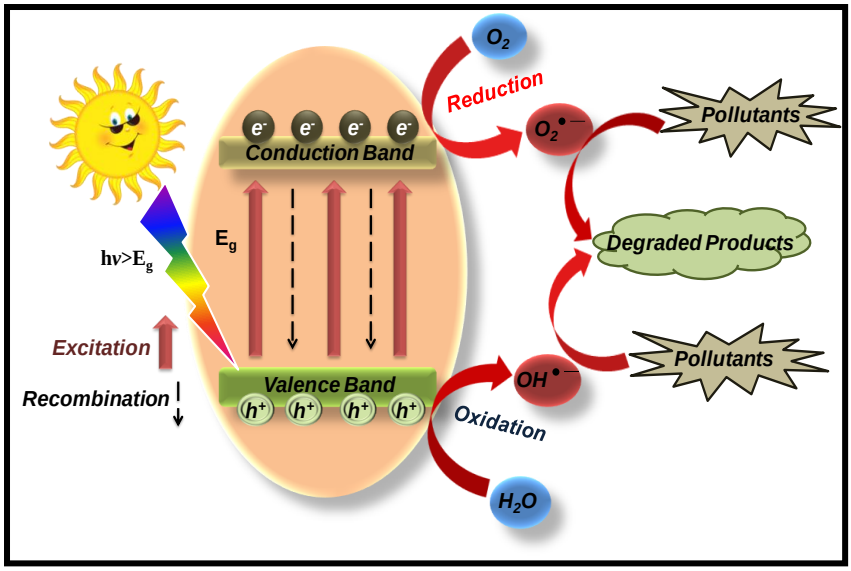


**Fig. 1.1** General mechanism for semiconductor photocatalytic degradation of pollutants.

In this regard, a wide range of photocatalysts for water purification has been developed, analyzed, and evaluated, which include metal oxides such as $TiO_2$, ZnO, $Fe_2O_3$;[22] sulfides such as CuS, ZnS;[23] tungstates such as $ZnWO_4$;[24] some ternary materials like titanates $SrTiO_3$, $BaTiO_3$;[25] transition metal dichalcogenides [26] for e.g., $MoS_2$, $MoSe_2$, etc. and even multi-component systems like $BiVO_4/Bi_2O_2CO_3$.[27] Tian *et al.* prepared porous $TiO_2$ catalyst through a hydrothermal technique using cetyltrimethylammonium bromide as a template, which shows better photocatalytic activity than Deggusa P25 under irradiation of UV light.[28] Chen *et al.* reported the preparation of ZnO photocatalyst from zinc acetate through sol-gel method. The prepared ZnO was analyzed for the degradation of different azo dyes, and the influence of calcination temperature on degradation efficiency was also optimized. MO was removed by 99.70% from ZnO produced at a calcination temperature of 400°C.[29] Similarly, Huang *et al.* explored the photocatalytic efficiency of $ZnWO_4$ catalyst by degrading formaldehyde and Rhodamine B (RhB) dye. The $ZnWO_4$ catalyst was prepared by the combination of hydrothermal and annealing processes. Due to excellent crystallization and a large surface area, the maximum photocatalytic efficiency was seen at 450°C for 1 hour.[30] $SrTiO_3$ nanocubes were made by Huang *et al.* using a hydrothermal technique in an alkaline environment using $TiO_2$ and $Sr(OH)_{28}H_2O$ as precursor materials at varied reaction temperatures, NaOH contents, and reaction times. The reaction temperature strongly influences the granular size of $SrTiO_3$ and the catalyst prepared at 130°C shows optimal degradation efficiency towards crystal violet dye.[31] Photocatalytic degradation of pollutants

by visible light active $MoS_2$ catalyst has also been reported. The $MoS_2$ catalyst was prepared by Huang *et al.* from L-cysteine and sodium molybdate via hydrothermal treatment, and the prepared catalyst was employed for the effective photocatalytic degradation of toxic pesticide thiobencarb.[32]

$TiO_2$ has received considerable attention among a diverse range of semiconductors due to its superior efficiency as a photocatalyst in UV irradiation and low cost. Many studies revealed that there were some limitations in photocatalysts, like 1) fast recombination of photogenerated $e^-/h^+$ pairs, which reduce the process's quantum yield; 2) the poor absorption of visible light limits its applicability in terms of technological benefit and resource; 3) catalysts lower surface coverage which decreases the efficiency of degradation.[33] As a result, many studies have been conducted to increase the photocatalytic efficiency in the visible region of the spectrum in order to fully utilize solar energy for practical purposes. One of the best methods to overcome this drawback is the use of visible light-active photocatalysts with lower band-gap energy.

### 1.1.3 Transition metal dichalcogenides (TMDCs)

Materials with thin 2D layered structures have gained a lot of attention because of their distinctive physicochemical features. 2D materials have a larger surface area due to their layered structure and also, the distance for migration of charge carriers from the interior to the surface is less.[34] These materials possess many "catalytically useful" defects and offer more active sites due to the presence of numerous unsaturated coordinating surface atoms. Hence, these materials are extensively used in the field of electro/photocatalysis.[35] Two-dimensional transition metal dichalcogenides (TMDCs) are layered materials that have received significant interest in a variety of applications. TMDCs have outstanding features such as a high surface-to-volume ratio, great charge transfer capacity, mechanical strength, and low bandgap energy due to visible light activity.[36] They are composed of transition metals (Mo, W, etc.) coupled with chalcogenides (S, Se, etc.). The transition metal atom layer is sandwiched between the two chalcogen atom layers (fig. 1.2).[37] The atoms in the same layer are bound together by strong covalent interactions, whereas two separate layers are held together via weak van der Waals bonds, allowing these discrete sheets to be isolated from each other.[36]

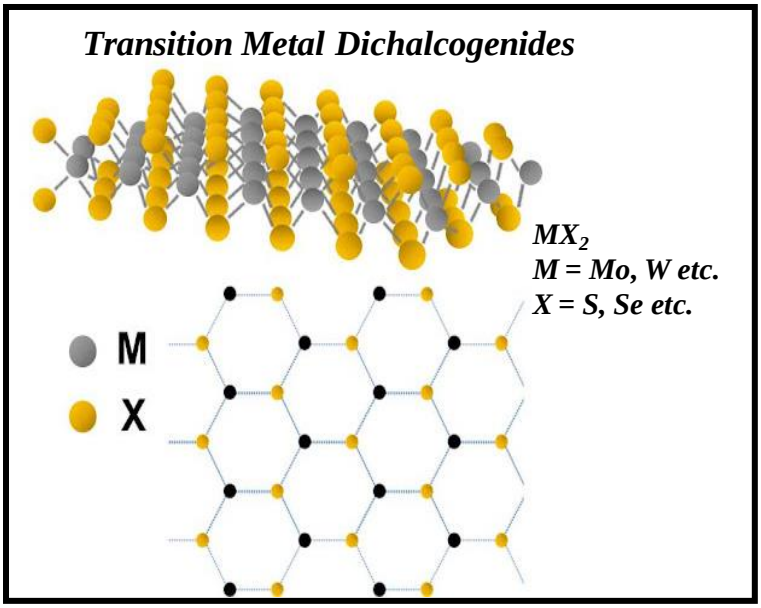


**Fig. 1.2** Structural representation of layered Transition Metal Dichalcogenides.[38]

Several ways for preparing 2D TMDCs with single or few layers have been investigated throughout the years. Significant work has been done related to the synthesis of controlled, large-scale, and regular atomic layers of various 2D TMDCs using several top-down and bottom-up techniques such as chemical or mechanical exfoliation, and chemical vapor deposition (CVD), etc.[39] Conventional techniques are very time consuming, utilize toxic chemicals, require higher heating rate and may still give rise to the poor yield of catalyst.[36] As a result, a more simple technique with increased processability and designability is required for practical electrocatalytic or photocatalytic applications. The microwave-assisted technique is one of the potential methods for facile, less-time consuming[40] synthesis of TMDCs catalysts. Furthermore, the use of microwave energy for rapid and uniform heating allows for faster synthesis while using less energy. Microwave-assisted synthesis has several advantages, including low-temperature synthesis, less reaction time, and the generation of well-exposed active sites through rapid local heating.[41]

### 1.1.4 TMDCs based Composites

Due to certain aspects such as high surface area, layered structures, less bandgap energy, as well as excellent light absorption and utilization, TMDCs have the great potential to act as a photocatalyst. The ultrathin layers of these 2D TMDCs possess a large

surface area and a high surface concentration of atoms, reducing the charge transfer distance and speeding up the electrocatalytic activity.[42] $MoS_2$ is one of the members of TMDC family and is found to be a catalyst with a wide-spectrum response because of its narrow bandgap (≈ 1.8 eV).[43] It has high natural abundance, high chemical stability, low cost, high catalytic performance, and more number of active surface sites. $MoS_2$ is an intrinsically p-type semiconductor with a sandwich-like layered framework of S-Mo-S layers, which is supported by attracting van der Waals forces. According to the literature, improving 2D materials with layered $MoS_2$ results in many active sites responsible for providing appropriate interfacial area and increasing catalytic response activity in the visible light range.[44] Given its many advantages, the weak electronic conductivity is a severe disadvantage when used as a photocatalytic semiconductor. Due to the high recombination efficiency of produced charge carriers, its catalytic activity is unsatisfactory.[45] This constraint may be overcome by the development of semiconductor heterojunctions, which could significantly enhance charge carrier separation as well as provide accessible active sites, hence increasing the photo/electrocatalytic performance of materials.[46]

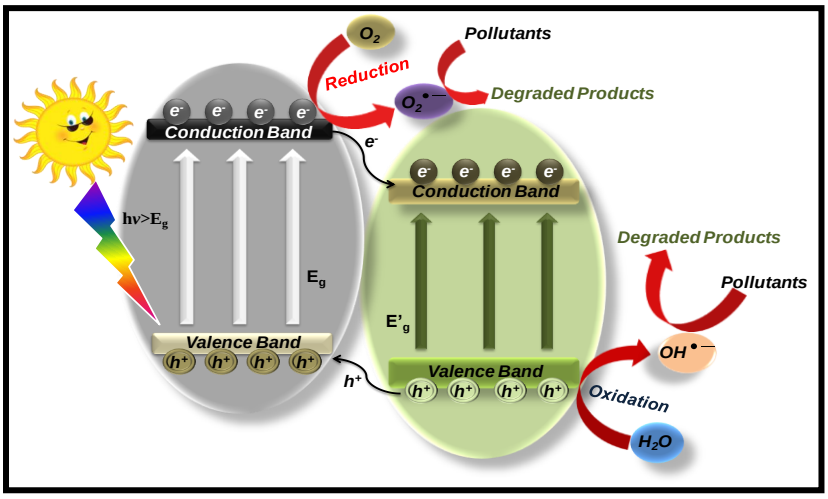


**Fig. 1.3** General mechanism for charge transfer via formation of heterojunction and degradation of pollutants.

Different energy bands of two semiconductors interact in heterojunction composite frameworks to generate a system that allows for fast and efficient charge separation while reducing the recombination rate for electron-hole pairs, as given in fig. 1.3. Photoinduced charges with a low rate of recombination result in increased photocatalytic performance.[47]

Using a variety of synthesis processes, several composites of TMDCs with different materials were developed. Di *et al.* in 2014 synthesized $MoS_2$ coupled BiOBr microspheres solvothermally for the enhanced photocatalytic degradation of RhB dye in visible light.[48] In 2013, Min *et al.* produced CdS/$MoS_2$ heterostructures with a branch-like morphology via a one-pot hydrothermal method. The as-prepared CdS/$MoS_2$ heterostructures exhibited enhanced photocatalytic activity and photostability for the degradation of organic dyes.[49] Li *et al.* reported the synthesis of novel $MoS_2$/$BiVO_4$ hetero-nanoflowers by a two-step hydrothermal approach which shows the enhanced photocatalytic activity. A possible formation mechanism of this heterostructure was also investigated.[50] In 2015, Vattikuti *et al.* synthesized the $MoS_2$ nanosheet decorated with $SnO_2$ mesoporous nanoparticles by a facile two-step method. The catalyst shows the enhanced photocatalytic degradation of RhB dye under UV light irradiation.[51] Chu *et al.* showed the synergetic effect of $TiO_2$ as co-catalyst on $MoS_2$ for the enhanced visible-light photocatalytic reduction of Cr(VI). The $MoSe_2$-$TiO_2$ composites were synthesized via a facile solvothermal method and a high Cr(VI) reduction rate of 91% was achieved under visible light irradiation.[52] Preparation and photocatalytic behavior of $MoS_2$ and $WS_2$ nanoclusters coupled with $TiO_2$ was reported by Ho *et al.*, which were prepared by an in-situ photoreduction deposition method.[53]

Mittal *et al.* studied the in-situ oxidative polymerization of aniline on hydrothermally synthesized $MoSe_2$ for enhanced photocatalytic degradation of organic dyes. The $MoSe_2$/PANI nanocomposite shows high degradation of methylene blue and methyl orange dyes under xenon arc lamp.[54] Also, Weng *et al.* synthesized a two-dimensional $MoS_2$ nanosheet coated with $Bi_2S_3$ discoids, and their photocatalytic activity was investigated by the photocatalytic reduction of Cr(VI) under visible light irradiation.[55] Yan *et al.* constructed a 2D graphene-like $MoS_2$/$C_3N_4$ composite by facile ethylene glycol (EG)-assisted solvothermal method. The obtained composite exhibited strong absorbing ability in the ultraviolet (UV) and visible regions, so it showed high photocatalytic activity in the degradation of methyl orange dye.[56] Zhu et al. synthesized nanocomposites of $NiS_2$/g-$C_3N_4$ by a facile hydrothermal method. The photocatalytic activities of as-prepared samples were evaluated by monitoring the photodecomposition of rhodamine B dye under visible light irradiation.[57] The novel p-n heterojunction photocatalyst, n-$BiVO_4$@p-$MoS_2$ with core-shell structure, was successfully fabricated by Zhao et al. for the first time through a facile

in-situ hydrothermal method. The $MoS_2$ shell thickness can be tuned by varying the concentration of the $MoS_2$ precursor. The photocatalytic performances of samples were systematically investigated via the photocatalytic reduction of $Cr^{6+}$ and oxidation of crystal violet (CV) under visible light irradiation.[58] By developing these TMDC based composites can provide photocatalysts with a high surface area, better light absorption tendency due to low energy band-gap, and reduced recombination rate owing to the charge transfer via heterojunction hence leading to enhanced degradation of hazardous pollutants.

## 1.2 Research Gaps

During our literature review, we realized that various semiconductor composites have been developed for the efficient degradation of pollutants. Most of the traditional photocatalysts are only UV light active as they have a wide band gap. Therefore, it is important to develop visible-light active photocatalysts which can easily degrade organic pollutants present in waste water in the presence of visible light or sunlight and also the catalysts that can be regenerated easily and reused several times. TMDCs are one of the potential catalysts that can efficiently be utilized for wastewater treatment. However, the methods reported in the literature are very time-consuming and require high temperature and pressure, so they are not cost-effective. Hence based on the literature study, some research gaps are outlined and given below:

- Almost all the traditional techniques for the preparation of TMDCs catalyst are time taking and require high temperature or pressure so these are not cost-effective and eco-friendly.
- Also, there is only very few literature, where microwave-assisted synthesis of TMDC's nanocomposites has been reported.
- Degradation of organic pollutants by using different nanocomposites of TMDC (e.g., $MoS_2$/g-$C_3N_4$, $MoS_2$/$MoSe_2$ and $MoS_2$/BiOCl, etc.) has also not been much studied in the literature.

## 1.3 Objectves

To overcome the aforementioned facts, the following aims were proposed for the synthesis of transition metal dichalcogenides based nanocomposites to enhance the

photocatalytic treatment of wastewater. The main purpose of this work is to prepare various composites of TMDC's for the effective degradation of organic pollutants. The specific objectives are as follows:

- Synthesis and characterization of visible light active composites of transition metal dichcalcogenides by using facile microwave or hydrothermal techniques.
- Use of synthesized catalysts in photocatalytic degradation of organic pollutants (e.g., dyes/pesticides/VOCs) in visible/UV/sun light.
- Variation of different reaction parameters (pH, concentration, illumination area etc.) to optimize the photocatalytic efficiency.

## References


(1) Hubeny, J.; Harnisz, M.; Korzeniewska, E.; Buta, M.; Zieliński, W.; Rolbiecki, D.; Giebułtowicz, J.; Nałęcz-Jawecki, G.; Płaza, G. Industrialization as a Source of Heavy Metals and Antibiotics Which Can Enhance the Antibiotic Resistance in Wastewater, Sewage Sludge and River Water. *PLoS One* **2021**, *16* (6), e0252691. https://doi.org/10.1371/journal.pone.0252691.

(2) Pasini, S. M.; Valério, A.; Yin, G.; Wang, J.; de Souza, S. M. A. G. U.; Hotza, D.; de Souza, A. A. U. An Overview on Nanostructured $TiO_2$–Containing Fibers for Photocatalytic Degradation of Organic Pollutants in Wastewater Treatment. *J. Water Process Eng.* **2021**, *40*, 101827. https://doi.org/10.1016/j.jwpe.2020.101827.

(3) Petronella, F.; Truppi, A.; Ingrosso, C.; Placido, T.; Striccoli, M.; Curri, M. L.; Agostiano, A.; Comparelli, R. Nanocomposite Materials for Photocatalytic Degradation of Pollutants. *Catal. Today* **2017**, *281*, 85–100. https://doi.org/10.1016/j.cattod.2016.05.048.

(4) Titchou, F. E.; Zazou, H.; Afanga, H.; El Gaayda, J.; Akbour, R. A.; Hamdani, M. Removal of Persistent Organic Pollutants (POPs) from Water and Wastewater by Adsorption and Electrocoagulation Process. *Groundw. Sustain. Dev.* **2021**, *13*, 100575. https://doi.org/10.1016/j.gsd.2021.100575.

(5) Bulgariu, L.; Escudero, L. B.; Bello, O. S.; Iqbal, M.; Nisar, J.; Adegoke, K. A.; Alakhras, F.; Kornaros, M.; Anastopoulos, I. The Utilization of Leaf-Based Adsorbents for Dyes Removal: A Review. *J. Mol. Liq.* **2019**, *276*, 728–747.

https://doi.org/10.1016/j.molliq.2018.12.001.

(6) Vigneshwaran, S.; Sirajudheen, P.; Karthikeyan, P.; Nabeena, C. P.; Meenakshi, S. Remediation of Persistent Organic Pesticides from Wastewater Matrices—Present and Future Conceptions. In *Energy, Environment, and Sustainability*; 2021; pp 7–37. https://doi.org/10.1007/978-981-16-0858-2_2.

(7) Rizzi, V.; Lacalamita, D.; Gubitosa, J.; Fini, P.; Petrella, A.; Romita, R.; Agostiano, A.; Gabaldón, J. A.; Fortea Gorbe, M. I.; Gómez-Morte, T.; Cosma, P. Removal of Tetracycline from Polluted Water by Chitosan-Olive Pomace Adsorbing Films. *Sci. Total Environ.* **2019**, *693*, 133620. https://doi.org/10.1016/j.scitotenv.2019.133620.

(8) Dutta, S.; Gupta, B.; Srivastava, S. K.; Gupta, A. K. Recent Advances on the Removal of Dyes from Wastewater Using Various Adsorbents: A Critical Review. *Materials Advances*. 2021, pp 4497–4531. https://doi.org/10.1039/d1ma00354b.

(9) Dalhat, M. H.; Ahmad, A. Removal of Pesticides from Water and Wastewater by Solar-Driven Photocatalysis. In *Development in Wastewater Treatment Research and Processes*; Elsevier, 2022; pp 435–458. https://doi.org/10.1016/B978-0-323-85583-9.00012-0.

(10) Rizzi, V.; Gubitosa, J.; Fini, P.; Petrella, A.; Romita, R.; Agostiano, A.; Cosma, P. A "Classic" Material for Capture and Detoxification of Emergent Contaminants for Water Purification: The Case of Tetracycline. *Environ. Technol. Innov.* **2020**, *19*, 100812. https://doi.org/10.1016/j.eti.2020.100812.

(11) Reddy, V. R.; Behera, B. Impact of Water Pollution on Rural Communities: An Economic Analysis. *Ecol. Econ.* **2006**, *58* (3), 520–537. https://doi.org/10.1016/j.ecolecon.2005.07.025.

(12) Rai, A. C.; Kumar, P.; Pilla, F.; Skouloudis, A. N.; Di Sabatino, S.; Ratti, C.; Yasar, A.; Rickerby, D. End-User Perspective of Low-Cost Sensors for Outdoor Air Pollution Monitoring. *Sci. Total Environ.* **2017**, *607–608*, 691–705. https://doi.org/10.1016/j.scitotenv.2017.06.266.

(13) Lucaci, A.-R.; Bulgariu, D.; Bulgariu, L. In Situ Functionalization of Iron Oxide Particles with Alginate: A Promising Biosorbent for Retention of Metal Ions. *Polymers (Basel).* **2021**, *13* (20), 3554. https://doi.org/10.3390/polym13203554.

(14) Palani, G.; Arputhalatha, A.; Kannan, K.; Lakkaboyana, S. K.; Hanafiah, M. M.; Kumar, V.; Marella, R. K. Current Trends in the Application of Nanomaterials for the Removal of

Pollutants from Industrial Wastewater Treatment—A Review. *Molecules* **2021**, *26* (9), 2799. https://doi.org/10.3390/molecules26092799.

(15) Bulgariu, L.; Bulgariu, D. Bioremediation of Toxic Heavy Metals Using Marine Algae Biomass; 2020; pp 69–98. https://doi.org/10.1007/978-3-030-17724-9_4.

(16) Stelo, F.; Kublik, N.; Ullah, S.; Wender, H. Recent Advances in $Bi_2MoO_6$ Based Z-Scheme Heterojunctions for Photocatalytic Degradation of Pollutants. *J. Alloys Compd.* **2020**, *829*, 154591. https://doi.org/10.1016/j.jallcom.2020.154591.

(17) Sharma, S.; Basu, S. Fabrication of Centimeter-Sized $Sb_2S_3/SiO_2$ Monolithic Mimosa Pudica Nanoflowers for Remediation of Hazardous Pollutants from Industrial Wastewater. *J. Clean. Prod.* **2021**, *280*, 124525. https://doi.org/10.1016/j.jclepro.2020.124525.

(18) Majumdar, A.; Pal, A. Recent Advancements in Visible-Light-Assisted Photocatalytic Removal of Aqueous Pharmaceutical Pollutants. *Clean Technol. Environ. Policy* **2020**, *22* (1), 11–42. https://doi.org/10.1007/s10098-019-01766-1.

(19) Jyotsna; Kaur, A.; Kansal, S. K.; Umar, A. β-$AgVO_3$ Nanowires/$TiO_2$ Nanoparticles Heterojunction Assembly with Improved Visible Light Driven Photocatalytic Decomposition of Hazardous Pollutants and Mechanism Insight. *Sep. Purif. Technol.* **2020**, *251*, 117271. https://doi.org/10.1016/j.seppur.2020.117271.

(20) Majumdar, A.; Ghosh, U.; Pal, A. Novel 2D/2D g-$C_3N_4$/$Bi_4NbO_8Cl$ Nano-Composite for Enhanced Photocatalytic Degradation of Oxytetracycline under Visible LED Light Irradiation. *J. Colloid Interface Sci.* **2021**, *584*, 320–331. https://doi.org/10.1016/j.jcis.2020.09.101.

(21) Mahamallik, P.; Pal, A. Degradation of Textile Wastewater by Modified Photo-Fenton Process: Application of Co(II) Adsorbed Surfactant-Modified Alumina as Heterogeneous Catalyst. *J. Environ. Chem. Eng.* **2017**, *5* (3), 2886–2893. https://doi.org/10.1016/j.jece.2017.05.044.

(22) Danish, M. S. S.; Estrella, L. L.; Alemaida, I. M. A.; Lisin, A.; Moiseev, N.; Ahmadi, M.; Nazari, M.; Wali, M.; Zaheb, H.; Senjyu, T. Photocatalytic Applications of Metal Oxides for Sustainable Environmental Remediation. *Metals (Basel).* **2021**, *11* (1), 80. https://doi.org/10.3390/met11010080.

(23) Munyai, S.; Hintsho-Mbita, N. C. Green Derived Metal Sulphides as Photocatalysts for Waste Water Treatment. A Review. *Curr. Res. Green Sustain. Chem.* **2021**, *4*, 100163.

https://doi.org/10.1016/j.crgsc.2021.100163.

(24) Ke, J.; Adnan Younis, M.; Kong, Y.; Zhou, H.; Liu, J.; Lei, L.; Hou, Y. Nanostructured Ternary Metal Tungstate-Based Photocatalysts for Environmental Purification and Solar Water Splitting: A Review. *Nano-Micro Lett.* **2018**, *10* (4), 69. https://doi.org/10.1007/s40820-018-0222-4.

(25) Solís, R. R.; Bedia, J.; Rodríguez, J. J.; Belver, C. A Review on Alkaline Earth Metal Titanates for Applications in Photocatalytic Water Purification. *Chem. Eng. J.* **2021**, *409*, 128110. https://doi.org/10.1016/j.cej.2020.128110.

(26) Islam, S. E.; Hang, D.-R.; Chen, C.-H.; Chou, M. M. C.; Liang, C.-T.; Sharma, K. H. Rational Design of Hetero-Dimensional C-ZnO/$MoS_2$ Nanocomposite Anchored on 3D Mesoporous Carbon Framework towards Synergistically Enhanced Stability and Efficient Visible-Light-Driven Photocatalytic Activity. *Chemosphere* **2021**, *266*, 129148. https://doi.org/10.1016/j.chemosphere.2020.129148.

(27) Madhusudan, P.; Ran, J.; Zhang, J.; Yu, J.; Liu, G. Novel Urea Assisted Hydrothermal Synthesis of Hierarchical $BiVO_4$/$Bi_2O_2CO_3$ Nanocomposites with Enhanced Visible-Light Photocatalytic Activity. *Appl. Catal. B Environ.* **2011**, *110*, 286–295. https://doi.org/10.1016/j.apcatb.2011.09.014.

(28) Tian, G.; Fu, H.; Jing, L.; Xin, B.; Pan, K. Preparation and Characterization of Stable Biphase $TiO_2$ Photocatalyst with High Crystallinity, Large Surface Area, and Enhanced Photoactivity. *J. Phys. Chem. C* **2008**, *112* (8), 3083–3089. https://doi.org/10.1021/jp710283p.

(29) Chen, X.; Wu, Z.; Liu, D.; Gao, Z. Preparation of ZnO Photocatalyst for the Efficient and Rapid Photocatalytic Degradation of Azo Dyes. *Nanoscale Res. Lett.* **2017**, *12* (1), 143. https://doi.org/10.1186/s11671-017-1904-4.

(30) Huang, G.; Zhu, Y. Synthesis and Photocatalytic Performance of $ZnWO_4$ Catalyst. *Mater. Sci. Eng. B* **2007**, *139* (2–3), 201–208. https://doi.org/10.1016/j.mseb.2007.02.009.

(31) Huang, S.-T.; Lee, W. W.; Chang, J.-L.; Huang, W.-S.; Chou, S.-Y.; Chen, C.-C. Hydrothermal Synthesis of $SrTiO_3$ Nanocubes: Characterization, Photocatalytic Activities, and Degradation Pathway. *J. Taiwan Inst. Chem. Eng.* **2014**, *45* (4), 1927–1936. https://doi.org/10.1016/j.jtice.2014.02.003.

(32) Huang, S.; Chen, C.; Tsai, H.; Shaya, J.; Lu, C. Photocatalytic Degradation of

Thiobencarb by a Visible Light-Driven $MoS_2$ Photocatalyst. *Sep. Purif. Technol.* **2018**, *197*, 147–155. https://doi.org/10.1016/j.seppur.2018.01.009.

(33) Monga, D.; Basu, S. Enhanced Photocatalytic Degradation of Industrial Dye by G-$C_3N_4$ /$TiO_2$ Nanocomposite: Role of Shape of $TiO_2$. *Adv. Powder Technol.* **2019**, *30* (5), 1089–1098. https://doi.org/10.1016/j.apt.2019.03.004.

(34) Ghosh, D.; Devi, P.; Kumar, P. Intercalation in 2D Transition Metal Chalcogenides: Interlayer Engineering and Applications. *Prog. Energy* **2021**, *4* (2), 022001. https://doi.org/10.1088/2516-1083/ac3c3d.

(35) Islam, S. E.; Hang, D.-R.; Chen, C.-H.; Sharma, K. H. Facile and Cost-Efficient Synthesis of Quasi-0D/2D ZnO/$MoS_2$ Nanocomposites for Highly Enhanced Visible-Light-Driven Photocatalytic Degradation of Organic Pollutants and Antibiotics. *Chem. - A Eur. J.* **2018**, *24* (37), 9305–9315. https://doi.org/10.1002/chem.201801397.

(36) Monga, D.; Sharma, S.; Shetti, N. P.; Basu, S.; Reddy, K. R.; Aminabhavi, T. M. Advances in Transition Metal Dichalcogenide-Based Two-Dimensional Nanomaterials. *Mater. Today Chem.* **2021**, *19*, 100399. https://doi.org/10.1016/j.mtchem.2020.100399.

(37) Hu, Z.; Wu, Z.; Han, C.; He, J.; Ni, Z.; Chen, W. Two-Dimensional Transition Metal Dichalcogenides: Interface and Defect Engineering. *Chem. Soc. Rev.* **2018**, *47* (9), 3100–3128. https://doi.org/10.1039/C8CS00024G.

(38) Mouri, S.; Miyauchi, Y.; Matsuda, K. Tunable Photoluminescence of Monolayer $MoS_2$ via Chemical Doping. *Nano Lett.* **2013**, *13* (12), 5944–5948. https://doi.org/10.1021/nl403036h.

(39) Zhou, X.; Sun, H.; Bai, X. Two-Dimensional Transition Metal Dichalcogenides: Synthesis, Biomedical Applications and Biosafety Evaluation. *Front. Bioeng. Biotechnol.* **2020**, *8*. https://doi.org/10.3389/fbioe.2020.00236.

(40) Kundu, S.; Ma, L.; Chen, Y.; Liang, H. Microwave Assisted Swift Synthesis of $ZnWO_4$ Nanomaterials: Material for Enhanced Photo-Catalytic Activity. *J. Photochem. Photobiol. A Chem.* **2017**, *346*, 249–264. https://doi.org/10.1016/j.jphotochem.2017.05.004.

(41) Choi, W.; Choudhary, N.; Han, G. H.; Park, J.; Akinwande, D.; Lee, Y. H. Recent Development of Two-Dimensional Transition Metal Dichalcogenides and Their Applications. *Mater. Today* **2017**, *20* (3), 116–130. https://doi.org/10.1016/j.mattod.2016.10.002.

(42) Monga, D.; Ilager, D.; Shetti, N. P.; Basu, S.; Aminabhavi, T. M. 2D/2d Heterojunction of $MoS_2$/g-$C_3N_4$ Nanoflowers for Enhanced Visible-Light-Driven Photocatalytic and Electrochemical Degradation of Organic Pollutants. *J. Environ. Manage.* **2020**, *274*, 111208. https://doi.org/10.1016/j.jenvman.2020.111208.

(43) Jaswal, A.; Kaur, M.; Singh, S.; Kansal, S. K.; Umar, A.; Garoufalis, C. S.; Baskoutas, S. Adsorptive Removal of Antibiotic Ofloxacin in Aqueous Phase Using RGO-$MoS_2$ Heterostructure. *J. Hazard. Mater.* **2021**, *417*, 125982. https://doi.org/10.1016/j.jhazmat.2021.125982.

(44) Sheng, B.; Yang, F.; Wang, Y.; Wang, Z.; Li, Q.; Guo, Y.; Lou, X.; Liu, J. Pivotal Roles of $MoS_2$ in Boosting Catalytic Degradation of Aqueous Organic Pollutants by Fe(II)/PMS. *Chem. Eng. J.* **2019**, *375*, 121989. https://doi.org/10.1016/j.cej.2019.121989.

(45) Yuan, Y.; Guo, R. tang; Hong, L. fei; Ji, X. yin; Li, Z. sheng; Lin, Z. dong; Pan, W. guo. Recent Advances and Perspectives of $MoS_2$-Based Materials for Photocatalytic Dyes Degradation: A Review. *Colloids and Surfaces A: Physicochemical and Engineering Aspects*. February 2021, p 125836. https://doi.org/10.1016/j.colsurfa.2020.125836.

(46) Belver, C.; Bedia, J.; Gómez-Avilés, A.; Peñas-Garzón, M.; Rodriguez, J. J. Semiconductor Photocatalysis for Water Purification. In *Nanoscale Materials in Water Purification*; Elsevier, 2019; pp 581–651. https://doi.org/10.1016/B978-0-12-813926-4.00028-8.

(47) Fu, Y.; Li, J.; Li, J. Metal/Semiconductor Nanocomposites for Photocatalysis: Fundamentals, Structures, Applications and Properties. *Nanomaterials* **2019**, *9* (3), 359. https://doi.org/10.3390/nano9030359.

(48) Di, J.; Xia, J.; Ge, Y.; Xu, L.; Xu, H.; Chen, J.; He, M.; Li, H. Facile Fabrication and Enhanced Visible Light Photocatalytic Activity of Few-Layer $MoS_2$ Coupled BiOBr Microspheres. *Dalt. Trans.* **2014**, *43* (41), 15429–15438. https://doi.org/10.1039/C4DT01652A.

(49) Min, Y.; He, G.; Xu, Q.; Chen, Y. Dual-Functional $MoS_2$ Sheet-Modified CdS Branch-like Heterostructures with Enhanced Photostability and Photocatalytic Activity. *J. Mater. Chem. A* **2014**, *2* (8), 2578. https://doi.org/10.1039/c3ta14240j.

(50) Li, H.; Yu, K.; Lei, X.; Guo, B.; Fu, H.; Zhu, Z. Hydrothermal Synthesis of Novel $MoS_2$/$BiVO_4$ Hetero-Nanoflowers with Enhanced Photocatalytic Activity and a

Mechanism Investigation. *J. Phys. Chem. C* **2015**, *119* (39), 22681–22689. https://doi.org/10.1021/acs.jpcc.5b06729.

(51) Vattikuti, S. V. P.; Byon, C.; Reddy, C. V.; Ravikumar, R. V. S. S. N. Improved Photocatalytic Activity of $MoS_2$ Nanosheets Decorated with $SnO_2$ Nanoparticles. *RSC Adv.* **2015**, *5* (105), 86675–86684. https://doi.org/10.1039/c5ra15159g.

(52) Chu, H.; Lei, W.; Liu, X.; Li, J.; Zheng, W.; Zhu, G.; Li, C.; Pan, L.; Sun, C. Synergetic Effect of $TiO_2$ as Co-Catalyst for Enhanced Visible Light Photocatalytic Reduction of Cr(VI) on $MoSe_2$. *Appl. Catal. A Gen.* **2016**, *521*, 19–25. https://doi.org/10.1016/j.apcata.2016.01.022.

(53) Ho, W.; Yu, J. C.; Lin, J.; Yu, J.; Li, P. Preparation and Photocatalytic Behavior of $MoS_2$ and $WS_2$ Nanocluster Sensitized $TiO_2$. *Langmuir* **2004**, *20* (14), 5865–5869. https://doi.org/10.1021/la049838g.

(54) Mittal, H.; Kumar, A.; Khanuja, M. In-Situ Oxidative Polymerization of Aniline on Hydrothermally Synthesized $MoSe_2$ for Enhanced Photocatalytic Degradation of Organic Dyes. *J. Saudi Chem. Soc.* **2019**, *23* (7), 836–845. https://doi.org/10.1016/j.jscs.2019.02.004.

(55) Weng, B.; Zhang, X.; Zhang, N.; Tang, Z. R.; Xu, Y. J. Two-Dimensional $MoS_2$ Nanosheet-Coated $Bi_2S_3$ Discoids: Synthesis, Formation Mechanism, and Photocatalytic Application. *Langmuir* **2015**, *31* (14), 4314–4322. https://doi.org/10.1021/la504549y.

(56) Yan, J.; Chen, Z.; Ji, H.; Liu, Z.; Wang, X.; Xu, Y.; She, X.; Huang, L.; Xu, L.; Xu, H.; Li, H. Construction of a 2D Graphene-Like $MoS_2/C_3N_4$ Heterojunction with Enhanced Visible-Light Photocatalytic Activity and Photoelectrochemical Activity. *Chem. - A Eur. J.* **2016**, *22* (14), 4764–4773. https://doi.org/10.1002/chem.201503660.

(57) Zhu, C.; Jiang, Z.; Wei, W.; Chen, L.; Liu, D.; Qian, K.; Lü, X.; Xie, J. Fabrication of Noble-Metal-Free $NiS_2$/g-$C_3N_4$ Hybrid Photocatalysts with Visible Light-Responsive Photocatalytic Activities. *Res. Chem. Intermed.* **2016**, *42* (8), 6483–6499. https://doi.org/10.1007/s11164-016-2475-1.

(58) Zhao, W.; Liu, Y.; Wei, Z.; Yang, S.; He, H.; Sun, C. Fabrication of a Novel p–n Heterojunction Photocatalyst n-$BiVO_4$@p-$MoS_2$ with Core–Shell Structure and Its Excellent Visible-Light Photocatalytic Reduction and Oxidation Activities. *Appl. Catal. B Environ.* **2016**, *185*, 242–252. https://doi.org/10.1016/j.apcatb.2015.12.023.

# CHAPTER 2:

## *2D/2D Heterojunction of $MoS_2$/g-$C_3N_4$ Nanoflowers for Enhanced Visible-Light Driven Catalytic Degradation of Organic Pollutants*

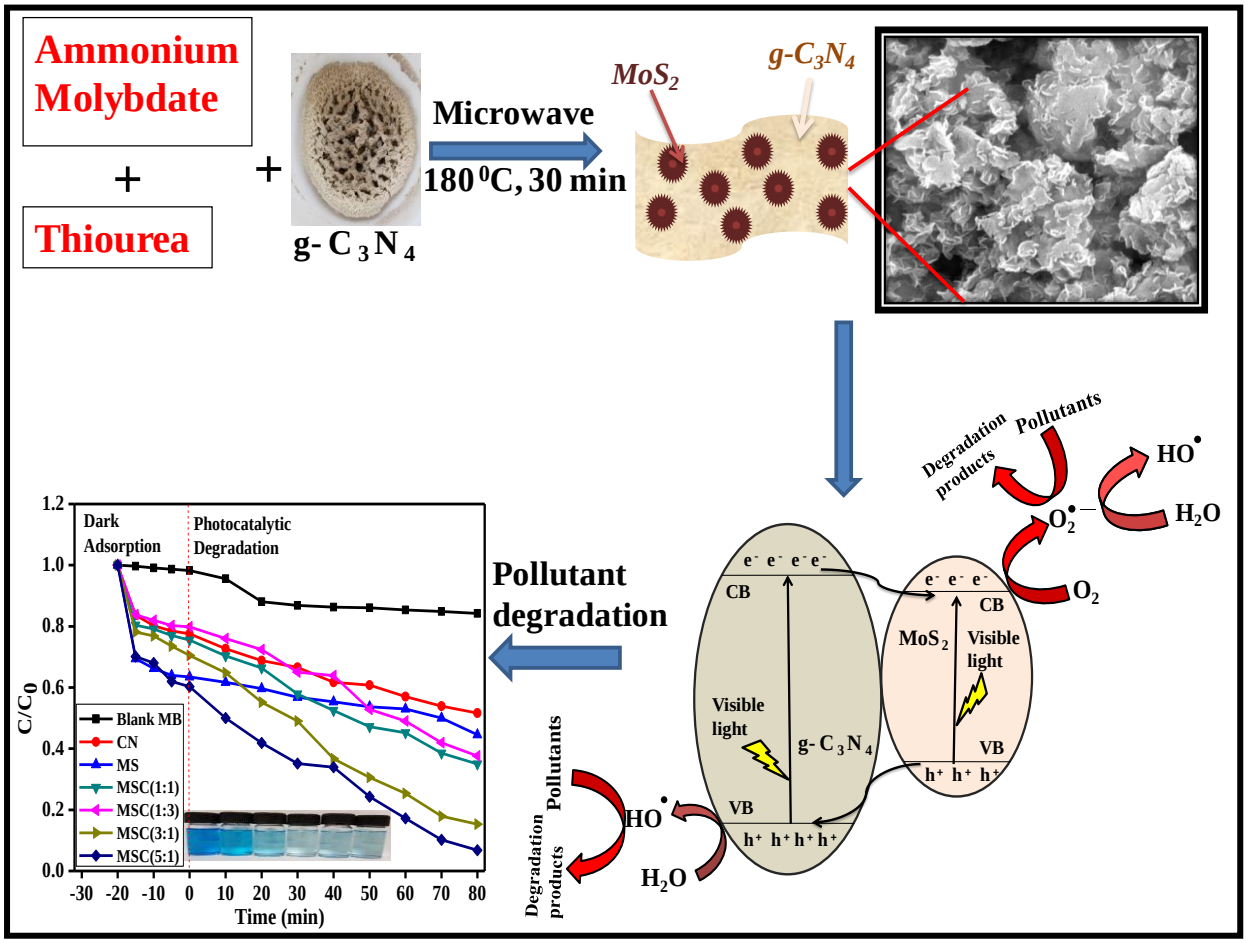


## Highlights

- ✓ $MoS_2$/g-$C_3N_4$ composites with different weight ratio were synthesized by microwave method.
- ✓ Visible light active nanocomposites are highly effective for toxic pollutant degradation.
- ✓ Degradation efficiency was remarkably affected by the amount of $MoS_2$ and g-$C_3N_4$.
- ✓ Electrochemical degradation of methylene blue was studied using $MoS_2$/g-$C_3N_4$ modified GCE.

## 2.1 Introduction

Dyes and pesticides from various industrial sectors pollute the water bodies and hence degradation of such pollutants from the wastewater sources is essential.[1] Dyes,[2] pharmaceuticals[3] and pesticides [4,5] are now target products in wastewater treatment. Methylene blue is a blue colored dye commonly used in textile and paper industries. The higher concentration of this pollutant can lead to various neurodegenerative diseases. The complex carbon structure along with nitrogen and sulfur moieties can also affect photosynthesis by absorbing different wavelength of light radiations. Fipronil is another colorless organic pollutant commonly used in agriculture fields and its minimal amount can cause many cardiovascular and hormonal issues in human beings. The structure of fipronil closely interacts with thyroid hormones thus disrupting the hormonal system in human beings.[6,7] The studies generally focus on the photocatalytic treatment of pollutants by developing photocatalysts that are very active and effective in the presence of visible light.[8]

Recently, polymeric semiconductor g-$C_3N_4$ (graphitic carbon nitride) has drawn an incredible attention in the area of photocatalysis.[9–11] Due to its high physico-chemical stability, facile and simple synthesis, "earth-ample" nature and captivating the structure of its electronic band, it is a broadly used material in photocatalysis, since it has a band gap energy of 2.7 eV, so active in the visible region.[12] Its photocatalytic degradation efficiency is fairly weak due to less light absorption tendency and also a high rate of electron-hole recombination. Therefore a photoactive material with g-$C_3N_4$ will provide the oxidation or reduction sites to decrease the recombination of charge, and also to trap the charge carriers.[13,14]

Generally, g-$C_3N_4$ is coupled with either other semiconductors or some transition metal dichalcogenides (TMDC) to increase its photocatalytic performance. Molybdenum disulfide ($MoS_2$) is an element of TMDC family, which is abundant in nature with its high chemical stability, low cost, and high catalytic performance. [15–18] The energy band levels of $MoS_2$ and g-$C_3N_4$ are optimum to one other and photocatalytic performance of $MoS_2$ is high under both UV and visible light irradiations as its band gap energy is 1.9 eV.[19] Furthermore, the photocatalysts having flower-like structure exhibit a greater interfacial transfer of electrons and have a lower rate of recombination than that of spherical nanoparticles.[16] Peng *et al.*[20] have prepared $MoS_2$/g-$C_3N_4$ hybrids for organic pollutant degradation using the hydrothermal methods to load $MoS_2$

nanoparticles onto g-$C_3N_4$ having the degradation efficiency of 60%. Graphene-like $MoS_2$/g-$C_3N_4$ was constructed through ethylene glycol-assisted solvothermal method by Yan *et al.*[21] for selective detection and analysis of trace heavy metal ions in aqueous samples. Li *et al.*[22] observed the variation of degradation efficiency for variable $MoS_2$/g-$C_3N_4$ prepared by different heating rates. But these techniques are time-consuming and require high temperature/pressure and hence, are not cost-effective and eco-friendly. Literature suggests scanty data on $MoS_2$/g-$C_3N_4$ nanocomposites synthesized using microwave-assisted techniques and hence, motivation to prepare $MoS_2$/g-$C_3N_4$ nanocomposites having a large surface area from the simple precursors, which can be both time and cost-effective.

Electrochemical methods have recently attracted much interest because they are more affordable, less tedious, sensitive, selective and offer an effective method to solve problems related to domestic, industrial and environment arenas. Innumerable studies have shown interest to degrade methylene blue dye via electrochemical method.[23–28] As per literature, no report is yet present where $MoS_2$/g-$C_3N_4$ hybrids modified GCE (glassy carbon electrode) for electrochemical oxidation of methylene blue. Hence an attempt has been made to degrade methylene blue dye at different ratios of $MoS_2$/g-$C_3N_4$ hybrids modified GCE ($MoS_2$/g-$C_3N_4$/GCE) at different pH values.

In this work, an attempt has been made to prepare a series of $MoS_2$/g-$C_3N_4$ nanocomposites with various weight ratios (1:1, 1:3, 3:1 and 5:1) and their photocatalytic activities was examined under the illumination of various light sources (UV, visible and sunlight). By changing the morphology and weight ratios, degradation efficiency can be modified. The degradation of methylene blue dye and fipronil pesticide was studied to determine the photo-electrocatalytic degradation of the dye and pesticide. A scavenger study was also done to determine the degradation mechanism. The effect of illumination area, pH, catalyst dose and reusability of the catalyst were studied.

## 2.2 Characterization methods and photo/electrocatalytic techniques

### 2.2.1 Characterization methods

Various optical, surface, and structure determining characterization techniques were used to examine the as-prepared nanocatalysts. The following sections provide thorough descriptions of several techniques:

- **UV-Visible Spectroscopy:** The Shimadzu UV-2450, was used to examine the absorption characteristics of liquid samples in the 190-1100 nm wavelength range. With diffuse reflectance spectroscopy (DRS, Shimazdu) and barium sulphate ($BaSO_4$) as an internal reference, the optical characteristics of powder solid samples of catalysts were examined.

- **Photolumiscence (PL) Spectroscopy:** PL emission spectra of different photocatalysts were analyzed on Shimadzu Fluorimeter, in the wavelength range of 200- 800nm The experiment was conducted by dispersing the samples in distilled water/ethanol mixture.

- **Surface area analyzer:** The surface area of the catalysts was determined using the Brunner-Emmet-Teller (BET) equation depending on $N_2$ adsorption-desorption using the BEL mini-II, Micro Trac Corp. Pvt. Ltd (Tokyo, Japan) instrument. To remove the adsorbed gas and water molecules, the sample is first heated (150-200$^oC$). Using liquid nitrogen, the analysis was carried out at -195$^oC$. The pore size and volume were determined using the Barrett-Joyner-Halenda (BJH) analytical curves.

- **X-ray diffraction (XRD) spectroscopy:** XRD method were utilized to study the diffraction pattern, phases, lattice planes and crystal structure of the catalyst using PANalytical Xpert Pro by Cu Kα at 1.54Å at 45 kV with a diffraction angle of 10-80$^o$ and 5$^o$/min scan speed.

- **Morphological studies:** Field Emission Scanning Electron Microscopy (FESEM), and transmission electron microscopy (TEM) were used to determine structural parameters such as shape and particle size of as-prepared nanocatalysts. The FESEM images were acquired through ZEISS FESEM at an accelerating voltage of 5 kV and the high resolution transmission electron microscope (HRTEM) of Thermofischer (model: Talos F200 S) has been used for the structural studies of the as-prepared catalyst.

- **Elemental analysis:** The XPS technique was used to investigate the quantitative elemental composition, oxidation state, and bonding of elements. Line profile or elemental colour dot EDS (Energy dispersive X-ray spectrometer) mapping was used to identify the composition of each element. The X-ray photon spectroscopy (XPS) was performed using PHI-5000 VersaProbe III system. Oxford INCA energy dispersive

spectrometer (EDS) operational at an accelerating voltage of 5 kV was employed to acquire SEM-EDS and elemental mapping images.

### 2.2.2 Photocatalytic and electrocatalytic studies

*Photocatalytic studies*

To determine the photocatalytic activity of the catalysts, a powder catalyst was put into the pollutant solution. The adsorption-desorption equilibrium was established by stirring the solution in a completely dark environment. Then the reaction solution was illuminated by either UV lamp having a $\lambda_{max}$ of 365 nm (100 WHg lamp), visible light (65W CFL lamp, Phillips, k > 400 nm with intensity of 125 W/m$^2$) or sunlight (at TIET, Patiala, India). The powder catalyst was removed from the solution by centrifugation. UV-Vis spectrophotometer (Shimadzu UV-2600) was employed to investigate the absorbance spectra of pollutant solution in 200-1100 nm wavelength range. The photodegradation efficiency was determined using the relation:

Degradation efficiency = $\{(C_0 - C) / C_0\} \times 100 = \{(A_0 - A)/ A_0\} \times 100$

where $C_0$, C: concentration of pollutant solution at 0 and t time, respectively and $A_0$ and A: absorbance of pollutant at 0 and t time, respectively.

COD (chemical oxygen demand) and TOC studies were also done to study raw industrial waste water degradation. The COD values were determined using the titrimetric method. TOC was used to study the mineralization of real waste water. The COD and TOC measurements were done before and after photocatalytic treatment of polluted water under visible light irradiation using photocatalyst.

Percent COD and TOC were calculated using:

$\%COD = \{(COD_0 - COD_t)/ COD_0\} \times 100$

where $COD_0$, $COD_t$ are the COD of real waste water at time '0' and't' respectively.

$\%TOC = \{(TOC_0 - TOC_t)/ TOC_0\} \times 100$

where $TOC_0$, $TOC_t$ are the TOC of real waste water at time '0' and't' respectively.

*Electrocatalytic studies*

The as-prepared samples were investigated for their electrocatalytic activity test using Bio-logic EC Lab SP300 standard setup. Out of the three electrodes in the system; platinum was used as the counter electrode, whereas the working electrode was prepared manually. For fabrication of working electrode, 1mg of the catalyst was mixed with 250 µL and the solution was sonicated for 25 min to achieve uniform dispersion of particles. The top of glassy carbon electrode (GCE), which has the surface area of 0.070 $cm^2$, was drop-casted by 20 µL of the above dispersed solution. A single drop of Nafion 117 solution (Sigma Aldrich) from 10 µLwas put onto the GCE top and was dried overnight. The measurements were done using a reversible hydrogen electrode (RHE) as the reference electrode in the 0.5M $H_2SO_4$ electrolyte solution.

## 2.3 Method of Synthesis

### Materials used

Analytical grade reagents and double distilled water for the preparation of solutions was used throughout the experiment. Urea $[CH_4N_2O]$, thiourea $[CH_4N_2S]$ and methylene blue dye $[C_{16}H_{18}ClN_3S$, $\lambda_{max}$ = 664 nm] was acquired from Spectrochem Pvt. Ltd. India. Ammonium molybdate tetrahydrate (98%) $[(NH_4)_6Mo_7O_{24}.4H_2O]$ was purchased from Loba Chemie Pvt. Ltd. India. Fipronil 5% SC was acquired from Bayer Crop Science Ltd. India. Phosphate buffer solution, I = 0.2 M (PBS) pH 3.0–9.0 to carry out the electrochemical measurements was prepared according to literature. Electrochemical experiments were performed in a 10ml electrochemical cell with 3 electrode system, with a counter electrode of platinum wire, a reference electrode of Ag/AgCl and different ratio of $MoS_2$ and g-$C_3N_4$ hybrids modified GCE (working electrode) connected to an electrochemical analyzer of CHI Company, USA (Model D630). For testing pH of the buffer solution the Elico pH meter was used.

### Graphitic carbon nitride (g-$C_3N_4$) synthesis

Firstly, urea (12 g) was loaded into a silica crucible and recrystallized by dissolving in 50 mL of water and kept in an oven (12 h). The recrystallized urea was covered with an aluminum foil and heated to 550°C in a muffle furnace by increasing the temperature of

10°C/min for 2 h. The yellow-brown colored solid g-$C_3N_4$ obtained was grounded using a mortar-pestle into fine powder and is denoted as CN.[29]

**Synthesis of $MoS_2$**

About 0.4 g of ammonium molybdate tetrahydrate and 0.8 g of thiourea were added in 10 mL of deionized water with stirring and sonication for 30 min and 1 hour respectively. After sonication, the solution was poured in a 30 mL microwave glass vial, kept in a microwave synthesizer (Anton Paar Monowave 300) to heat up the solution at 180°C for 30 min. The resultant mixture with black colour solid was washed with deionized water 5-6 times by centrifugation. After washing, the black coloured mixture was dried at 60°C in a hot air oven. The mat-black coloured powder obtained was $MoS_2$ and denoted as MS.[30,31]

**Synthesis of different weight ratios of $MoS_2$/g-$C_3N_4$ nanocomposites (1:1, 1:3, 3:1 and 5:1)**

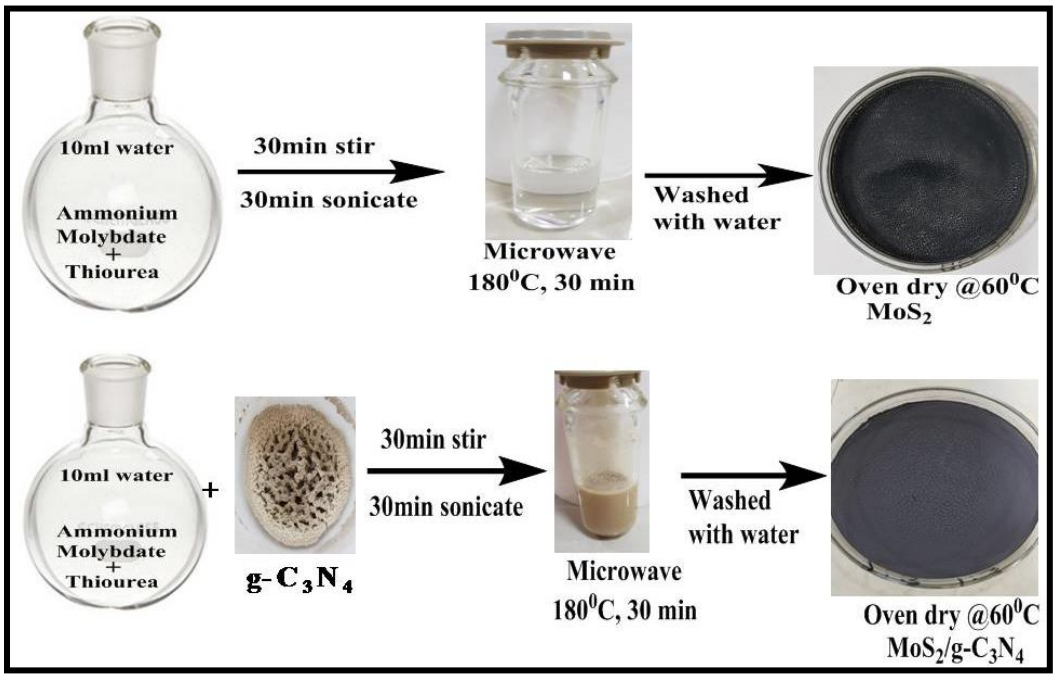


**Scheme 2.1.** Synthesis scheme for different $MoS_2$/g-$C_3N_4$ catalysts.

Four different $MoS_2$/g-$C_3N_4$ nanocomposites were synthesized with variable weight ratios. In general, 0.4 g of ammonium molybdate tetrahydrate and 0.8 g of thiourea were added in 10 mL of distilled water and a desired amount of g-$C_3N_4$ was taken into the solution under stirring and sonication for 30 min and 1 hour, respectively. After sonication, the mixture was poured in a 30 mL microwave glass vial and the solution was heated in a

microwave at 180°C for 30 min. The resultant mixture with grayish-black colour was washed with deionized water 5-6 times by centrifugation and allowed to be dried at 60°C in a hot air oven for 6 h. The shining grayish-black coloured crystals of $MoS_2$/g-$C_3N_4$ nanocomposite [32] were obtained that are named as MSC (1:1), MSC (1:3), MSC (3:1), and MSC (5:1), where inside bracket denote the weight ratios of $MoS_2$ and g-$C_3N_4$. The pictorial representation to synthesize $MoS_2$/g-$C_3N_4$ nanocomposites is shown in Scheme 2.1.

**Preparation of electrodes**

The synthesized MSC photocatalysts were dispersed with the help of ultrasonicator in deionized water (10 mL). To polish the surface of GCE, particles of alumina (3.0 nm size) were used. To remove the settled particles on the surface of electrode, the electrode was rinsed first with ethanol and then with deionized water. After that 25 µL of $MoS_2$/g-$C_3N_4$ hybrids suspension was coated onto the clean GCE and then dried in air. Cyclic voltammograms in phosphate buffer solution (pH 7) were recorded with potential window between -0.50 V and 0.20 V to activate the electrode.

## 2.4 Characterization studies

### 2.4.1 XPS spectral studies

The XPS survey spectra of MSC composite (Fig. 2.1a) confirms the presence of C, Mo, N and S elements. Two peaks observed in C1s spectra (Fig. 2.1b), one at 284.30 eV and the other at 287.5 eV attributes to the adventitious carbon and coordination of N-C=N present in g-$C_3N_4$, respectively. Also, the two peaks in Mo 3d spectra at 227.8 eV and 231.8 eV in Fig. 2.1c belong to Mo $3d_{5/2}$ and Mo $3d_{3/2}$, correspondingly. One more peak at 225.1 eV appeared in this region and belongs to S 2s of $MoS_2$. A peak of O 1s in Fig. 2.1d at 531 eV is attributed to the adsorbed $CO_2$ or $H_2O$. Fig. 2.1e shows the spectrum of S; one peak at 161.3 eV is attributed to S $2p_{3/2}$, and one peak around 163 eV corresponds to S $2p_{1/2}$. The N1s peaks in Fig. 2.1f could be deconvoluted as one peak at 398.14 eV related to the presence of C=N-C coordination in the sample, whereas the peak at 399.6 eV is due to N-$(C)_3$ and the one at 403.29 eV belongs to N-H structures of the nanocomposite.[33,34]

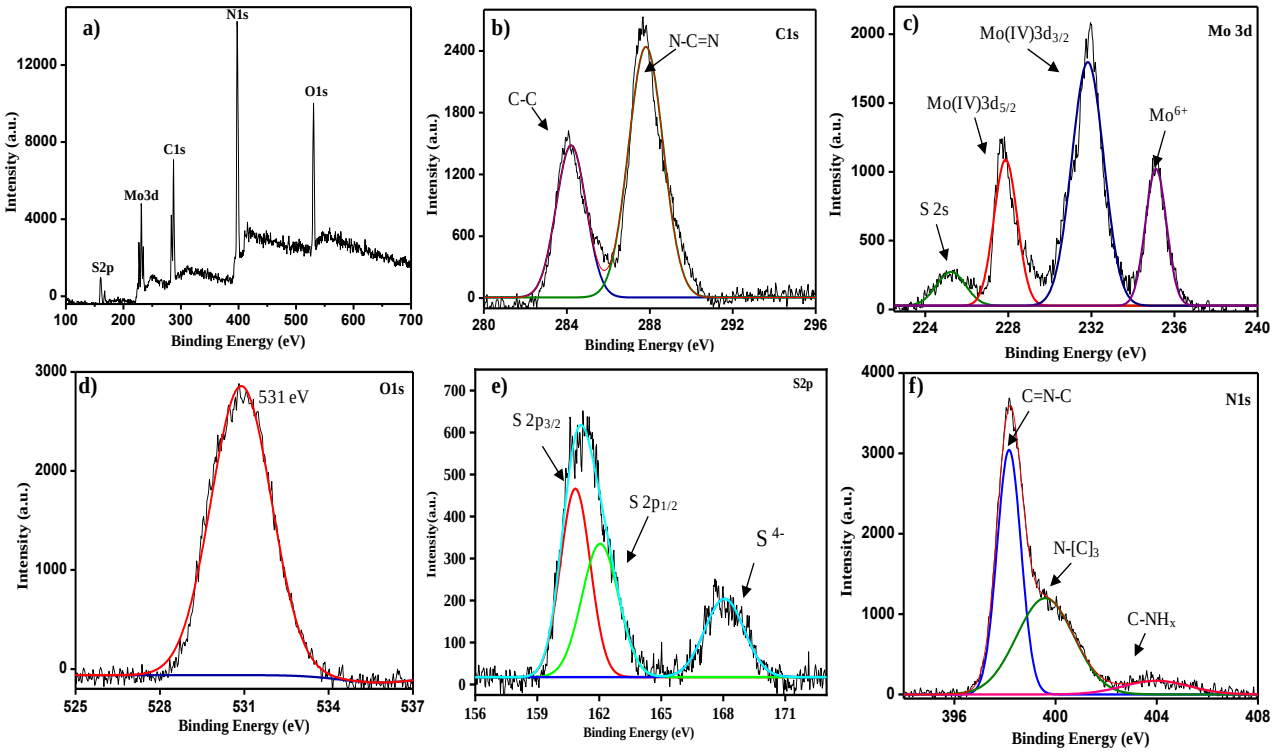


**Fig. 2.1.** XPS spectra of $MoS_2$/g-$C_3N_4$ (1:1) nanocomposite; (a) survey spectrum and deconvoluted peaks for (b) C 1s, (c) Mo 3d, (d) O 1s, (e) S 2p and (f) N 1s.

### 2.4.2 Photoluminiscence studies

The transfer behavior of charge carriers can be analyzed through the photoluminescence (PL) emission spectrum. In the present study the PL spectra of CN, MS, MSC (1:1, 1:3, 3:1 and 5:1) are shown in Fig. 2.2. If more charge carriers recombine then the intensity of PL spectra is higher. So lower the intensity of PL spectrum suggests that higher the number of charge carriers which take part in the degradation process.[35] The PL spectrum of all the nanocomposites exhibits a broad emission peak centered around 440 nm. The pure g-$C_3N_4$ exhibit the highest PL intensity among the samples. The intensity of PL spectra suggests that higher charge carriers are available for the degradation after the addition of $MoS_2$ in the composite. As the PL intensity of MSC (5:1) is the lowest among all the composites and it indicates that the lower recombination rate which might be responsible for its higher photocatalytic activity.

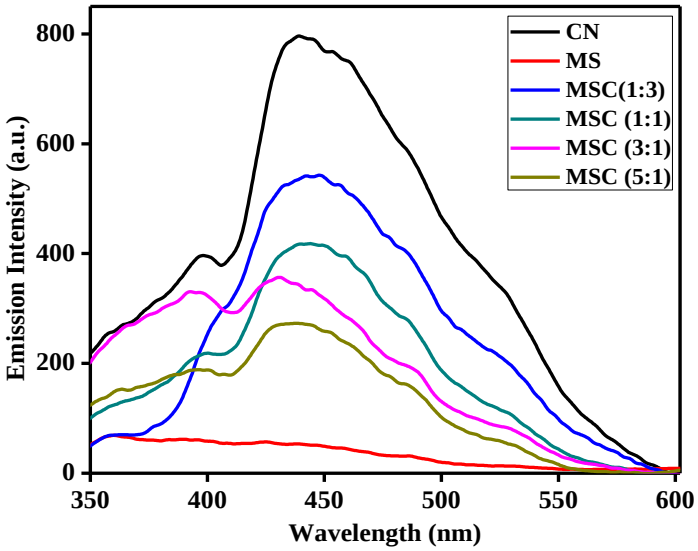


**Fig. 2.2.** PL spectra of $MoS_2$, g-$C_3N_4$ and MSC composites.

### 2.4.3 UV-Visible DRS

Absorption spectra of the catalysts are introduced in Fig. 2.3a. The energy band gaps of all the photocatalysts (CN, MS, MSC (1:1, 1:3, 3:1 and 5:1) are determined using the tauc plot shown in Fig. 2.3b. The energy band gap of pure CN and MS are at ~2.6 eV and 2.04 eV, respectively. With increasing concentration of $MoS_2$ in the nanocomposite the band gap follows the order: CN> MS> MSC(1:1)> MSC(1:3)> MSC(3:1)> MSC(5:1). With the lowering of band gap energy, adsorption of light shifts more to the visible section thus enhancing the photocatalytic performance of the nanocomposites in the visible region.

By using this band gap energy, the band gap edge potential of the conduction band valence band can be determined by using the following formula: [36]

$$EVB = X - E_e + 0.5\ E_g$$

$$ECB = EVB - E_g$$

Where EVB is the valence band edge potential, ECB is the conduction band edge potential. X represents the absolute electronegativity of the semiconductor materials. $E_e$ is the estimated energy of the free electrons on the hydrogen scale, which is approximately 4.5 eV. [37] $E_g$ is the band gap mobility of the semiconductor materials. By using the above equation, the calculated valence band (VB) and conduction band (CB) edge potentials for

the $MoS_2$ are 1.33 eV and -0.70 eV respectively. Whereas the VB and CB band edge potential for g-$C_3N_4$ are 1.61 eV and -1.09 eV respectively. Through the material interface these edge potentials favors the migration of photogenerated charge carriers.

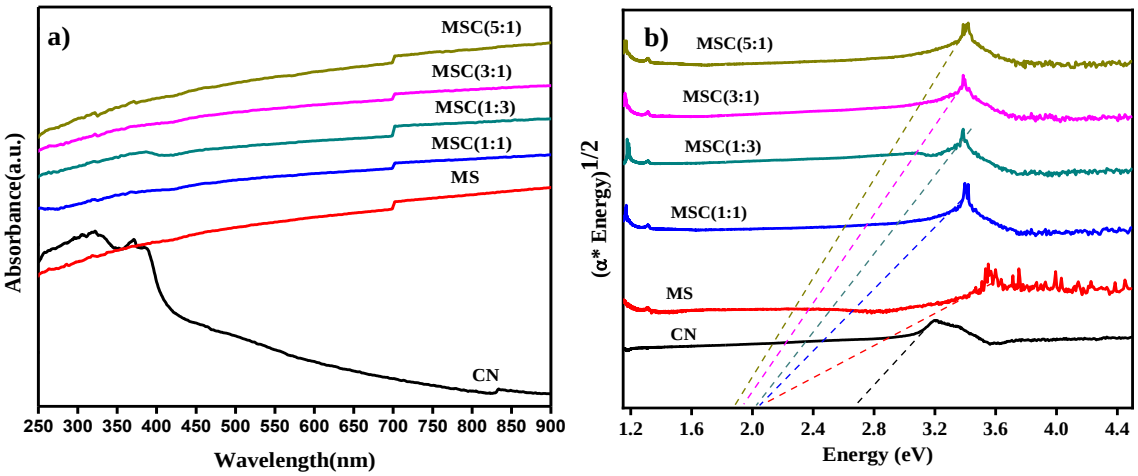


**Fig. 2.3.** (a) UV-visible diffuse reflectance spectra and (b) Tauc plots of as prepared composites.

### 2.4.4 XRD

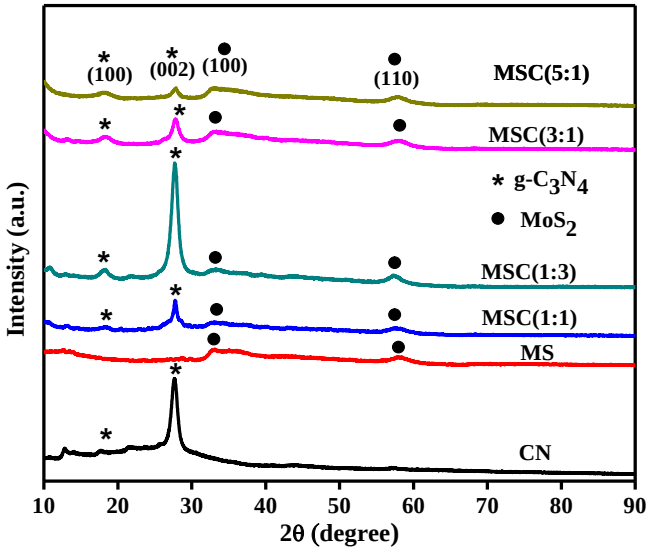


**Fig. 2.4.** XRD patterns of as-prepared $MoS_2$, g-$C_3N_4$ and MSC composites.

Diffraction patterns of MS, CN and different composites of MSC are represented in Fig. 2.4. The diffraction peaks observed at 2θ ~ 32.9° (100) and 58.1° (110) are the characteristic diffraction peaks of $MoS_2$ (JCPDS 37-1492). The peaks observed at 2θ ~ 12.7° (100) and at 28° (002) (JCPDS 87-1526) are ascribed to the crystal planes of g-$C_3N_4$

(CN). Spectra of all the composites show the presence of both types of peaks, which confirms the successful incorporation of $MoS_2$ into g-$C_3N_4$.[15,20]

### 2.4.5 Nitrogen sorption studies

The Fig. 2.5 shows the $N_2$ adsorption-desorption isotherms of $MoS_2$ (MS) and different composites of $MoS_2$ and g-$C_3N_4$. Fig. 2.5a confirms that all the samples prepared have the Langmuir type-IV isotherm including the characteristics of mesoporous nature. The distribution of pore size as illustrated by the BJH curve (Fig. 2.5b) validates the incidence of mesopores in the as prepared samples.

**Table 2.1.** Specific surface area, mean pore diameter, and pore volume of as-prepared materials.

| | **MS** | **CN** | **MSC(1:1)** | **MSC(1:3)** | **MSC(3:1)** | **MSC(5:1)** |
|---|---|---|---|---|---|---|
| **Specific surface area ($m^2/g$)** | 73 | 52 | 12 | 4.9 | 35 | 47 |
| **Mean pore diameter (nm)** | 22.7 | 35.1 | 17.3 | 19.0 | 17.1 | 18.2 |
| **Mesopore volume ($cm^3/g$)** | 0.682 | 0.310 | 0.053 | 0.023 | 0.181 | 0.209 |
| **Total pore volume ($cm^3/g$)** | 0.701 | 0.321 | 0.054 | 0.024 | 0.188 | 0.212 |

The specific surface area, mesopore volume, mean pore diameter and total pore volume of $MoS_2$ and g-$C_3N_4$ composites as given in Table 2.1, demonstrate that the prepared nanocomposites have a lower surface area than those of pure $MoS_2$ (MS) and g-$C_3N_4$ (CN). However, the surface area for MSC (5:1) is highest (47 $m^2/g$) among all the nanocomposites, which is responsible for the higher degradation efficiency.

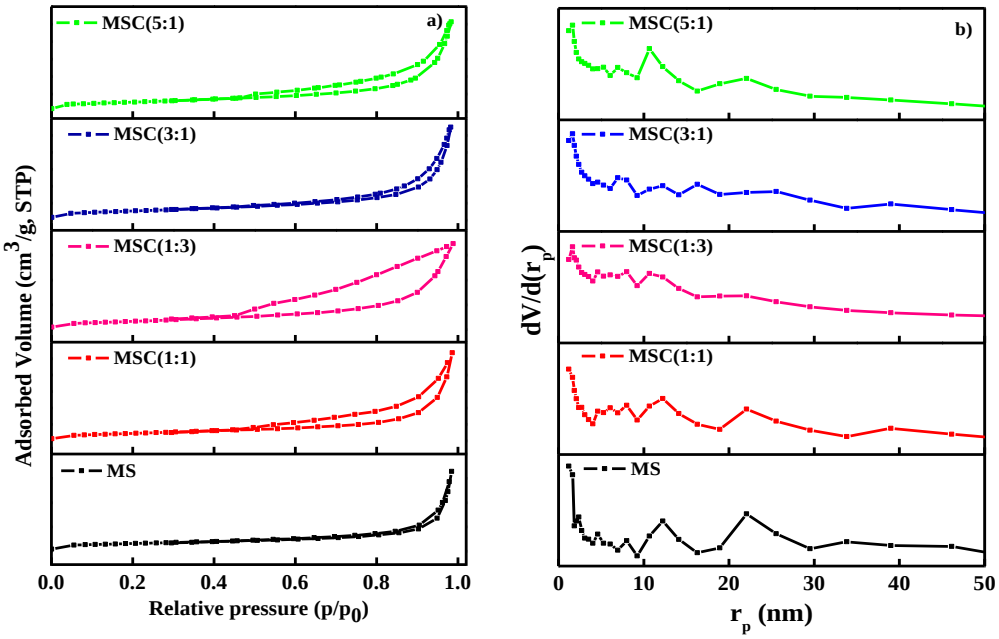


**Fig. 2.5.** (a) BET adsorption-desorption isotherm and (b) BJH pore size distribution curve for as-prepared materials.

### 2.4.6 EDS and elemental mappting

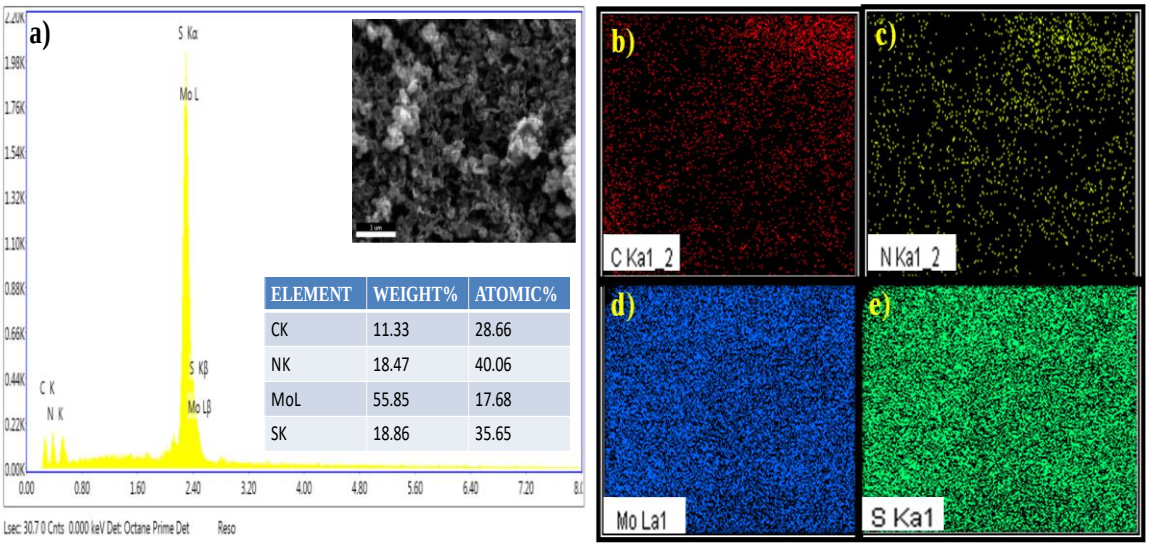


**Fig. 2.6. (a-e)** EDS and elemental mapping of MSC(5:1) composite.

The EDS spectrum (Fig. 2.6a) shows the presence of Mo, S, C and N elements in the composite in a definite ratio. The elemental color mapping of MSC(5:1) nanocomposite (fig.

2.6b-e) shows the homogenous distribution of the elements present in the sample, which is also responsible for high photocatalytic efficiency.

### 2.4.7 FESEM

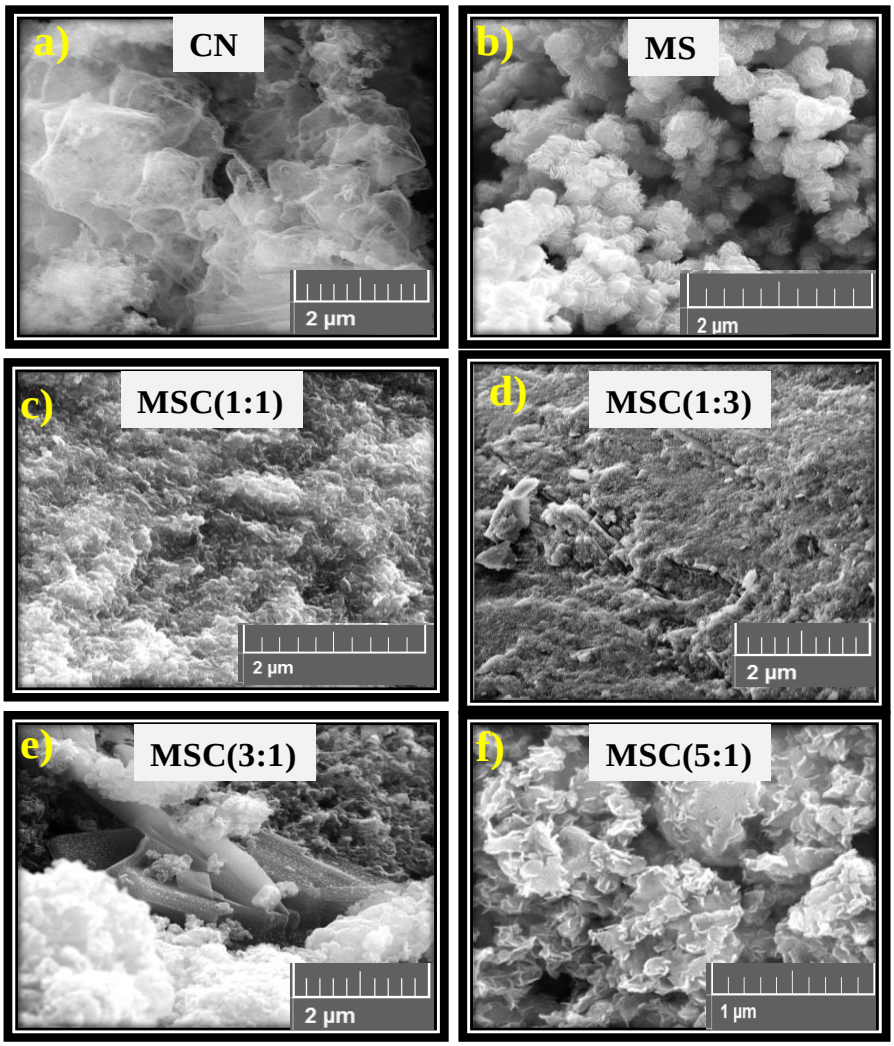


**Fig. 2.7.** FESEM micrographs of (a) g-$C_3N_4$ (CN) (b) $MoS_2$ (MS), and (c-f) MSC composites.

FESEM micrographs of CN, MS, and the nanocomposites shown in Fig. 2.7(a-f) confirm the sheet-like structure of g-$C_3N_4$ Fig. 2.7a. The formation of flower-like $MoS_2$ can be seen in Fig. 2.7b. The FESEM images of composites show the presence of both sheet-like structure of g-$C_3N_4$ and flower-like structure of $MoS_2$ (Fig. 2.7c- 2.7f). As seen from Fig. 2.7f, the flower-like structure in MSC(5:1) is more prominent since the amount of $MoS_2$ is much higher compared with the quantity of g-$C_3N_4$.

### 2.4.8 HRTEM

The Fig. 2.8 shows HRTEM micrographs of $MoS_2$ (MS) and $MoS_2$/g-$C_3N_4$ (MSC(5:1). The presence of flower-like structures in $MoS_2$ is confirmed in Fig. 2.8a, while Fig 2.8b shows the presence of mesopores in the sample. HRTEM images of MSC(5:1) has the character of both sheet-like g-$C_3N_4$ and flower-like $MoS_2$ in the sample (Fig. 2.8c and 2.8d). As shown in Fig. 2.8d the HRTEM image indicated the presence of 0.615 nm lattice spacing[20] which could be ascribed to the (002) crystal plane of $MoS_2$, though it did not appear in the XRD spectra of $MoS_2$ in Fig. 2.4. This might be due to the low number of $MoS_2$ layers leading to very low intensity or absence of XRD peak since it is past the identification furthest reaches of our XRD. The pores are also present in MSC(5:1) nanocomposite, which is responsible for the high surface area.

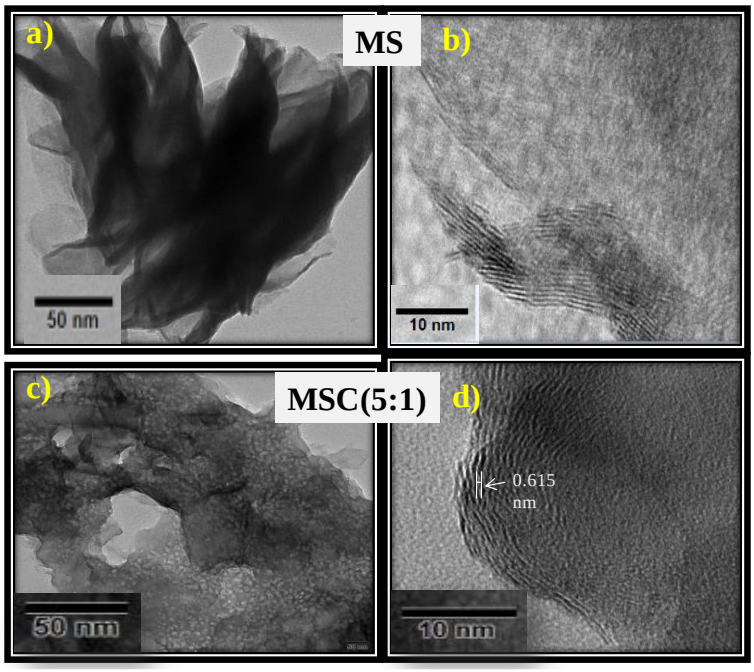


**Fig. 2.8.** TEM and HRTEM images of (a,b) $MoS_2$ and (c,d) MSC (5:1) composite.

## 2.5 Photocatalytic studies

### 2.5.1 Photocatalytic degradation of dye and pesticide

Approximately 1 mg of the catalysts (CN, MS, and MSC) was put into the methylene blue dye solution (20 mL of 5 ppm). The adsorption-desorption equilibrium was built up by stirring the suspension for 20 min under completely dark environment. Then illuminating it with UV light, visible light and sunlight upto 80 min. The degradation of methylene blue was

monitored with the absorbance of dye at the wavelength of 664 nm ($\lambda_{max}$) by UV-visible spectrophotometer. Fig. 2.9a shows the kinetic analysis of the methylene blue dye degradation in visible light, which shows that among all the nanocomposites, MSC (5:1) shows the best catalytic activity. The higher surface area and lower recombination rate of MSC (5:1) nanocomposite compared to other composites might be responsible for its high degradation efficiency. The percent (%) degradation of methylene blue by MSC (5:1) nanocomposite under the illumination of visible light is ~ 94%. To establish the difference between direct and indirect photodegradation, similar experiments were performed with colorless pesticide, fipronil (5-amino-1-[2,6-dichloro-4-(trifluoromethyl)phenyl]-4-(trifluoromethanesulfinyl)-1*H*-pyrazole-3-carbonitrile). About 2 mg of MSC (5:1) was put into 10 mL of 600 ppm fipronil solution. To attain adsorption-desorption equilibrium, stir the suspension in a completely dark environment for 20 min. The solution was irradiated by visible light for 60 min. Fig. 2.9b indicates the kinetic analysis of fipronil degradation of 77% of fipronil, which confirmed that indirect photodegradation occurred.

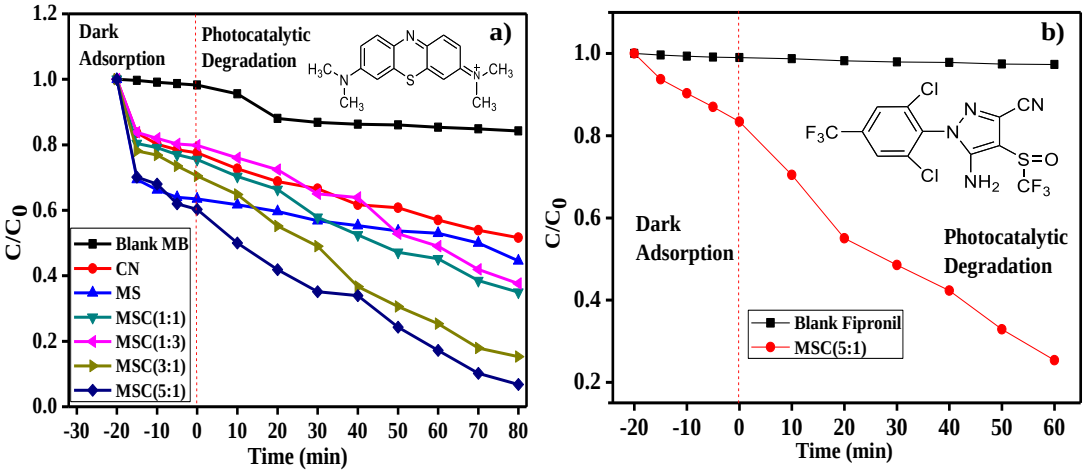


**Fig 2.9.** Time study of photocatalytic degradation of (a) methylene blue by as-synthesized materials, (b) colorless pesticide fipronil by MSC(5:1) nanocomposite.

To compare the degradation efficiency of different photocatalysts, we have studied photocatalytic methylene blue degradation in different light illumination as shown in Fig. 2.10. According to this study, the catalyst is highly active in visible light as well as in sunlight, which makes it an efficient photocatalyst for wastewater treatment.

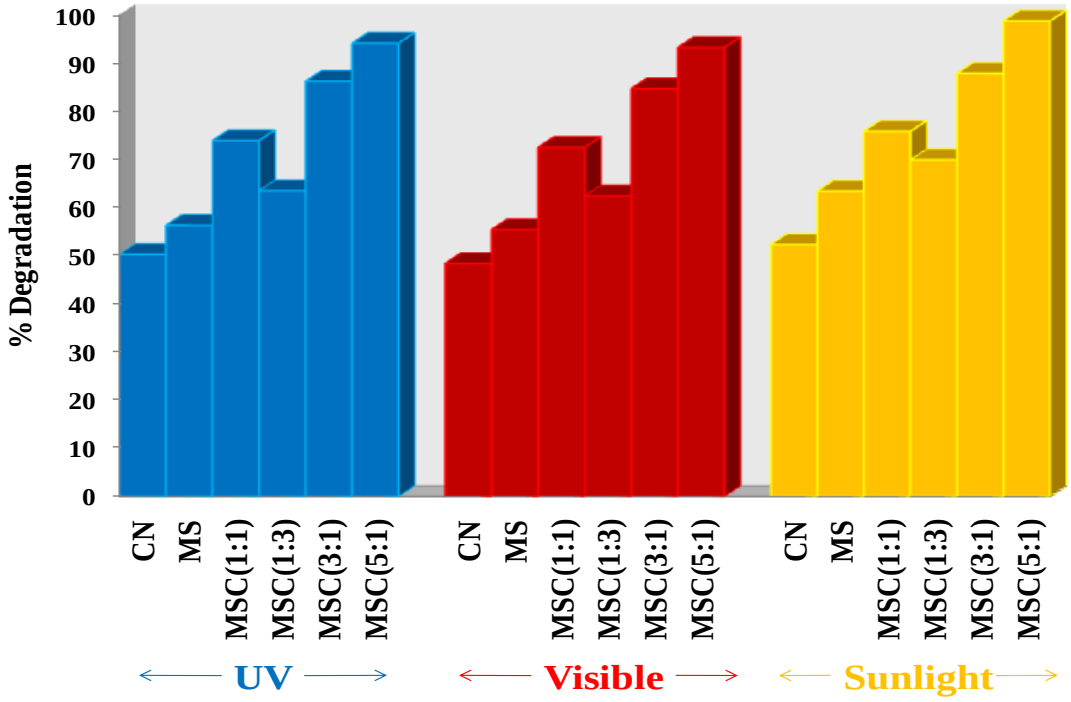


**Fig. 2.10.** Percent photocatalytic methylene blue dye degradation in UV, visible and sunlight by CN, MS, MSC nanocomposites.

A comparison with the literature can be seen in Table 2.2, from which one can conclude that the materials developed are one of the best photocatalysts with a high rate constant and hence, may be used for near-complete removal of toxic pollutants.

**Table 2.2.** A comparative study for dye degradation by $MoS_2$ and g-$C_3N_4$ based nanocomposites.

| **Photocatalyst** | **Pollutant** | **Catalyst concentration (g/L)** | **Degradation (%)** | **Degradation rate ($min^{-1}$)** | **Reaction time (min)** | **Ref.** |
|---|---|---|---|---|---|---|
| **$Fe^0$ doped g-$C_3N_4$/$MoS_2$** | Rhodamine B | 6 | 81.4 | 0.013 | 120 | [38] |
| **$TiO_2$/$MoS_2$/$TiO_2$** | Methyl orange | - | 89.86 | 0.017 | 150 | [39] |
| **N-$TiO_{2-x}$@$MoS_2$** | Methyl orange | 5 | 91.8 | 0.0211 | 120 | [40] |
| **$MoS_2$/ZnO** | Phenol Red | 0.6 | 90 | - | 80 | [41] |

| | | | | | | |
|---|---|---|---|---|---|---|
| **$MoS_2/C_3N_4$** | Methyl orange | - | 74 | 0.022 | 180 | [42] |
| **g-$C_3N_4$** | Methylene Blue | 0.1 | 52.3 | 0.004 | 100 | Present |
| **$MoS_2$** | Methylene Blue | 0.1 | 63.4 | 0.0038 | 100 | Present |
| **$MoS_2$/g-$C_3N_4$(1:1)** | Methylene Blue | 0.1 | 75.8 | 0.0097 | 100 | Present |
| **$MoS_2$/g-$C_3N_4$(1:3)** | Methylene Blue | 0.1 | 69.9 | 0.0096 | 100 | Present |
| **$MoS_2$/g-$C_3N_4$(3:1)** | Methylene Blue | 0.1 | 87.8 | 0.0199 | 100 | Present |
| **$MoS_2$/g-$C_3N_4$(5:1)** | Methylene Blue | 0.1 | 98.7 | 0.0261 | 100 | Present |

### 2.5.2 Optimum catalyst concentration

To determine the optimum quantity of photocatalyst for dye degradation the photocatalytic methylene blue degradation was studied by varying the catalyst dose. For this, different amounts of MSC (5:1) catalysts were taken in 15 mL of methylene blue solution (5 ppm) and then irradiated with visible light for 80 min. It was observed from Fig. 2.11a that efficiency of degradation enhanced with rise in catalyst concentrations (0.1 mg/mL to 0.8 mg/mL). When the catalyst concentration was increased to 0.4 mg/mL, degradation efficiency was much increased, after which saturation in degradation efficiency was observed (from 0.4 to 0.8 mg/mL). This could be because of increase in the scattering and opacity due to increased concentration of catalyst in dye solution.

### 2.5.3 Scavenger study

To determine the photocatalytic mechanism and to investigate the species responsible for the degradation, we have used various scavengers like methanol (scavenges $h^+$), DMSO (scavenges $^{\bullet}OH$ radicals) and ascorbic acid (scavenges $O_2^{-\bullet}$ radicals).[43] Due to its lower

splitting energy methanol reacts with the photogenerated holes on the surface of photocatalyst to form formaldehyde and hydrogen. The free electron pairs of its oxygen atoms allows DMSO molecules to transfer electrons and accept hydrogen bonds, hence it is a potent scavenger of •OH radicals. Ascorbic acid traps superoxide radicals and form ascorbate free radicals and then dehydroascorbate.[28,36,38] For this experiment, solutions of these scavengers ($10^{-3}$ M) were prepared and experiments were performed by taking 1 mg of MSC (5:1) photocatalyst in 10 mL of solutions with 5 ppm methylene blue dye solution, which was stirred in visible light for 80 min. The percent degradation in the presence of scavenger (methanol, DMSO and ascorbic acid) and without any scavenger was compared. Fig. 2.11b shows that holes play the significant job in methylene blue degradation as the minimum percent degradation was observed in case of methanol. The superoxide ions are also responsible for the degradation since percent degradation decreased considerably in case of ascorbic acid scavenger. However, the hydroxyl radicals are the less important species for the reaction as the percent degradation is affected minimally in the presence of DMSO scavenger.

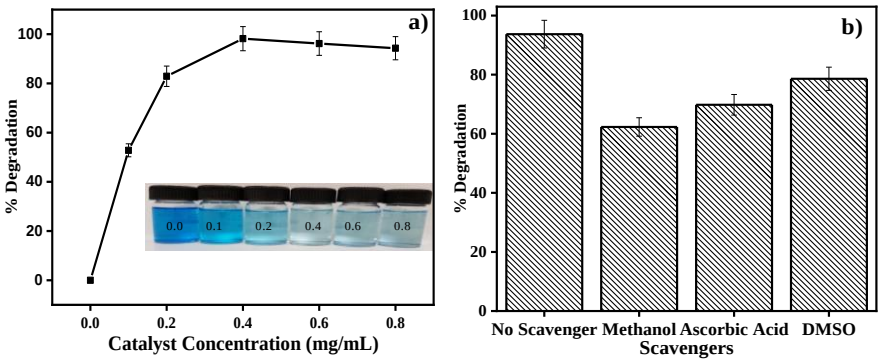


**Fig. 2.11.** Effect of (a) catalyst concentration and (b) different scavengers on degradation efficiency of the MSC (5:1) photocatalyst.

### 2.5.4 Reusability

To separate the powder catalyst after degradation of dye is a major challenge, but could be easily achieved by centrifugation after the degradation process. The as-prepared catalysts could be easily separated by centrifugation because adsorption of methylene blue dye was not permanent over the photocatalyst surface. To reuse, the recovered catalyst was washed several times with distilled water and using centrifugation. It was observed that photocatalytic activity of MSC (5:1) nanocomposite almost remained the same up to 5

consecutive cycles, which suggests the high photo-stability of the catalyst (Fig. 2.12a). EDS and XRD analysis of the nanocomposite after 5 degradation cycles indicate that elemental state and crystallinity of MSC composites was not much disturbed, which is responsible for its high degradation efficiency even after 5 runs (Fig. 2.12b,c).

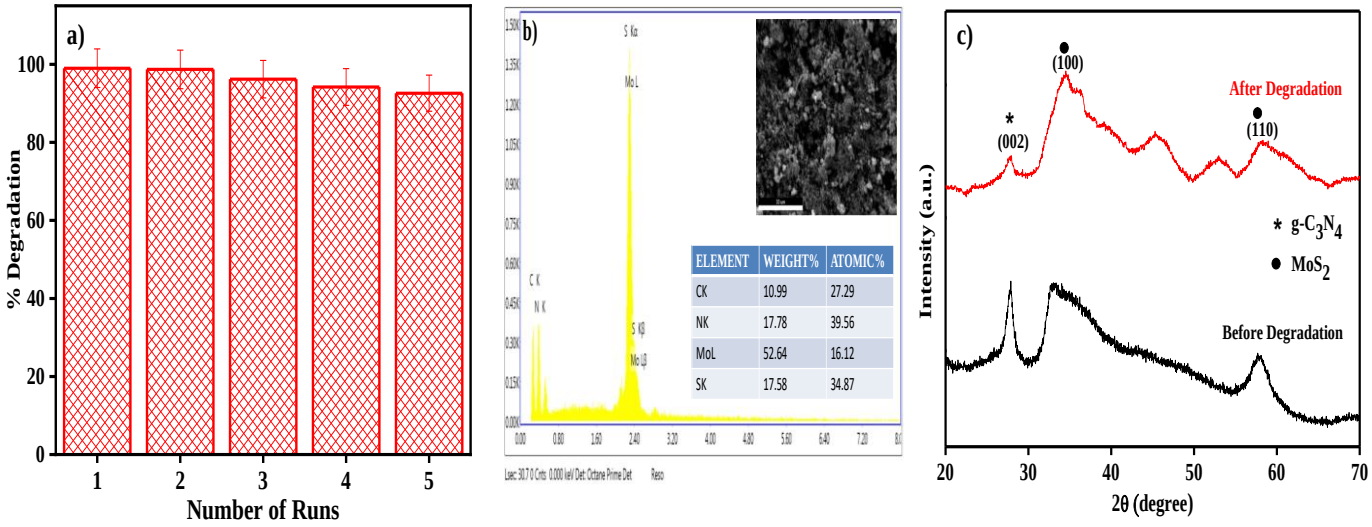


**Fig. 2.12.** MSC (5:1) photocatalyst (a) Degradation efficiency for methylene blue dye degradation upto 5 runs, (b) EDS spectra after degradation cycles and (c) comparison of XRD spectra before and after 5 degradation cycles.

### 2.5.5 Effect of illumination area

The reactor surface area also has an effect on degradation efficiency of the catalyst. We have studied the effect of illumination area of the photocatalyst surface on the degradation efficiency of MSC (5:1) nanocomposite. A higher percent degradation of methylene blue was observed if the surface area of catalyst exposed to light was more as shown in Fig. 2.13a.

### 2.5.6 Effect of pH

The capacity of the photocatalyst to adsorb the contaminations on its surface is significantly affected by the pH of the solution, which further affects the catalyst degradation efficiency. To study the variation of degradation efficiency with pH of solution, we have prepared aqueous solutions of methylene blue dye having various pH values. Solutions were prepared by the addition of 0.01N NaOH and 0.1N HCl solution. From these experiments, it was found that pzc of the catalyst was at ~pH 3 (Fig. 2.13b) and above this pH, surface of the

photocatalyst was negatively charged. Methylene blue is a cationic dye, so methylene blue adsorption on the photocatalyst surface occurs at pH>3 and its degradation is lower at pH below the pzc of the photocatalyst due to the positively charged catalyst surface. Consequently, the efficiency of degradation is higher at pH 5 to pH 7. The increase in adsorption efficiency is because of the electrostatic interactions among the cationic molecules of dye and photocatalyst surface which is negatively charged. Hence, in this pH range (pH>3), adsorption of methylene blue (a cationic dye) is better due to which its photodegradation is enhanced. The observation from Fig. 2.13c shows that the catalyst is more effective at pH 5 to pH 7.

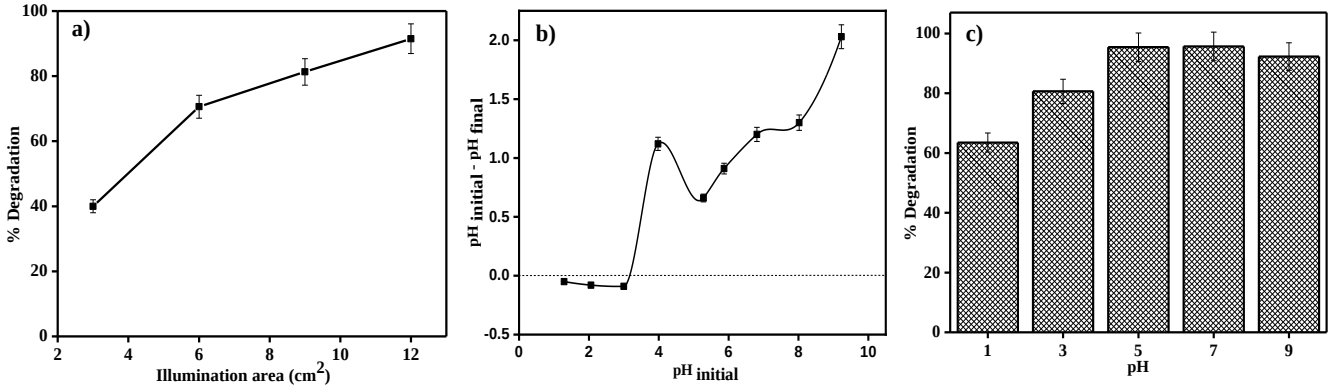


**Fig. 2.13.** Effect of (a) effective illumination area, (b) point zero charge of catalyst and (c) pH of methylene blue dye solution on degradation efficiency of MSC (5:1) nanocomposite.

### 2.5.7 Photocatalysis mechanism

Scheme 2.2 shows the mechanism for photocatalytic degradation of methylene blue and fipronil by MSC nanocomposite. As indicated by their band gap energies, both $MoS_2$ and g-$C_3N_4$ are active in visible light. When the catalyst is subjected to visible light, electrons from the valence band (VB) of $MoS_2$ and g-$C_3N_4$ get excited to the respective conduction bands (CB). The electrons from CB of g-$C_3N_4$ get transferred to CB of $MoS_2$. Due to this, electrons in the conduction band of $MoS_2$ react with the molecular oxygen to generate free $O_2^{\bullet -}$ radicals, which may directly oxidize and break the pollutant molecule or may further convert water molecules to $HO^{\bullet}$, which would then oxidize the pollutants to form degraded products.[34,42] Also, the holes generated in the VB of g-$C_3N_4$ react with $H_2O$ to produce powerful oxidative species such as

$HO^{\bullet}$, which further oxidize the methylene blue and fipronil molecules to form $CO_2$ and $H_2O$ or other degraded less harmful products.[44,45]

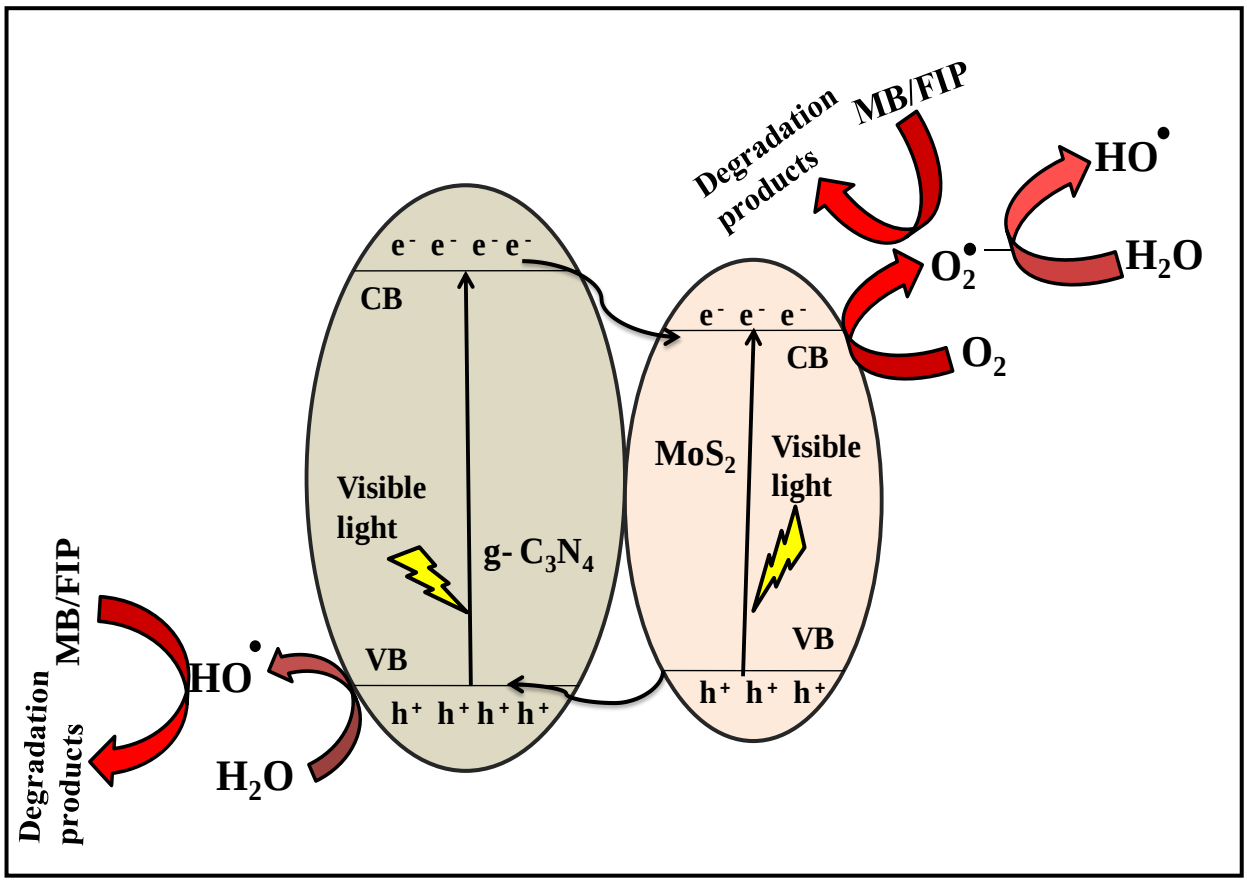


**Scheme 2.2.** Proposed mechanism for degradation of organic pollutants by $MoS_2$/g-$C_3N_4$.

## 2.6 Electrocatalytic studies

### 2.6.1 Effect on methylene blue at MSC hybrids as electrode modifier

The influence of different ratios of MS and CN, (1:0, 0:1, 1:1, 1:3, 3:1 and 5:1), hybrids modified GCE were investigated on the peak current response for 10 µM methylene blue using a cyclic voltammetric technique. Electrode surface was coated with the nanocomposite suspension of 25 µL. Fig. 2.14A confirms that the highest peak current was observed for MSC (5:1) hybrid compared to the individual MS, CN, and other modifiers. Hence, MSC (5:1) hybrid was established as an electrode modifier to catalyze electro-oxidation of 10 µM methylene blue, which was used further.

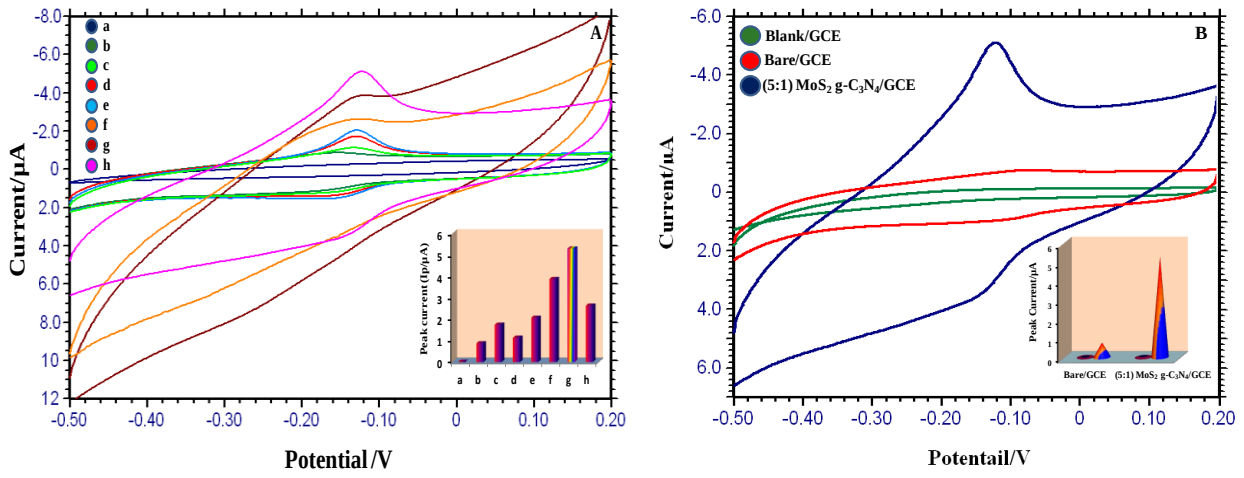


**Fig. 2.14. (A)** Cyclic voltammogram of 10 µM of methylene blue at different ratio of MS, CN and MSC hybrids modified GCE (pH: 7; scan rate: 0.05V; concentration of modifier: 25 µL); a) Blank; b) bare GCE; c) CN; d) MSC (1:3); e) MSC (1:1); f) MS; g) MSC (3:1); h) MSC (5:1); inset shows the curves of peak current versus different ratio of $MoS_2$ and g-$C_3N_4$ hybrids. **(B)** Cyclic voltammetric behavior of 10 µM of methylene blue at $MoS_2$/ g-$C_3N_4$ (5:1) modified GCE (pH: 7; scan rate: 0.05V; concentration of modifier: 25 µL).

### 2.6.2 Electrochemical behavior

The cyclic voltametric technique was utilized to investigate the electrochemical behaviour of 10 µm methylene blue at pH 7 with a potential window from -0.50 V to 0.20 V as shown in Fig. 2.14B. As there was no peak for the solution of supporting electrolyte without methylene blue, so the one peak observed belongs to the methylene blue oxidation on the surface of the electrode. Even if scan rate was reversed the peak was still present indicating that the process is redox reversible at the electrode. Within the sight of 10 µM methylene blue, a sharp peak current was observed with MSC (5:1) modified GCE. The highest peak current was obtained for MSC (5:1) modified GCE, while a least peak current was obtained for GCE, which shows that the modified electrode has a 15-20 times intensification in the peak current. Further when compared with the GCE where the oxidation occurs at -0.08 V, the oxidation of methylene blue for MSC (5:1) occurs at a low potential (-0.12 V). Also, the reduction of methylene blue occurs at a lower potential of -0.14 V for MSC (5:1) when compared to GCE, where the reduction occurs at -0.10 V.

### 2.6.3 Effect of pH

The solution pH may impact the electrode surface reaction, analyte response, hybrid material (MSC (5:1) nanocomposite) and its catalytic behavior. Therefore, CV techniques were used to study the electrochemical behaviour of 10.0 µM methylene blue and analyzed over 3 to 9.2 pH range in 0.2 M PBS (Fig. 2.15). As can be seen from the graph, one observes a less positive displacement of peak potentials with increase of pH of PBS solution, which shows the association of protons in the reaction and easy oxidation of methylene blue.[46–49] The maximum peak current observed for methylene blue was at pH 7.0 as shown in Fig. 2.13, which was used in further studies.

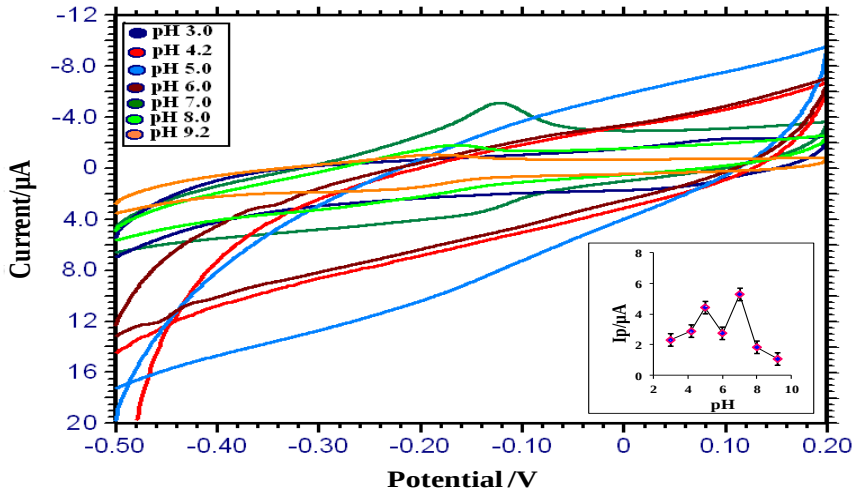


**Fig. 2.15.** Cyclic voltammograms obtained for 10 µM of methylene blue at MSC (5:1) hybrids modified GCE in buffer solution of different pH $\upsilon$=0.05 $Vs^{-1}$; (a) 3.0; (b) 4.2; (c) 5.0; (d) 6.0; (e) 7.0; (f) 8.0; (g) 9.2. (Insight: Variation of peak currents *Ip* / µ*A* versus pH).

### 2.6.4 Effect of scan rate

By varying the sweep rates in voltammograms, reaction mechanisms at the modified electrodes can be determined. Thus, by keeping pH at 7.0 (PBS), CV's of 10 µM of methylene blue for MSC (5:1) nanocomposite were recorded at varying sweep rates as shown in Fig. 2.16. From Fig. 2.16A one can observe, a linear increase of Ip values with υ. The square root of sweep rate ($\upsilon^{1/2}$) shows a linear correlation with the peak current which confirms adsorption-controlled process according to the equation Ip (µA) = 52.47 $\upsilon^{1/2}$ (V/s) – 0.4435; $R^2$=0.9879. Also, log Ip vs log υ plot shows the value of slope as 1.023 and confirms the linearity (Fig. 2.16B). Based on

this observation, the electrochemical response was an adsorption-controlled process [50], [51] following the equation: log Ip (μA) =1.0296 log υ (V/s) + 1.7803 where $R^2$ = 0.98. The plot of Ep vs log υ is also linear as shown in Fig. 2.16C with the deduced equation of regression as: Ep (V) = 0.1288+0.049 log υ (V/s); $R^2$ = 0.959.

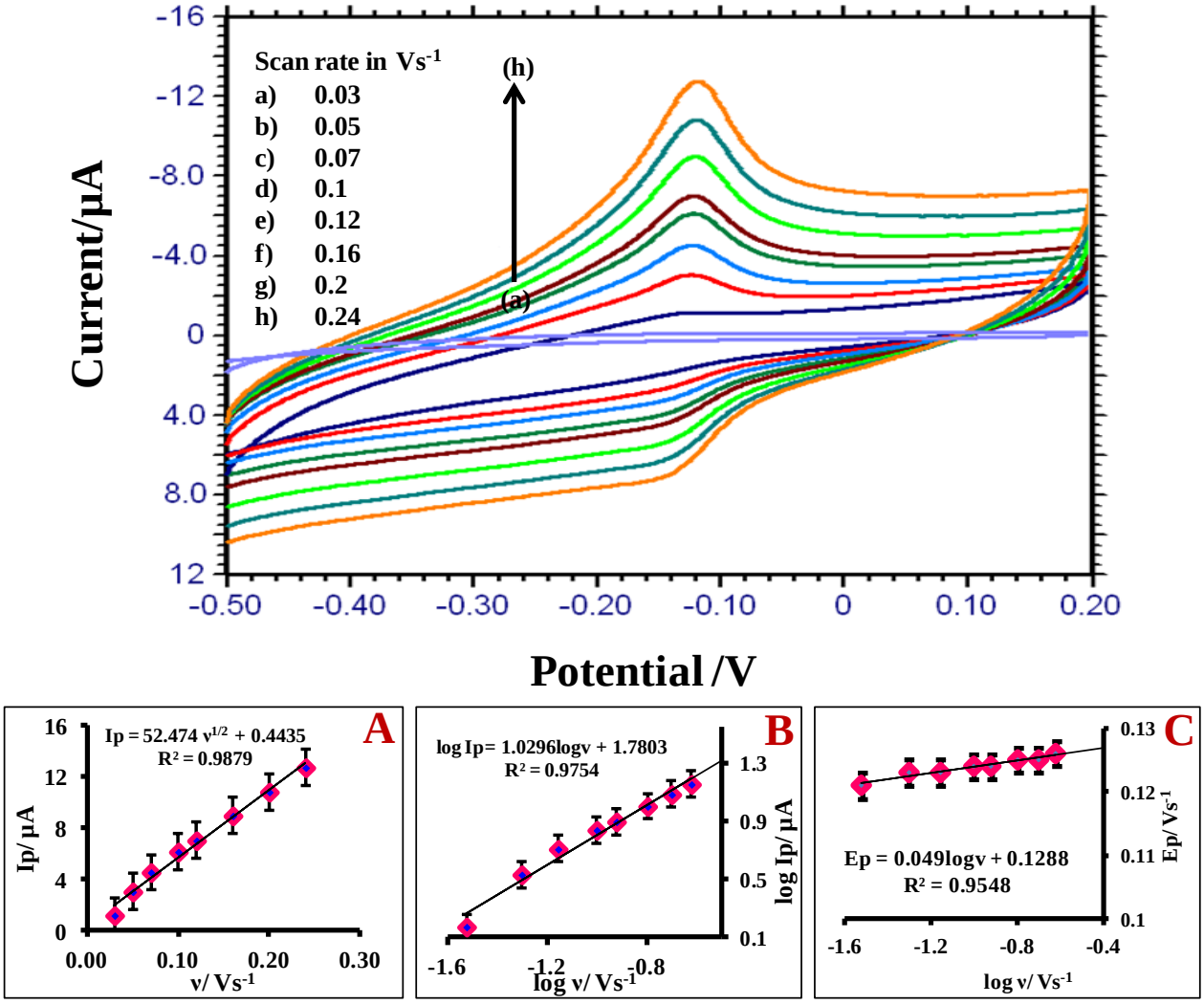


**Fig. 2.16.** Cyclic voltammograms obtained for 10 μM of methylene blue at MSC (5:1) nanocomposite modified GCE in pH 7 at different scan rate. **A:** Plot of Ip (μA) versus $υ^{1/2}$ (V/s); **B:** Plot of log Ip (μA) versus log υ (V/s); **C:** log Ep versus log υ.

### 2.6.5 Oxidation degradation mechanism

In a pH range of 3.0 to 9.2, one sharp and reversible signal was observed for methylene blue studied using MSC (5:1) hybrids modified GCE. In neutral media (at pH 7), oxidation-reduction of methylene blue at $MoS_2$/g-$C_3N_4$/GCE exhibits maximum peak

current. Based on the obtained results, electrochemical redox reaction of methylene blue involved two electrons and two protons reaction mechanism. The redox reaction mechanism pathway of methylene blue is shown in Fig. 2.17 and the product was identified as leucomethylene blue, which is colorless.[52]

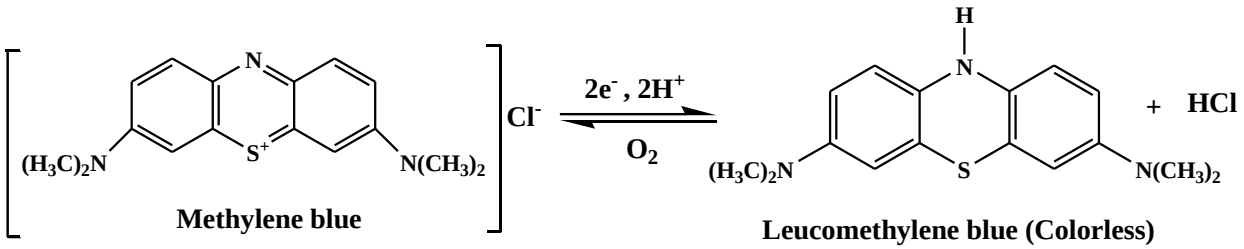


**Fig. 2.17.** Electrochemical redox reaction mechanism pathway for methylene blue.

## References


(1) Sharma, S.; Basu, S. Highly Reusable Visible Light Active Hierarchical Porous $WO_3/SiO_2$ Monolith in Centimeter Length Scale for Enhanced Photocatalytic Degradation of Toxic Pollutants. *Sep. Purif. Technol.* **2020**, *231*, 115916. https://doi.org/10.1016/j.seppur.2019.115916.

(2) Singh, J.; Kumar, V.; Kim, K.-H.; Rawat, M. Biogenic Synthesis of Copper Oxide Nanoparticles Using Plant Extract and Its Prodigious Potential for Photocatalytic Degradation of Dyes. *Environ. Res.* **2019**, *177*, 108569. https://doi.org/10.1016/j.envres.2019.108569.

(3) Fekadu, S.; Alemayehu, E.; Dewil, R.; Van der Bruggen, B. Pharmaceuticals in Freshwater Aquatic Environments: A Comparison of the African and European Challenge. *Sci. Total Environ.* **2019**, *654*, 324–337. https://doi.org/10.1016/j.scitotenv.2018.11.072.

(4) Aliste, M.; Garrido, I.; Flores, P.; Hellín, P.; Vela, N.; Navarro, S.; Fenoll, J. Reclamation of Agro-Wastewater Polluted with Thirteen Pesticides by Solar Photocatalysis to Reuse in Irrigation of Greenhouse Lettuce Grown. *J. Environ. Manage.* **2020**, *266*, 110565. https://doi.org/10.1016/j.jenvman.2020.110565.

(5) Srivastava, V.; Zare, E. N.; Makvandi, P.; Zheng, X. qi; Iftekhar, S.; Wu, A.; Padil, V. V. T.; Mokhtari, B.; Varma, R. S.; Tay, F. R.; Sillanpaa, M. Cytotoxic Aquatic Pollutants and

Their Removal by Nanocomposite-Based Sorbents. *Chemosphere*. **2020,** 127324. https://doi.org/10.1016/j.chemosphere.2020.127324.

(6) Rathi, A.; Basu, S.; Barman, S. Adsorptive Removal of Fipronil from Its Aqueous Solution by Modified Zeolite HZSM-5: Equilibrium, Kinetic and Thermodynamic Study. *J. Mol. Liq.* **2019**, *283*, 867–878. https://doi.org/10.1016/j.molliq.2019.02.140.

(7) Saad, A. M.; Abukhadra, M. R.; Abdel-Kader Ahmed, S.; Elzanaty, A. M.; Mady, A. H.; Betiha, M. A.; Shim, J.-J.; Rabie, A. M. Photocatalytic Degradation of Malachite Green Dye Using Chitosan Supported ZnO and Ce–ZnO Nano-Flowers under Visible Light. *J. Environ. Manage.* **2020**, *258*, 110043. https://doi.org/10.1016/j.jenvman.2019.110043.

(8) Wang, S.; Li, Z.; Guan, Y.; Lu, L.; Shi, Z.; Weng, P.; Yan, S.; Zou, Z. Visible Light Driven TaON/$V_2O_5$ Heterojunction Photocatalyst for Deep Elimination of Volatile-Aromatic Compounds. *Appl. Catal. B Environ.* **2019**, *245*, 220–226. https://doi.org/10.1016/j.apcatb.2018.12.067.

(9) Mishra, A.; Mehta, A.; Basu, S.; Shetti, N. P.; Reddy, K. R.; Aminabhavi, T. M. Graphitic Carbon Nitride (g–$C_3N_4$)–Based Metal-Free Photocatalysts for Water Splitting: A Review. *Carbon N. Y.* **2019**, *149*, 693–721. https://doi.org/10.1016/j.carbon.2019.04.104.

(10) Mishra, A.; Basu, S.; Shetti, N. P.; Reddy, K. R.; Aminabhavi, T. M. Photocatalysis of Graphene and Carbon Nitride-Based Functional Carbon Quantum Dots. In *Nanoscale Materials in Water Purification*; 2018. https://doi.org/10.1016/B978-0-12-813926-4.00035-5.

(11) Reddy, K. R.; Reddy, C. V.; Nadagouda, M. N.; Shetti, N. P.; Jaesool, S.; Aminabhavi, T. M. Polymeric Graphitic Carbon Nitride (g-$C_3N_4$)-Based Semiconducting Nanostructured Materials: Synthesis Methods, Properties and Photocatalytic Applications. *Journal of Environmental Management*. 2019. https://doi.org/10.1016/j.jenvman.2019.02.075.

(12) Sun, L.; Xiang, L.; Zhao, X.; Jia, C. J.; Yang, J.; Jin, Z.; Cheng, X.; Fan, W. Enhanced Visible-Light Photocatalytic Activity of Bioi/Biocl Heterojunctions: Key Role of Crystal Facet Combination. *ACS Catal.* **2015**, *5* (6), 3540–3551. https://doi.org/10.1021/cs501631n.

(13) Cao, S.; Yu, J. G-$C_3N_4$ -Based Photocatalysts for Hydrogen Generation. *J. Phys. Chem. Lett.* **2014**, *5* (12), 2101–2107. https://doi.org/10.1021/jz500546b.

(14) Zhao, Z.; Sun, Y.; Dong, F. Graphitic Carbon Nitride Based Nanocomposites: A Review. *Nanoscale* **2015**, *7* (1), 15–37. https://doi.org/10.1039/C4NR03008G.

(15) Chandra, P.; Prakash, R. *Nanobiomaterial Engineering: Concepts and Their Applications in Biomedicine and Diagnostics*; Chandra, P., Prakash, R., Eds.; Springer Singapore: Singapore, 2020. https://doi.org/10.1007/978-981-32-9840-8.

(16) Lu, D.; Wang, H.; Zhao, X.; Kondamareddy, K. K.; Ding, J.; Li, C.; Fang, P. Highly Efficient Visible-Light-Induced Photoactivity of Z-Scheme g-$C_3N_4$/Ag/$MoS_2$ Ternary Photocatalysts for Organic Pollutant Degradation and Production of Hydrogen. *ACS Sustain. Chem. Eng.* **2017**, *5* (2), 1436–1445. https://doi.org/10.1021/acssuschemeng.6b02010.

(17) Darvishi, M.; Foroutan, M. Molecular Investigation of Water Adsorption on $MoS_2$ and Graphene Surfaces. *J. Mol. Liq.* **2017**, *225*, 1–10. https://doi.org/10.1016/j.molliq.2016.11.045.

(18) Kumar, A.; Purohit, B.; Maurya, P. K.; Pandey, L. M.; Chandra, P. Engineered Nanomaterial Assisted Signal-amplification Strategies for Enhancing Analytical Performance of Electrochemical Biosensors. *Electroanalysis* **2019**, *31* (9), 1615–1629. https://doi.org/10.1002/elan.201900216.

(19) Fu, S.; Yuan, W.; Yan, Y.; Liu, H.; Shi, X.; Zhao, F.; Zhou, J. Highly Efficient Visible-Light Photoactivity of Z-Scheme $MoS_2$/$Ag_2CO_3$ Photocatalysts for Organic Pollutants Degradation and Bacterial Inactivation. *J. Environ. Manage.* **2019**, *252*, 109654. https://doi.org/10.1016/j.jenvman.2019.109654.

(20) Peng, W.; Li, X. Synthesis of $MoS_2$/g-$C_3N_4$ as a Solar Light-Responsive Photocatalyst for Organic Degradation. *Catal. Commun.* **2014**, *49*, 63–67. https://doi.org/10.1016/j.catcom.2014.02.008.

(21) Yan, J.; Chen, Z.; Ji, H.; Liu, Z.; Wang, X.; Xu, Y.; She, X.; Huang, L.; Xu, L.; Xu, H.;

Li, H. Construction of a 2D Graphene-Like $MoS_2/C_3N_4$ Heterojunction with Enhanced Visible-Light Photocatalytic Activity and Photoelectrochemical Activity. *Chem. - A Eur. J.* **2016**, *22* (14), 4764–4773. https://doi.org/10.1002/chem.201503660.

(22) Li, Q.; Zhang, N.; Yang, Y.; Wang, G.; Ng, D. H. L. High Efficiency Photocatalysis for Pollutant Degradation with $MoS_2/C_3N_4$ Heterostructures. *Langmuir*, **2014,** 30, 8965-8972. https://doi.org/10.1021/la502033t.

(23) Payra, S.; Challagulla, S.; Bobde, Y.; Chakraborty, C.; Ghosh, B.; Roy, S. Probing the Photo- and Electro-Catalytic Degradation Mechanism of Methylene Blue Dye over ZIF-Derived ZnO. *J. Hazard. Mater.* **2019,** 373, 377-388. https://doi.org/10.1016/j.jhazmat.2019.03.053.

(24) Sangeetha, S.; Krishnamurthy, G.; Raghavan, M. S. Electrochemical Sensing and Photocatalytic Degradation of Methylene Blue (methylene blue) Dye by Cobalt-Beta Hydroxy Benzoate Complex. *Mater. Sci. Semicond. Process.* **2019,** 101, 164-173. https://doi.org/10.1016/j.mssp.2019.05.016.

(25) Fadillah, G.; Saleh, T. A.; Wahyuningsih, S.; Ninda Karlina Putri, E.; Febrianastuti, S. Electrochemical Removal of Methylene Blue Using Alginate-Modified Graphene Adsorbents. *Chem. Eng. J.* **2019,** 378, 122140. https://doi.org/10.1016/j.cej.2019.122140.

(26) Jalali, K.; Pajootan, E.; Bahrami, H. Elimination of Hazardous Methylene Blue from Contaminated Solutions by Electrochemically Magnetized Graphene Oxide as a Recyclable Adsorbent. *Adv. Powder Technol.* **2019**, *30* (10), 2352–2362. https://doi.org/10.1016/j.apt.2019.07.018.

(27) Wu, Y. H.; Wu, T.; Lin, Y. W. Photoelectrocatalytic Degradation of Methylene Blue on Cadmium Sulfide–Sensitized Titanium Dioxide Film. *Mater. Res. Bull.* **2019,** 118, 110500. https://doi.org/10.1016/j.materresbull.2019.110500.

(28) Christian, G. D.; Purdy, W. C. The Residual Current in Orthophosphate Medium. *J. Electroanal. Chem.* **1962**, 3, 363-367. https://doi.org/10.1016/0022-0728(62)80012-6.

(29) Monga, D.; Basu, S. Enhanced Photocatalytic Degradation of Industrial Dye by G-

$C_3N_4/TiO_2$ Nanocomposite: Role of Shape of $TiO_2$. *Adv. Powder Technol.* **2019**, *30* (5), 1089–1098. https://doi.org/10.1016/j.apt.2019.03.004.

(30) Ouerfelli, J.; Srivastava, S. K.; Bernède, J. C.; Belgacem, S. Effect of Microwaves on Synthesis of $MoS_2$ and $WS_2$. *Vacuum* **2008**, 83, 308-312. https://doi.org/10.1016/j.vacuum.2008.06.005.

(31) Li, J.; Liu, X.; Pan, L.; Qin, W.; Chen, T.; Sun, Z. $MoS_2$-Reduced Graphene Oxide Composites Synthesized via a Microwave-Assisted Method for Visible-Light Photocatalytic Degradation of Methylene Blue. *RSC Adv.* **2014**, *4* (19), 9647–9651. https://doi.org/10.1039/c3ra46956e.

(32) Tian, Y.; Ge, L.; Wang, K.; Chai, Y. Synthesis of Novel $MoS_2$/g-$C_3N_4$ Heterojunction Photocatalysts with Enhanced Hydrogen Evolution Activity. *Mater. Charact.* **2014**, 87, 70-73. https://doi.org/10.1016/j.matchar.2013.10.020.

(33) Shen, H.; Zhao, X.; Duan, L.; Liu, R.; Li, H. Enhanced Visible Light Photocatalytic Activity in $SnO_2$@g-$C_3N_4$ Core-Shell Structures. *Mater. Sci. Eng. B* **2017**, *218*, 23–30. https://doi.org/10.1016/j.mseb.2017.01.006.

(34) Cao, Y.; Gao, Q.; Li, Q.; Jing, X.; Wang, S.; Wang, W. Synthesis of 3D Porous $MoS_2$/g-$C_3N_4$ Heterojunction as a High Efficiency Photocatalyst for Boosting $H_2$ Evolution Activity. *RSC Adv.* **2017**, *7* (65), 40727–40733. https://doi.org/10.1039/C7RA06774G.

(35) Liao, G.; Zhu, D.; Li, L.; Lan, B. Enhanced Photocatalytic Ozonation of Organics by G-$C_3N_4$ under Visible Light Irradiation. *J. Hazard. Mater.* **2014**, *280*, 531–535. https://doi.org/10.1016/j.jhazmat.2014.08.052.

(36) Hu, X.; Deng, F.; Huang, W.; Zeng, G.; Luo, X.; Dionysiou, D. D. The Band Structure Control of Visible-Light-Driven RGO/ZnS-$MoS_2$ for Excellent Photocatalytic Degradation Performance and Long-Term Stability. *Chem. Eng. J.* **2018**, *350*, 248–256. https://doi.org/10.1016/j.cej.2018.05.182.

(37) Zhang, J.; Ren, F.; Deng, M.; Wang, Y. Enhanced Visible-Light Photocatalytic Activity of a g-$C_3N_4$/$BiVO_4$ Nanocomposite: A First-Principles Study. *Phys. Chem. Chem. Phys.*

**2015**, *17* (15), 10218–10226. https://doi.org/10.1039/c4cp06089j.

(38) Wang, X.; Hong, M.; Zhang, F.; Zhuang, Z.; Yu, Y. Recyclable Nanoscale Zero Valent Iron Doped G-$C_3N_4$/$MoS_2$ for Efficient Photocatalysis of RhB and Cr(VI) Driven by Visible Light. *ACS Sustain. Chem. Eng.* **2016**, 4, 4055-4063. https://doi.org/10.1021/acssuschemeng.6b01024.

(39) Liu, X.; Xing, Z.; Zhang, H.; Wang, W.; Zhang, Y.; Li, Z.; Wu, X.; Yu, X.; Zhou, W. Fabrication of 3 D Mesoporous Black $TiO_2$/$MoS_2$/$TiO_2$ Nanosheets for Visible-Light-Driven Photocatalysis. *ChemSusChem* **2016**, *9* (10), 1118–1124. https://doi.org/10.1002/cssc.201600170.

(40) Liu, X.; Xing, Z.; Zhang, Y.; Li, Z.; Wu, X.; Tan, S.; Yu, X.; Zhu, Q.; Zhou, W. Fabrication of 3D Flower-like Black N-$TiO_{2-x}$@$MoS_2$ for Unprecedented-High Visible-Light-Driven Photocatalytic Performance. *Appl. Catal. B Environ.* **2017**, *201*, 119–127. https://doi.org/10.1016/j.apcatb.2016.08.031.

(41) Awasthi, G. P.; Adhikari, S. P.; Ko, S.; Kim, H. J.; Park, C. H.; Kim, C. S. Facile Synthesis of ZnO Flowers Modified Graphene like $MoS_2$ Sheets for Enhanced Visible-Light-Driven Photocatalytic Activity and Antibacterial Properties. *J. Alloys Compd.* **2016,** 682, 208-215. https://doi.org/10.1016/j.jallcom.2016.04.267.

(42) Shi, L.; Liang, L.; Wang, F.; Liu, M.; Sun, J. Enhanced Photocatalytic Activity of Degrading Rhodamine B Over $MoS_2$/g-$C_3N_4$ Photocatalyst Under Visible Light . *Energy Environ. Focus* **2018**, 4, 74-81 https://doi.org/10.1166/eef.2015.1137.

(43) Aanchal; Barman, S.; Basu, S. Complete Removal of Endocrine Disrupting Compound and Toxic Dye by Visible Light Active Porous G-$C_3N_4$/H-ZSM-5 Nanocomposite. *Chemosphere* **2020**, *241*, 124981. https://doi.org/10.1016/j.chemosphere.2019.124981.

(44) Liu, Y.; Xu, X.; Zhang, J.; Zhang, H.; Tian, W.; Li, X.; Tade, M. O.; Sun, H.; Wang, S. Flower-like $MoS_2$ on Graphitic Carbon Nitride for Enhanced Photocatalytic and Electrochemical Hydrogen Evolutions. *Appl. Catal. B Environ.* **2018**, 239, 334-344. https://doi.org/10.1016/j.apcatb.2018.08.028.

(45) Tavker, N.; Sharma, M. Designing of Waste Fruit Peels Extracted Cellulose Supported Molybdenum Sulfide Nanostructures for Photocatalytic Degradation of RhB Dye and Industrial Effluent. *J. Environ. Manage.* **2020**, *255*, 109906. https://doi.org/10.1016/j.jenvman.2019.109906.

(46) Pandikumar, A.; Soon How, G. T.; See, T. P.; Omar, F. S.; Jayabal, S.; Kamali, K. Z.; Yusoff, N.; Jamil, A.; Ramaraj, R.; John, S. A.; Lim, H. N.; Huang, N. M. Graphene and Its Nanocomposite Material Based Electrochemical Sensor Platform for Dopamine. *RSC Adv.* **2014**, *4* (108), 63296–63323. https://doi.org/10.1039/C4RA13777A.

(47) Bukkitgar, S. D.; Shetti, N. P. Electrochemical Behavior of an Anticancer Drug 5-Fluorouracil at Methylene Blue Modified Carbon Paste Electrode. *Mater. Sci. Eng. C* **2016,** 65, 262-268. https://doi.org/10.1016/j.msec.2016.04.045.

(48) Bukkitgar, S. D.; Shetti, N. P.; Kulkarni, R. M. Construction of Nanoparticles Composite Sensor for Atorvastatin and Its Determination in Pharmaceutical and Urine Samples. *Sensors Actuators, B Chem.* **2018**, 255, 1462-1470. https://doi.org/10.1016/j.snb.2017.08.150.

(49) Shetti, N. P.; Nayak, D. S.; Kuchinad, G. T.; Naik, R. R. Electrochemical Behavior of Thiosalicylic Acid at γ-$Fe_2O_3$ Nanoparticles and Clay Composite Carbon Electrode. *Electrochim. Acta* **2018**, 269, 204-211. https://doi.org/10.1016/j.electacta.2018.02.170.

(50) Bond, A. M. Electroanalytical Techniques in Clinical Chemistry and Laboratory Medicine (by J. Wang). *TrAC Trends Anal. Chem.* **1989**, *8* (8), 313. https://doi.org/10.1016/0165-9936(89)85067-8.

(51) Shetti, N. P.; Nayak, D. S.; Malode, S. J.; Kakarla, R. R.; Shukla, S. S.; Aminabhavi, T. M. Sensors Based on Ruthenium-Doped $TiO_2$ Nanoparticles Loaded into Multi-Walled Carbon Nanotubes for the Detection of Flufenamic Acid and Mefenamic Acid. *Anal. Chim. Acta* **2019**, *1051*, 58–72. https://doi.org/10.1016/j.aca.2018.11.041.

(52) AA, O. Kinetic Study of Decolorization of Methylene Blue with Sodium Sulphite in Aqueous Media: Influence of Transition Metal Ions. *J. Phys. Chem. Biophys.* **2014**, 4, 1-7. https://doi.org/10.4172/2161-0398.1000136.

# CHAPTER 3:

## *Tuning the Photocatalytic Properties of $MoS_2/MoSe_2$ Heterostructures by Varying the Weight Ratios for Enhanced Wastewater Treatment in Visible light*

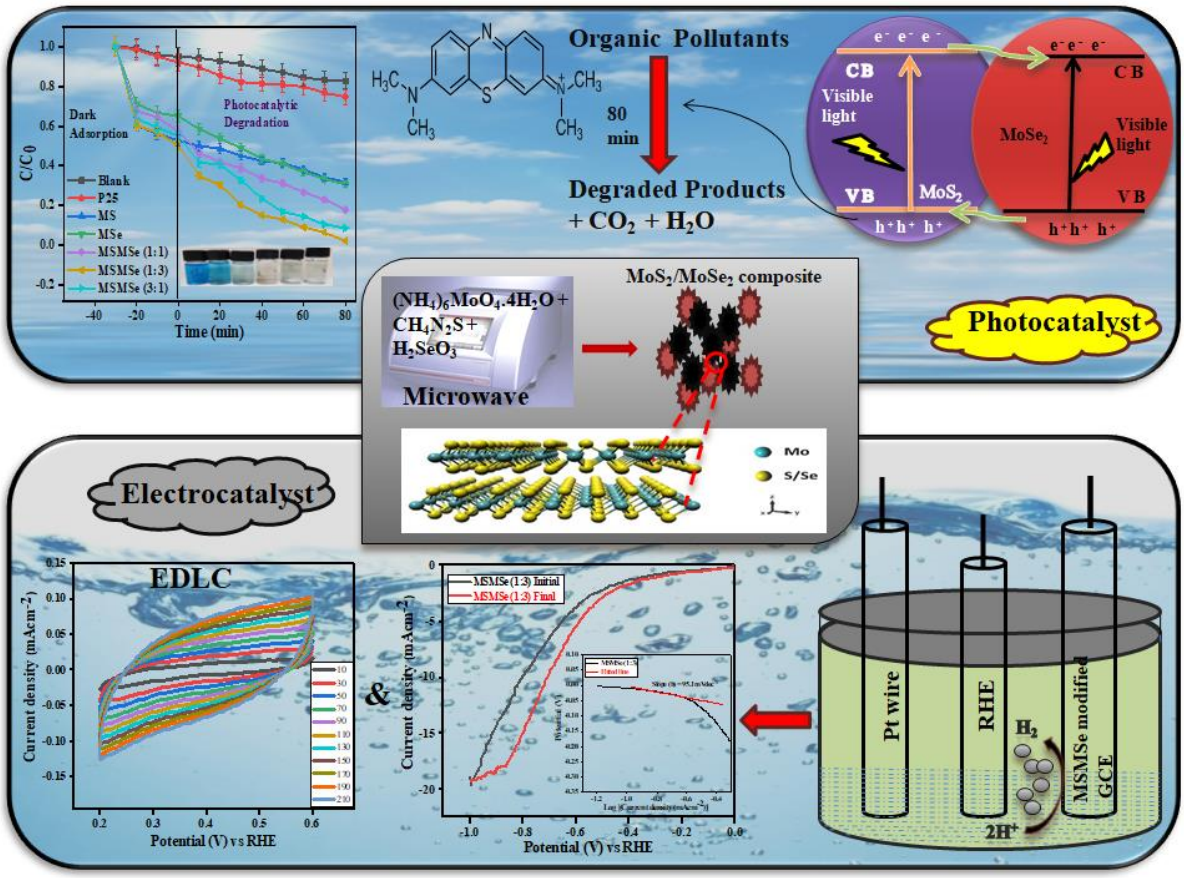


## Highlights

- ✓ Different weight-ratios of $MoS_2/MoSe_2$ composites prepared by microwave technique.
- ✓ Composites show enhanced photocatalytic waste-water treatment in visible-light.
- ✓ The effect of pH, catalyst dose and illumination area were also optimized.
- ✓ Catalysts show excellent HER activity with stable high current density.
- ✓ Composites possess high EDLC value/capacitance resistance for energy storage.

## 3.1 Introduction

Conserving water and energy is crucial not only for our current needs but also for the future of mankind. The world is achieving new heights with the development of science, technology, society, and mankind but at the cost of our limited resources.[1] The available water resources are getting contaminated gradually [2] and there is an enormous requirement for clean water, so it is at most important to pay heed to the treatment of wastewater.[3] Also, conventional energy sources are depleting rapidly, and their burning causes environmental hazards like global warming and climate change.[4] Thereby, researchers are putting an emphasis on the development of alternative efficient energy sources (like hydrogen energy) which are eco-friendly, everlasting, abundant, renewable, and can replace the existing energy sources potentially.[5] Photocatalysis is a fascinating approach to attenuate the problem of environmental pollution especially water pollution[6] although many other techniques have also been studied. It has the potential to degrade the organic compounds to almost completely degraded products like water and carbon dioxide or some less complex and non-toxic compounds.[7] A trend of hydrogen production from water splitting either through photocatalysis or electrocatalysis was observed with the increasing technology. The production of hydrogen as an energy source through hydrogen evolution reaction (HER) by electrochemical water splitting is one of the best ways for the green, renewable and non-toxic hydrogen production.[8]

The two-dimensional (2D) materials formed by the combination of different 2D semiconductive materials are the potential candidates for various applications like catalysis, energy storage and electronics etc. by tuning its electronic properties. Transition metal dichalcogenides (TMDC, $MX_2$ where M = Mo, W and X = S, Se, and Te) is the class of 2D materials with a wide range of promising application prospects.[9] These metal sulfides, selenides, etc. possess a special layered structure that acts as a support to anchor semiconductor nanoparticles and to provide more active sites to function and reduce electron mobility.[10] $MoS_2$ is found to be a catalyst with a wide-spectrum response because of its narrow bandgap (≈ 1.8 eV). It has high natural abundance, high chemical stability, low cost, high catalytic performance, and more number of surface active sites.[11] However, the catalytic performance of $MoS_2$ is unsatisfying due to the high recombination efficiency of generated charge carriers. This restraint can be overwhelmed by the construction of semiconductor

heterojunctions which may effectively improve the separation efficiency of charge carriers and provide more exposed active sites which further enhance the photo/electrocatalytic activity of materials.[12]

$MoSe_2$ is an interesting narrow-band-gap semiconductor that has a lamellar crystal structure, whose basic crystal unit is built of Se-Mo-Se sandwich layers similar to $MoS_2$. From theoretical band-structure calculations and photoelectron spectroscopy analyses, it is indicated that the energy gap of $MoSe_2$ (1.4 - 1.7 eV) matches the solar spectrum very well.[13] It is also reported that $MoSe_2$ possesses very high anti-photo-corrosion stability because the optical transitions of $MoSe_2$ are between nonbonding metal'd' states. Both of these outstanding features of $MoSe_2$ greatly benefit its potential use in catalytic related applications, such as photo-electrochemical solar cells, contamination remediating agents, and hydrogen production from water splitting.[14] Recently, $MoS_2$ and $MoSe_2$ nanocomposites have been obtained by various physical and chemical strategies including chemical vapor deposition (CVD), electro-deposition, colloidal synthesis, sonochemical synthesis, and solvothermal conversions. Most of the methods are very complicated and need to be carried out at high temperatures.[15] The vertically aligned $MoS_2$-$MoSe_2$ nanosheets were synthesized by Yang *et al.* the liquid-phase sonication method. Yang prepared a few-layered $MoS_2$ from the exfoliation of bulk $MoS_2$ by sonication and the $MoSe_2$ was synthesized by solvothermal technique taking exfoliated $MoS_2$ as a template.[16] The hydrothermal route was used by Li *et al.* for the fabrication of $MoS_2$/$MoSe_2$ heterostructures. First $MoS_2$ was prepared by the hydrothermal reaction of $Na_2MoO_4$ with $CH_4N_2S$ and the $MoSe_2$ was prepared by the selenization of as-prepared $MoS_2$ nanosheets.[17] Ren *et al.* fabricated $MoSe_2$@$MoS_2$ composites by a two-step hydrothermal method. The $Na_2MoO_4$ and hydrazine hydrate with Se powder was used to prepare $MoSe_2$ nanosheets, and these nanosheets were added to $Na_2MoO_4$ and L-cysteine for hydrothermal treatment to prepare $MoSe_2$@$MoS_2$ core-shell composites.[18] However, the poor solubility and lower density of selenium often lead to less contact between reactants which results in an incomplete reaction. Besides, hydrazine hydrate presents higher toxicity which is not suitable for extensive use.[19] The microwave-assisted synthesis presents various advantages like low-temperature synthesis, short reaction time, and formation of well-exposed .active sites .by instantaneous heating via microwaves. It is an energy saving process which provide higher yield in shorter preparation time hence

lowering the cost of processing for material preparation. Also the internal heating, in contrast to external heating, can prevent the reaction from agglomerating and has been shown to be more environmentally friendly than traditional methods.[20]

In this work, an attempt has been made to prepare a series of $MoS_2$/$MoSe_2$ nanocomposites with various weight ratios (1:1, 1:3, and 3:1) from a facile microwave technique. The composites were prepared in-situ to ensure the formation of high-quality heterostructures. Their photocatalytic performance was investigated by the degradation of methylene blue dye, fipronil pesticide, and real industrial wastewater under irradiation of different light sources (UV, Visible, and sunlight). The weight ratio effect of $MoS_2$ and $MoSe_2$ on the photocatalytic activity was studied which shows that $MoS_2$/$MoSe_2$ (1:3) composite shows the best catalytic activity for pollutants degradation. The scavenger study has been done to determine the degradation mechanism. The effect of illumination area, pH, and catalyst dose on the photoactivity of the catalyst was also studied. The reusability efficiency of the catalyst was also optimized by several degradation studies and catalyst characterization after degradation. The electrochemical water splitting performance and stability of the synthesized composites was analyzed in the acidic medium. The electric double layer (EDLC, $C_{dl}$) storage capacity and high capacitance retention rate for 2500 CV cycles show its promising application as electrode material for supercapacitors.

## 3.2 Characterization methods and photo/electrocatalytic studies

Refer to Section 2.2 chapter 2

## 3.3 Synthesis of catalysts

**Synthesis of pure $MoS_2$ and $MoSe_2$ and their composites**

A series of $MoS_2$/$MoSe_2$ composites with different weight ratios were prepared. For the fabrication of $MoS_2$/$MoSe_2$ composites, firstly, precursors of $MoS_2$ (0.5 g $(NH_4)_6Mo_7O_{24}.4H_2O$ and 1.1 g $CH_4N_2S$) (acquired from Loba Chemie Pvt. Ltd. India) were added in 30 mL ethylene glycol. Following dissolution, the desired quantity of selenous acid (based on weight ratios of 1:1, 1:3, and 3:1) was introduced into the present mixture. After stirring for 30 min, the suspension was sonicated for an hour to achieve full distribution of the precursors. The thoroughly distributed slurry was then transferred to a microwave vial

(30 mL) and treated for 20 min at 180°C in a microwave synthesizer. Upon cooling, the resulting precipitates were properly cleaned via deionized water and ethanol using centrifugal technique. At last, the rinsed precipitates were dried in a hot air oven for and the acquired dry catalysts were given names MSMSe (1:1), MSMSe (3:1), and MSMSe (1:3) according to the weight ratios of $MoS_2$ and $MoSe_2$ respectively. Pure $MoS_2$ and $MoSe_2$ were also prepared at similar conditions by using precursors of only one compound.[21] A diagrammatic representation of synthesis procedure for $MoS_2/MoSe_2$ catalysts is shown in Scheme 3.1.

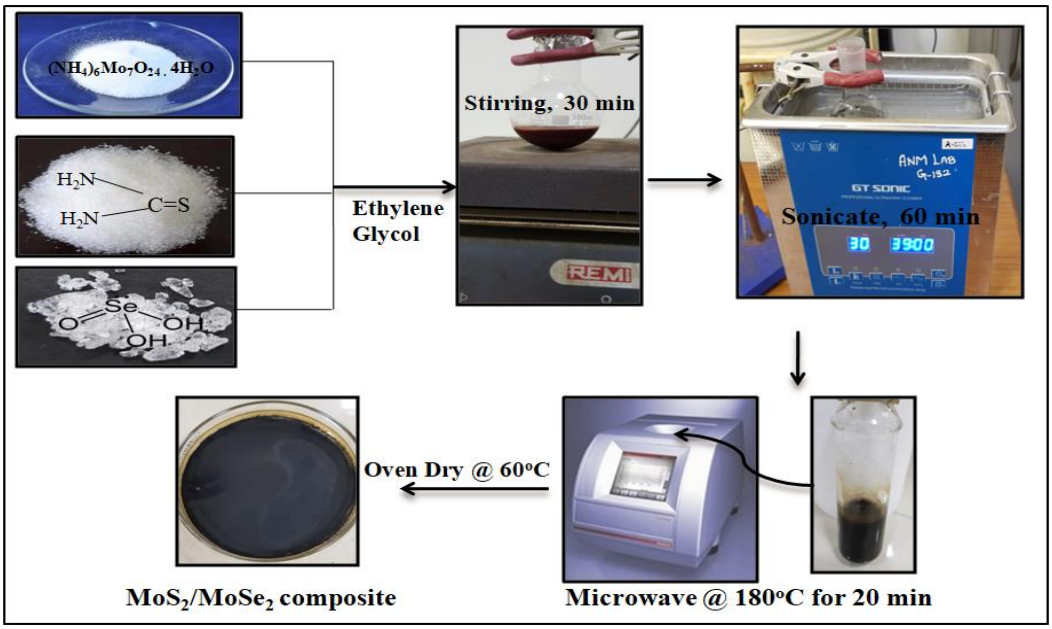


**Scheme 3.1** Schematic illustration for the synthesis of $MoS_2/MoSe_2$ composites.

## 3.4 Material characterization

### 3.4.1 XPS

The chemical state of $MoS_2/MoSe_2$ nanocomposites was explored by using XPS analysis. The survey spectra in Fig. 3.1a show the presence of Mo, S, and Se elements in the composites. In Fig. 3.1b there are three peaks, centered around 229.2 eV and 232.2 eV, which belongs to Mo(IV) $3d_{5/2}$ and Mo(IV) $3d_{3/2}$ correspondingly indicating the presence of $Mo^{+4}$ in the heterostructure. The higher energy peak detected at 235.3 eV arises from the 6+ oxidation state of Mo, probably due to the formation of $MoO_3$. The peak appeared due to oxidation of sample exposed to air during XPS analysis.[22] The peaks in Fig. 3.1c could be fitted to S $2p_{1/2}$ and S $2p_{3/2}$ at 161.3 and 162.1 eV, respectively. The binding energies of Se $3d_{3/2}$ and Se $3d_{1/2}$ in Fig. 3.1d is located at 54.5

eV and 55.4 eV for Se $3p_{3/2}$ and Se $3p_{1/2}$ at 160.5eV and 168 eV which attributes to the $Se^{-2}$ in the prepared composites.[16]

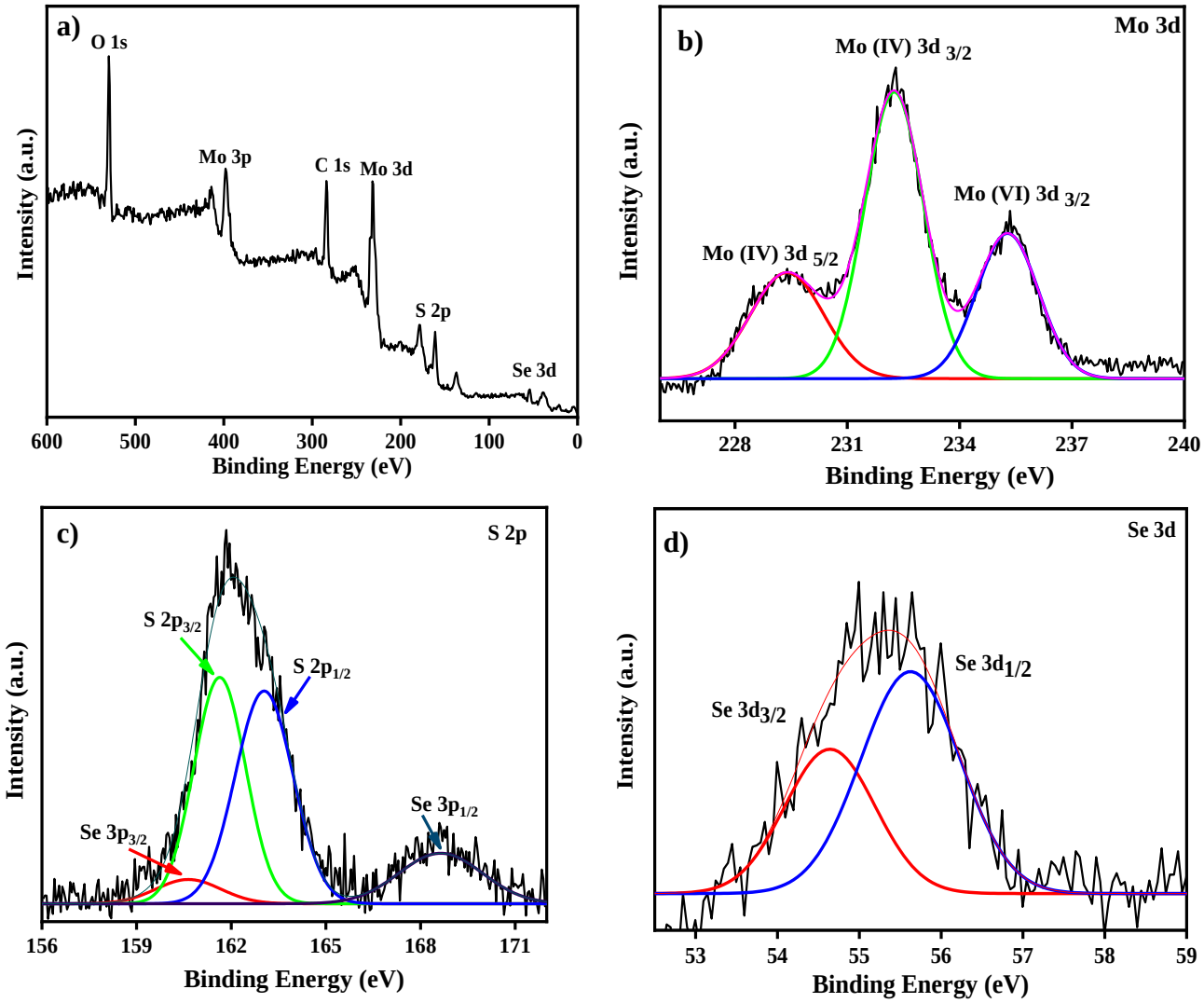


**Fig. 3.1** XPS analysis (a) survey spectra of $MoS_2/MoSe_2$ (1:1) nanocomposite, (b), (c), and (d) are the high-resolution spectra of Mo 3d, S 2p and Se 3d, respectively.

### 3.4.2 EDS and Color mapping

Energy-dispersive X-ray spectroscopy results (Fig. 3.2a) reveal the coexistence and homogeneous distribution of Mo, S, and Se elements in $MoS_2/MoSe_2$ composite, indicating a uniform distribution of $MoS_2$ and $MoSe_2$ in the heterostructures. The elemental color mapping of MSMSe (1:1) nanocomposite with corresponding FESEM image shows the elements (Mo, S and Se) present in the sample (Fig. 3.2 b-e).

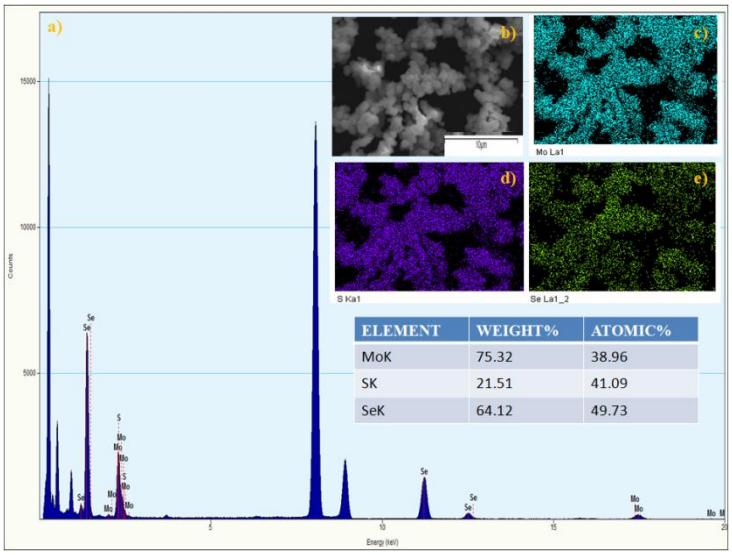


**Fig. 3.2** (a) EDS spectra and (b – e) color mapping of MSMSe (1:1) photocatalyst.

### 3.4.3 UV-Visible DRS

Fig. 3.3 (a) and (b) represents the UV-visible DRS spectra of as-prepared $MoS_2$/$MoSe_2$ composites. Both $MoS_2$ and $MoSe_2$ exhibited a wide light absorption range in visible light (fig 3.3c). The broad absorption starting around 450nm is attributed to the direct transition from the deep valence band to the conduction band of $MoS_2$ and $MoSe_2$.[23] It was observed that pure $MoS_2$ and $MoSe_2$ have a bandgap of 2.21 eV and 1.66 eV respectively (inset of fig. 3.3c), which demonstrates, both are active in the visible region of light. The bandgap of MSMSe (1:1) and MSMSe (3:1) composites are 1.99 eV and 2.1 eV respectively, signifying the good absorption of visible light. The narrow bandgap of MSMSe (1:3) composite (~1.89 eV) compared with other composites might be responsible for the high photocatalytic activity of this composite due to better light absorption. The value of the conduction band (CB) and valence band (VB) was also determined by the equations:[24]

$$EVB = X - E_e + 0.5\ E_g$$

$$ECB = EVB - E_g$$

Here EVB and ECB represent the energy of the valence band and conduction band respectively and $E_g$ is the bandgap of the sample and $E_e$ is the free electron energy estimated on the hydrogen scale which has a fixed value of 4.5 eV. The X in the equation stands for the total

electronegativity of the compound.[25] Putting the values in the above equations the value of EVB and ECB for $MoS_2$ were found to be 1.25eV and -0.94eV respectively. Similarly, the valence band and conduction band energy of $MoSe_2$ was calculated to be 1.46eV and -0.20eV. Due to the matching energy levels between $MoS_2$ and $MoSe_2$, the heterojunction formed between these two materials could assist the movement and separation of photogenerated charge carriers which enhance the photocatalytic activity of the composite.

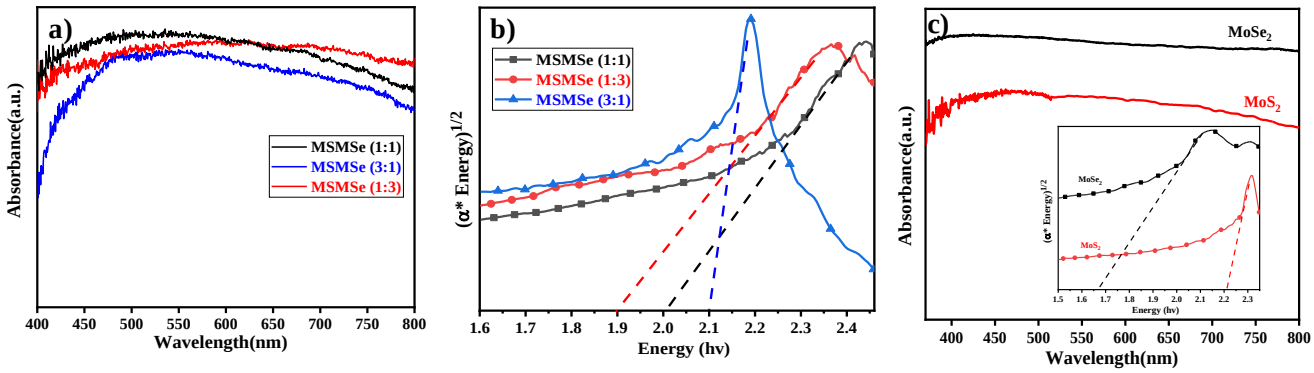


**Fig. 3.3** (a) UV-Visible DRS absorption spectra and (b) Tauc plots of MSMSe (1:1, 1:3 and 3:1) composites and (c) UV-Visible absorption spectra of pure $MoS_2$ and $MoSe_2$ with their corresponding Tauc plots in the inset.

### 3.4.4 Photoluminescence Study

The catalytic response of a material is highly dependent on the recombination rate of charges. The low photoluminescence (PL) intensity implies adequate charge separation viability and a low recombination rate of electrons and holes.[26] In the current study, the PL-spectra of as-synthesized materials were evaluated as shown in Fig. 3.4. The broad PL spectra of samples consist of two overlapping Gaussian peaks: one is centered at ~420 nm while the other one at ~490 nm (Fig. 3.4). The lower energy PL emission can be ascribed to the transition between quantized energy levels and the other peak is might be due to defect state mediated transition.[27,28] The PL intensity of all the composites prepared was lower than the pure $MoSe_2$ which indicates that the photocatalytic activity of the composites is higher as compared to individual components because of the higher separation efficiency of the photo-induced charges in the composites. However, better separation of the charges in composites is the result of the formation of heterojunctions between $MoS_2$ and $MoSe_2$ which results in better electron transport. Moreover,

the PL intensity of MSMSe (1:3) is the lowest among the composites, it consequences the highest catalytic efficacy.

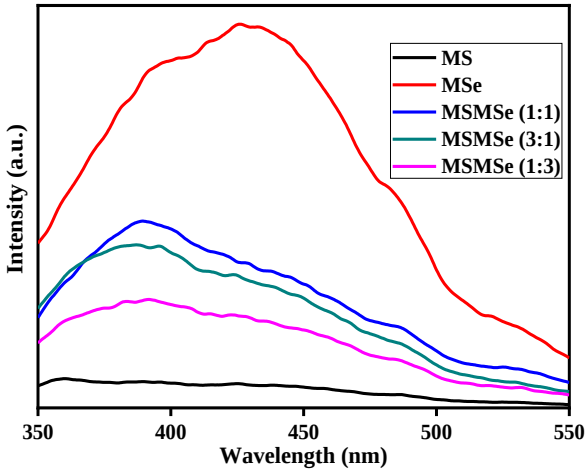


**Fig. 3.4.** Photoluminiscence spectra of MS, MSe and MSMSe (1:1, 1:3 and 3:1) composites.

### 3.4.5 XRD

The XRD patterns of $MoS_2/MoSe_2$ composites are shown in fig. 3.5. In the composites and pure $MoSe_2$, the diffraction peaks of both $MoSe_2$ and Se [29] are present at 23.3º, 29.8º, 41.2º, 43.7º, 45.1º, 48º, 51.6º, 56º, 61.6º, 65.1º, 68.2º which represent (022), (004), (006), (102), (111), (105), (201), (110), (103), (200) and (203) (hkl) planes respectively (JCPDS file no 77–1715) and intensity of these peaks increases as the amount of $MoSe_2$ in the composite increases.[30,31] The diffraction peaks of $MoS_2$ in the composite are present at 32.6º and 57.4º which corresponds to (100) and (110) planes of $MoS_2$ (JCPDS 37-1492). The XRD pattern of pure $MoS_2$ having diffraction peaks at 32.9º and 58º is shown in the inset of fig. 3.5. Both $MoS_2$ and $MoSe_2$ are present in hexagonal crystal systems and 2H phase in the catalyst.[32,33] The diffraction peak of $MoSe_2$ at 29.8º gets broaden with a decrease in intensity as the amount of $MoS_2$ increases in the composite (MSMSe (3:1)). As observed from the spectra that the composites have sharp peaks implying the high crystalline nature of the composites. But compared with the pure $MoS_2$ and $MoSe_2$ the peaks in the composite are slightly shifted and this type of trend implies close contact and higher interaction between $MoS_2$ and $MoSe_2$ in the composites.[34]

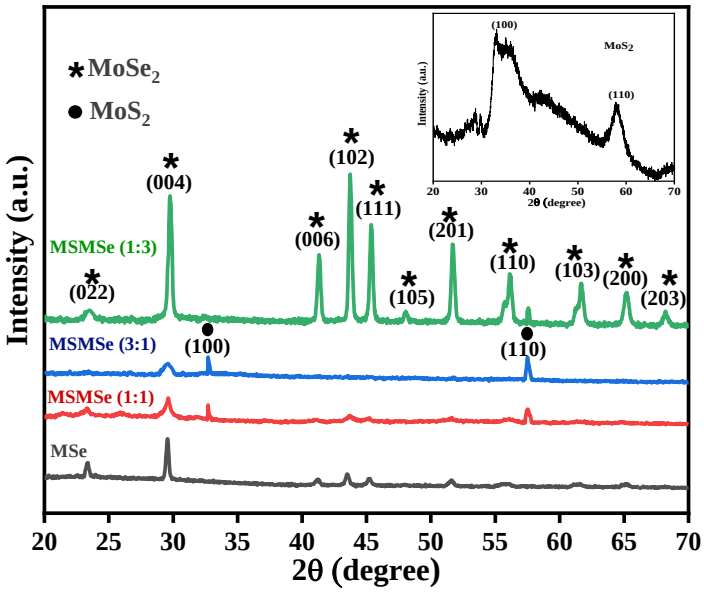


**Fig. 3.5** XRD diffraction patterns of as-prepared MSMSe catalysts.

### 3.4.6 Surface area studies

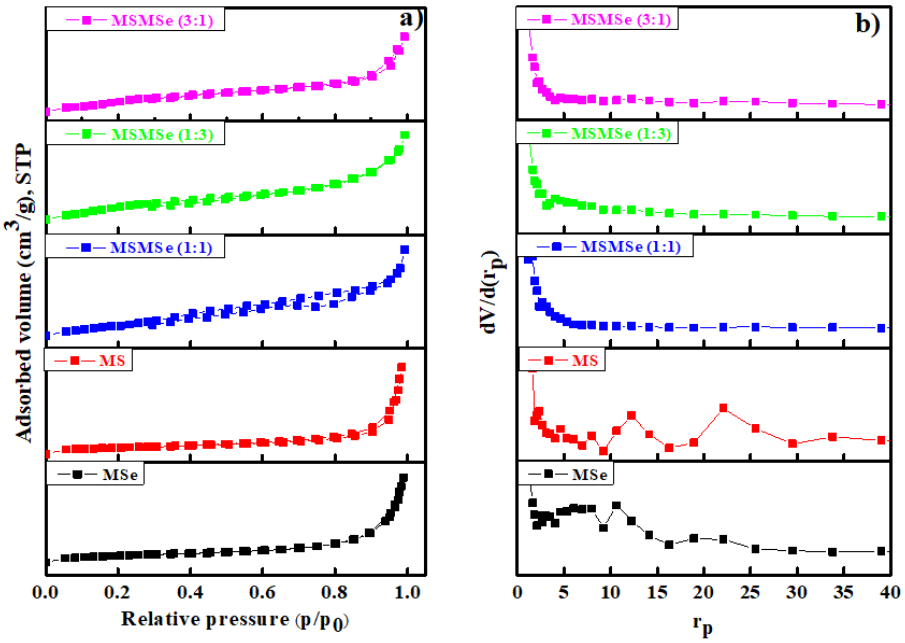


**Fig. 3.6.** (a) Adsorption-desorption isotherms and (b) BJH pore size distribution curves for MSMSe nanocomposites.

To analyze the surface area of the as-prepared nanocomposites, specific surface area analysis was carried out. Fig. 3.6a represents the type IV langmuir adsorption isotherm with sharp

branches of H1 hysteresis loop of all the composites along with bare $MoS_2$ and $MoSe_2$, which validate the mesoporous nature of the as-prepared samples. To figure out the pore size distribution of the samples, the BJH method (Fig. 3.6b) was followed. From table 3.1, we can observe that the surface area and pore volume of the pure $MoS_2$ is quite high.

The surface area and the pore volume of the composites are higher as compared to pure $MoSe_2$. However, the surface area increases form MSMSe (1:1) < MSMSe (3:1) < MSMSe (1:3) which is directly responsible for the better photo/electrocatalytic efficiency of MSMSe (1:3) composite due to better adsorption of pollutants and more catalytically active surface area for HER.

**Table 3.1.** Surface area and pore size distribution analysis of the $MoS_2/MoSe_2$ samples.

| **Samples** | **MS** | **MSe** | **MSMSe (1:1)** | **MSMSe (3:1)** | **MSMSe (1:3)** |
|---|---|---|---|---|---|
| Specific surface area ($m^2/g$) | 73 | 38 | 44 | 50 | 60 |
| Mean pore diameter (nm) | 22.7 | 15.8 | 16.2 | 18.2 | 20.4 |
| Mesopore volume ($cm^3/g$) | 0.682 | 0.603 | 0.612 | 0.615 | 0.671 |
| Total Pore volume ($cm^3/g$) | 0.701 | 0.621 | 0.639 | 0.664 | 0.688 |

### 3.4.7 FESEM

The FESEM pictures of the as-prepared composites are shown in fig. 3.7 (a-f). These images reveal that all the prepared composites consist of small and flat disk-like particles. FESEM pictures depict that there is an irregularity on the surface of the composites. It is difficult to differentiate the surface morphology of different composites from these FESEM images. The high-resolution image of MSMSe (1:3) composite (fig. 3.7d) indicates that

there are irregular plate/disk-like structures which may lead to the increased surface area of the catalyst, and further helps in the photo/electrocatalytic activity of the catalyst.

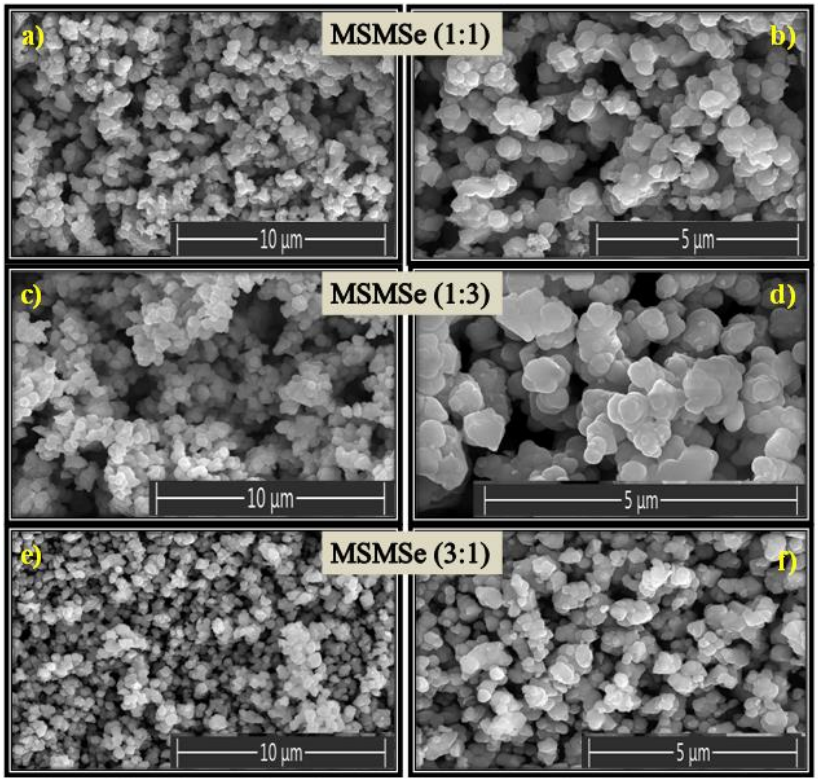


**Fig. 3.7** FESEM images of (a and b) MSMSe (1:1), (c and d) MSMSe (1:3) and (e and f) MSMSe (3:1) catalysts.

### 3.4.8 TEM

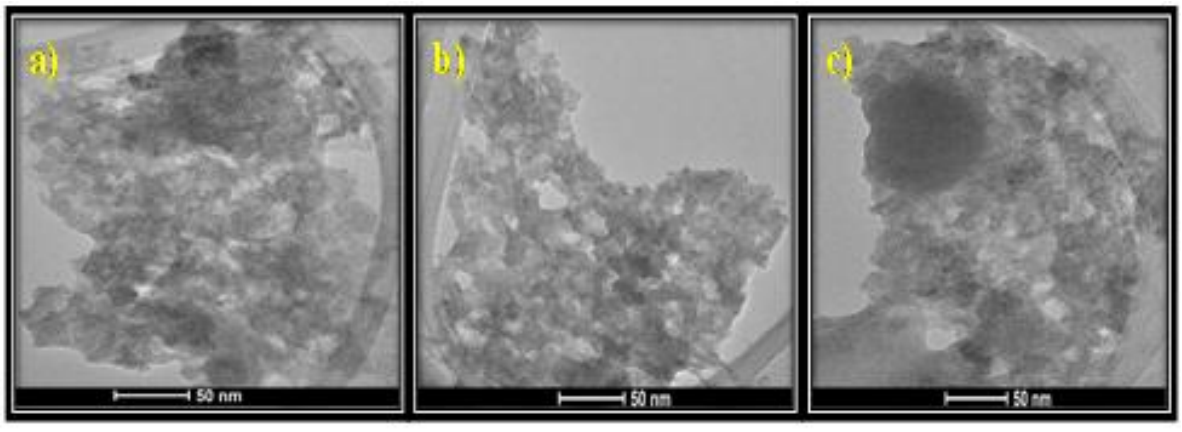


**Fig. 3.8** TEM images of (a) MSMSe (1:1), (b) MSMSe (3:1) and (c) MSMSe (1:3) nanocomposites.

The Fig. 3.8 (a, b and c) represents the TEM images of the as-prepared MSMSe composites which shows the presence of small aggregated spherical particles. From the TEM images, it is difficult to differentiate between different composites. The close contact of $MoS_2$ and $MoSe_2$ in the composites can be observed from the image. Moreover, the small pores present in the samples validate that the composite possesses a high surface area which is responsible for the high catalytic activity of the composites.

## 3.5 Photocatalytic studies

### 3.5.1 Photodegradation of Dye and pesticide

To determine the degradation efficiency of the catalysts, the kinetic analysis was carried out with methylene blue (methylene blue) and fipronil pesticide. About 20mL (5 ppm) of methylene blue dye solution having 0.1g/L of the as-prepared catalysts was allowed to stir firstly in dark for 30 min to attain adsorption equilibrium and then in visible light for 80 min for photodegradation. To compare the effectiveness of the catalyst, a similar degradation experiment was performed with all the composites as well as bare $MoS_2$ and $MoSe_2$. The degradation efficiency, rate constants, and synergy factors of as-prepared catalysts were analyzed. The photocatalysts show much higher degradation efficiency (Fig. 3.9) than commercial $TiO_2$ nanopowder (Degussa, P25). It was observed that the photocatalytic efficacy of all the prepared composites was higher than the individual $MoS_2$ and $MoSe_2$ catalysts (Fig. 3.9a). The synergy attained from the combination of $MoS_2$ and $MoSe_2$ photocatalytic system can be determined with help of synergy factor (R) as follows:

$$R = \frac{k_{MoS2/MoSe2}}{k_{MoS2} + k_{MoSe2}} \quad (3)$$

Where $k_{MoS2/MoSe2}$, $k_{MoS2}$, and $k_{MoSe2}$ in the equation 3 are the photodegradation rate constants of $MoS_2/MoSe_2$ composite, pure $MoS_2$, and pure $MoSe_2$ respectively.[35] The synergy factors for different MSMSe composites calculated from the above equation are 0.98, 1.34, and 1.73 for MSMSe (1:1), MSMSe (3:1), and MSMSe (1:3) photocatalysts respectively. Although the photocatalytic activity of all the composites was high, however the best degradation efficiency (~ 94%) was achieved by MSMSe (1:3) catalyst with a high rate constant of 0.033 $min^{-1}$ and strong synergistic effect (R = 1.73). This high efficiency is may be due to the higher surface area (confirmed from BET surface area analysis) and lower recombination rate

(confirmed from PL studies) of MSMSe (1:3) nanocomposite which facilitates the higher adsorption on the catalyst surface and degradation process.

Likewise, to make the differentiation that the system of photocatalysis is direct or indirect, the photodegradation of colorless pesticide fipronil was conducted. For this purpose, about 10 mL (600 ppm) of fipronil solution and 2 mg of the prepared catalysts were allowed to stir in the dark for 30 min and then in visible light up to 80 min for photodegradation. The studies were also conducted in similar conditions without adding any catalyst to the solution, which shows only 8% degradation in light. Whereas after adding the catalyst, the efficiency of degradation increases by up to 80% (Fig. 3.9b) with a high rate constant of 0.0168 $min^{-1}$ by MSMSe (1:3) composite, which confirms that the photodegradation was indirect.

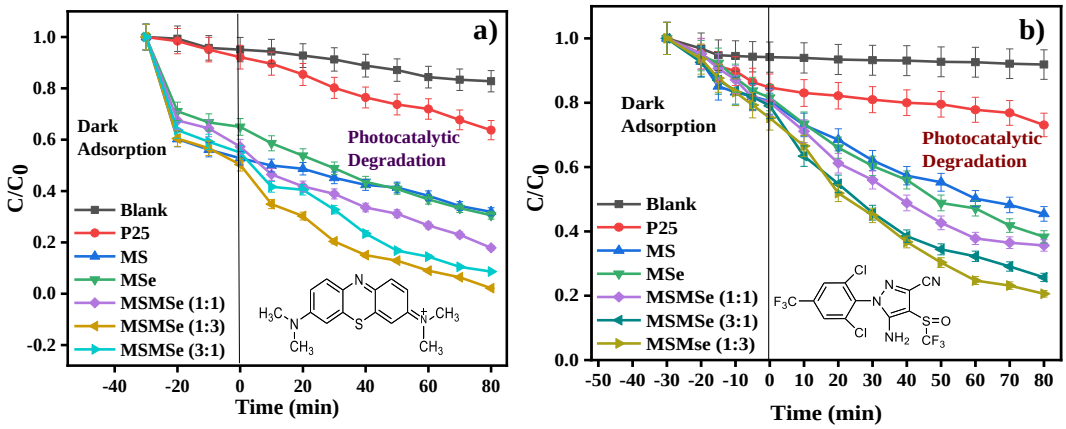


**Fig. 3.9** Kinetic plots for photodegradation of (a) methylene blue dye and (b) fipronil pesticide.

To draw the correlation among different light sources, a similar trial was led in UV light and sunlight with MSMSe (1:3) as a catalyst and summarized in table 3.2. The degradation efficiency is excellent under all the light sources which confirms that only the small amount of catalyst is highly effective in UV, Visible as well as in naturally and abundantly available sunlight irradiation.

**Table 3.2** Photocatalytic activities of MSMSe (1:3) composite for methylene blue degradation under different light sources.

| Light Source | Percent Degradation (%) | Rate constant ($min^{-1}$) |
|---|---|---|
| **Ultraviolet** | 96±5 | 0.0338 |
| **Visible** | 94±5 | 0.0332 |
| **Sunlight** | 97±5 | 0.0345 |

**Table 3.3** Photocatalytic activity comparison of as-prepared $MoS_2/MoSe_2$ catalysts with literature.

| Photocatalyst | Pollutant | Catalyst concentration (g/L) | Degradation (%) | Degradation rate ($min^{-1}$) | Reaction time (min) | Ref. |
|---|---|---|---|---|---|---|
| **Crystalline $MoSe_2$** | Rhodamine B | 2 | 90 | 0.019 | 120 | [36] |
| **$MoSe_2/SrTiO_3$** | Methyl orange | 0.2 | 99.46 | - | 70 | [37] |
| **$TiO_2/MoS_2/TiO_2$** | Methyl orange | - | 89.86 | 0.017 | 150 | [38] |
| **$SnO_2/MoS_2$** | Methylene Blue | - | 58.5 | 0.022 | 120 | [39] |
| **$Fe_2O_3/MoS_2$** | Methylene Blue | 0.1 | 84 | - | 120 | [40] |
| **$MoSe_2/pg\text{-}C_3N_4$** | Tetracycline | 0.5 | 92 | 0.0281 | 80 | [41] |
| **$TiO_2$ (Degussa P25)** | Methylene Blue | 0.1 | 33 | 0.0036 | 80 | Present Study |
| **$MoS_2$** | Methylene Blue | 0.1 | 68 | 0.0088 | 80 | Present Study |
| **$MoSe_2$** | Methylene Blue | 0.1 | 69.4 | 0.0103 | 80 | Present Study |
| **$MoS_2/MoSe_2$ (1:1)** | Methylene Blue | 0.1 | 82.1 | 0.0188 | 80 | Present Study |
| **$MoS_2/MoSe_2$ (3:1)** | Methylene Blue | 0.1 | 91.3 | 0.0257 | 80 | Present Study |
| **$MoS_2/MoSe_2$ (1:3)** | Methylene Blue | 0.1 | 94 | 0.0332 | 80 | Present Study |

Table 3.3 shows the comparison of degradation efficiency of as-prepared photocatalysts with similar kind of catalysts reported in the literature, which shows that the as-prepared catalysts are one of the efficient photocatalysts with a high value of degradation efficiency and rate constant in visible light.

### 3.5.2 Catalyst concentration effect

The optimum concentration of catalysts was determined by varying the catalyst dose and carrying out the photodegradation of methylene blue dye in visible light. For this, the concentration of MSMSe (1:3) catalyst was varied from 0.1 to 0.8 g/L in 20 mL of methylene blue dye solution (5 ppm). From Fig. 3.10a, we can see that as the concentration rises from 0.1 to 0.4 g/L there is a significant increase in the degradation efficacy after 80 min of photodegradation. However, after this, if the concentration was further increased (0.4 to 0.8 g/L), there was no noticeable increase in the efficiency. The saturation in degradation efficiency may be due to the increase in light scattering due to a highly opaque solution.

### 3.5.3 Illumination area effect

The role of the total effective illumination area was as well investigated in visible light using MSMSe (1:3) as a photocatalyst. About 1 mg of the catalyst was stirred in 20 mL of methylene blue dye (5ppm) solution in the visible light for 80 min.

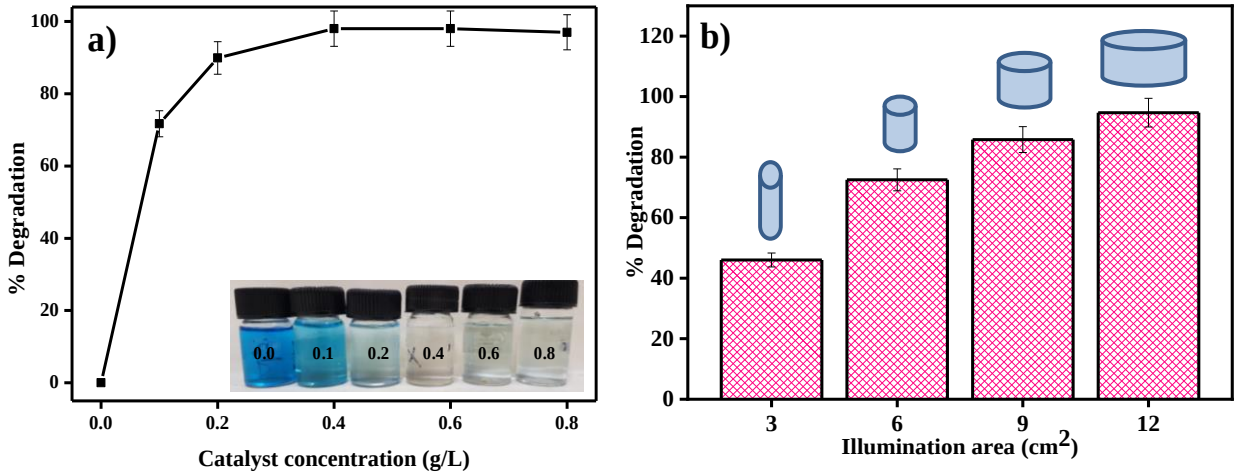


**Fig. 3.10** Effect of (a) catalyst amount and (b) effective illumination area of exposed solution on the degradation efficiency of MSMSe (1:3) photocatalyst.

The diameter of the reaction surface was varied by using vessels of different sizes keeping all other parameters same throughout the experiment. The distance between the light source and the upper layer of the solution was kept constant (10 cm) while using different vessels. There is an increase in the degradation efficacy with an increase in the area of the exposed reaction mixture to light irradiation (Fig. 3.10b). The greater the exposed area of the reaction mixture more will be the absorption of light which further facilitates the photocatalytic degradation of the pollutants and thus showing an increase in degradation efficiency.

### 3.5.4 Solution pH effect

The capacity of the photocatalyst to absorb contaminations on its surface is significantly impacted by the pH of the solution, which further influences the efficiency of degradation. To study the influence of pH on degradation efficacy, point zero charge (pzc) of the catalyst surface was measured.

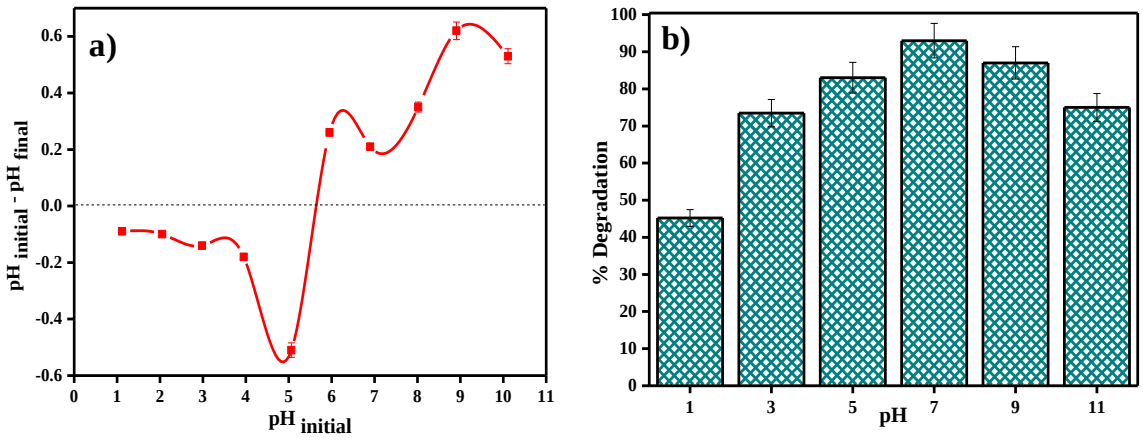


**Fig. 3.11** Plots showing (a) point zero charge of catayst, and (b) effect of methylene blue dye solution pH on photodegradation by the MSMSe (1:3) nanocomposite.

The studies were carried out by varying the pH of methylene blue dye solution using 0.1N HCl or NaOH solution. In 20mL of the methylene blue dye solution, 1mg of MSMSe (1:3) photocatalyst was added and the pH value before and after the treatment was noted. The results of the study show that the pzc of the catalyst was around pH 5.6 (Fig. 3.11a). This shows that there was no significant degradation occurs in acidic pH (below pH 5.6). This is because the adsorption of cationic adsorbents (methylene blue) is supported if pH > pzc where the catalyst

species exist as $M\text{-}O^-$ (M is the metal).[42] As methylene blue dye is cationic so it will absorb more productively on the catalyst surface above pH 5.6. So, the maximum degradation efficiency was observed at pH 7 as shown in Fig. 3.11b. However, at higher basic pH (above pH 9) the degradation efficacy decreases as precipitates of metal hydroxides may get accumulated on the catalyst surface which deactivates the catalyst.

### 3.5.5 Real wastewater treatment

Real industrial wastewater was utilized to measure the viability of the as-synthesized catalyst dependent on the ideal conditions. The amount of organic matter in the wastewater was determined with the help of COD (Chemical Oxygen Demand) and TOC (Total Organic Carbon) techniques. The COD value of industrial wastewater without any treatment was found to be 1950 mg/L, which shows that the amount of organic matter in the wastewater is high. So photodegradation of this wastewater by MSMSe (1:3) catalyst under optimum conditions (4mg catalyst in 50mL wastewater) was carried out and the COD and TOC removal percentage were analyzed at regular time intervals as shown in Fig. 3.12a. After 240 min of photodegradation, the COD and TOC removal percentage were increased to 65% and 51.5% respectively. As we have used raw industrial wastewater so we followed higher degradation time for better mineralization of pollutants. The increase in removal percentage with time shows that the organic matter present in the wastewater is mineralizing to relatively simpler compounds. Moreover, the average oxidation state (AOS) and carbon oxidation state (COS) values were calculated from equations below in order to determine the biodegradability variation of real industrial wastewater:[43]

$$AOS = 4 - 1.5[COD/TOC]$$

$$COS = 4 - 1.5[COD/TOC_i]$$

The values of AOS and COS variables have a range of +4 to -4 for the most oxidized form i.e. $CO_2$ and the most reduced form i.e. methane.[44] The initial AOS value of real industrial wastewater without any treatment was 1.73 which increased up to 2.37 and 3.2 for AOS and COS respectively after the photocatalytic degradation. The results show that the biodegradability of real wastewater has been increased in the presence of MSMSe (1:3) photocatalyst and the catalyst is effective for the treatment of effluents than the physico-chemical treatment performed by the industries.

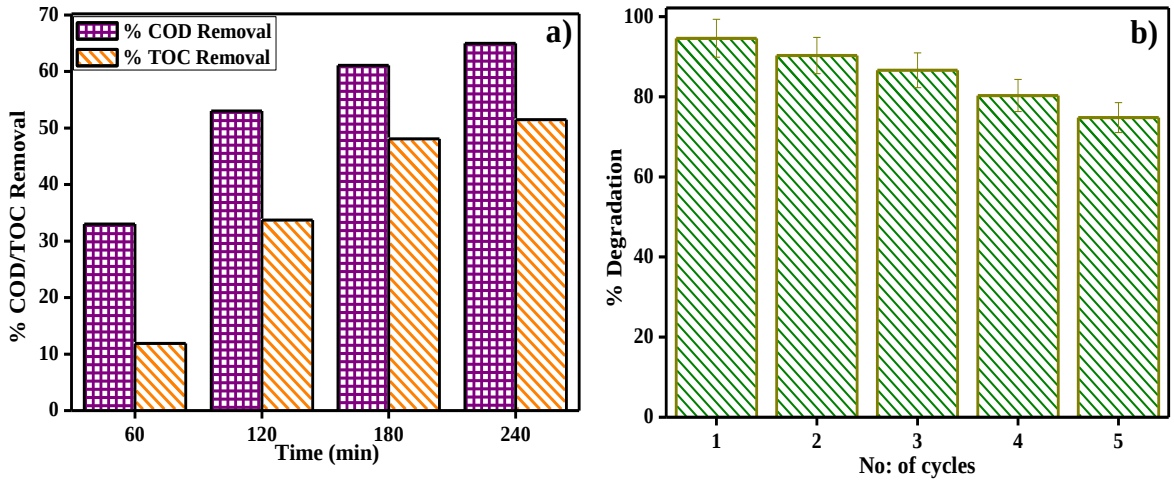


**Fig. 3.12** (a) Percent COD and TOC removal in real textile wastewater, (b) reusability upto 5 runs in methylene blue dye solution with MSMSe (1:3) photocatalyst.

### 3.5.6 Reusable photocatalyst

One of the major challenges in the photodegradation method of pollutant removal is that the catalyst cannot be reused, as dye molecules might react with the catalyst or the separation of the catalyst from the solution is very tedious. The as-prepared catalysts are not only easily separable by mere centrifugation but can also be reused with great effectiveness. The reproducibility of the catalyst was investigated by stirring MSMSe (1:3) catalyst in 20mL of methylene blue dye (5ppm) under visible light for 80 min and after the degradation; the catalyst was separated by centrifugation with distilled water washing. Then the regained catalyst was used again and the process was repeated up to 5 runs as shown in Fig. 3.12b. The results show that after 5 runs the degradation efficacy of the catalyst was still very high (~75%), which confirms that the catalyst is highly reusable.

To confirm the reusable nature of the catalyst the XRD pattern, FESEM image, PL spectra, and BET isotherms of MSMSe (1:3) nanocomposite before and after 5 cycles of photocatalytic degradation is shown in Fig. 3.13. The majority of diffraction peaks of the catalyst are still present even after 5 cycles of degradation (Fig. 3.13a) verifies that the crystal structure of MSMSe (1:3) nanocomposite is not disturbed after the reaction which is due to the high photocorrosion resistance of $MoSe_2$. The peaks after the degradation are still sharp which shows that the crystallinity of the catalyst was maintained even after many degradation cycles. Also, the morphology of the catalyst remains intact as shown by the FESEM image of MSMSe (1:3)

composite after 5 cycles of degradation (Fig. 3.13b). Fig. 3.13c shows the PL spectra before and after degradation up to 5 cycles. There is a slight increase in the PL intensity after degradation, which may be due to the deactivation of some active sites.

The surface area of the MSMSe (1:3) photocatalyst before degradation was 60 $m^2/g$ which decreases to 48 $m^2/g$ after 5 cycles of degradation which is still high and this confirms that the pollutants were not permanently adsorbed over the surface of the catalyst and thus show high degradation efficiency even after several degradation cycles. The BET isotherms of the MSMSe (1:3) catalyst before and after degradation cycles were shown in fig. 3.13d. All these studies confirm that the catalyst is highly stable and reusable with great degradation efficiency.

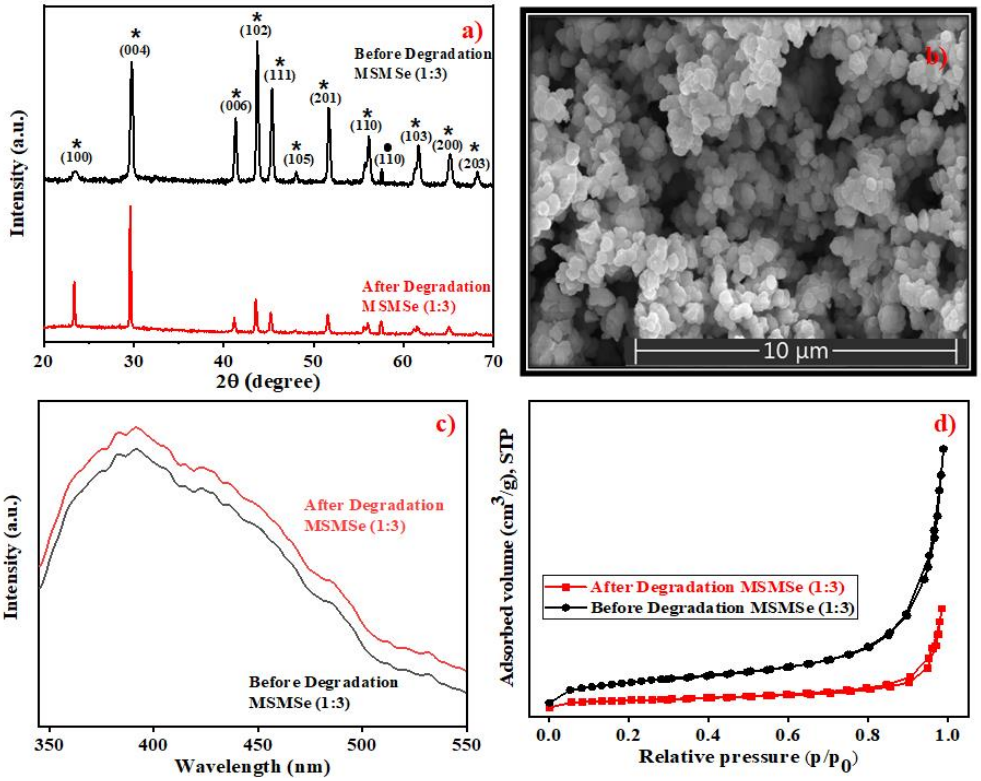


**Fig. 3.13.** (a) The XRD spectra, (b) FESEM image, (c) photoluminescence spectra, and BET adsorption isotherms of MSMSe (1:3) catalyst before and after 5 cycles of photocatalytic degradation of methylene blue.

### 3.5.7 Plausible photocatalysis mechanism

To determine the major species governing photocatalytic degradation and mechanism of photocatalysis, scavenger studies were carried out with different scavengers like methanol,

DMSO, and ascorbic acid for trapping holes ($h^+$), electrons ($e^-$), and superoxide radicals ($O_2^{-\bullet}$), respectively.[45] The degradation efficiency was carried out by comparing the activity of MSMSe (1:3) catalyst in the absence and presence of different scavengers as shown in Fig. 3.14. The results demonstrate that the catalytic efficiency was most affected in the case of methanol as the degradation efficiency decreases to 54% in presence of methanol which means holes participate maximum in the degradation process. However, the degradation efficacy was significantly decreased in the case of ascorbic acid (60.8%), which confirms the role of superoxide radicals in degradation. This shows that the degradation of dye was influenced primarily by the holes and superoxide radicals.

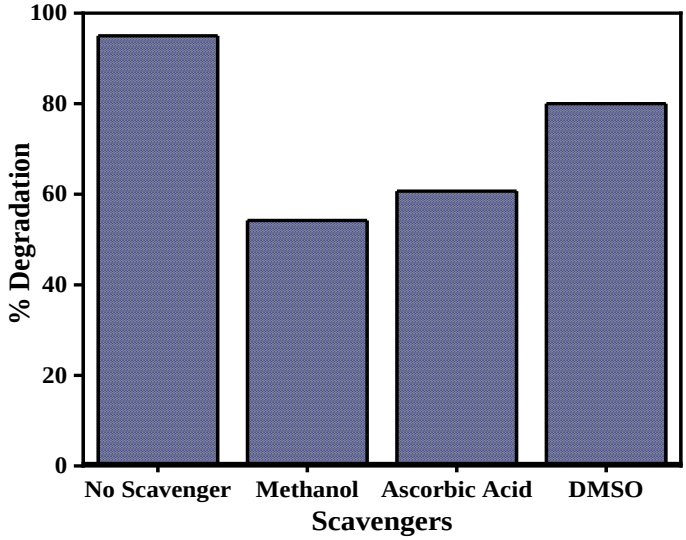


**Fig. 3.14** Degradation efficiency of MSMSe (1:3) photocatalyst in the presence of different scavengers.

Therefore, based on trapping experiments the plausible mechanism of photocatalysis is shown in scheme 3.2. As the bandgap energies of $MoS_2$ and $MoSe_2$ are tunable and both are active in the visible light, so as it absorbs light energy, the electrons in its valence band get excited to their conduction band level leaving the holes behind. Due to the formation of heterojunction between the two semiconductors, these electron-holes do not recombine and thus a charge separation occurs. Now these electrons in the CB react with the molecular oxygen forming the superoxide radicals which can either further react with a water molecule to form hydroxyl radicals or can directly degrade the pollutants. On the other hand, the holes created in the VB can react with water to form hydroxyl radicals which further cause the degradation of

pollutants to either $CO_2$ and water or relatively simpler products. The probable reaction steps are:

$MoS_2/MoSe_2 + h\nu \longrightarrow e^- + h^+$

$H_2O + h^+ \longrightarrow H_2O^+ \longrightarrow OH^- + h^+$

$O_2 + e^- \longrightarrow O_2^{-\bullet} + h^+$

$H_2O^+ \longrightarrow OH^- + h^+$

$OH^- + h^+ \longrightarrow OH^\bullet$

$OH^\bullet / O_2^{-\bullet} + \text{Pollutants} \longrightarrow \text{Degraded Products}$

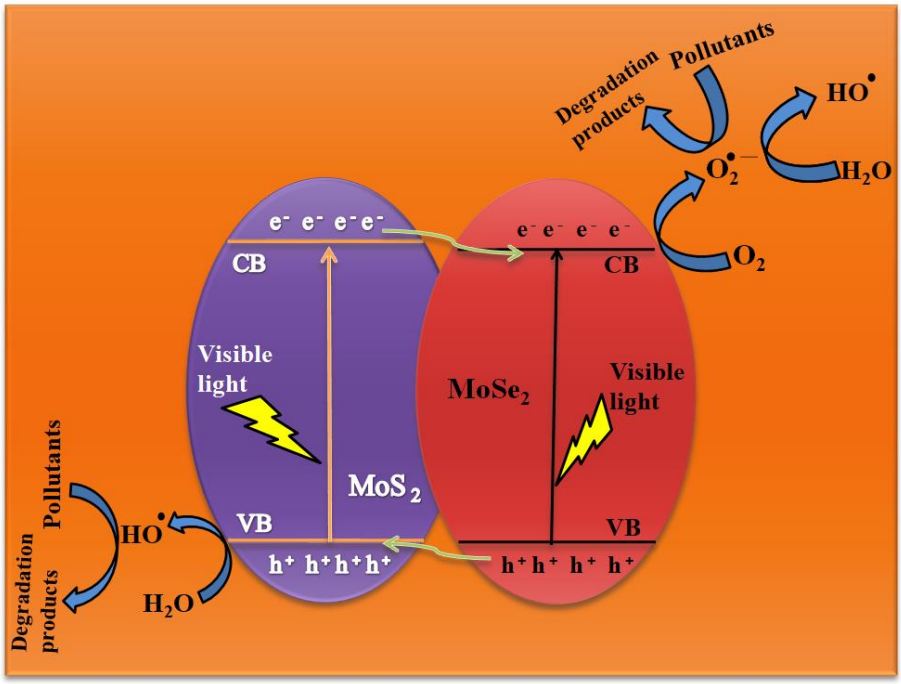


**Scheme 3.2.** Plausible photocatalytic degradation mechanism by MSMSe catalyst.

## 3.6 Electrocatalytic Studies

### 3.6.1 HER activity

The electrochemical activities of as-synthesized nanocomposites were analyzed in 0.5 M $H_2SO_4$. The polarization curves in acidic medium obtained for as-prepared composites are shown by linear sweep voltammetry (LSV) plots in Fig. 3.15 (a-c). These plots show a maximum current density of –3.76 $mAcm^{-2}$ and –4.52 $mAcm^{-2}$ at a potential of –1 V for MSMSe (1:1) and MSMSe (3:1) composites respectively. However, the maximum current density of –19.4 $mAcm^{-2}$ has been obtained for MSMSe (1:3) catalyst at –1 V potential (Fig. 3.15c) in the acidic medium.

The MSMSe (1:3) composite exhibits high surface area and the presence of micropores and mesopores with enlarged pore volume, which increases the active surface characteristics of the composite and hence results in enhanced HER performance.[22] The MSMSe composites show high current density even with very low mass loading which confirms high efficiency of the prepared catalysts.

The performance and efficiency of the electrocatalyst were most prominently defined by its stability which is required in the present time. The stability of MSMSe nanocomposites was determined by the cyclic voltammetry (CV) technique performed for 2500 cycles at a scan rate of 100 $mVs^{-1}$ in 0.2 to 0.6 V voltage window. The polarization curves obtained after the 2500 CV cycles of the composites show that for MSMSe (1:1) and MSMSe (1:3) composites, there is a negligible loss in current density as the maximum current density of – 3.74 $mAcm^{-2}$ and – 19.32 $mAcm^{-2}$ was observed even after 2500 CV cycles as shown in fig. 3.15a and 3.15c. The combination of $MoS_2$ and $MoSe_2$ gives rise to a synergistic effect which provides an open porous space to facilitate the charge transfer within the interlaced arrays so we observe high stability in current density. Moreover, the higher stability of the as-synthesized composites is attributed to their high acidic corrosion resistance under continuous CV cycling (under continuous oxidation/reduction process). However, in the case of MSMSe (3:1) composite, there is a slight decrease of current density to –3.28 $mAcm^{-2}$ after 2500 CV cycles. This is due to the higher charge transfer resistance in $MoS_2$ as the metallic character of $MoS_2$ is lower as compared to $MoSe_2$ (as the metallic nature of S is less).[46]

To determine the mechanism responsible for the HER and electrocatalytic performance, Tafel slope is one of the most important analysis. The following steps determine the probable mechanism responsible for HER performance:[47]

Volmer: $H_3O^+ + M(e^-) \longrightarrow MH_{ads} + H_2O$

Heyrovsky: $H_3O^+ + MH_{ads} + M(e^-) \longrightarrow 2M + H_2O + H_2$

Tafel: $2MH_{ads} \longrightarrow 2M + H_2$

Here the M determines the species active sites and $MH_{ads}$ denote the hydrogen adsorbed intermediate. In the Volmer reaction on the catalyst surface a proton gets attached and then

through Heyrovsky and Tafel reactions the produced hydrogen leaves the surface of catalyst. If the Tafel slope of the reaction is ~120 $mVdec^{-1}$ then the reaction proceeds through Volmer-Heyrovsky pathway whereas if the value is ~30 $mVdec^{-1}$ then the reaction follows Volmer-Tafel pathway. The reaction rate will be higher if the value of Tafel slope is smaller with respect to the given potential.[48]

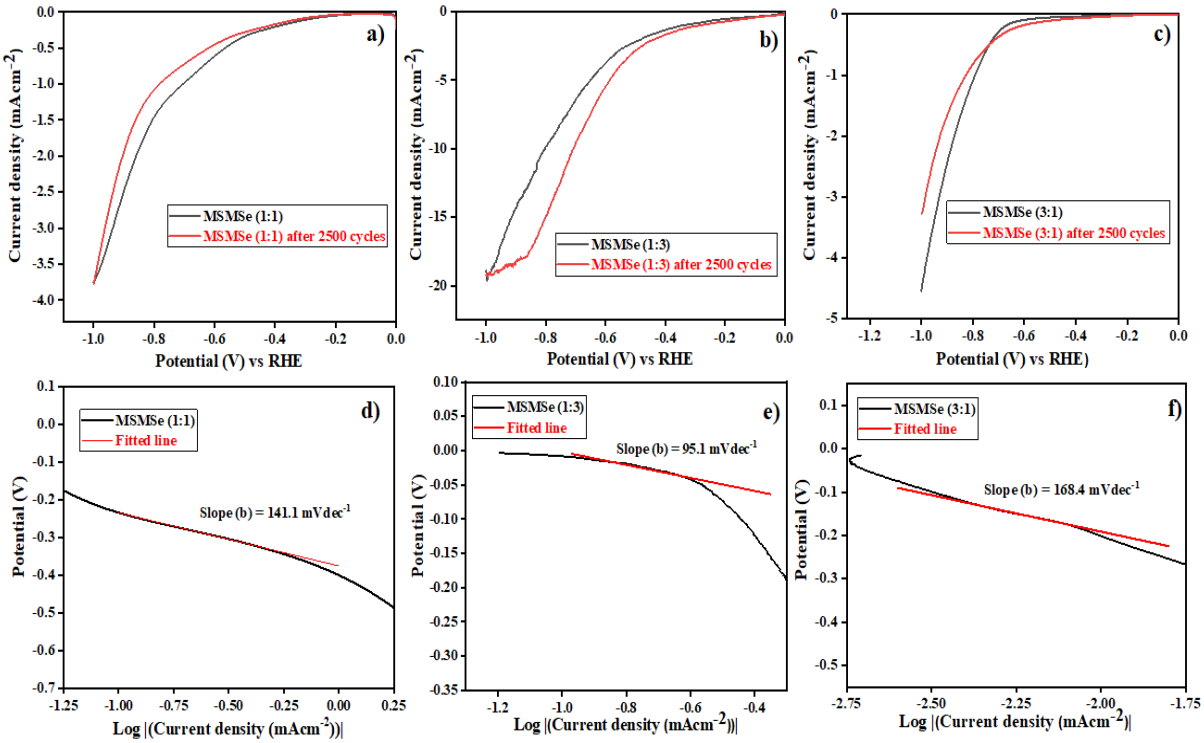


**Fig. 3.15** LSV plots of (a) MSMSe (1:1), (b) MSMSe (1:3) and (c) MSMSe (3:1) composites in acidic medium and Tafel plots of (d) MSMSe (1:1), (e) MSMSe (1:3) and (f) MSMSe (3:1) composites.

The Tafel slopes of the MSMSe composites are shown in the insets of their LSV plots (fig. 3.15 (d-f)). The value of Tafel slope for MSMSe (1:1), MSMSe (1:3) and MSMSe (3:1) are 141.1, 95.1 and 168.4 $mVdec^{-1}$ respectively in acidic medium. This shows that in an acidic electrolyte, the rate-determining step (RDS) for HER is the Volmer-Heyrovsky reaction. The lower value of Tafel slope for MSMSe (1:3) nanocomposite shows the faster charge transfer kinetics in the heterostructure. The edge sites of $MoS_2/MoSe_2$ are the active species in an acidic medium for HER. So the lower Tafel slope value in MSMSe (1:3) shows a higher number of active edge sites in the composite which may be due to its higher surface area. The values predict that adsorption of $H^+$ ion is fast but the desorption process is slow due to higher surface area and

pore size. The active sites get more exposed due to the abundant interfaces in $MoS_2/MoSe_2$ heterostructure for the electrochemical reaction. The high stability of MSMSe nanocomposites and faster charge transfer kinetics on the active edge sites of heterostructure makes them potential catalysts for HER.

### 3.6.2 Electric Double Layer Capacitance (EDLC) or $C_{dl}$

The storage capacity of the as-synthesized nanocomposites has been determined from the CV plots performed at various scan rates of 10-210 $mVs^{-1}$ in the voltage window of 0.2 to 0.6 V as shown in fig. 3.16 (a-c). The rectangular shape of CV plots suggests that the reactions are reversible and occur without faradic reaction and attributes to the EDLC ($C_{dl}$) storage capability. By plotting the scan rate *vs* current density variation ($\Delta J = J_{cathodic} - J_{anodic}$ at 0.4V) the calculated $C_{dl}$ values (fig. 3.17a) comes out to be 500.0, 607.0, and 647.1 $\mu Fcm^{-2}$ for MSMSe (1:1), MSMSe (1:3) and MSMSe (3:1) respectively suggesting that the $MoS_2$ and $MoSe_2$ heterojunction leads to the higher energy storage performance due to the presence of more exposed active sites in the heterostructure.

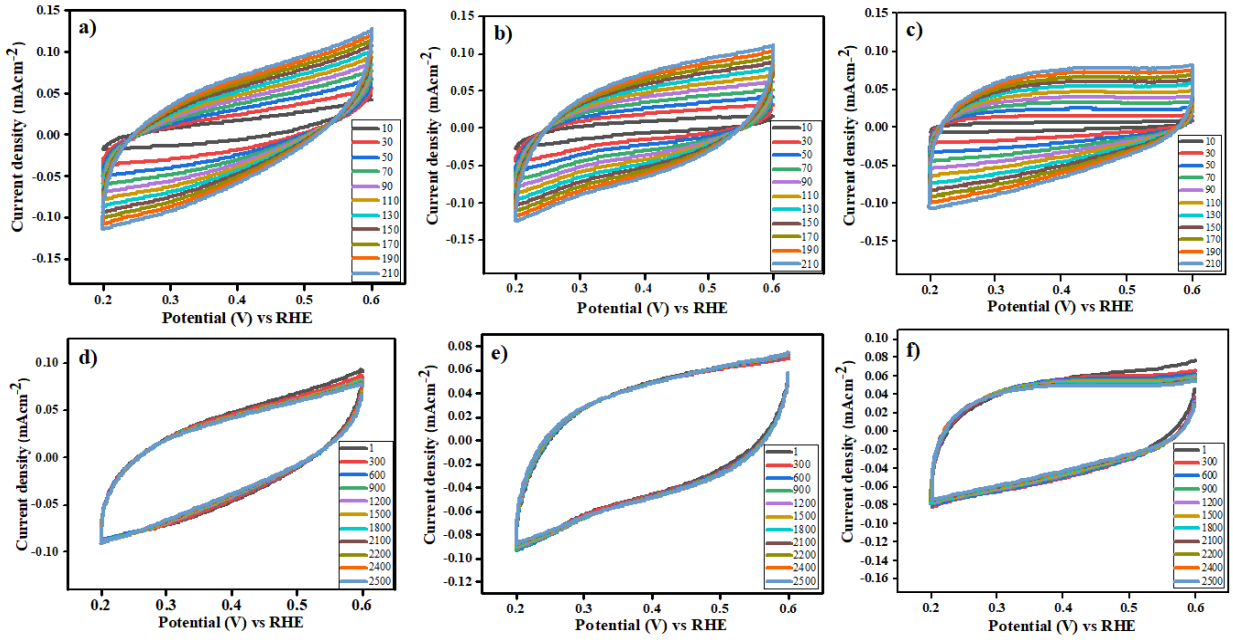


**Fig. 3.16** CV plots of (a) MSMSe (1:1), (b) MSMSe (1:3), and (c) MSMSe (3:1) at multiple scan rates and CV plots for 2500 cycles of (d) MSMSe (1:1), (e) MSMSe (1:3), and (f) MSMSe (3:1).

From the CV plots, one can observe that even when the CV was performed at a lower speed (10 $mVs^{-1}$) there was no change observed in the shape of CV plots, only the voltage/area was enhanced. It also shows that the prepared composites show higher electrochemical active surface area (ECAS) and results in the enhancement of their electrochemical performance. The stability and charge storage ability is the vital parameter for electrode fabrication for electrochemical capacitors. The capacitance retention was determined via CV analysis at a fixed scan rate of 100 $mVs^{-1}$ for 2500 CV cycles in an acidic medium in a 0.2 to 0.6 V voltage range for MSMSe composites (fig. 3.16 (d-f)).

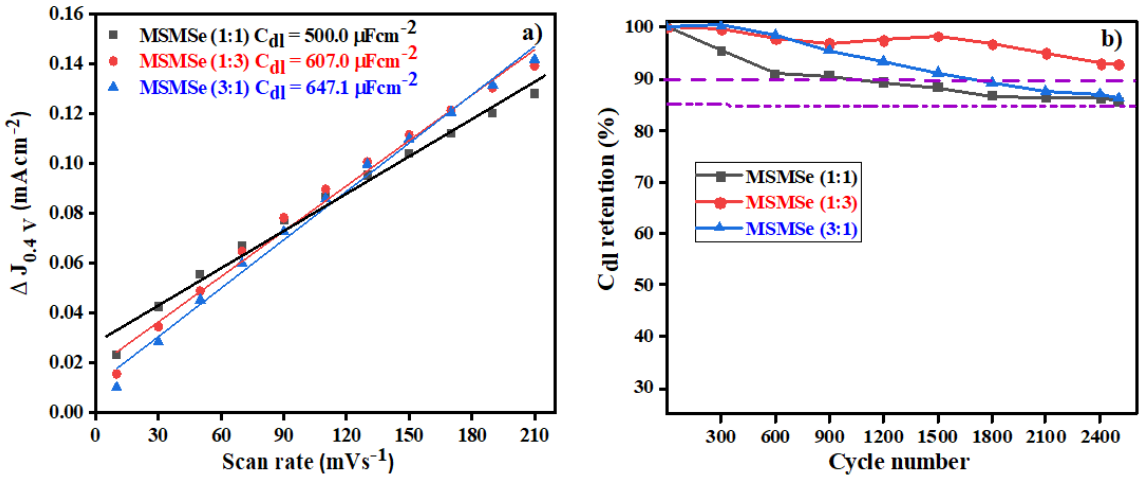


**Fig. 3.17** (a) EDLC plot and (b) capacitance retention with a number of cycles for MSMSe composites.

It can be observed from the figures that the shape of CV plots was retained even after 2500 cycles. The only change was observed in the first CV cycle after which all the CV cycles remain the same. The enhanced retention of capacitance in acidic medium was confirmed by plotting the % capacitance retention with respect to CV cycle number (fig. 3.17b), which shows that MSMSe (1:3) has the highest capacitance retention of ~94% for 2500 CV cycles compared with bare $MoS_2$ in literature showing stability up to only 1000 cycles.[49] All above results confirm that the as-prepared MSMSe composites are the potential electrode material for capacitor applications.

## References


(1) Sharma, S.; Kundu, A.; Basu, S.; Shetti, N. P.; Aminabhavi, T. M. Sustainable Environmental Management and Related Biofuel Technologies. *J. Environ. Manage.* **2020**, *273*, 111096. https://doi.org/10.1016/j.jenvman.2020.111096.

(2) Sharma, S.; Basu, S.; Shetti, N. P.; Nadagouda, M. N.; Aminabhavi, T. M. Microplastics in the Environment: Occurrence, Perils, and Eradication. *Chem. Eng. J.* **2021**, *408*, 127317. https://doi.org/10.1016/j.cej.2020.127317.

(3) Aanchal; Barman, S.; Basu, S. Complete Removal of Endocrine Disrupting Compound and Toxic Dye by Visible Light Active Porous G-$C_3N_4$/H-ZSM-5 Nanocomposite. *Chemosphere* **2020**, *241*, 124981. https://doi.org/10.1016/j.chemosphere.2019.124981.

(4) Sharma, S.; Basu, S.; Shetti, N. P.; Aminabhavi, T. M. Waste-to-Energy Nexus for Circular Economy and Environmental Protection: Recent Trends in Hydrogen Energy. *Sci. Total Environ.* **2020**, *713*, 136633. https://doi.org/10.1016/j.scitotenv.2020.136633.

(5) Wilken, M.; Siewert, I. Electrocatalytic Hydrogen Production with a Molecular Cobalt Complex in Aqueous Solution. *ChemElectroChem* **2020**, *7* (1), 217–221. https://doi.org/10.1002/celc.201901913.

(6) Rajagopal, S.; Paramasivam, B.; Muniyasamy, K. Photocatalytic Removal of Cationic and Anionic Dyes in the Textile Wastewater by $H_2O_2$ Assisted $TiO_2$ and Micro-Cellulose Composites. *Sep. Purif. Technol.* **2020**, *252*, 117444. https://doi.org/10.1016/j.seppur.2020.117444.

(7) Sharma, S.; Basu, S. Fabrication of Centimeter-Sized $Sb_2S_3$/$SiO_2$ Monolithic Mimosa Pudica Nanoflowers for Remediation of Hazardous Pollutants from Industrial Wastewater. *J. Clean. Prod.* **2021**, *280*, 124525. https://doi.org/10.1016/j.jclepro.2020.124525.

(8) Chen, Z.; Wu, H.; Li, J.; Wang, Y.; Guo, W.; Cao, C.; Chen, Z. Defect Enhanced CoP/Reduced Graphene Oxide Electrocatalytic Hydrogen Production with Pt-like Activity. *Appl. Catal. B Environ.* **2020**, *265*, 118576. https://doi.org/10.1016/j.apcatb.2019.118576.

(9) Monga, D.; Sharma, S.; Shetti, N. P.; Basu, S.; Reddy, K. R.; Aminabhavi, T. M. Advances in Transition Metal Dichalcogenide-Based Two-Dimensional Nanomaterials. *Mater. Today Chem.* **2021**, *19*, 100399. https://doi.org/10.1016/j.mtchem.2020.100399.

(10) Amin, B.; Singh, N.; Schwingenschlögl, U. Heterostructures of Transition Metal Dichalcogenides. *Phys. Rev. B* **2015**, *92* (7), 075439. https://doi.org/10.1103/PhysRevB.92.075439.

(11) Li, L.; Yin, X.; Sun, Y. Facile Synthesized Low-Cost $MoS_2$/CdS Nanodots-on-Nanorods Heterostructures for Highly Efficient Pollution Degradation under Visible-Light Irradiation. *Sep. Purif. Technol.* **2019**, *212*, 135–141. https://doi.org/10.1016/j.seppur.2018.11.032.

(12) Shi, Z.; Xu, P.; Shen, X.; Zhang, Y.; Luo, L.; Duoerkun, G.; Zhang, L. $TiO_2$/$MoS_2$ Heterojunctions-Decorated Carbon Fibers with Broad-Spectrum Response as Weaveable Photocatalyst/Photoelectrode. *Mater. Res. Bull.* **2019**, *112*, 354–362. https://doi.org/10.1016/j.materresbull.2019.01.005.

(13) Xie, T.; Liu, Y.; Wang, H.; Wu, Z. Layered $MoSe_2$/$Bi_2WO_6$ Composite with P-N Heterojunctions as a Promising Visible-Light Induced Photocatalyst. *Appl. Surf. Sci.* **2018**, *444*, 320–329. https://doi.org/10.1016/j.apsusc.2018.03.072.

(14) Shi, Y.; Hua, C.; Li, B.; Fang, X.; Yao, C.; Zhang, Y.; Hu, Y.-S.; Wang, Z.; Chen, L.; Zhao, D.; Stucky, G. D. Highly Ordered Mesoporous Crystalline $MoSe_2$ Material with Efficient Visible-Light-Driven Photocatalytic Activity and Enhanced Lithium Storage Performance. *Adv. Funct. Mater.* **2013**, *23* (14), 1832–1838. https://doi.org/10.1002/adfm.201202144.

(15) Chen, Y. Z.; Medina, H.; Wang, S. W.; Su, T. Y.; Li, J. G.; Yen, W. C.; Cheng, K. Y.; Kuo, H. C.; Shen, G.; Chueh, Y. L. Low-Temperature and Ultrafast Synthesis of Patternable Few-Layer Transition Metal Dichacogenides with Controllable Stacking Alignment by a Microwave-Assisted Selenization Process. *Chem. Mater.* **2016**, *28* (4), 1147–1154. https://doi.org/10.1021/acs.chemmater.5b04579.

(16) Yang, J.; Zhu, J.; Xu, J.; Zhang, C.; Liu, T. $MoSe_2$ Nanosheet Array with Layered MoS2 Heterostructures for Superior Hydrogen Evolution and Lithium Storage Performance. *ACS Appl. Mater. Interfaces* **2017**, *9* (51), 44550–44559. https://doi.org/10.1021/acsami.7b15854.

(17) Li, S.; Zang, W.; Liu, X.; Pennycook, S. J.; Kou, Z.; Yang, C.; Guan, C.; Wang, J. Heterojunction Engineering of $MoSe_2$/$MoS_2$ with Electronic Modulation towards Synergetic Hydrogen Evolution Reaction and Supercapacitance Performance. *Chem. Eng.*

*J.* **2019**, *359*, 1419–1426. https://doi.org/10.1016/j.cej.2018.11.036.

(18) Ren, X.; Wei, Q.; Ren, P.; Wang, Y.; Chen, R. Synthesis of Flower-like $MoSe_2$@$MoS_2$ Nanocomposites as the High Efficient Water Splitting Electrocatalyst. *Mater. Lett.* **2018**, *231*, 213–216. https://doi.org/10.1016/j.matlet.2018.08.049.

(19) Song, W.; Wang, K.; Jin, G.; Wang, Z.; Li, C.; Yang, X.; Chen, C. Two-Step Hydrothermal Synthesis of CoSe/$MoSe_2$ as Hydrogen Evolution Electrocatalysts in Acid and Alkaline Electrolytes. *ChemElectroChem* **2019**, *6* (18), 4842–4847. https://doi.org/10.1002/celc.201901382.

(20) Lee, Y. B.; Kim, S. K.; Ji, S.; Song, W.; Chung, H.-S.; Choi, M. K.; Lee, M.; Myung, S.; Lim, J.; An, K.-S.; Lee, S. S. Facile Microwave Assisted Synthesis of Vastly Edge Exposed 1T/2H-$MoS_2$ with Enhanced Activity for Hydrogen Evolution Catalysis. *J. Mater. Chem. A* **2019**, *7* (8), 3563–3569. https://doi.org/10.1039/C8TA12080C.

(21) Monga, D.; Ilager, D.; Shetti, N. P.; Basu, S.; Aminabhavi, T. M. 2D/2d Heterojunction of $MoS_2$/g-$C_3N_4$ Nanoflowers for Enhanced Visible-Light-Driven Photocatalytic and Electrochemical Degradation of Organic Pollutants. *J. Environ. Manage.* **2020**, *274*, 111208. https://doi.org/10.1016/j.jenvman.2020.111208.

(22) Kaur, N.; Mir, R. A.; Pandey, O. P. Electrochemical and Optical Studies of Facile Synthesized Molybdenum Disulphide ($MoS_2$) Nano Structures. *J. Alloys Compd.* **2019**, *782*, 119–131. https://doi.org/10.1016/j.jallcom.2018.12.145.

(23) Midya, A.; Ghorai, A.; Mukherjee, S.; Maiti, R.; Ray, S. K. Hydrothermal Growth of Few Layer 2H-$MoS_2$ for Heterojunction Photodetector and Visible Light Induced Photocatalytic Applications. *J. Mater. Chem. A* **2016**, *4* (12), 4534–4543. https://doi.org/10.1039/C5TA09003B.

(24) Hu, X.; Deng, F.; Huang, W.; Zeng, G.; Luo, X.; Dionysiou, D. D. The Band Structure Control of Visible-Light-Driven RGO/ZnS-$MoS_2$ for Excellent Photocatalytic Degradation Performance and Long-Term Stability. *Chem. Eng. J.* **2018**, *350*, 248–256. https://doi.org/10.1016/j.cej.2018.05.182.

(25) Ansari, S. A.; Cho, M. H. Simple and Large Scale Construction of $MoS_2$-g-$C_3N_4$ Heterostructures Using Mechanochemistry for High Performance Electrochemical Supercapacitor and Visible Light Photocatalytic Applications. *Sci. Rep.* **2017**, *7* (1), 43055. https://doi.org/10.1038/srep43055.

(26) Hu, X.; Zeng, X.; Liu, Y.; Lu, J.; Yuan, S.; Yin, Y.; Hu, J.; McCarthy, D. T.; Zhang, X. Nano-Layer Based 1T-Rich $MoS_2$/g-$C_3N_4$ Co-Catalyst System for Enhanced Photocatalytic and Photoelectrochemical Activity. *Appl. Catal. B Environ.* **2020**, *268*, 118466. https://doi.org/10.1016/j.apcatb.2019.118466.

(27) Bhattacharya, D.; Mukherjee, S.; Mitra, R. K.; Ray, S. K. Size-Dependent Optical Properties of $MoS_2$ Nanoparticles and Their Photo-Catalytic Applications. *Nanotechnology* **2020**, *31* (14), 145701. https://doi.org/10.1088/1361-6528/ab61ce.

(28) Ghorai, A.; Ray, S. K.; Midya, A. MoSe2 Nanosheets with Tuneable Optical Properties for Broadband Visible Light Photodetection. *ACS Appl. Nano Mater.* **2021**, *4* (3), 2999–3006. https://doi.org/10.1021/acsanm.1c00129.

(29) Fan, C.; Wei, Z.; Yang, S.; Li, J. Synthesis of $MoSe_2$ Flower-like Nanostructures and Their Photo-Responsive Properties. *RSC Adv.* **2014**, *4* (2), 775–778. https://doi.org/10.1039/C3RA42564A.

(30) Siddiqui, I.; Mittal, H.; Kohli, V. K.; Gautam, P.; Ali, M.; Khanuja, M. Hydrothermally Synthesized Micron Sized, Broom-Shaped $MoSe_2$ Nanostructures for Superior Photocatalytic Water Purification. *Mater. Res. Express* **2018**, *5* (12), 125020. https://doi.org/10.1088/2053-1591/aae241.

(31) Harpeness, R.; Gedanken, A.; Weiss, A. M.; Slifkin, M. A. Microwave-Assisted Synthesis of Nanosized $MoSe_2$. *J. Mater. Chem.* **2003**, *13* (10), 2603. https://doi.org/10.1039/b303740a.

(32) Wang, Z.; Ma, L.; Chen, W.; Huang, G.; Chen, D.; Wang, L.; Lee, J. Y. Facile Synthesis of $MoS_2$/Graphene Composites: Effects of Different Cationic Surfactants on Microstructures and Electrochemical Properties of Reversible Lithium Storage. *RSC Adv.* **2013**, *3* (44), 21675. https://doi.org/10.1039/c3ra43699c.

(33) Liu, Y.; Zhu, M.; Chen, D. Sheet-like $MoSe_2$/C Composites with Enhanced Li-Ion Storage Properties. *J. Mater. Chem. A* **2015**, *3* (22), 11857–11862. https://doi.org/10.1039/C5TA02100F.

(34) Fu, S.; Yuan, W.; Yan, Y.; Liu, H.; Shi, X.; Zhao, F.; Zhou, J. Highly Efficient Visible-Light Photoactivity of Z-Scheme $MoS_2$/$Ag_2CO_3$ Photocatalysts for Organic Pollutants Degradation and Bacterial Inactivation. *J. Environ. Manage.* **2019**, *252*, 109654. https://doi.org/10.1016/j.jenvman.2019.109654.

(35) Kar, S.; Ibrahim, S.; Pal, T.; Ghosh, S. Enhance Solar-Light-Driven Photocatalytic Degradation of Norfloxacin Aqueous Solution by RGO-Based $Cd_xZn_{1-x}S$ Alloy Composite with Band-Gap Tuneability. *ChemistrySelect* **2020**, *5* (1), 54–60. https://doi.org/10.1002/slct.201903755.

(36) Shi, Y.; Hua, C.; Li, B.; Fang, X.; Yao, C.; Zhang, Y.; Hu, Y. S.; Wang, Z.; Chen, L.; Zhao, D.; Stucky, G. D. Highly Ordered Mesoporous Crystalline $MoSe_2$ Material with Efficient Visible-Light-Driven Photocatalytic Activity and Enhanced Lithium Storage Performance. *Adv. Funct. Mater.* **2013**, *23* (14), 1832–1838. https://doi.org/10.1002/adfm.201202144.

(37) Zhou, X.; Yao, J.; Yang, M.; Ma, J.; Zhou, Q.; Ou, E.; Zhang, Z.; Sun, X. Synthesis of $MoSe_2/SrTiO_3$ Heterostructures with Enhanced Ultraviolet-Light-Driven and Visible-Light-Driven Photocatalytic Properties. *Nano* **2018**, *13* (04), 1850038. https://doi.org/10.1142/S1793292018500388.

(38) Liu, X.; Xing, Z.; Zhang, H.; Wang, W.; Zhang, Y.; Li, Z.; Wu, X.; Yu, X.; Zhou, W. Fabrication of 3D Mesoporous Black $TiO_2/MoS_2/TiO_2$ Nanosheets for Visible-Light-Driven Photocatalysis. *ChemSusChem* **2016**, *9* (10), 1118–1124. https://doi.org/10.1002/cssc.201600170.

(39) Rani, A.; Singh, K.; Patel, A. S.; Chakraborti, A.; Kumar, S.; Ghosh, K.; Sharma, P. Visible Light Driven Photocatalysis of Organic Dyes Using $SnO_2$ Decorated $MoS_2$ Nanocomposites. *Chem. Phys. Lett.* **2020**, *738*, 136874. https://doi.org/10.1016/j.cplett.2019.136874.

(40) Khabiri, G.; Aboraia, A. M.; Soliman, M.; Guda, A. A.; Butova, V. V.; Yahia, I. S.; Soldatov, A. V. A Novel $\alpha$-$Fe_2O_3$@$MoS_2$QDs Heterostructure for Enhanced Visible-Light Photocatalytic Performance Using Ultrasonication Approach. *Ceram. Int.* **2020**, *46* (11), 19600–19608. https://doi.org/10.1016/j.ceramint.2020.05.021.

(41) Wang, Y.; Xiao, X.; Chen, J.; Lu, M.; Zeng, X. 1T Phase Boosted $MoSe_2$/Pg-$C_3N_4$ with Z-Scheme Heterojunction for Enhanced Photocatalytic Degradation of Contaminants. *Appl. Surf. Sci.* **2020**, *510* (November 2019), 145341. https://doi.org/10.1016/j.apsusc.2020.145341.

(42) Sharma, S.; Basu, S. Highly Reusable Visible Light Active Hierarchical Porous $WO_3/SiO_2$ Monolith in Centimeter Length Scale for Enhanced Photocatalytic Degradation of Toxic

Pollutants. *Sep. Purif. Technol.* **2020**, *231* (June 2019), 115916. https://doi.org/10.1016/j.seppur.2019.115916.

(43) Ahmadi, M.; Ramezani Motlagh, H.; Jaafarzadeh, N.; Mostoufi, A.; Saeedi, R.; Barzegar, G.; Jorfi, S. Enhanced Photocatalytic Degradation of Tetracycline and Real Pharmaceutical Wastewater Using MWCNT/$TiO_2$ Nano-Composite. *J. Environ. Manage.* **2017**, *186*, 55–63. https://doi.org/10.1016/j.jenvman.2016.09.088.

(44) Jorfi, S.; Barzegar, G.; Ahmadi, M.; Darvishi Cheshmeh Soltani, R.; alah Jafarzadeh Haghighifard, N.; Takdastan, A.; Saeedi, R.; Abtahi, M. Enhanced Coagulation-Photocatalytic Treatment of Acid Red 73 Dye and Real Textile Wastewater Using UVA/Synthesized MgO Nanoparticles. *J. Environ. Manage.* **2016**, *177*, 111–118. https://doi.org/10.1016/j.jenvman.2016.04.005.

(45) Rathi, A.; Basu, S.; Barman, S. Adsorptive Removal of Fipronil from Its Aqueous Solution by Modified Zeolite HZSM-5: Equilibrium, Kinetic and Thermodynamic Study. *J. Mol. Liq.* **2019**, *283*, 867–878. https://doi.org/10.1016/j.molliq.2019.02.140.

(46) Sharma, M. D.; Mahala, C.; Basu, M. 2D Thin Sheet Heterostructures of $MoS_2$ on $MoSe_2$ as Efficient Electrocatalyst for Hydrogen Evolution Reaction in Wide PH Range. *Inorg. Chem.* **2020**, *59* (7), 4377–4388. https://doi.org/10.1021/acs.inorgchem.9b03445.

(47) Mir, R. A.; Pandey, O. P. Influence of Graphitic/Amorphous Coated Carbon on HER Activity of Low Temperature Synthesized β-$Mo_2C$@C Nanocomposites. *Chem. Eng. J.* **2018**, *348*, 1037–1048. https://doi.org/10.1016/j.cej.2018.05.041.

(48) Mir, R. A.; Kaur, G.; Pandey, O. P. Facile Process to Utilize Carbonaceous Waste as a Carbon Source for the Synthesis of Low Cost Electrocatalyst for Hydrogen Production. *Int. J. Hydrogen Energy* **2020**, *45* (44), 23908–23919. https://doi.org/10.1016/j.ijhydene.2019.11.239.

(49) Ghorai, A.; Ray, S. K.; Midya, A. Ethylenediamine-Assisted High Yield Exfoliation of $MoS_2$ for Flexible Solid-State Supercapacitor Application. *ACS Appl. Nano Mater.* **2019**, *2* (3), 1170–1177. https://doi.org/10.1021/acsanm.8b02002.

# CHAPTER 4:

## *2D BiOCl Nanorods Decorated with 2D $MoS_2$ Nanosheets for Visible Light-driven Photocatalytic Detoxification of Organic and Inorganic Pollutants*

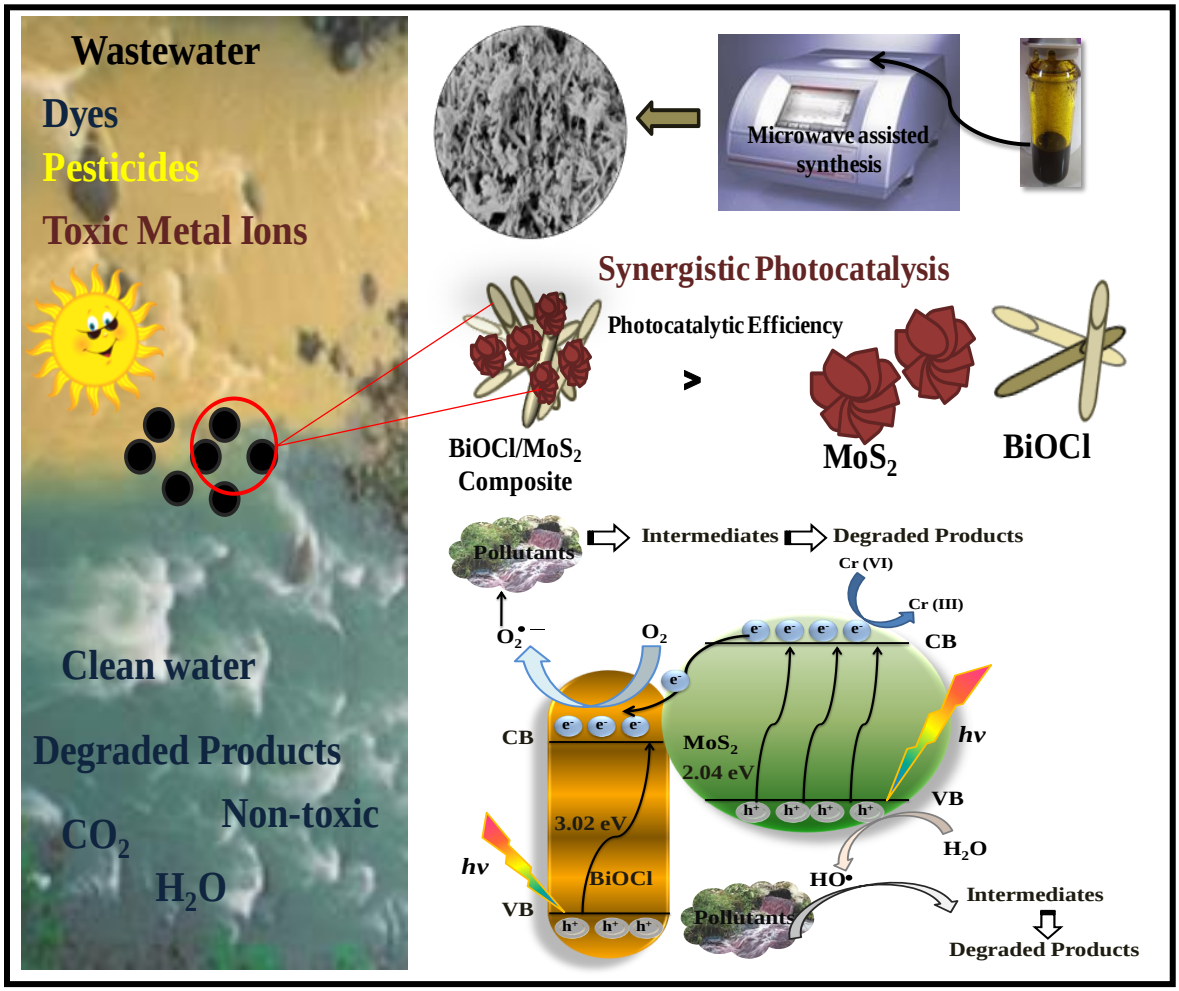


## Highlights

- ✓ $BiOCl/MoS_2$ nanorods were prepared using in-situ microwave technique.
- ✓ Composites show characteristic morphological/surface properties.
- ✓ Show effective detoxification of organic/inorganic pollutants under visible light.
- ✓ Practical efficiency confirms by high COD/TOC removal from industrial wastewater.

## 4.1 Introduction

Environmental remediation is one of the major worldwide concerns debated over in the past decades, one of them being water pollution. It poses severe health issues for living beings and a threat to the ecosystem.[1] Dyes, pesticides, and toxic metal ions are some of the abundant contaminants which need to be treated due to their daily use, enormous discharge from various industries, high toxicity level as well as complicated degradation.[2] Methylene blue is an organic dye extensively used in the dye, textile, and plastic industries. MB is also used in the area of biology to prepare various staining methods, such as Jenner's and Wright's stains.[3] However, MB can cause serious complications in humans, including high blood pressure, nausea, shock, vomiting, the development of Heinz bodies, excessive perspiration, jaundice, and mental disorientation.[4,5] Similarly, fipronil is also a toxic organic pollutant and cause serious health hazards as described in the previous chapters.[6] Not only organic pollutants but some inorganic metals are also responsible for water contamination. Chromium ion pollution is mostly caused by industrial plants, such as those involved in leather processing, wood preservation, pigments, and paint manufacturing.[7,8] Chromium is commonly found in the aquatic environment as Cr(III) and Cr(VI), and while the first is important to human metabolism at extremely low levels, the second one is toxic and carcinogenic. Cr(VI) is mostly eliminated from wastewaters after it is catalytically reduced to Cr(III) and precipitated as Cr(III) hydroxide.[9-11] So potential semiconductor photocatalysts are required which can efficiently degrade the organic pollutants as well as can also reduce Cr(VI) to Cr(III). Particularly, forming 2D/2D heterostructures is a promising method to produce large contact areas and quick charge transfer.

Bismuth oxyhalides have drawn a major consideration for their astounding photocatalytic activities. Due to the layered arrangements and good photo-electronic characteristics, BiOCl has been used in various procedures showing up with great photocatalytic performance.[12] BiOCl comprises layers of $[Bi_2O_2]^{2+}$ inserted between two ions of Cl, which facilitates the reduced recombination of charge carriers owing to inner static electric fields.[13] One of the crucial drawbacks of BiOCl is that due to its huge band gap (~3.5 eV) it can only use the photons in the UV region of the spectrum.[14] In this manner, the practical usage of BiOCl as a wide-range photocatalyst is restricted.[15] In request to improve the catalytic activity of BiOCl in natural light, numerous attempts have been made to synthesize the visible light active BiOCl based catalysts

either by bringing in oxygen vacancies, integrating sites for doping, or combining with other semiconductors having narrow bandgap.[16]

$MoS_2$ is one of the members of transition metal dichalcogenides[17] and has drawn extensive consideration in the field of photocatalysis. Interestingly, $MoS_2$ is an inherently p-type semiconductor containing a sandwich-like stacked structure of S−Mo−S layers reinforced by attractive van der Waals forces.[18] As its band gap is between 1.4 to 2.1 eV so it absorbs photons in the visible region.[19] The use of $MoS_2$ as a photocatalyst is well exploited due to its abundance in nature with high chemical stability, low cost, and high catalytic performance. From the literature, it was envisaged that the improvement of 2D materials with layered $MoS_2$ gives rise to a large number of active sites that are responsible for providing sufficient interfacial area and enhancing the photocatalytic response activity.[20]

In the present work, a new facile, one-pot, and fast microwave-assisted synthetic procedure was used for the preparation of an effective photocatalyst BiOCl/$MoS_2$ with variable weight ratios. The structural, morphological and optical characterizations were carried out for the as-prepared photocatalyst. The photocatalytic performance was estimated by detoxification of methylene blue dye, fipronil pesticide, industrial wastewater, and chromium (VI) metal. Variation of catalytic activity with solution pH, catalyst dose, and illumination area was examined. The reusability of the catalyst was determined by running the catalyst for several cycles. Also, the mechanism of degradation was examined with the help of scavenger studies.

## 4.2 Characterization and photocatalytic studies

Refer to section 2.2 chapter 2

## 4.3 Methodology

***Synthesis of BiOCl and $MoS_2$ nanocomposites*:** The catalysts were prepared using simple precursors and microwave-assisted technique. The required amount of $Bi(NO_3)_3.5H_2O$ and KCl (Loba Chemie) was mixed in 30 mL ethylene glycol through stirring. Afterwards, the required amount of ammonium molybdate and thiourea (according to weight ratios 1:1, 3:1, and 1:3) was added to the above suspension with stirring. The resulting mixture was sonicated for 1 hour to ensure complete dispersion. After that, the mixture was transferred to a microwave vial for

heating at 180°C (20 min). After heating, the precipitates were thoroughly washed with distilled water via centrifugation and dried at 60°C in an oven to obtain black powder catalyst. A schematic representation of synthesis process is shown in scheme 4.1. The weight ratios of BiOCl to $MoS_2$ ranges from 1:1, 1:3 to 3:1 and named as BOCMS(1:1), BOCMS(1:3) and BOCMS(3:1) respectively. The pure BiOCl and $MoS_2$ were also prepared through similar procedure for comparison purposes and named as BOC and MS, respectively as given in our previous report.[21]

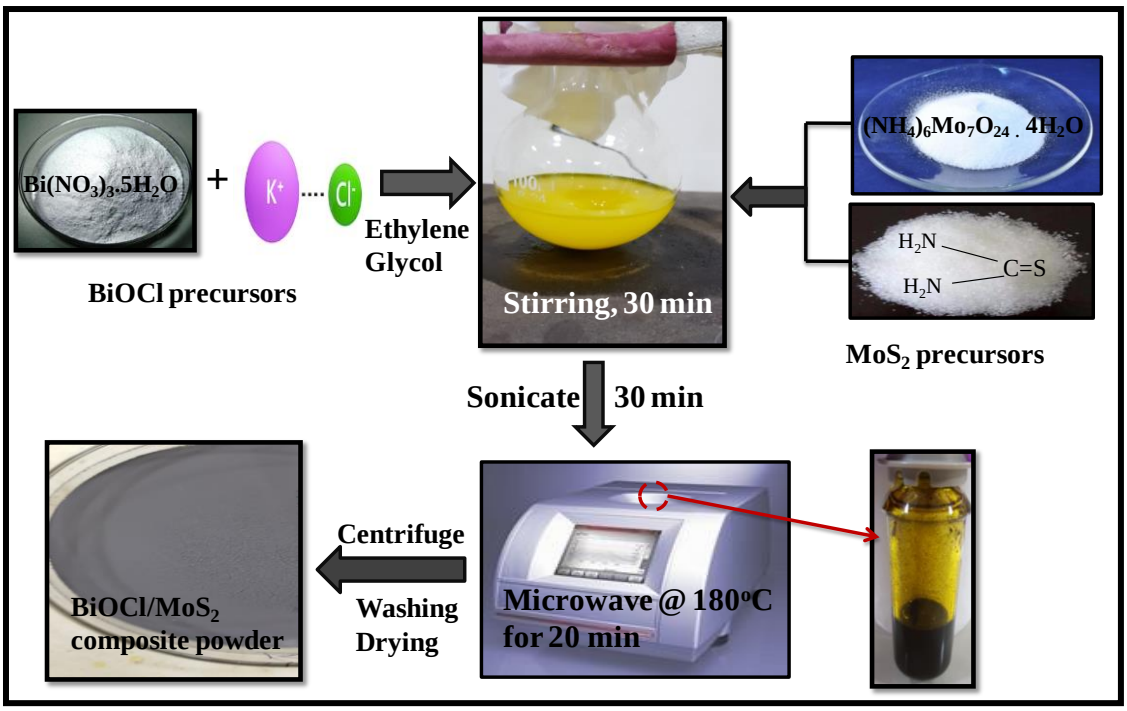


**Scheme 4.1.** Schematic representation for the synthesis of BiOCl/$MoS_2$ composite.

## 4.4 Material Characterization

### 4.4.1 XPS analysis

The surface valence state of different elements in the BOCMS composite was explored by the XPS characterization technique. The existence of Bi, O, Cl, Mo, and S elements on the surface was confirmed with the survey spectra (fig. 4.1a) as in accordance with EDS studies. The two main peaks of Bi at 159.9 eV and 165.2 eV displayed in fig. 4.1b corresponds to Bi $4f_{7/2}$ and Bi $4f_{5/2}$ state indicating the existence of Bi in +3 oxidation state. The peak in O1s spectra at 530.1 eV (fig. 4.1c) is the characteristic peak of Bi-O bonded oxygen species in

BiOCl lattice and a small peak around 534.2 eV corresponds to adsorbed oxygen on the surface of sample.[25] The Cl 2p spectra can be assigned into two peaks of Cl $2p_{3/2}$ and Cl $2p_{1/2}$ located at 198.5 eV and 200.1 eV, respectively (fig. 4.1d). The high-resolution spectrum of Mo 3d can be resolved into two peaks located at 229.8 eV and 232.6 eV (fig. 4.1e) is attributed to Mo $3d_{5/2}$ and Mo $3d_{3/2,}$ respectively indicating Mo is present in +4 oxidation state in the composite. The peak at 235.6 eV signifies the presence of $Mo^{6+}$ which could be due to the incorporation of O atoms in $MoS_2$. Similarly, the peaks of S 2p spectra could be fitted to S $2p_{1/2}$ and S $2p_{3/2}$ at 161.5 and 162.1 eV, respectively, as displayed in fig. 4.1f.[25]

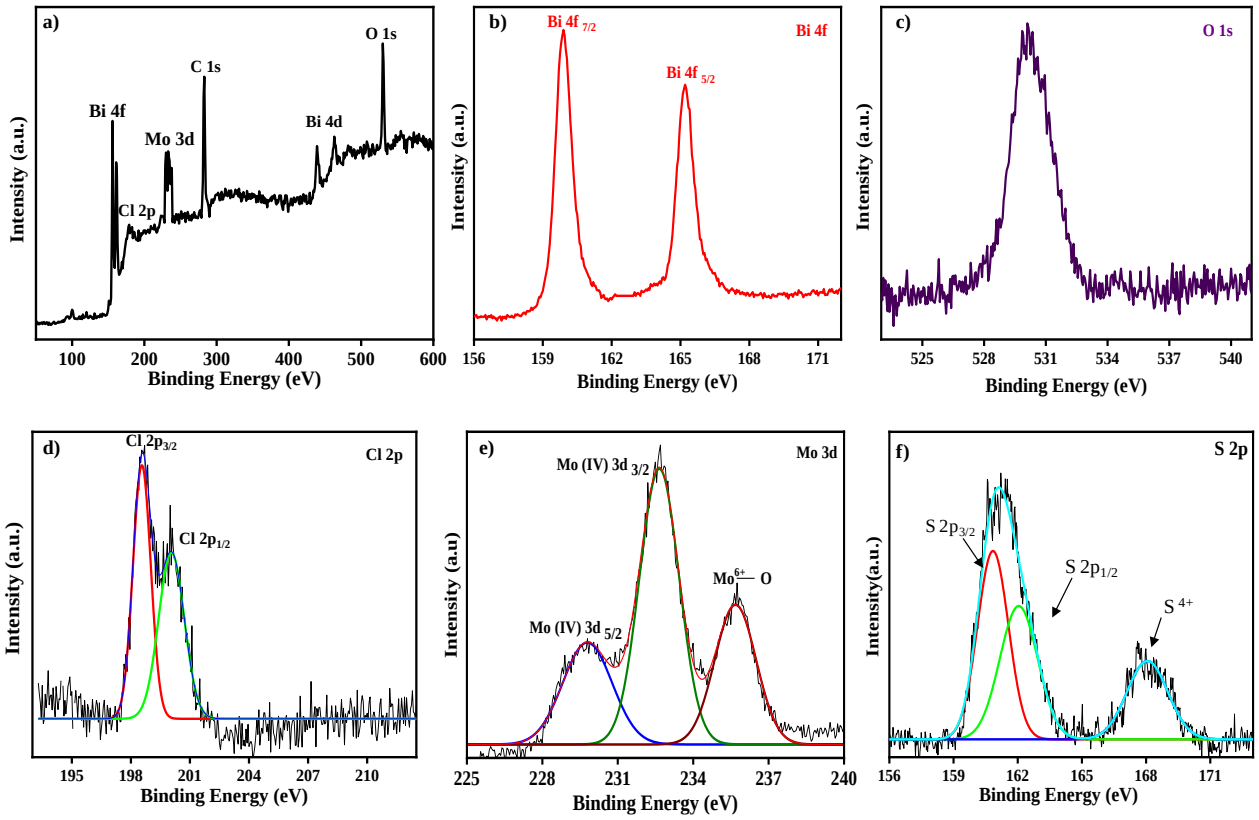


**Fig. 4.1** (a) Survey scan, (b-f) high resolution XPS spectra of Bi 4f, O 1s, Cl 2p, Mo 3d and S 2p elements in BOCMS (1:3) catalyst.

### 4.4.2 EDS and elemental mapping

Energy-dispersive X-ray spectroscopy results (fig. 4.2a) reveal the coexistence and homogeneous distribution of Bi, O, Cl, Mo, and S elements in BiOCl/$MoS_2$ composite, indicating a uniform distribution of BiOCl and $MoS_2$ in the heterostructures. The elemental

color mapping of BOCMS (1:3) nanocomposite with corresponding FESEM image shows the elements Bi, O, Cl, Mo, and S are present in the sample (fig. 4.2 b-g).

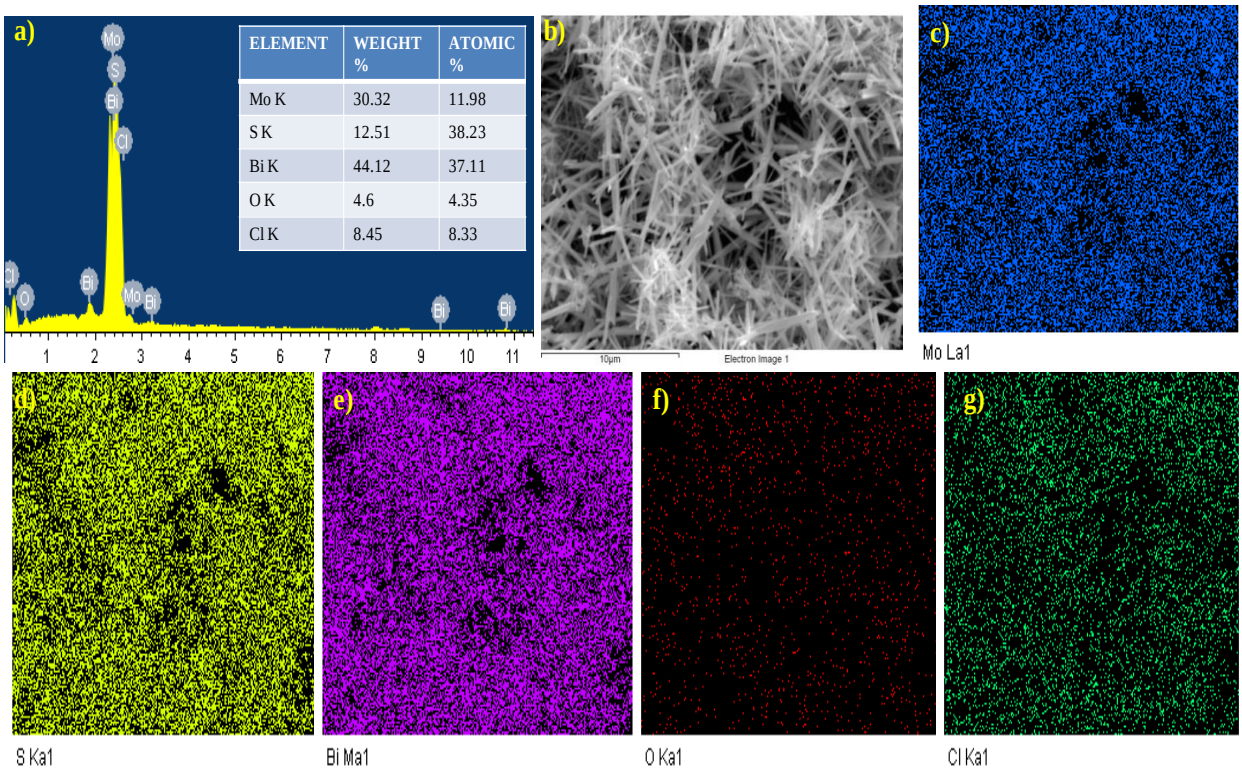


| ELEMENT | WEIGHT % | ATOMIC % |
|---|---|---|
| Mo K | 30.32 | 11.98 |
| S K | 12.51 | 38.23 |
| Bi K | 44.12 | 37.11 |
| O K | 4.6 | 4.35 |
| Cl K | 8.45 | 8.33 |

**Fig. 4.2.** (a) EDS spectra, (b) SEM image and the corresponding elemental mapping spectra of (c) Mo, (s) S, (e) Bi, (f) O and (g) Cl elements in BOCMS composite.

### 4.4.3 Optical properties (DRS band gap and PL studies)

The optical properties of the catalyst play an important role in influencing the photocatalytic performance of the catalyst. The light absorption property of the as-prepared catalyst was measured using UV-Visible DRS spectroscopy. The absorption edge of BiOCl is limited below 370 nm in the UV range of spectrum corresponding to the literature reports, but composites show increased visible light absorption in the visible range which signifies the intimate interfacial contact among BiOCl and $MoS_2$ in the composites (fig. 4.3a). The introduction of $MoS_2$ into BiOCl significantly increases the visible light absorption due to decrease in band gap energy. The band gap values calculated from the Tauc plots of samples are given in fig. 4.3b. The band gap energy of BOCMS (1:1) and BOCMS (3:1) composites appears to be ~2.63 eV and 2.80 eV respectively, and hence both are active under visible

light. The narrow band gap energy (2.29 eV) of the BOCMS (1:3) composite makes it an efficient catalyst to absorb the visible light irradiations and thus enhancing its photocatalytic activity for wastewater treatment.

The corresponding positions of valence bands ($E_{VB}$) and conduction bands ($E_{CB}$) of BiOCl and $MoS_2$ can be determined from band gap value by using the following equation:[26]

$EVB = X - E_e + 0.5\ E_g$

$ECB = EVB - E_g$

The energy band gap ($E_g$) of BiOCl and $MoS_2$ as determined from the tauc plot was about 3.02eV and 2.04eV, respectively. X in the equation represents the value of absolute electronegativity for BiOCl and $MoS_2$. $E_e$ in the above equation denotes the energy of the free electrons (4.5 eV) on the hydrogen scale.[26] Hence, the value of $E_{VB}/E_{CB}$ for BiOCl and $MoS_2$ were found to be 3.35eV/ 0.33eV and 1.33eV/-0.7eV respectively.

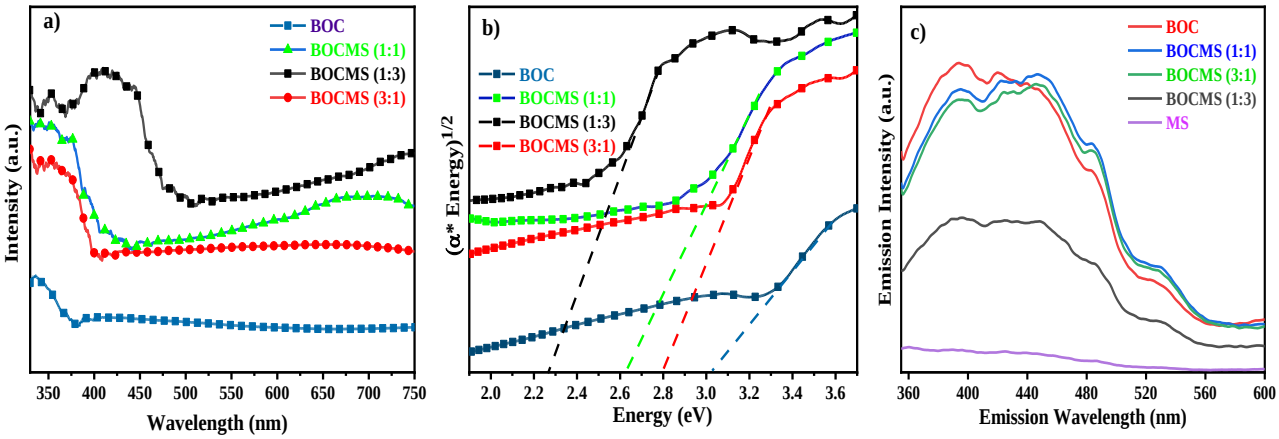


**Fig. 4.3** (a) UV-Visible absorption spectrum, (b) Tauc plot, and (c) photoluminescence spectra of BOCMS catalysts.

To elucidate the combination of charges in photocatalysts, the photoluminescence spectra of as-prepared catalysts were analyzed. The intensity of PL spectra varies with the recombination of photogenerated charges as the lower intensity corresponds to the lower recombination of electrons and holes.[27] The main peak for pure BiOCl was observed around 400nm. The PL emission peak of all the BOCMS composites is less intense than that of pure BiOCl catalyst (fig. 4.3c) which signifies the rate of charge recombination was controlled in composites. Among the composites, the minimum PL intensity was observed for BOCMS (1:3) catalyst indicating the least charge recombination in this composite resulting in a better photocatalytic performance of this composite.

### 4.4.4 XRD

The crystal phase of as-prepared catalysts was analyzed using X-ray diffraction studies displayed in fig. 4.4. The high intensity peaks in BOC catalyst at 2θ = 11.6°, 23.9°, 25.8°, 32.0°, 33.4°, 36.5°, 40.7°, 46.5°, 49.6°, 53.9°, 55.1°, and 58.6° could be indexed to the (001), (002), (101), (110), (102), (003), (112), (200), (113), (211), (104), and (212) crystal planes respectively, indicating the tetragonal phase of BiOCl [22] corresponding to JCPDS card no: 06-0249. Some other peaks of lower intensity representing the different planes of BiOCl are also present. The XRD spectra of composites show the presence of characteristic peaks of $MoS_2$ along with the peaks of BiOCl. The diffraction peaks at 2θ = 15.6° and 28.4° corresponds to the (002) and (004) planes of $MoS_2$ (JCPDS card no: 37–1492) in the BOCMS composites respectively.[23] The peak observed at 2θ = 22.4° is indexed to (040) plane of $MoO_3$ which might be due to the formation of oxides.[24] All the planes of BiOCl are present in the composites indicating the insertion of $MoS_2$ did not interfere with the lattice structure of BiOCl. But the slight shift of peaks in the composite compared to pure BiOCl spectra indicating the close contact between BiOCl and $MoS_2$.

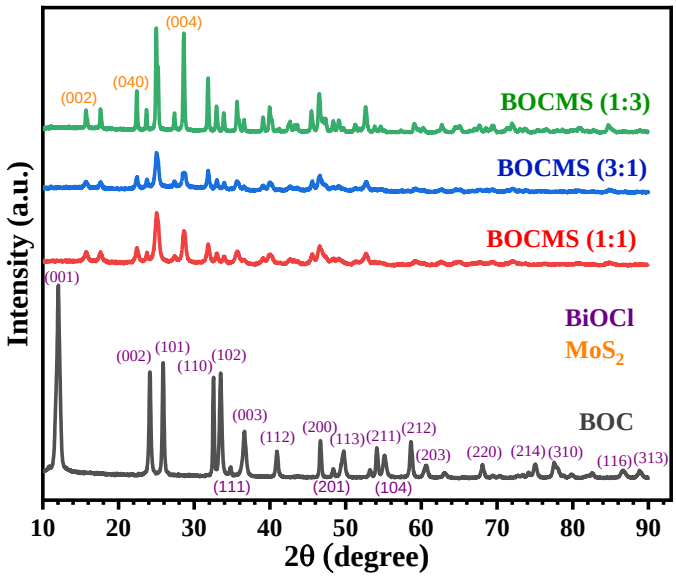


**Fig. 4.4** XRD diffraction pattern of as-prepared BOCMS photocatalysts.

### 4.4.5 Surface area analysis

The surface area characteristics of as-prepared catalysts were analyzed using BET surface area analysis. The adsorption-desorption isotherms of BOCMS composites with bare BiOCl

and $MoS_2$ in fig. 4.5a shows the H1 hysteresis loop with type IV Langmuir adsorption, signifying the mesoporous nature of samples. The pore size distribution analyzed from BJH method reveals that both mesopores and macropores are present in the as-prepared catalysts (fig. 4.5b). Table 4.1 lists the comparison of specific surface area, mesopore volume, and pore size of the composites along with pure BiOCl and $MoS_2$.

**Table 4.1.** Surface properties of the as-prepared BiOCl/$MoS_2$ catalysts.

| | BOC | MS | BOCMS (1:1) | BOCMS (3:1) | BOCMS (1:3) |
|---|---|---|---|---|---|
| **Specific surface area ($m^2$/g)** | 11 | 68 | 30 | 15 | 42 |
| **Mean pore diameter (nm)** | 23.8 | 35.1 | 34.6 | 32.3 | 42.2 |
| **Mesopore volume ($cm^3$/g)** | 0.0242 | 0.682 | 0.0710 | 0.0507 | 0.148 |
| **Total pore volume ($cm^3$/g)** | 0.0299 | 0.701 | 0.0748 | 0.0561 | 0.154 |

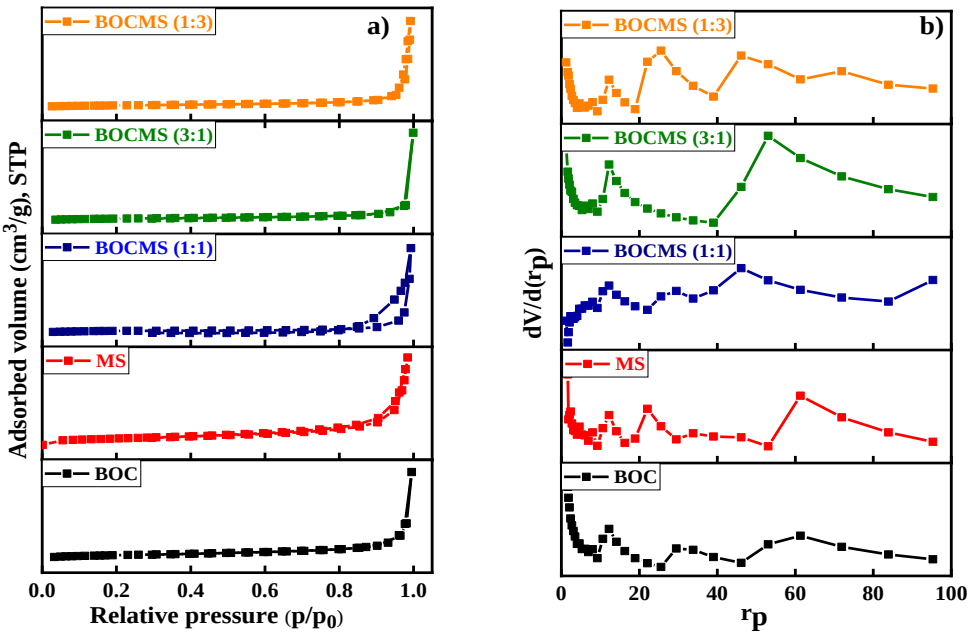


**Fig. 4.5.** The (a) $N_2$ sorption isotherms and (b) BJH pore size distribution curves of as-prepared catalysts.

The surface area of pure BiOCl was initially less but when combined with $MoS_2$, the surface area of the composites increases due to the higher surface area of $MoS_2$. The BOCMS (1:3) composite shows a higher surface area of ~42 $m^2/g$ in comparison with BOCMS (1:1) and BOCMS (3:1) which is eventually responsible for its higher adsorption property leading to better degradation performance.

### 4.4.6 Morphology analysis

The Morphological analysis of the catalysts was done using FESEM and HRTEM characterization techniques. The FESEM micrographs of as-prepared catalyst are given in fig. 4.6a-e. Images of pure BiOCl catalyst in fig. 4.6a shows the formation of thin BiOCl nanorods with hollow ends (inset of fig. 4.6a) arranged in the form of a nanoflower. The FESEM images of pure $MoS_2$ catalyst in fig. 4.6b shows the presence of small flowers formed of nanosheets (inset of fig. 4.6b). FESEM micrographs of BOCMS (1:3) composite demonstrate that the surface of BiOCl nanorods is partially covered with small discrete $MoS_2$ nanosheets. The presence of rod-shaped BiOCl with dispersed small $MoS_2$ nanosheets in BOCMS (1:1) and BOCMS (3:1) catalysts was confirmed from the fig. 4.6c-d. In fig. 4.6e, BiOCl is almost completely covered with $MoS_2$ as the amount of $MoS_2$ is higher in BOCMS (1:3) composite indicating the change of morphology with the weight ratio in the catalyst.

The microstructural details of the catalyst were studied with the help of HRTEM analysis. The TEM image (fig. 4.6g) of pure BiOCl show the presence of long BiOCl rods with sharp ends and possesses a very high aspect ratio of 1:10 having an average width and length of 105nm and 1056nm respectively. The sharp nanorods of different lengths are randomly arranged on each other forming a cluster of rods. However, the TEM image (fig. 4.6f) of BOCMS (1:3) composite shows the presence of BiOCl rods with scattered $MoS_2$ indicating the intimate contact between the two, giving rise to a synergistic effect of the composite. The lattice fringes are shown in the inset of fig. 4.6f displays the clear interplanar spacing of 0.369 nm which corresponds to the (002) plane of BiOCl. The interplanar spacing of 0.307 nm was also observed which attributes to the (004) plane of $MoS_2$ as displayed in the inset of fig. 4.6f.

The corresponding selected area electron diffraction (SAED) pattern of BOCMS (1:3) catalyst in fig. 4.6h could be indexed to [010] zone indicates single-crystalline nature of the photocatalyst, displaying the (001) and (101) diffraction planes of BiOCl with an interfacial angle of 61.1$^o$ which matches well with the theoretical value.[28] The (004) and (102) planes in the

pattern belong to $MoS_2$ in the sample. SAED pattern indicates that crystal lattices of the two components are aligned at an angle of 31.1$^o$ between (001) and (004) planes of BiOCl and $MoS_2$ respectively in the composite.

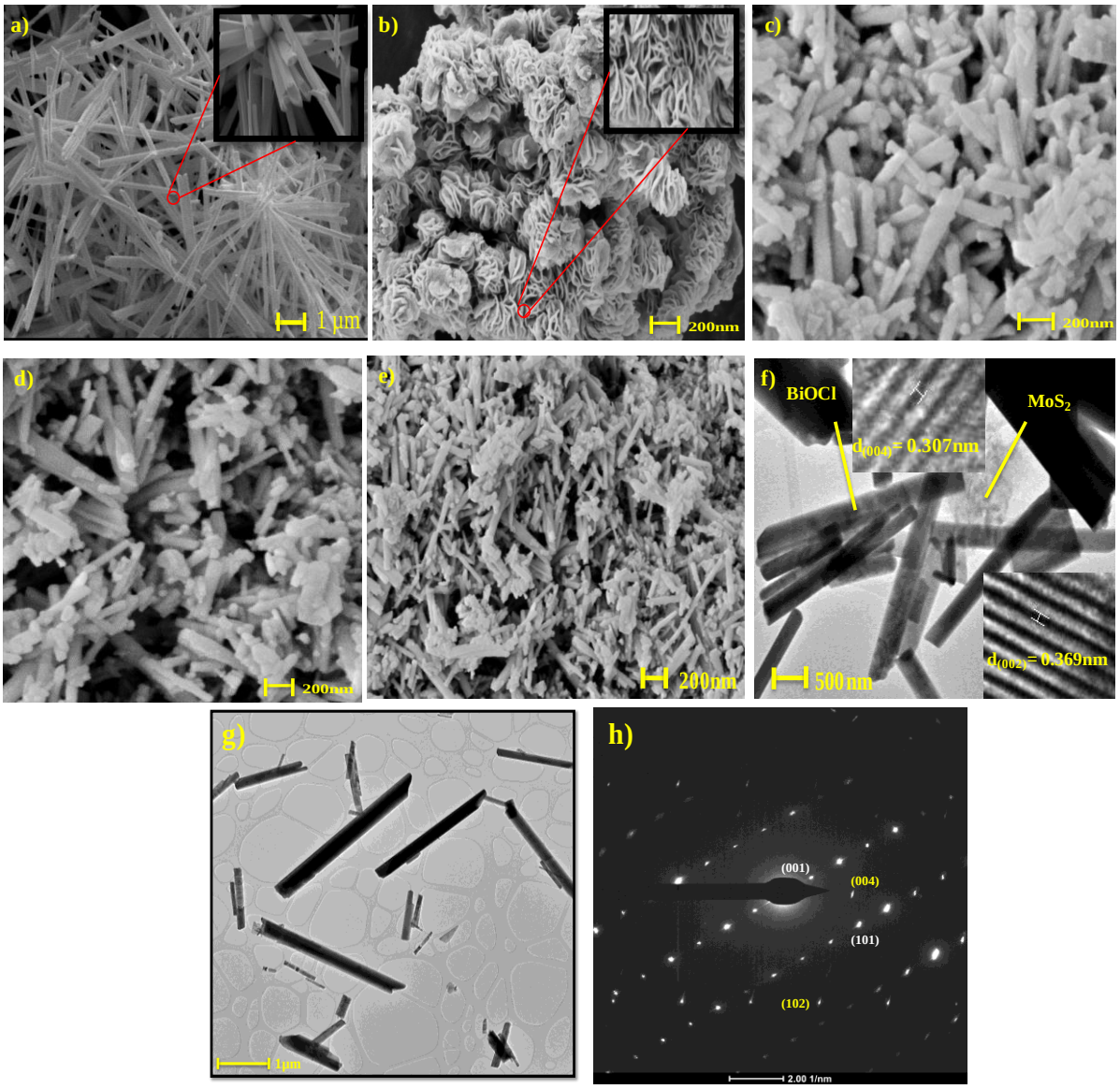


**Fig. 4.4** FESEM micrographs of (a) pure BiOCl, (b) pure $MoS_2$, (c) BOCMS (1:1), (d) BOCMS (3:1), (e) BOCMS (1:3) catalyst, TEM image of (f) BOCMS (1:3) catalyst and (g) pure BiOCl catalyst, and (h) SAED pattern of BOCMS (1:3) catalyst.

## 4.5 Photocatalytic activity

### 4.5.1 Dye and pesticide degradation

Methylene blue dye (5 ppm) and fipronil pesticide (600 ppm) were chosen as representatives to evaluate the activity of BOCMS composites for organic pollutant degradation. To illustrate the photocatalytic nature of the reaction, control experiments were performed without adding any catalyst. As observed from fig. 4.7a and 4.8b, there is no significant decrease in the concentration of these pollutants in the absence of catalyst. The degradation performances of as-prepared catalysts were analyzed by adding 3 mg of the catalyst into 15 mL of methylene blue dye and fipronil pesticide solution. The degradation efficiency of pure BiOCl and pure $MoS_2$ catalyst came out to be 45.9% and 53.9% for methylene blue dye. Similarly, photodegradation of fipronil pesticide in the presence of bare BiOCl and $MoS_2$ show 40.5% and 50.6% degradation respectively under visible light irradiation. The low photodegradation activity was due to the high recombination rate of charge carriers and lower surface area. Also, the higher band gap energy of BiOCl makes it less active in visible light. Under similar conditions, BOCMS (1:1), BOCMS (3:1), and BOCMS (1:3) catalysts show enhanced photocatalytic degradation efficiency of 80.04%, 70.4%, and 93.5% respectively for methylene blue dye. Similarly, photodegradation of fipronil pesticide was also enhanced by 73.3%, 62.1%, and 88.7% in the presence of BOCMS (1:1), BOCMS (3:1), and BOCMS (1:3) composites respectively. The rate constants (*k*) were determined through pseudo-first-order kinetics plots, as shown in fig. 4.7 (d and e). The *k* values follow the order BOCMS (1:3) > BOCMS (1:1) > BOCMS (3:1) > $MoS_2$ > BiOCl. BOCMS (1:3) has the highest *k*, which is 5.8 times as high as that of pure BiOCl for methylene blue dye degradation under visible light. The synergy attained from the combination of BiOCl and $MoS_2$ photocatalytic system can be determined with the help of synergy factor (R) from the following equation:[29]

$$R = \frac{k_{BiOCl/MoS2}}{k_{BiOCl} + k_{MoS2}}$$

Where $k_{BiOCl/MoS2}$, $k_{BiOCl}$, and $k_{MoS2}$ in the above equation are photodegradation rate constants of BiOCl/$MoS_2$ composite, pure BiOCl and $MoS_2$ respectively. The synergy factors for different BOCMS composites calculated from the above equation are 1.30, 0.89, and 2.29 for BOCMS (1:1), BOCMS (3:1), and BOCMS (1:3) photocatalysts, respectively. Due to the formation of

heterojunction and high synergistic effect between these layered materials which suppress the recombination of charges, the degradation efficiency increases. The maximum synergy factors, as well as photodegradation efficiency in visible light, were shown by BOCMS (1:3) composite which might be due to its higher surface area and lower band gap resulting in better adsorption of pollutants on catalytic surface and higher photocatalytic activity in visible light.

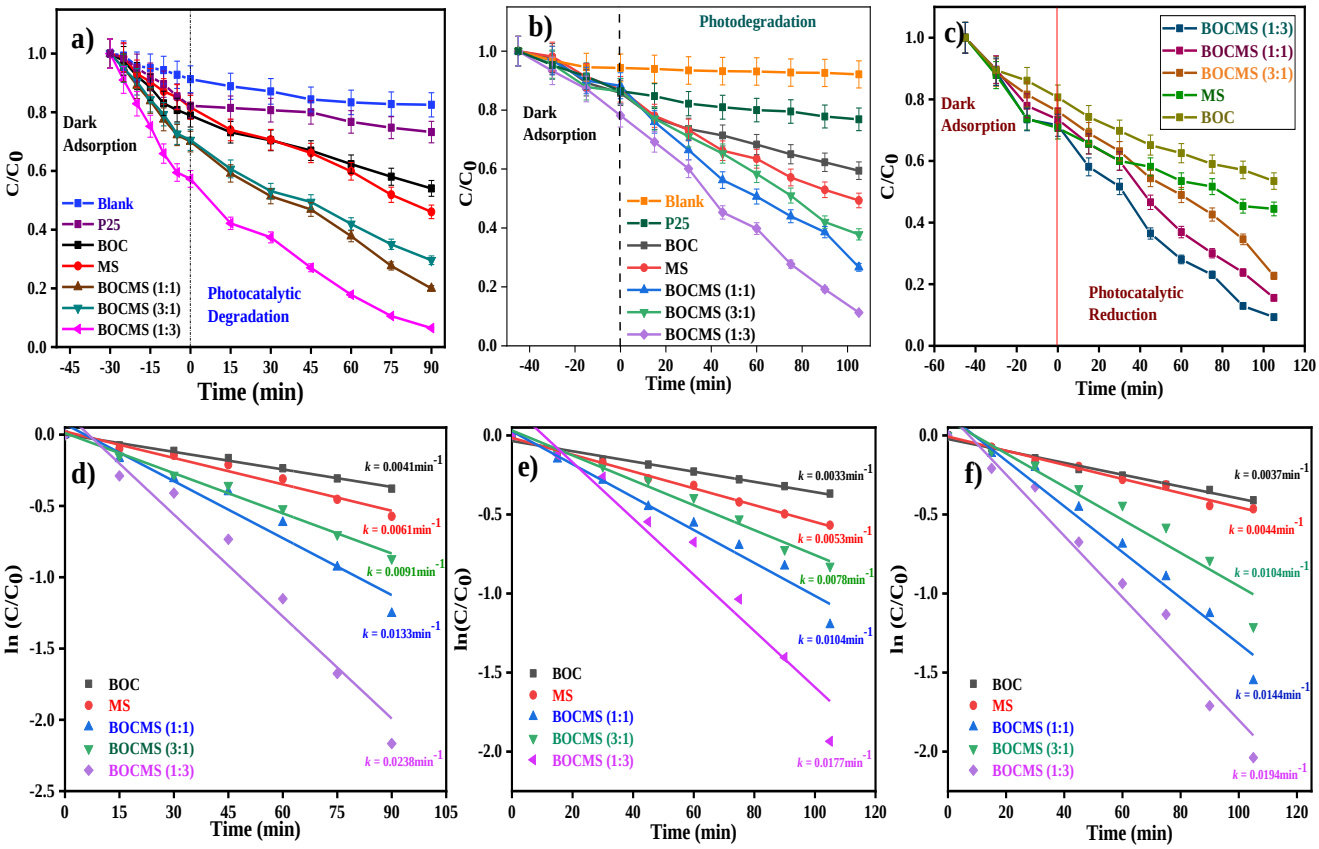


**Fig. 4.7** Kinetic analysis showing photodegradation of (a) methylene blue dye, (b) fipronil pesticide, and (c) Cr(VI) solution, and Pseudo-first-order kinetics plots for (a) methylene blue dye degradation, (b) fipronil degradation and (c) Cr(VI) reduction under visible-light irradiation in the presence of BOC, MS and BOCMS composites.

### 4.5.2 Cr (VI) reduction

In order to study the catalytic activity of BOCMS composite towards inorganic pollutant degradation, photocatalytic reduction of Cr(VI) ions was analyzed. In water, Cr(VI) ions mainly occur in the form of $Cr_2O_7^{2-}$, so potassium dichromate is generally used as representative to

analyze the reduction.[30] A comparative experiment was conducted with the as-prepared catalysts keeping all the conditions similar. The kinetic analysis was performed by adding 4mg of the catalyst into 15 mL of $K_2Cr_2O_7$ solution (100 ppm) at pH~3. The suspension was allowed to attain adsorption-desorption equilibrium in dark and then irradiated with visible light for 90 min. The photoreduction of Cr(VI) solution by the as-prepared samples is displayed in fig. 4.7c and the rate constants values were determined by pseudo-first order kinetics plots given in fig SI4c. Among all the synthesized catalysts, the highest photocatalytic efficiency was shown by BOCMS (1:3) with 90.6 % removal efficiency and a rate constant of 0.0194 $min^{-1}$ within 90 min irradiation time, which is due to better visible light absorption property and higher surface area of the catalyst compared to BOCMS (1:1) and BOCMS (3:1) composites. The cycling experiments with BOCMS (1:3) catalyst and Cr(VI) solution were carried out to determine photocatalytic reusability of catalyst in Cr(VI) solution (fig. 4.7f). The degradation efficiency of 68% was observed after 5 photocatalytic cycles exhibiting high reusability tendency of the catalyst. The result signifies that the as-prepared catalyst possesses high photocatalytic efficiency and stability for Cr(VI) reduction and can effectively be used in the treatment of wastewater with toxic inorganic metal ions along with organic contaminants.

### 4.5.3 Optimum catalyst concentration

The catalyst was further used to determine the optimum concentration for the best degradation efficiency. For this study, a variable amount of BOCMS (1:3) catalyst was added to 25 mL methylene blue dye (5 ppm) and 20 mL fipronil pesticide (600ppm) solution. All other conditions of degradation reaction were kept similar. Fig. 4.8a shows the variation of degradation efficacy in methylene blue dye and fipronil with catalyst amount varying from 1g/L to 10g/L. At first, the degradation efficiency of both the pollutants increases to a maximum with increasing catalyst amount. The degradation efficiency for methylene blue dye reaches a maximum (96.4%) at a catalyst concentration of 6 g/L and for fipronil, the maximum degradation efficiency of 86.3% was observed at 4 g/L. On further increasing the catalyst amount (>6 g/L for methylene blue and >4 g/L for fipronil), no significant change was observed in the degradation efficacy due to an increase in light scattering and opacity of solution as light could not infiltrate the solution properly. So the optimum concentration of BOCMS (1:3) catalyst is 6 g/L and 4 g/L for efficient degradation of methylene blue dye and fipronil pesticide, respectively.

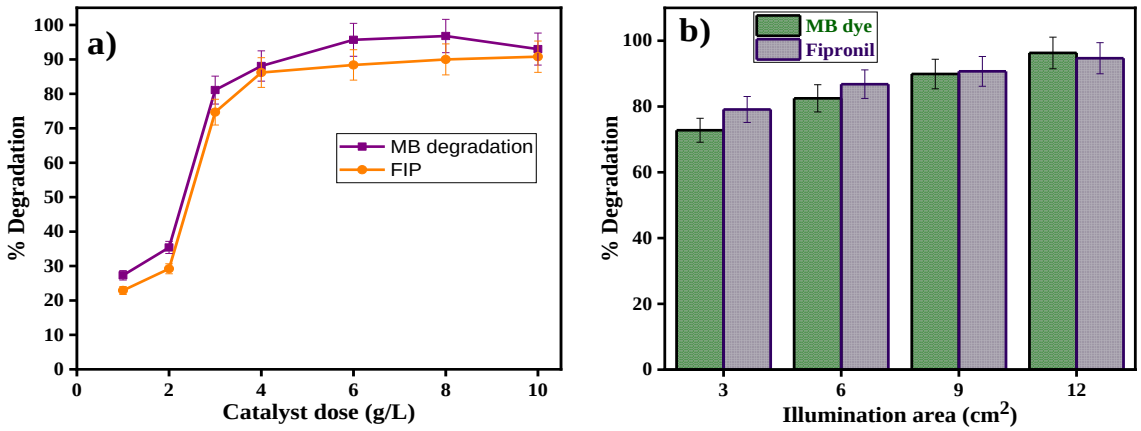


**Fig. 4.8** Plots showing the effect of (a) catalyst concentration, and (b) illumination area on photodegradation by the BOCMS (1:3) nanocomposite.

### 4.5.4 Illumination area effect

The role of effective illumination area on the degradation efficiency of the catalyst was studied using BOCMS (1:3) as a catalyst under visible light. In this experiment, the reaction vessels of different diameters were used to vary the surface area of the solutions exposing to the light irradiation. About 0.3 g/L of the catalyst was added to the same volume (15 mL) of methylene blue dye (5ppm) solution keeping the same distance between the light source and upper layer of sample. The degradation efficiency was increased with the increasing illumination area (fig.4.8b) due to better light infiltration and absorption by the catalyst.

### 4.5.5 Point Zero Charge of catalyst

Knowing the point of zero charge (pzc) of the photocatalysts is very important to determine the behavior of electrostatic interactions between the photocatalyst and pollutant. The pzc of the catalyst could be determined by varying the pH of photocatalyst suspension. The solution pH was adjusted using 0.1N $H_2SO_4$ and 0.1N NaOH solution. In order to determine the pzc of BOCMS (1:3) catalyst, the catalyst (3 mg) was dispersed to the methylene blue dye solution (15mL) having pH values varying from pH 1 to 10. The pH value of suspension before and after the adsorption process was observed and the difference between the two values was calculated. The pH value where the difference in pH value is zero is the pzc of the catalyst. The results

represented in fig. 4.9a indicates that pzc of the catalyst is around pH 4.4. So the catalyst surface is negatively charged below this pH and positively charged above pH 4.4.

### 4.5.6 Optimum pH of the solution

In the photocatalytic process, pH of the solution is one of the most important factors that can affect the degradation efficiency by influencing the adsorption of pollutants on the catalyst surface. The influence of change in pH value of methylene blue dye and fipronil solution was determined by analyzing the degradation performances of the catalysts at different pH values from 1 to 9. From the above results, the $pH_{pzc}$ of BOCMS (1:3) nanocomposite was determined which was at pH~4.4. The maximum degradation of methylene blue dye and fipronil pesticide by BOCMS (1:3) catalyst was observed at pH 5 and pH 3, respectively. It can be observed from fig. 4.9b that the photo-degradation of methylene blue dye increases initially in acidic medium (pH 1 to 5) and then show a slight decrease in neutral and alkaline medium (pH 7 to 9). The optimum pH for methylene blue dye degradation was found to be 5 as justified from pzc of the catalyst (4.4). The surface of catalyst is weakly negatively charged above the pzc value enhancing the adsorption of cationic methylene blue dye on the surface and hence improving the photodegradation efficacy. Whereas, below the pzc value the surface is occupied with positive charges coming from the $H^+$ ions in the solution, so there are repulsive forces between the positively charged catalyst surface and methylene blue dye leading to poor adsorption of the pollutant on the catalyst surface.

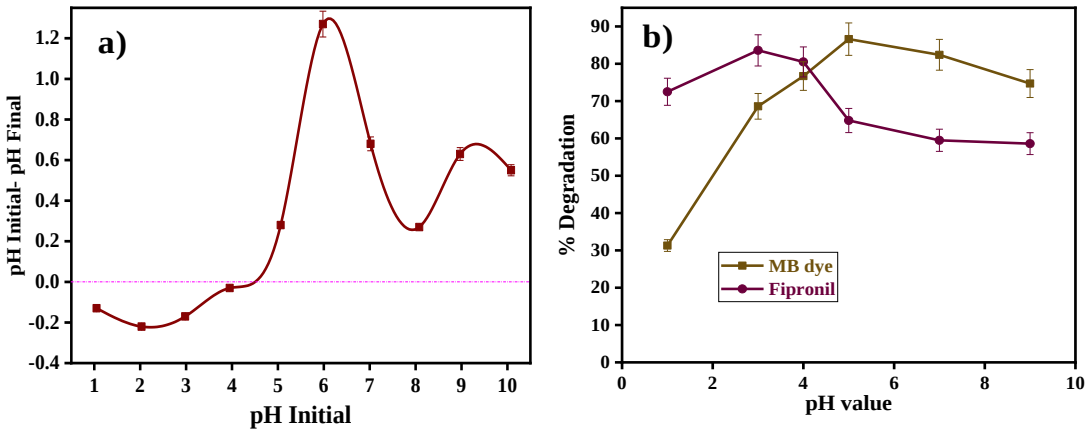


**Fig. 4.9** (a) point zero charge of BOCMS (1:3) catalyst and (b) effect of methylene blue dye/fipronil solution pH on degradation efficiency of BOCMS (1:3) catalyst.

On the other hand, fipronil being an anionic pesticide show better interaction with the catalyst in an acidic medium, and hence the optimum pH for fipronil degradation is pH 3 (fig. 4.9b). As the pH increases further, repulsive electrostatic forces between anionic fipronil and negatively charged catalyst surface increase which leads to lower adsorption and degradation of fipronil.

### 4.5.7 Real wastewater degradation

Textile industrial wastewaters are among the most unsafe wastewaters when they are released in the water bodies without any treatment. An environmentally economic advancement strategy in the textile industry has required novel innovations to decrease water toxicity levels. The mineralization of industrial wastewater was analyzed through the COD (Chemical Oxygen Demand) and TOC (Total Organic Carbon) methods. The raw wastewater without any pretreatment shows high COD and TOC values indicating a high percentage of organic pollutants in the effluent. During the photodegradation of industrial wastewater with 4mg BOCMS (1:3) catalyst under visible light for 240 min, the percent COD and TOC removal of wastewater was analyzed at regular time intervals as shown in fig. 4.10a. The higher time for degradation was applied for better mineralization of pollutants as the wastewater was used for photodegradation without any pretreatment. The photodegradation by present catalyst show 75% COD and 62.3% TOC removal after 240 min.

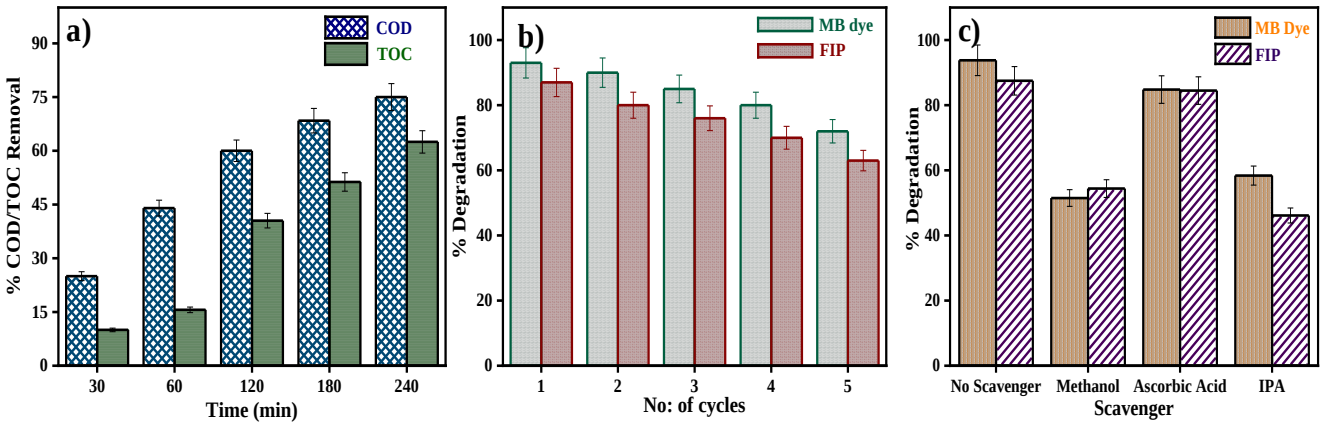


**Fig. 4.10** Plots of (a) percent COD and TOC removal in real textile wastewater, (b) catalyst reusability and (c) scavenger studies in methylene blue dye and fipronil with BOCMS (1:3) photocatalyst.

The increasing percent of COD and TOC removal suggest that organic matter is mineralizing to simpler molecules. The biodegrada0bility of the wastewater was determined by calculating the average oxidation state (AOS) and carbon oxidation state (COS) from the equation below:[32]

$AOS = 4 – 1.5[COD/TOC]$

$COS = 4 – 1.5[COD/TOC_i]$

The AOS and COS variables have range from +4 for $CO_2$ (most oxidized form) to -4 for methane (most reduced form). Without any pretreatment, the initial AOS value of the wastewater was 1.73 which increased after photocatalytic degradation up to 2.48 and 3.43 for AOS and COS, respectively suggesting that BOCMS (1:3) photocatalyst increases the biodegradability of the wastewater. So the catalyst is effective for the treatment of effluents than the physico-chemical treatment performed by the industries.

### 4.5.8 Reusability

For large-scale practical applications, the reusability of catalysts is of paramount significance. Hence the photocatalytic stability of catalyst up to multiple degradation cycles is important to analyze. The reusability of as-prepared BOCMS (1:3) catalyst (3mg) was analyzed for 5 successive runs in 25mL methylene blue dye (5ppm) and fipronil (600ppm) solution under visible light. The catalyst was separated from the suspension by centrifugation and washed with distilled water after every run. The comparison of degradation efficiency after each cycle is shown in fig. 4.10b. The composite shows high photocatalytic stability with the degradation efficiency of 72% and 62.9% for methylene blue dye and fipronil, respectively after 5 consecutive degradation cycles.

The stability of catalyst was also determined by the analysis of structural, optical, and morphological properties of BOCMS (1:3) catalyst after degradation cycles. The surface area analysis of the catalyst after degradation indicates its specific surface area is ~35$m^2$/g confirming the pollutants are not permanently adsorbed on the catalyst surface. The sorption isotherms of before and after 5 degradations are displayed in fig. 4.11a. There are no significant changes in the optical properties of the catalyst as confirmed from the PL spectra of the catalyst before and after degradation cycles (fig. 4.11b). A slight increase in intensity was observed after degradation

which might be due to the inactivation of some active sites. The XRD analysis after degradation reveals that most of the planes are present in the spectra (fig. 4.11c) and the peaks are sharp indicating the crystalline nature of the catalyst is remains intact after degradation. As observed from the FESEM image (fig. 4.11d), the morphological properties of the catalyst also remain intact after degradation cycles indicating the high stability of the catalyst. All these studies confirm that the catalyst is highly stable and reusable with great degradation efficiency.

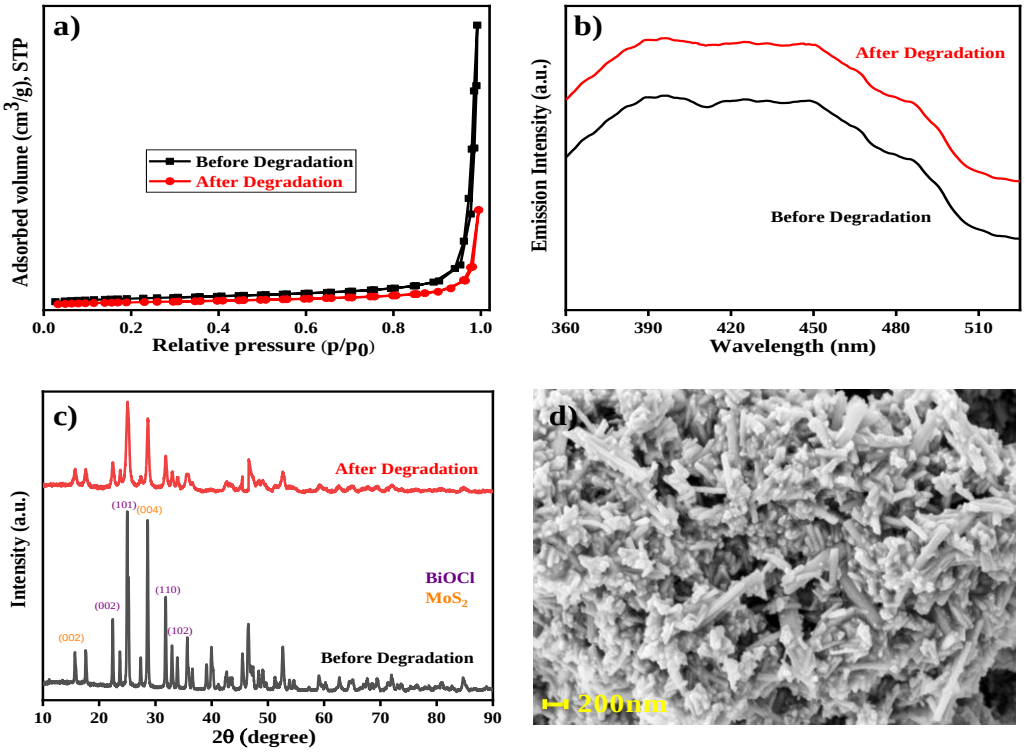


**Fig. 4.11** (a) BET adsorption-desorption isotherms, (b) PL spectra, (c) XRD spectra, and FESEM image of BOCMS (1:3) photocatalyst before and after 5 cycles of methylene blue photocatalytic degradation.

### 4.5.9 Mechanism for degradation

Trapping experiments were conducted to investigate the major species responsible for the degradation of the pollutants. Scavengers like ascorbic acid, methanol, and isopropyl alcohol (IPA) of $10^{-3}$ M concentrations in methylene blue dye and fipronil solutions were used for trapping the superoxide radicals ($O_2^{-}\bullet$), holes ($h^+$), and hydroxyl radicals ($^{\bullet}OH$), respectively. The experiments were performed with 3mg of the BOCMS (1:3) catalyst in 15mL of the above-

prepared solutions under visible light irradiation.[31] As observed from fig. 4.10c, the degradation process was significantly inhibited in presence of methanol scavenger indicating holes are the major species responsible for the degradation of methylene blue dye. However, for fipronil, the photodegradation was most affected in the presence of IPA and methanol. This indicates that hydroxyl radicals (•OH) and holes are the dominant species for fipronil degradation. The results imply that photodegradation of methylene blue dye and fipronil was majorly governed by the holes and hydroxyl radicals, respectively which are dominantly participating in the degradation mechanism.

Based on these observations, the plausible mechanism for photocatalysis of pollutants is shown in scheme 4.2. Since the CB potential of $MoS_2$ (-0.7eV) was more negative as compared to BiOCl (0.33eV), and the VB potential of BiOCl (3.35eV) was more positive compared to $MoS_2$ (1.33eV), a staggered band position was formed by two semiconductors. The $MoS_2$ in BOCMS catalyst being active in the visible light absorbs the energy of photons falling on it with the energy equal to or greater than its band gap. This energy excites the electrons in the valence band (VB) to the conduction band (CB) of the catalyst, creating holes in the VB and an excess of electrons in the CB of $MoS_2$. Then, the excited-state electrons produced in the CB of $MoS_2$ can be transferred into the CB of the coupled BiOCl due to joint electric fields between the two materials. Due to the formation of heterojunction between the two semiconductors, these electron-holes do not recombine and thus a charge separation occurs. The electrons in the CB are good reductants which reduces the adsorbed $O_2$ on the catalyst surface to $O_2^{-\bullet}$ radicals. This can further produce $^{\bullet}OH$ radicals by reacting with water. These reactive species result in the degradation of toxic pollutants. In addition, the photogenerated holes in the VB also help in the decomposition of pollutants either by reacting directly with pollutants or forming $^{\bullet}OH$ radicals. The probable degradation reaction steps are:

$$BiOCl/MoS_2 + h\nu \longrightarrow e^- + h^+$$

$$H_2O + h^+ \longrightarrow H_2O^+ \longrightarrow OH^- + h^+$$

$$O_2 + e^- \longrightarrow O_2^{-\bullet} + h^+$$

$$H_2O^+ \longrightarrow OH^- + h^+$$

$$OH^- + h^+ \longrightarrow {}^{\bullet}OH$$

$$^{\bullet}OH / O_2^{-\bullet} + \text{Pollutants} \longrightarrow \text{Degraded Products}$$

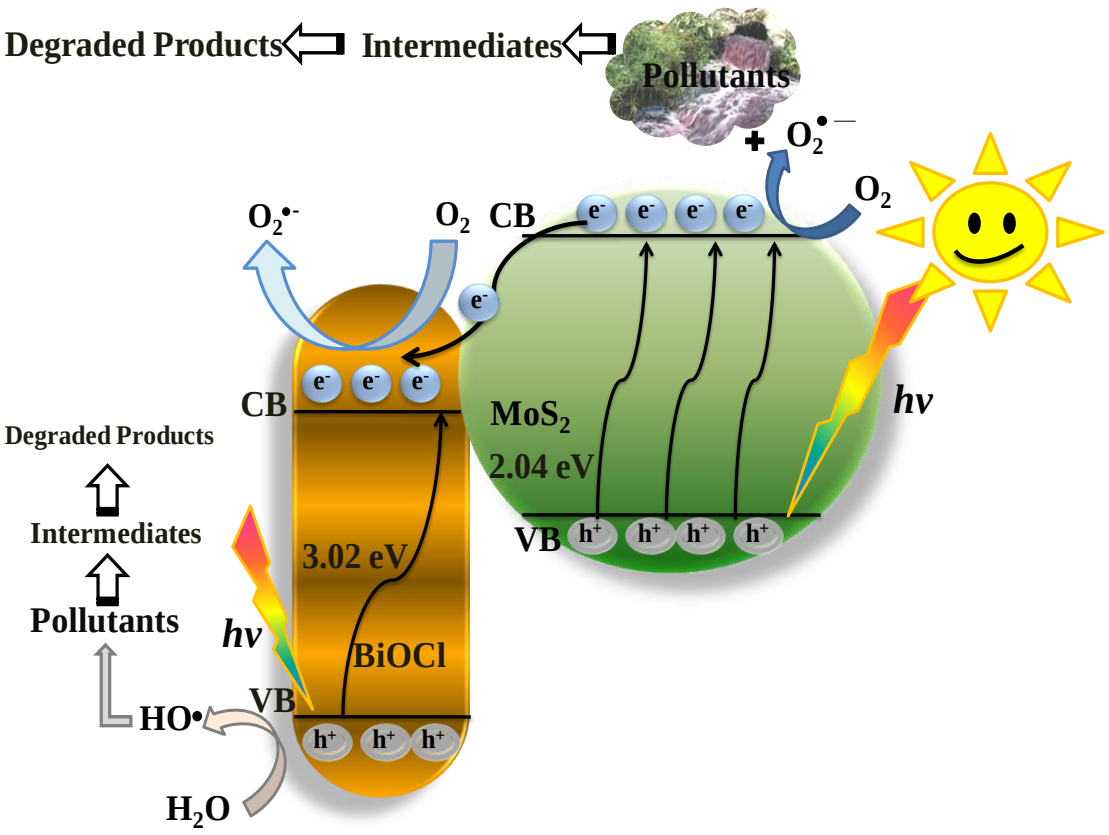


**Scheme 4.2** Plausible mechanism for photodegradation of wastewater pollutants by BOCMS catalyst.

## References


(1) Sharma, S.; Basu, S.; Shetti, N. P.; Nadagouda, M. N.; Aminabhavi, T. M. Microplastics in the Environment: Occurrence, Perils, and Eradication. *Chem. Eng. J.* **2021**, *408*, 127317. https://doi.org/10.1016/j.cej.2020.127317.

(2) Aanchal; Barman, S.; Basu, S. Complete Removal of Endocrine Disrupting Compound and Toxic Dye by Visible Light Active Porous g-$C_3N_4$/H-ZSM-5 Nanocomposite. *Chemosphere* **2020**, *241*, 124981. https://doi.org/10.1016/j.chemosphere.2019.124981.

(3) Suganthi, N.; Thangavel, S.; Kannan, K. Hibiscus Subdariffa Leaf Extract Mediated 2-D Fern-like ZnO/$TiO_2$ Hierarchical Nanoleaf for Photocatalytic Degradation. *FlatChem* **2020**, *24*, 100197. https://doi.org/10.1016/j.flatc.2020.100197.

(4) Sharma, S.; Basu, S. Highly Reusable Visible Light Active Hierarchical Porous $WO_3$/$SiO_2$

Monolith in Centimeter Length Scale for Enhanced Photocatalytic Degradation of Toxic Pollutants. *Sep. Purif. Technol.* **2020**, *231* (June 2019), 115916. https://doi.org/10.1016/j.seppur.2019.115916.

(5) Singla, S.; Sharma, S.; Basu, S.; Shetti, N. P.; Reddy, K. R. Graphene/Graphitic Carbon Nitride-Based Ternary Nanohybrids: Synthesis Methods, Properties, and Applications for Photocatalytic Hydrogen Production. *FlatChem* **2020**, *24*, 100200. https://doi.org/10.1016/j.flatc.2020.100200.

(6) Kong, D.; Fan, H.; Yin, D.; Zhang, D.; Pu, X.; Yao, S.; Su, C. $AgFeO_2$ Nanoparticle/$ZnIn_2S_4$ Microsphere p–n Heterojunctions with Hierarchical Nanostructures for Efficient Visible-Light-Driven $H_2$ Evolution. *ACS Sustain. Chem. Eng.* **2021**, *9* (7), 2673–2683. https://doi.org/10.1021/acssuschemeng.0c07638.

(7) Zhang, D.; Liu, X.; Wang, S.; Fan, B.; Shao, Z.; Su, C.; Pu, X. Enhanced Charges Separation to Improve Hydrogen Production Efficiency by Organic Piezoelectric Film Polarization. *J. Alloys Compd.* **2021**, *869*, 159390. https://doi.org/10.1016/j.jallcom.2021.159390.

(8) Singh, J.; Sharma, S.; Aanchal; Basu, S. Synthesis of $Fe_2O_3/TiO_2$ Monoliths for the Enhanced Degradation of Industrial Dye and Pesticide via Photo-Fenton Catalysis. *J. Photochem. Photobiol. A Chem.* **2019**, *376* (March), 32–42. https://doi.org/10.1016/j.jphotochem.2019.03.004.

(9) Sharma, S.; Basu, S. Fabrication of Centimeter-Sized $Sb_2S_3/SiO_2$ Monolithic Mimosa Pudica Nanoflowers for Remediation of Hazardous Pollutants from Industrial Wastewater. *J. Clean. Prod.* **2021**, *280*, 124525. https://doi.org/10.1016/j.jclepro.2020.124525.

(10) Shao, Z.; Meng, X.; Lai, H.; Zhang, D.; Pu, X.; Su, C.; Li, H.; Ren, X.; Geng, Y. Coralline-like $Ni_2P$ Decorated Novel Tetrapod-Bundle Cd0.9Zn0.1S ZB/WZ Homojunctions for Highly Efficient Visible-Light Photocatalytic Hydrogen Evolution. *Chinese J. Catal.* **2021**, *42* (3), 439–449. https://doi.org/10.1016/S1872-2067(20)63597-5.

(11) Monga, D.; Basu, S. Enhanced Photocatalytic Degradation of Industrial Dye by G-$C_3N_4/TiO_2$ Nanocomposite: Role of Shape of $TiO_2$. *Adv. Powder Technol.* **2019**, *30* (5),

1089–1098. https://doi.org/10.1016/j.apt.2019.03.004.

(12) Hou, J.; Dou, Q.; Jiang, T.; Yin, J.; Liu, J.; Li, Y.; Zhang, G.; Wang, X. BiOCl/Cattail Carbon Composites with Hierarchical Structure for Enhanced Photocatalytic Activity. *Sol. Energy* **2020**, *211*, 1263–1269. https://doi.org/10.1016/j.solener.2020.10.051.

(13) Wang, D.-H.; Gao, G.-Q.; Zhang, Y.-W.; Zhou, L.-S.; Xu, A.-W.; Chen, W. Nanosheet-Constructed Porous BiOCl with Dominant {001} Facets for Superior Photosensitized Degradation. *Nanoscale* **2012**, *4* (24), 7780. https://doi.org/10.1039/c2nr32533k.

(14) Zhang, D.; Su, C.; Yao, S.; Li, H.; Pu, X.; Geng, Y. Facile in Situ Chemical Transformation Synthesis, Boosted Charge Separation, and Increased Photocatalytic Activity of $BiPO_4$/BiOCl p-n Heterojunction Photocatalysts under Simulated Sunlight Irradiation. *J. Phys. Chem. Solids* **2020**, *147*, 109630. https://doi.org/10.1016/j.jpcs.2020.109630.

(15) Pan, J.; Liu, J.; Zuo, S.; Khan, U. A.; Yu, Y.; Li, B. Structure of Z-Scheme CdS/CQDs/BiOCl Heterojunction with Enhanced Photocatalytic Activity for Environmental Pollutant Elimination. *Appl. Surf. Sci.* **2018**, *444*, 177–186. https://doi.org/10.1016/j.apsusc.2018.01.189.

(16) Zhang, S.; Wang, D.; Song, L. A Novel F-Doped BiOCl Photocatalyst with Enhanced Photocatalytic Performance. *Mater. Chem. Phys.* **2016**, *173*, 298–308. https://doi.org/10.1016/j.matchemphys.2016.02.016.

(17) Liu, Q.; Zhu, H.; Ma, Q.; Liu, M.; Wang, B.; Tang, C.; Wang, Y.; Wu, Q.; Wang, X.; Hu, Z. Ultrathin $MoS_2$ Nanosheets Hybridizing with Reduced Graphene Oxide for High-Performance Pseudocapacitors. *FlatChem* **2021**, *26*, 100212. https://doi.org/10.1016/j.flatc.2020.100212.

(18) Monga, D.; Sharma, S.; Shetti, N. P.; Basu, S.; Reddy, K. R.; Aminabhavi, T. M. Advances in Transition Metal Dichalcogenide-Based Two-Dimensional Nanomaterials. *Mater. Today Chem.* **2021**, *19*, 100399. https://doi.org/10.1016/j.mtchem.2020.100399.

(19) Chen, Q.; Zhao, C.; Wang, Y.; Chen, Y.; Ma, Y.; Chen, Z.; Yu, J.; Wu, Y.; He, Y.

Synthesis of $MoS_2/YVO_4$ Composite and Its High Photocatalytic Performance in Methyl Orange Degradation and $H_2$ Evolution. *Sol. Energy* **2018**, *171*, 426–434. https://doi.org/10.1016/j.solener.2018.06.112.

(20) Nayak, S.; Swain, G.; Parida, K. Enhanced Photocatalytic Activities of RhB Degradation and $H_2$ Evolution from in Situ Formation of the Electrostatic Heterostructure $MoS_2$/NiFe LDH Nanocomposite through the Z-Scheme Mechanism via p–n Heterojunctions. *ACS Appl. Mater. Interfaces* **2019**, *11* (23), 20923–20942. https://doi.org/10.1021/acsami.9b06511.

(21) Monga, D.; Ilager, D.; Shetti, N. P.; Basu, S.; Aminabhavi, T. M. 2D/2d Heterojunction of $MoS_2$/g-$C_3N_4$ Nanoflowers for Enhanced Visible-Light-Driven Photocatalytic and Electrochemical Degradation of Organic Pollutants. *J. Environ. Manage.* **2020**, *274*, 111208. https://doi.org/10.1016/j.jenvman.2020.111208.

(22) Wu, D.; Wang, X.; Wang, H.; Wang, F.; Wang, D.; Gao, Z.; Wang, X.; Xu, F.; Jiang, K. Ultrasonic-Assisted Synthesis of Two Dimensional BiOCl/$MoS_2$ with Tunable Band Gap and Fast Charge Separation for Enhanced Photocatalytic Performance under Visible Light. *J. Colloid Interface Sci.* **2019**, *533*, 539–547. https://doi.org/10.1016/j.jcis.2018.08.084.

(23) Zhu, J.; Shen, Y.; Yu, X.; Guo, J.; Zhu, Y.; Zhang, Y. A Facile Two-Step Method to Synthesize Immobilized CdS/BiOCl Film Photocatalysts with Enhanced Photocatalytic Activities. *J. Alloys Compd.* **2019**, *771*, 309–316. https://doi.org/10.1016/j.jallcom.2018.08.317.

(24) Hu, X.; Zeng, X.; Liu, Y.; Lu, J.; Yuan, S.; Yin, Y.; Hu, J.; McCarthy, D. T.; Zhang, X. Nano-Layer Based 1T-Rich $MoS_2$/g-$C_3N_4$ Co-Catalyst System for Enhanced Photocatalytic and Photoelectrochemical Activity. *Appl. Catal. B Environ.* **2020**, *268*, 118466. https://doi.org/10.1016/j.apcatb.2019.118466.

(25) Al Marzouqi, F.; Al Farsi, B.; Kuvarega, A. T.; Al Lawati, H. A. J.; Al Kindy, S. M. Z.; Kim, Y.; Selvaraj, R. Controlled Microwave-Assisted Synthesis of the 2D-BiOCl/2D-g-$C_3N_4$ Heterostructure for the Degradation of Amine-Based Pharmaceuticals under Solar Light Illumination. *ACS Omega* **2019**, *4* (3), 4671–4678.

https://doi.org/10.1021/acsomega.8b03665.

(26) Li, B.; Jiang, L.; Li, X.; Ran, P.; Zuo, P.; Wang, A.; Qu, L.; Zhao, Y.; Cheng, Z.; Lu, Y. Preparation of Monolayer $MoS_2$ Quantum Dots Using Temporally Shaped Femtosecond Laser Ablation of Bulk $MoS_2$ Targets in Water. *Sci. Rep.* **2017**, *7* (1), 11182. https://doi.org/10.1038/s41598-017-10632-3.

(27) Prakash, N. G.; Dhananjaya, M.; Narayana, A. L.; Maseed, H.; Srikanth, V. V. S. S.; Hussain, O. M. Improved Electrochemical Performance of RGO-Wrapped $MoO_3$ Nanocomposite for Supercapacitors. *Appl. Phys. A* **2019**, *125* (8), 488. https://doi.org/10.1007/s00339-019-2779-2.

(28) Jiang, J.; Zhao, K.; Xiao, X.; Zhang, L. Synthesis and Facet-Dependent Photoreactivity of BiOCl Single-Crystalline Nanosheets. *J. Am. Chem. Soc.* **2012**, *134* (10), 4473–4476. https://doi.org/10.1021/ja210484t.

(29) Kar, S.; Ibrahim, S.; Pal, T.; Ghosh, S. Enhance Solar-Light-Driven Photocatalytic Degradation of Norfloxacin Aqueous Solution by RGO-Based Cd x Zn 1-x S Alloy Composite with Band-Gap Tuneability. *ChemistrySelect* **2020**, *5* (1), 54–60. https://doi.org/10.1002/slct.201903755.

(30) Dong, R.; Zhong, Y.; Chen, D.; Li, N.; Xu, Q.; Li, H.; He, J.; Lu, J. Morphology-Controlled Fabrication of CNT@$MoS_2$/$SnS_2$ Nanotubes for Promoting Photocatalytic Reduction of Aqueous Cr(VI) under Visible Light. *J. Alloys Compd.* **2019**, *784*, 282–292. https://doi.org/10.1016/j.jallcom.2019.01.032.

(31) Bai, W.; Tian, X.; Yao, R.; Chen, Y.; Lin, H.; Zheng, J.; Xu, Y.; Lin, J. Preparation of Nano-$TiO_2$@polyfluorene Composite Particles for the Photocatalytic Degradation of Organic Pollutants under Sunlight. *Sol. Energy* **2020**, *196*, 616–624. https://doi.org/10.1016/j.solener.2019.12.066.

(32) Ahmadi, M.; Ramezani Motlagh, H.; Jaafarzadeh, N.; Mostoufi, A.; Saeedi, R.; Barzegar, G.; Jorfi, S. Enhanced Photocatalytic Degradation of Tetracycline and Real Pharmaceutical Wastewater Using MWCNT/$TiO_2$ Nano-Composite. *J. Environ. Manage.* **2017**, *186*, 55–63. https://doi.org/10.1016/j.jenvman.2016.09.088.

# CHAPTER 5:

## *Facile Assembly of 2D $MoS_2$/GO Composites with Ag Nanoparticles for Visible Light-Driven Photocatalytic Abatement of Recalcitrant Pollutants*

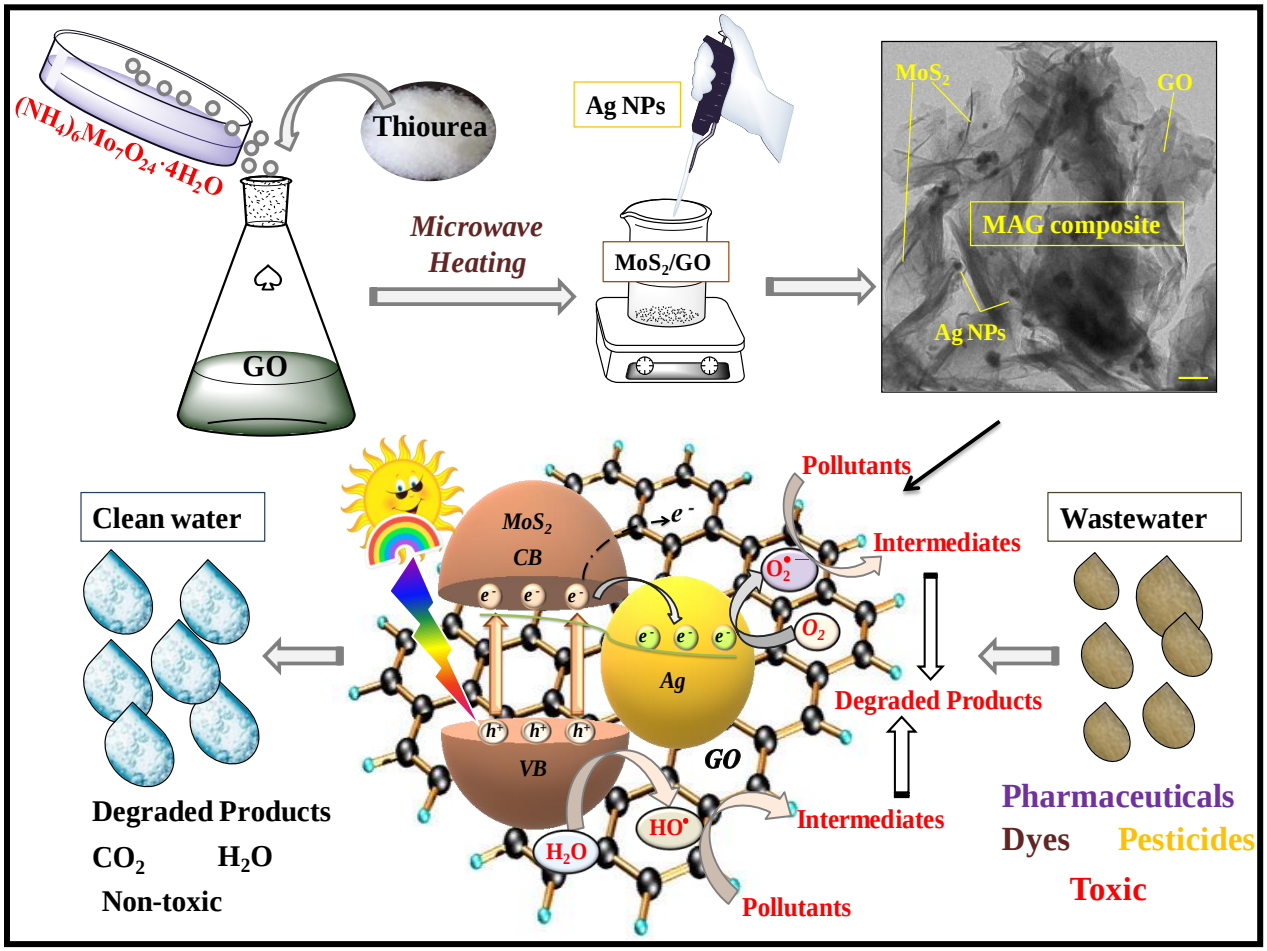


## Highlights

- $MoS_2$/Ag/GO composite with different weight-ratio prepared via microwave-route.
- Effective photodegradation of antibiotic/pesticide was done under visible light.
- Catalyst show effective real wastewater degradation with high COD/TOC removal.
- Catalyst with high efficiency/photostability is efficient for wastewater treatment.

## 5.1 Introduction

Growing industrialization and urbanization have resulted in massive energy generation and, as a result, environmental pollution, primarily chemical discharge, which had a massive impact on all living beings.[1] The use of pesticides (e.g., fipronil (FIP)) in crops causes a slew of cardiovascular and metabolic issues as mentioned in the previous chapters.[2,3] Also, the antibiotic (e.g. tetracycline (TC)) contamination caused by human overuse of medications has sparked worldwide concern due to the long-term environmental consequences and dangers to ecosystem creatures[4]. The prolonged half-life of antibiotics in residual organic-mineral sediments and fluids demonstrates their persistence as emergent contaminants in the environment.[5] The risk involved with this persistence is that many antibiotic-resistant microbiota may thrive, affecting human health and ecosystems.[6] Based on the mentioned research, semiconductor photocatalysis technology emerges as the times required.

Semiconductor materials are crucial in photocatalysis for efficient solar energy conversion. Among these, a transition metal dichalcogenide such as molybdenum disulfide ($MoS_2$) with an ultrathin layered structure and a significant band gap of around 1.8 eV is an outstanding material.[1] Though this comparatively narrow band is favorable for the production of photoexcited electrons, the catalytic action of pure $MoS_2$ is insufficient due to the recombination of the photoexcited carrier. Furthermore, the appealing chemical ability of $MoS_2$ is well recognized to be mostly due to its sulfur edge, whereas random packing and aggregation drastically limit its uses.[7] Hence, developing novel techniques for enhancing photogenerated carrier segregation and transport efficacy, as well as regulating the assembling state of $MoS_2$ nanostructures, remains highly desirable. As a result, modifications to $MoS_2$, such as by forming heterojunctions with one or may be more semiconductors and doping with non-metal or transition metal ions, have piqued the interest of researchers in the fields of degradation, adsorption, and optoelectronics.[8]

Graphene is an atomically dense, 2D nanosheet-like structure made up of $sp^2$ hybridized carbon atoms organized in a “honeycomb-like” pattern that can act as an efficient charge carrier for semiconductors at ambient temperature.[9] The presence of surface O-groups allows graphene oxide (GO) to contact with various inorganic/organic molecules, allowing for the straightforward synthesis of a diverse spectrum of functional composites with unique

characteristics. Furthermore, surface deposition of various functional compounds is promoted due to its large surface area and aids in the chemical adsorption ability of the material.[10]

Noble metal ions (e.g., Pd, Ag, Pt, and Au) might be inserted as nanoparticles (NPs) to improve the catalytic effectiveness of materials. Silver NPs are thought to be suitable for this application due to their excellent optical characteristics, better chemical stability, and non-toxic nature.[11] Different metals have previously been doped onto $MoS_2$, but Ag-doped $MoS_2$ and GO has received little attention. Besides, Ag NPs-doped $MoS_2$ was prepared by via hydrothermal method having various amount (2.5, 5, 7.5, 10 wt%) of Ag dopant. The catalyst showed excellent improvement in photocatalytic degradation of methylene blue (methylene blue) dye relative to pure $MoS_2$ and it was observed that $MoS_2$ with 0.1 wt% doping of Ag NPs shows the best photocatalytic activity.[12] Lu *et al.*[13] fabricated a composite of g-$C_3N_4$/Ag/$MoS_2$ in a flower-like structure of diameter about 0.4−0.6μm. The as-prepared Z-scheme photocatalyst showed excellent degradation of rhodamine B dye and exhibited a high rate of $H_2$ evolution from water. Similarly, a photocatalyst incorporating Ag NPs, graphene, and $TiO_2$ was prepared in ethanol using a combination sol-gel/solvothermal approach. The results indicated that the Ag/$TiO_2$/rGO composites had a good efficiency for degrading methylene blue dye by >79 % in visible light.[14] rGO suppresses the recombination of charges and enhances the separation of $e^-/h^+$ in $TiO_2$ via joining $TiO_2$ and Ag NPs as a potential conductor. The light absorption is increased by insertion of Ag NPs as they created a surface plasmon resonance effect.[15] Consequently, the resultant composite had a wide surface area and enhanced photocatalytic activity to degrade methylene blue molecules when exposed to visible light.[14] Despite the fact that numerous types of $MoS_2$ or GO-based composite materials have been prepared, to the best of our knowledge, the facile synthesis of $MoS_2$/Ag NPs/GO-based ternary composite materials for the photodegradation of recalcitrant pollutants is scarce.

In this work, variable weight ratios of $MoS_2$/GO heterostructures decorated with Ag NPs were prepared through a facile, less time-consuming microwave-assisted method. The as-prepared composites were utilized in the degradation of TC and FIP in visible light. Analysis of various parameters like catalyst amount, pH, and exposed light area was done. The stability was verified via using the photocatalyst for many runs. Trapping studies were

carried out to establish the photodegradation mechanism. The practical efficiency of the catalyst was investigated by photodegradation of real industrial wastewater.

## 5.2 Characterization and photocatalytic studies

Refer to section 2.2 chapter 2

## 5.3 Material and Methods

***Materials used:*** Analytical grade reagents and double distilled water for the preparation of solutions were used throughout the experiment. Tetracycline [$C_{22}H_{24}N_2O_8$, $\lambda_{max}$ = 357nm] was acquired from Sigma Aldrich Pvt. Ltd. Ammonium molybdate tetrahydrate (98%) [$(NH_4)_6Mo_7O_{24}.4H_2O$], graphite powder, sodium nitrate ($NaNO_3$), potassium permanganate ($KMnO_4$) ferrous ammonium sulphate (FAS) and potassium dichromate ($K_2Cr_2O_7$) was purchased from LobaChemie Pvt. Ltd. India. $H_2O_2$ was obtained from RANKEM Pvt. Ltd. Fipronil 5% SC was acquired from Bayer Crop Science Ltd. India. $AgNO_3$ was obtained from *Qualikems* Fine Chem Pvt. Ltd.Real wastewater was procured from textile industry, Ludhiana, India.

***Synthesis of Graphene Oxide (GO):*** GO was prepared from graphite powder via Hummer's method. In a standard procedure, 23 mL concentrated $H_2SO_4$ was mixed with 0.5 g graphite powder and 0.5 g $NaNO_3$. After that, the suspension was immersed in an ice cube tray to maintain a constant temperature around 20$^oC$. The mixture was allowed to stir for 4 hours to ensure complete dispersion. Now, 3 g of $KMnO_4$ was added gradually to the above mixture under 1hour of stirring while keeping the mixture in an ice bath. After complete addition, the mixture was diluted with 100 mL deionized water.[16] It is very important to keep the mixture on an ice bath while adding distilled water as the temperature of the reaction increases during addition. After cooling down, 5 mL of 30% $H_2O_2$ was added dropwise to the above mixture. The precipitates were washed with 5% HCl and deionized water for several runs and the GO obtained was dried in an oven overnight to get dry graphene oxide powder.[17]

***Synthesis of $MoS_2$:*** Pure $MoS_2$ was prepared according to our previously reported microwave-assisted method. Ammonium molybdate tetrahydrate ($(NH_4)_6Mo_7O_{24}.4H_2O$) and thiourea ($CH_4N_2S$) were used as precursors for the synthesis of $MoS_2$ and these precursors are heated in the Anton Parr Microwave at 180$^oC$ for 20 min. The resulting mixture was washed with water and dried in an oven at 60$^oC$ to obtain powder $MoS_2$ (labeled as MS).[18]

***Synthesis of Ag NPs:*** The following procedure was used to prepare Ag NPs from $AgNO_3$ as described in the literature. For the synthesis, about 500 µL of 0.01 M $AgNO_3$ solution was added in a 15 mL aqueous solution of fructose (50 mg/mL). Afterwards, 1 M NaOH solution was added dropwise under constant stirring till the appearance of yellow color which indicates the formation of Ag NPs.[15]

***Preparation of $MoS_2$ and GO composites decorated with Ag NPs:***

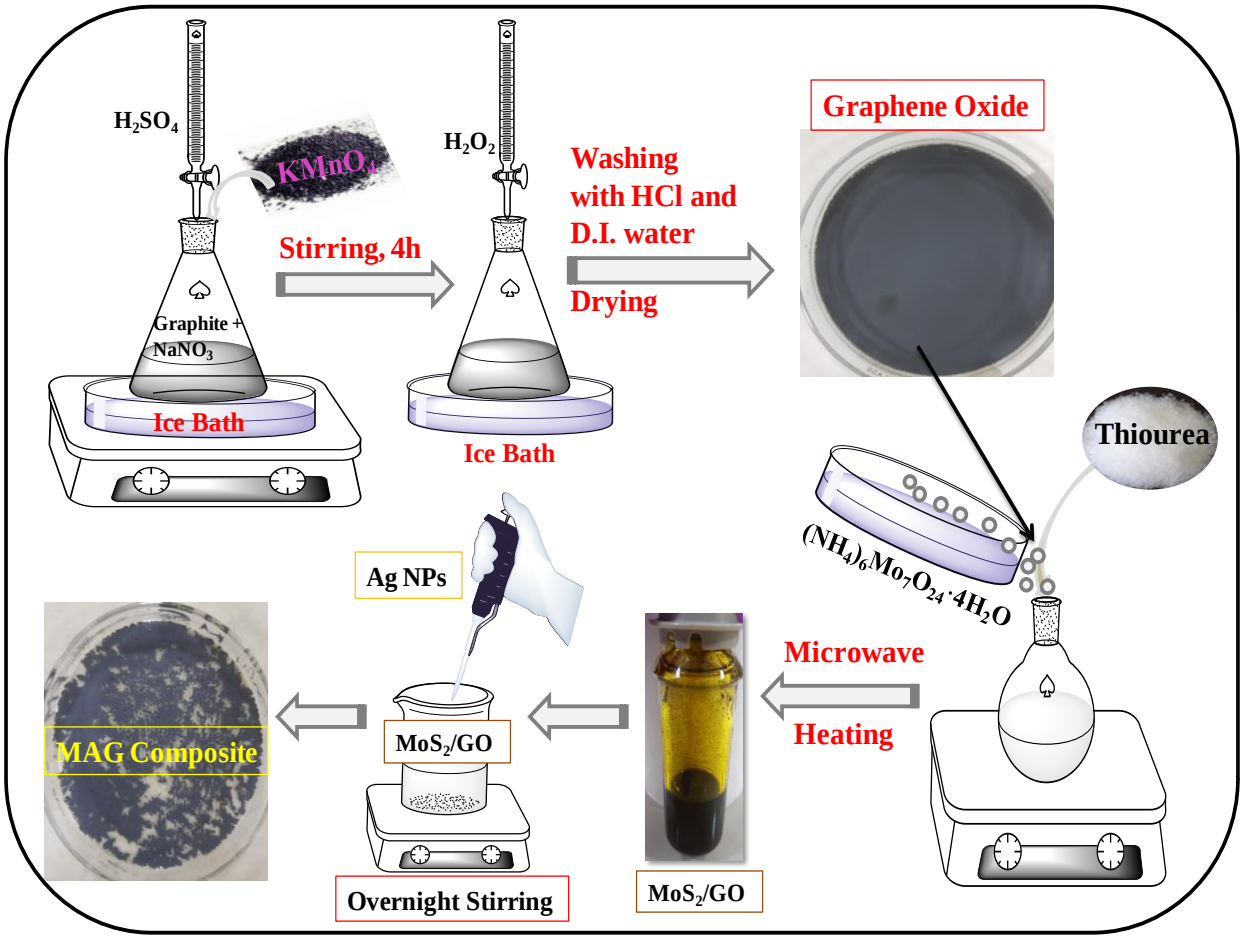


**Scheme 5.1** Schematic representation of the steps for the preparation of MAG composites.

In a typical synthesis procedure, about 0.5 g $(NH_4)_6Mo_7O_{24}.4H_2O$ and 1.1 g $CH_4N_2S$ were dissolved in 30 mL deionized water. After dissolving, the required amount (according to wt. ratios 1:1, 1:3 and 3:1) of synthesized GO was mixed into the above solution. To ensure thorough dispersion of GO and $MoS_2$ precursors, the mixture was allowed to sonicate for 1 hour after stirring at room temperature. The completely dispersed mixture was further

shifted to a microwave vial (30mL) and heated in a microwave synthesizer at 180°C for 20 min. After cooling down, the resultant mixture was washed thoroughly with deionized water and ethanol through centrifugation. Finally, the washed sample was put in a hot air oven for drying at 60°C for 24 hours. The as-obtained dry black powders were named according to the weight ratios as MAG 1:1, MAG 1:3 and MAG 3:1. About 500 µL of freshly prepared Ag NPs solution and 500 mg of the as-synthesized composite were added into 20 mL (3:1) water-ethanol solution and allowed to stir overnight at room temperature. Afterward, the mixture was washed with deionized water and dried at 60°C to obtain dry powders. A brief schematic representation for the preparation of MAG composites is given above in scheme 5.1.

## 5.4 Characterization Results

### 5.4.1 Surface area

The surface area and pore nature of synthesized materials was determined using BET surface area measurements. The $N_2$ sorption isotherms represented in fig. 5.1a illustrates type IV Langmuir isotherms indicating the mesoporous nature of prepared catalysts. The composite's consistency and pore structure were confirmed via presence of H1 hysteresis loops with sharp branches of adsorption-desorption. The pore size distribution was deduced by following the BJH plot as given in fig. 5.1b indicates the presence of micro and mesopores in the catalysts.

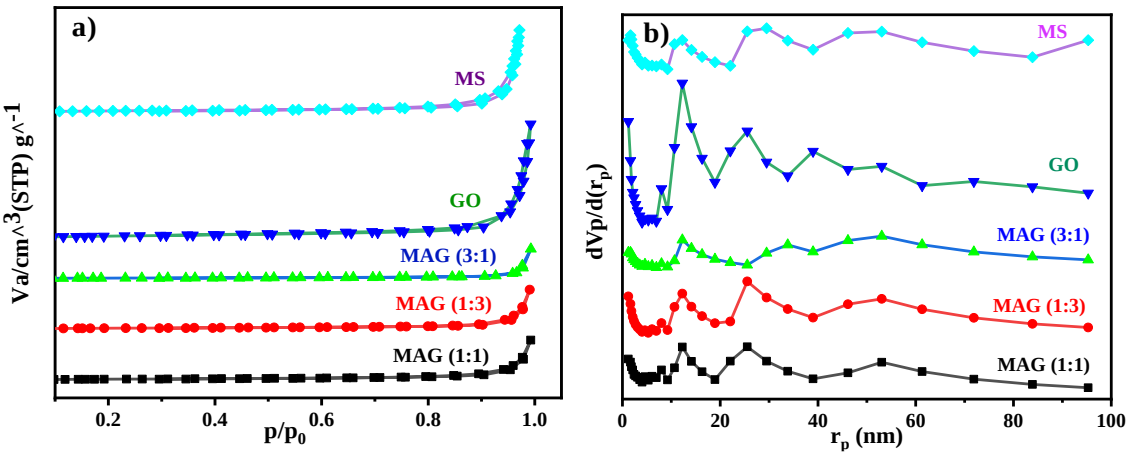


**Fig. 5.1** (a) Nitrogen adsorption-desorption isotherms and (b) BJH plot of the as-prepared catalysts.

The surface area, pore-volume, and pore diameter of the produced materials are tabularized in Table 5.1. The values indicate that the specific surface area of as-prepared GO (200 $m^2/g$) is sufficient for excellent adsorption, whereas pure $MoS_2$ (68 $m^2/g$) has a comparatively lower surface area. Combining $MoS_2$ and GO in composite gives catalysts with a large surface area, which is ideal for adsorption and, eventually, degradation of pollutants.

Among the composites, maximum surface area of ~116 $m^2/g$ was observed in the case of MAG 1:3, which could be due to the higher amount of GO in the composite; hence it might be the reason for its better adsorption property in the dark. As a result, GO plays an important function in increasing surface area by serving as a support.

**Table 5.1** Surface area, pore volume and pore diameter of as-synthesized MAG catalysts.

| **Catalyst** | **GO** | **MS** | **MAG (1:1)** | **MAG (3:1)** | **MAG (1:3)** |
|---|---|---|---|---|---|
| **Specific Surface area ($m^2/g$)** | 200 | 68 | 100 | 88 | 116 |
| **Total Pore Volume ($cm^3/g$)** | 0.886 | 0.234 | 0.634 | 0.421 | 0.698 |
| **Pore Diameter (nm)** | 18.3 | 35.7 | 27.8 | 31.4 | 21.3 |

### 5.4.2 UV-Vis DRS studies

Solid-state UV–Vis spectroscopy with 200-900 nm absorbance range was used to examine the optical characteristics of $MoS_2$/Ag/GO composites (1:1, 1:3, and 3:1) as displayed in fig. 5.2a. In the spectra, all the composites exhibit a peak around 230 nm, which is attributed to the $\pi \rightarrow \pi^*$ aromatic transition of C=C bond directed to restoring of complete conjugated framework carbon $sp^2$ atoms. There is also a small shoulder peak obtained around 300 nm, which

arises due to n→π* of the C=O transition bond.[19] In UV–Vis spectra, the nanocomposites exhibited a strong absorption edge in the visible range owing to surface-plasmon-resonance of Ag NPs as well as due to visible light active $MoS_2$, which further validates it to be an active photocatalyst for the removal of pollutants. Optical bandgap energy was calculated through the Tauc plot, as shown in fig. 5.2b. The equation is shown here:[20]

$$(\alpha h\nu)^{1/2} = h\nu - E_g$$

where α, h, $E_g$, ν are absorption coefficient, Planck constant, bandgap energy, and light frequency, respectively. The optical band gap values of MAG (1:1) and MAG (1:3) calculated from the Tauc plots were found to be 2.36 eV and 2.98 eV, respectively. However, the optical band gap value of MAG (3:1) comes out at 2.15 eV, allowing effective absorption of visible light, which might be responsible for its better photodegradation activity than other composites.

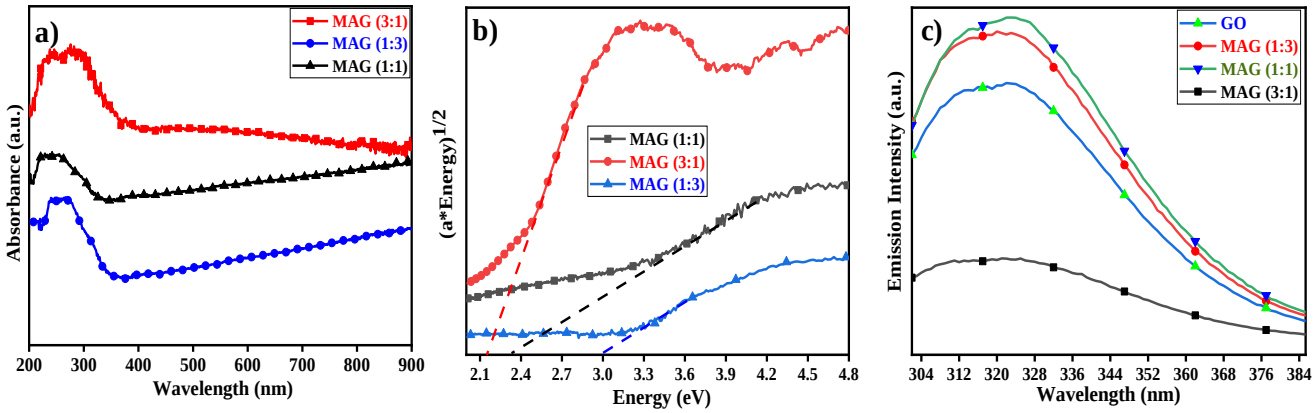


**Fig. 5.2.** (a) UV-Visible DRS spectra, (b) Tauc plot and (c) PL emission spectra of as-prepared MAG catalysts.

### 5.4.3 Photoluminescence (PL) studies

In the photodegradation process, charge carrier recombination plays an important role. The recombination probability of $e^-/h^+$ pair is likewise less when PL intensity is less, whereas separation of charges is high. At a excitation wavelength of 280 nm, the PL spectra of all samples were observed.[19] Graphite is a semiconductor with a zero energy bandgap and not shows any photoluminescence activity. Carbon vacancies and functional groups of oxides in GO and rGO nanosheets can transform graphene into any carbon nanocluster with enhanced

semiconducting and photo-luminescent characteristics. The PL spectra of GO and MAG composites show a peak centered around 325 nm, attributed to $e^-/h^+$ combination in the $sp^2$ carbon-cluster local state joined with $sp^3$ matrix.[19] Incorporating $MoS_2$ and Ag NPs in GO leads to a sharp decrease in PL peak intensity at 325 nm (fig. 5.2c), indicating enhanced separation of $e^-/h^+$ pair via heterojunction formation. Under light irradiation, strong interactions among Ag, GO, and $MoS_2$ can promote segregation of $e^-/h^+$ pair, where electrons can simply hop to CB of $MoS_2$, blocking direct recombination of $e^-/h^+$ pair.

### 5.4.4 XRD studies

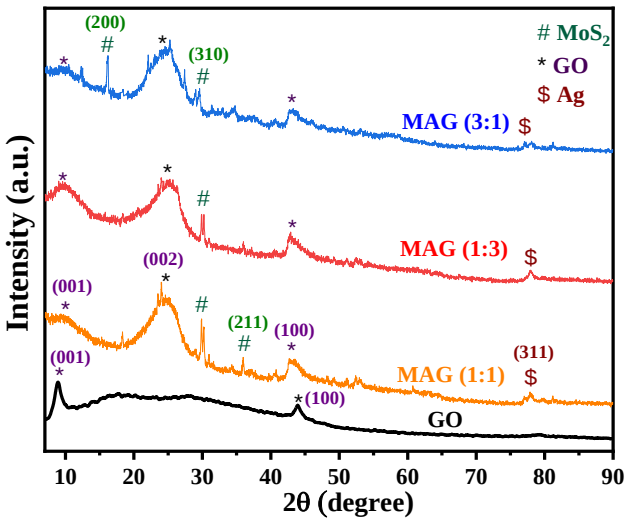


**Fig. 5.3** XRD diffraction patterns of bare GO and MAG (1:1, 1:3, and 3:1) nanocomposites.

The crystal structure of the as-prepared samples was analyzed through XRD analysis presented in fig. 5.3. In the spectra of pure GO, the characteristic peak present at 2ɵ=9.1° and 44°, corresponding to the (001) and (100) affirms the formation of GO.[17,21] In case of MAG composites, the presence of both the diffraction peaks indicates that incorporating $MoS_2$ did not affect the crystal structure of GO, however, the peaks are slightly shifted owing to the formation of heterojunction. The other peak present around 24.8$^o$ attributes to the formation of rGO (002) during the synthesis of $MoS_2$ in the composites. In MAG composites, the diffraction peaks for $MoS_2$ are present at 16.1$^o$, 30.2$^o$, and 35.1$^{o,}$ which could be indexed to (200), (310) and (211) planes of hexagonal $MoS_2$ according to JCPDS#73-1508. Only a single peak for Ag in MAG composites was found at 2ɵ=77.2$^o$ corresponding to (311) diffraction plane (JCPDS#04-0783) of

Ag, which might be because of low amount of Ag.[22] Presence of diffraction patterns of $MoS_2$, Ag and GO in samples indicates the successful formation of MAG ternary composite.

### 5.4.5 XPS studies

The XPS characterization technique was used to investigate the surface valence state of elements in the MAG (1:1) composite. The survey spectrum confirms the existence of C, O, Ag, Mo, and S elements (fig. 5.4a), which was consistent with EDS analyses. The high-resolution spectrum of Mo 3d can be resolved into two peaks located at 229.9 eV and 232.7 eV (fig. 5.4b) is attributed to Mo $3d_{5/2}$ and Mo $3d_{3/2}$, respectively indicating Mo is present in +4 oxidation state in the composite. The presence of $Mo^{6+}$ is indicated by the peak at 235.7 eV, which could be attributed to the insertion of oxygen in $MoS_2$.[23,24] In S 2p spectra peaks at 161 eV and 162.7 eV could be fitted to S $2p_{3/2}$ and S $2p_{1/2}$, respectively (fig. 5.4c). Besides, the S at 164 eV and 167.5 eV corresponded to $S_2^{2-}$and $S^{4+}$ species in $SO_3^{2-}$.[18] Two convoluted peaks at 368.2 eV and 374.3 eV were observed for the spectra of Ag 3d (fig. 5.4d), which attributes to Ag $3d_{5/2}$ and Ag $3d_{3/2}$.[15]

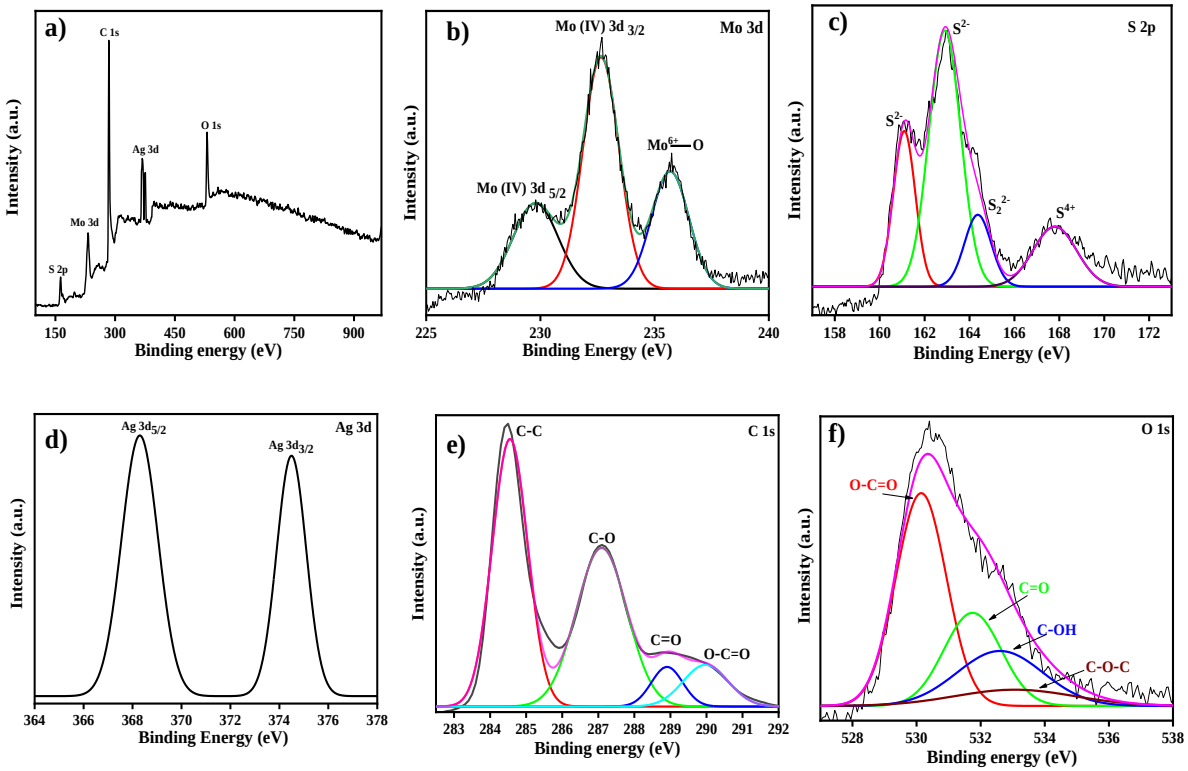


**Fig. 5.4** (a) Survey scan and XPS high resolution spectra of (b) Mo3d, (c) S2p, (d) Ag 3d, (e) C1s and (f) O1s in MAG composite.

In fig. 5.4e the peak present at 284.5 eV in C1s spectra belongs to C-C bond present in GO. Furthermore, the peaks at 287 eV, 288.9 eV, and 289.3 eV were assigned to carbon oxygen bonds C-O, C=O, and O-C=O, confirming the presence of oxygen functional groups in the GO network.[25] Similarly, the high-resolution spectrum of O 1s (fig. 5.4f) can be resolved into four peaks at 530.5 eV, 531.9 eV, 532.9 eV and 533.4 eV which corresponds to O-C=O, C=O, C-OH and C-O-C bonds, respectively in GO.[26]

### 5.4.6 Morphology studies

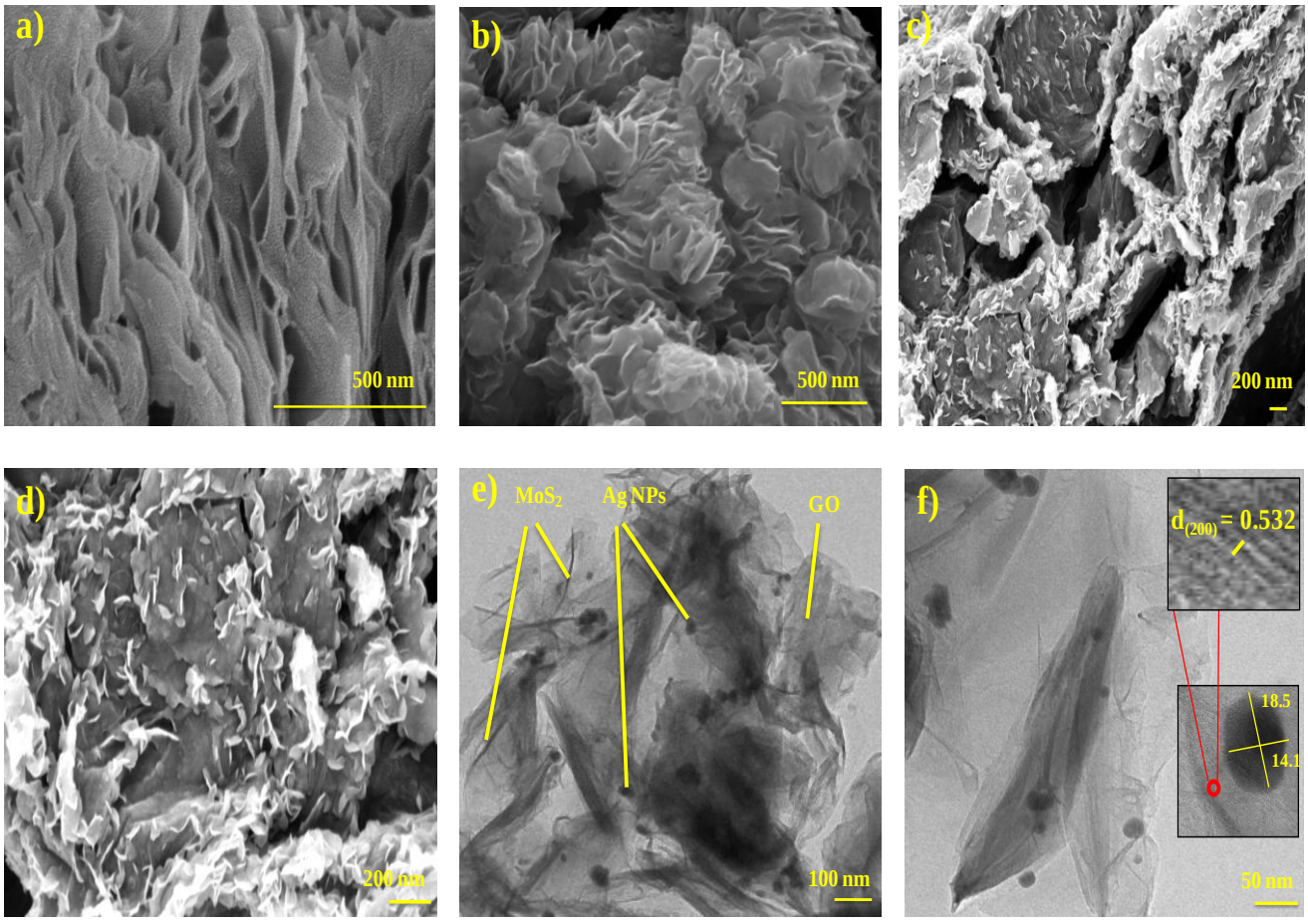


**Fig. 5.5.** FESEM images of (a) bare GO sheets, (b) bare $MoS_2$, (c and d) MAG (1:1) at different magnifications, (e and f) TEM images of MAG (1:1) composite at different resolutions where inset showing lattice fringes and presence of Ag NP in the composite.

To evaluate the microstructure and morphology of the as-prepared samples, scanning and transmission electron microscopy (SEM and TEM, respectively) pictures are acquired.SEM

micrograph in fig. 5.5a intuitively represents the surface structure of prepared GO nanosheets. The micrograph indicates the presence of long thin sheets overlapped on each other. The large spacing between nanosheets possesses numerous pores hence validating the high surface area of graphene oxide. $MoS_2$ exhibits a 3D flower-like spherical structure with a rather uniform texture, which is composed of numerous thin 2D nanosheets/nanopetals (fig. 5.5b). In, fig. 5.5c and 5.5d present the SEM images of $MoS_2$/Ag/GO (1:1) composite, in which all these $MoS_2$ nanopetals are intimately attached on the thin GO sheets, demonstrating a very uniform distribution. Furthermore, as shown in fig. 5.5d the composite's surfaces have gotten rougher, which could be due to the addition of Ag nanoparticles. For better understanding, the TEM image of $MoS_2$/Ag/GO (1:1) composite is shown in fig. 5.5e in which Ag NPs are well dispersed into the GO and $MoS_2$ nanosheets surface. Additionally, small $MoS_2$ nanopetals scattered on stacked GO sheets can be clearly observed, which conforms well to the results of the preceding SEM observations. The inset of fig. 5.5f shows the magnified image of Ag NPs with the major and minor radius of 18.5 and 14.1 nm, respectively. In addition, it can be seen from the inset of fig. 5.5f that the crystal lattice stripes of the $MoS_2$ nanopetals are 0.532 nm with corresponds to (200) crystal plane in accordance with JCPDS#73-1508.

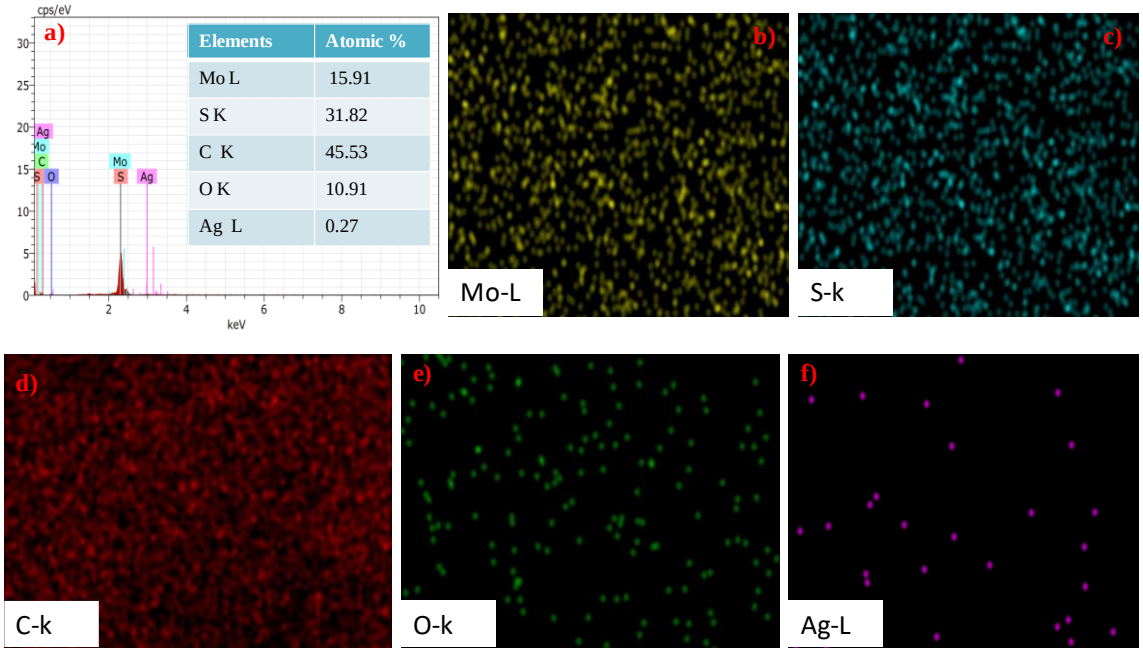


**Fig. 5.6.** (a) EDS spectra, and (b-f) color mapping spectra of Mo, S, C, O and Ag elements present in MAG composite.

The elemental content and their distribution in ternary MAG (1:1) nanocomposite were determined by EDS (in fig. 5.6a) and elemental mapping analyses (in fig. 5.6 b-f), respectively. The appearance of Mo, S, C, O, and Ag elements without any other impurities confirms the exceptional quality of the nanostructure. The foregoing findings demonstrate that the $MoS_2$/Ag/GO ternary photocatalyst was successfully formed.

## 5.5 Photocatalytic activity

### *5.5.1 Photodegradation of TC and FIP*

The photocatalytic ability of the $MoS_2$/Ag/GO composites was investigated via the photodegradation of pollutants TC, and FIP with concentrations 10, and 600 ppm, respectively. The photolysis of TC (fig. 5.7a) and FIP (fig. 5.7c) in the absence of catalyst manifested only ~23.9% and 10% degradation, respectively in 165 min under visible light. The photocatalytic degradation of TC and FIP using 0.25 and 0.2 g/L of as-prepared catalysts, respectively, was performed. The composite of MAG (3:1) exhibited maximum removal efficiency with 90.7 and 88.7% photodegradation of TC and FIP, respectively (fig. 5.7 a,c). A comparison was drawn between the catalytic activities of the prepared composites with bare $MoS_2$, GO catalyst, commercial $TiO_2$ P25 powder and with other reported similar catalysts from literature which demonstrated that all the as-prepared composites possess supreme photoactivity as given in table 5.2.

Eq. utilized to determine the rate constant, depicted as follows:

$$\ln (C/C_0) = -kt$$

Where $k$ denotes the rate constant, $C_0$ denotes the concentration at time = '0' and C represents the concentration at a time 't'.The rate constant values were 0.0186 $min^{-1}$ for TC degradation (fig. 5.7b) while 0.0177 $min^{-1}$ for FIP degradation by MAG (3:1) catalyst (fig. 5.7d) and the values (as listed in Table 5.2) were higher in comparison to other composites as well as to $MoS_2$, and GO.

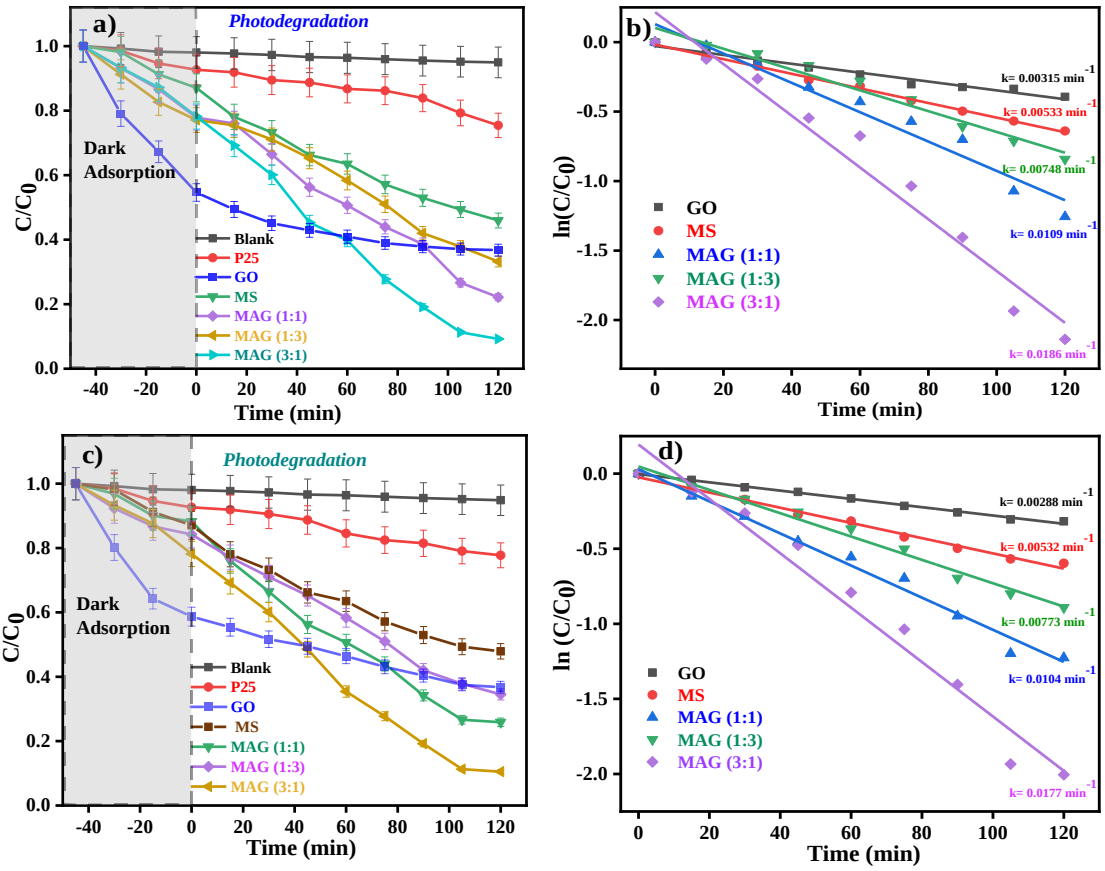


**Fig. 5.7** Plots of kinetic analysis and pseudo-first-order kinetic graph for photodegradation of (a,b) TC and (c,d) FIP by as-prepared MAG catalysts.

The synergy attained by the formation of $MoS_2$/Ag/GO photocatalyst can be calculated using synergy factor (R) from the eq.:[27]

$$R = \frac{k_{MoS2/Ag/GO}}{k_{MoS2} + k_{GO}} \quad (3)$$

The synergy factors for degradation of TC by different MAG catalysts calculated from the above equation are 1.29, 2.21, and 0.89 for MAG (1:1), MAG (3:1), and MAG (1:3) photocatalysts, respectively. The recombination of charges was suppressed in the composites due to the formation of heterojunction and high synergistic effect between these materials; hence the degradation efficiency of MAG composites increases.

**Table 5.2** Comparison of photocatalytic activity and rate constant of different catalysts with MAG composites.

| **Photocatalysts** | **Pollutant** | **Catalyst concentration (g/L)** | **Degradation (%)** | **Degradation rate ($min^{-1}$)** | **Reaction time (min)** | **Ref.** |
|---|---|---|---|---|---|---|
| **Magnetic GO/ZnO** | Tetracycline | 1 | 74 | 0.014 | 100 | [28] |
| **Ag/GO** | Rhodamine | 0.25 | 82 | 0.028 | 60 | [29] |
| **$MoS_2$/ZnO** | Phenol Red | 0.6 | 90 | - | 80 | [30] |
| **$MoS_2$/$ZnSO_3$** | Tetracycline | 0.5 | 80.2 | 0.022 | 60 | [31] |
| **$MoS_2$/$Fe_3O_4$** | Tetracycline | 0.5 | 79.53 | 0.0140 | 100 | [32] |
| **GO** | Tetracycline/ Fipronil | 0.25/ 0.2 | 60.3/ 58.6 | 0.0031/ 0.0028 | 120 | Present work |
| **$MoS_2$** | Tetracycline/ Fipronil | 0.25/ 0.2 | 54.8/ 50.6 | 0.0053/ 0.0051 | 120 | Present work |
| **$MoS_2$/Ag/GO (1:1)** | Tetracycline/ Fipronil | 0.25/ 0.2 | 76.7/ 71.8 | 0.0109/ 0.0104 | 120 | Present work |
| **$MoS_2$/Ag/GO (1:3)** | Tetracycline/ Fipronil | 0.25/ 0.2 | 66.7/ 60.1 | 0.0074/ 0.0077 | 120 | Present work |
| **$MoS_2$/Ag/GO (3:1)** | Tetracycline/ Fipronil | 0.25/ 0.2 | 90.7/ 85.2 | 0.0186/ 0.0177 | 120 | Present work |

### *5.5.2 Optimum catalyst dose*

Catalyst concentration was varied to optimize the best degradation activity. The study was done by performing the photocatalytic degradation of TC and FIP pollutants with various MAG (3:1) catalyst concentrations (0.1, 0.4, 0.6, 0.8 and 1.0 g/L) as shown in fig. 5.8a. The maximum photodegradation efficiency was achieved at 0.6 g/L in the case of TC and 0.4 g/L for FIP pollutants. Following subsequent increases in catalyst amount (>0.6 g/L for TC and >0.4 g/L for FIP), no significant change in degrading efficacy was seen due to the rise in the scattering of light and opacity of solution as light couldn't permeate the solution properly.

### *5.5.3 Illumination area*

Using vessels of various diameters, the influence of total illumination area on catalyst photodegradation effectiveness was investigated. Keeping all other parameters same, the photodegradation of TC and FIP was performed with 0.4 g/L of MAG (3:1) catalyst in different vessels so that the solution area coming in contact with the light directly is thereby different. The gap between the solution's upper layer and light source was kept constant and the degradation was performed under visible light for 120 min. The enhancement in degradation efficiency with increasing the reactor area can be observed in fig. 5.8b, which is attributed to the improved absorption of visible light photons with increasing area.

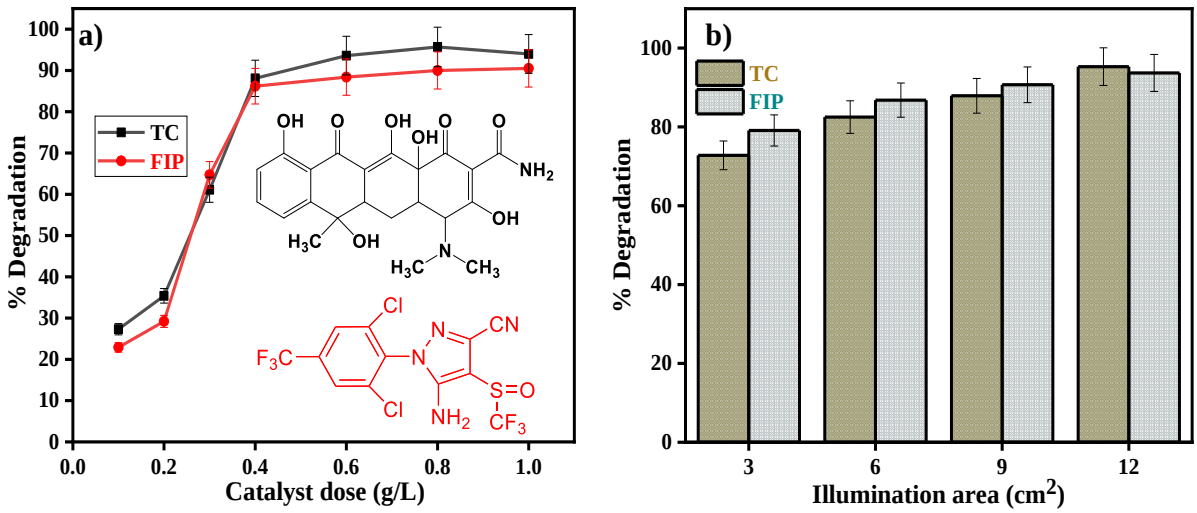


**Fig. 5.8** Plots showing variation of photodegradation activity of MAG (3:1) catalyst with (a) catalyst concentration and (b) effective illumination area of reaction.

### *5.5.4 Effect of pH*

The photodegradation activity of the as-prepared catalysts was studied throughout a pH range of 1, 3, 5, 7, 9, and 10 to assess the influence of pH value of TC and FIP solution. The pH changes can be attributed to the catalyst's surface charge at various pH values, as well as the pollutant's electrical charges. Firstly, the catalyst's point of zero charge (pzc) was found by changing the pH of the photocatalyst suspension from 1 to 11. (fig. 5.9a). The pzc value of MAG (3:1) photocatalyst was estimated to be ~5.9. This indicates that the catalyst surface is dominated by negative charges at pH>5.9, whereas at pH<5.9 the surface of catalyst is positively charged. The photodegradation with MAG (3:1) catalyst (4mg) was performed at different pH values of TC (20 mL) and FIP (20 mL) solution as shown in fig. 5.9b.

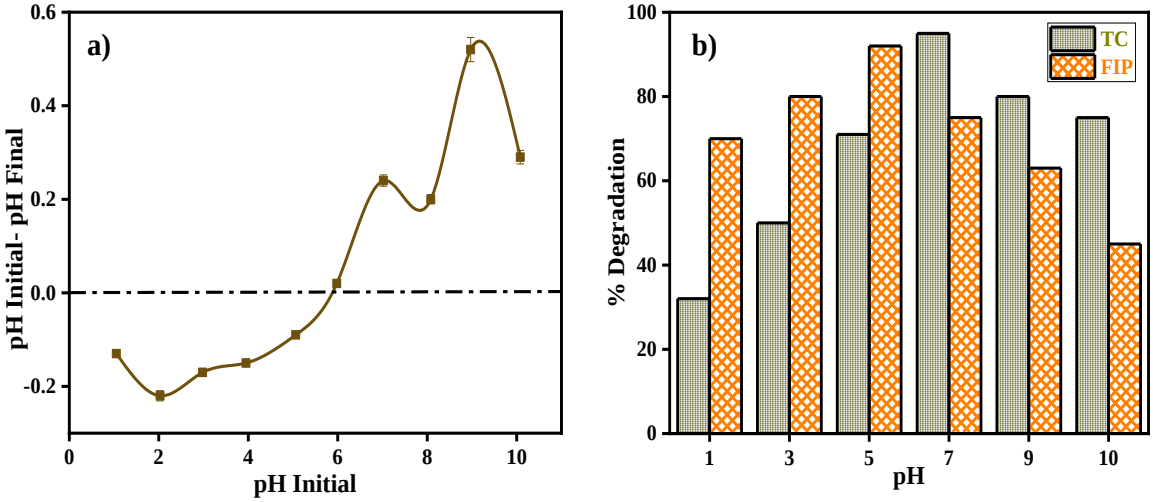


**Fig. 5.9** (a) point zero charge of MAG (3:1) catalyst and (b) variation MAG (3:1) catalyst degradation efficiency with pH of TC and FIP solution.

In the case of TC, the maximum degradation efficiency was observed at neutral pH 7. As TC exists in cationic form ($TC^+$) at pH<3.3 (pKa of TC), in the zwitter ionic form ($TC^{\pm}$) in the range of pH 3.3-7.7 and for pH>7.7 in anionic form ($TC^-$).[33] The degradation efficiency was lower in pH range 1-3 as the $TC^+$ repels with the positively charged surface of the catalyst (pzc=5.9). Above this range, as the electrostatic interactions between catalyst surface and $TC^{\pm}$ increase, the efficiency increases, leading to maximum photodegradation at pH7. Thereafter, the efficacy again decreases for pH>7 which is attributed to repulsion between $TC^-$ and negatively charged catalyst (pzc=5.9). In the case of FIP pesticide, the degradation was facilitated in the

acidic pH 1-5 with the maximum efficiency at pH 5, which is attributed to the strong electrostatic interactions between positively charged catalyst surfaces (pH<5.9) and the anionic pollutant. After this pH, the efficiency declines and in the basic range (pH 9-10) as the repulsion between the negatively charged catalyst and FIP increases which leads towards the lower adsorption and hence degradation of the pollutant.

### *5.5.5 Reusability*

Given the practical large-scale application, photocatalyst durability is quite essential. As a result, it is critical to investigate the material's photocatalytic stability over several degradation cycles. The reproducible nature of as-prepared MAG (3:1) composite (4mg) was optimized for 5 successive degradation runs in 20mL TC and FIP solution (fig. 5.10a). After performing the degradation of pollutants, the retrieved photocatalyst was washed multiple times with deionized water, later dried, and then reused for the next cycle. The degradation efficiency of MAG (3:1) catalyst for both TC (65%) and FIP (58%) remains high even after 5 cycles of degradation representing the high reusability of catalyst.

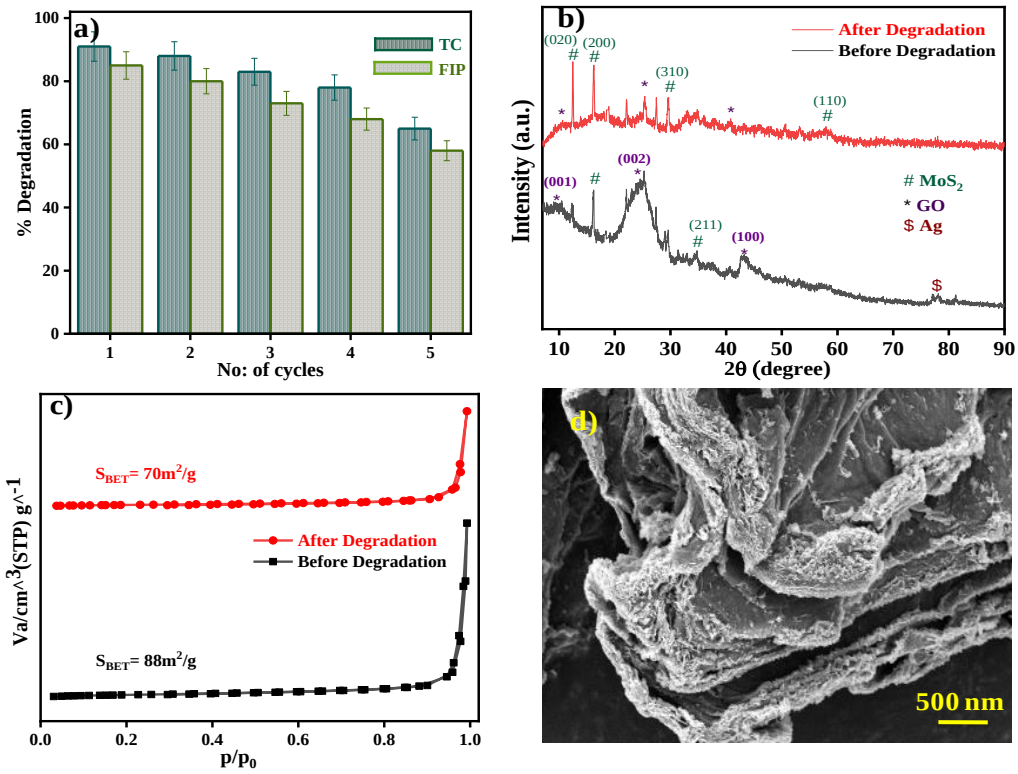


**Fig. 5.10** (a) Reusability studies, (b) XRD, (c) $N_2$ sorption isotherms, (d) SEM image of MAG catalyst before and after five photodegradation cycles with MAG (3:1) catalyst.

The photostability of the catalyst was further confirmed via characterization of the catalyst after photodegradation cycles. The XRD peaks of MAG (3:1) composite (fig. 5.10b) remain intact after photodegradation suggesting the crystal structure of the composite was maintained. Some additional peaks are identified, which might be due to the formation of $MoO_3$. In fig. 5.10c the type IV isotherm after degradation determines that the mesoporous nature of the catalyst was maintained after the photocatalytic reaction. As the pollutants are not permanently adsorbed over the surface of the MAG (3:1) catalyst, so the surface area before ($S_{BET}$ = 88 $m^2/g$) and after ($S_{BET}$ = 70 $m^2/g$) photodegradation was not significantly decreased. The SEM image of MAG (3:1) catalyst (fig. 5.10d) indicates that the surface morphology was not much disturbed after degradation. The results demonstrate that the as-prepared catalyst is highly reusable and could be beneficial in large-scale applications.

### *5.5.6 Industrial wastewater degradation*

It is crucial to determine the practical degradation efficiency of catalysts for the mineralization of industrial wastewaters. To reduce water toxicity levels, an ecologically economic advancement strategy in the sectors has demanded unique solutions. Without any pretreatment, the COD and TOC levels in raw wastewater were high, suggesting a significant organic contaminant percentage in the effluent. The conditions followed during the photodegradation of wastewater are: 0.4 g/L MAG (3:1) catalyst; neutral pH and time = 180 min. At regular time intervals, the % COD and TOC removal of wastewater was observed as shown in fig. 5.11a.The photocatalytic degradation by the prepared composite shows 70.4% COD and 55.1% TOC removal after 180 min under visible light. As the degradation was done without any physicochemical pretreatment, the high turbidity content hinders the infiltration of appropriate light energy and catalyst for the photocatalytic removal of refractory organic pollutants in the effluent. However, the increasing % COD/TOC removal validates the mineralization of organic matter to simpler molecules. Also, the original AOS (average oxidation state) value of the wastewater was 1.69 before any treatment, which increased to 2.47 and 3.31 for AOS and COS(carbon oxidation state), respectively, indicating that the MAG (3:1) composite boosts the biodegradability of the wastewater. As a result, the catalyst can be more effective than the physicochemical treatments used by industries for effluent treatment.

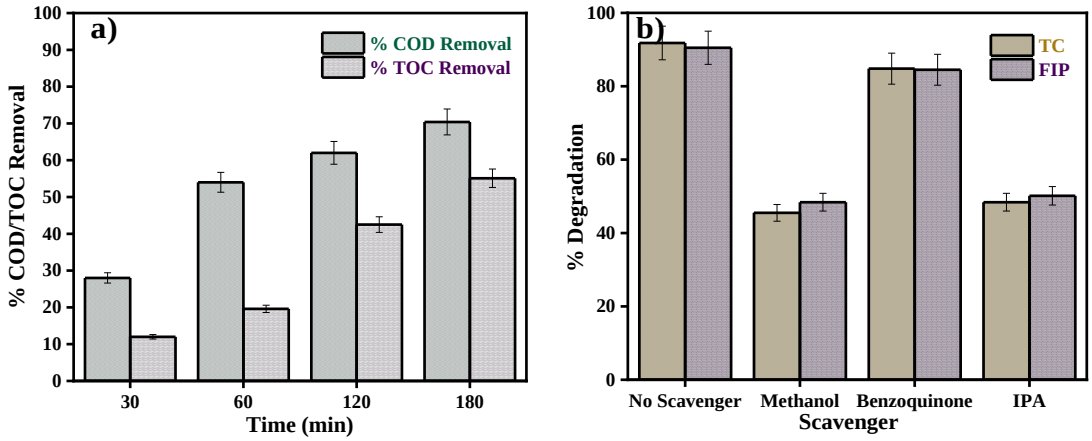


**Fig. 5.11** (a) COD and TOC removal analysis of real wastewater and (b) scavenger experiments with MAG (3:1) catalyst.

### 5.5.7 Mechanism of degradation

Scavenger analyses were carried out in order to identify the active species that play a critical part in the degradation process. For trapping hydroxyl radicals ($^{\bullet}OH$), holes ($h^+$), and superoxide radicals ($O_2^{-\bullet}$),different quenchers like isopropyl alcohol (IPA), methanol and benzoquinone were used, respectively.[34] The experiments were carried out with 4mg MAG (3:1) catalyst in 20 mL of TC and FIP solutions with different scavengers under visible light irradiation. It is evident from fig. 5.11b that, the degradation was significantly inhibited in the presence of both methanol and IPA for TC, as well as FIP indicating the holes and $^{\bullet}OH$ radicals, are actively participating in the degradation process. On the other hand, the presence of benzoquinone ($O_2^{-\bullet}$ scavenger) does not affect the degradation efficiency much. The findings show that the photodegradation of TC and FIP was mostly governed by holes and $^{\bullet}OH$, which play a significant role in the degradation pathway. Based on these findings, scheme 5.2 depicts an integrative approach for the photocatalysis of contaminants in wastewater. In the presence of light, $MoS_2$ in the composite absorbs photons with energy greater than its band gap resulting in the excitation of $e^-$ from the valence band (VB) to conduction band (CB) and producing $h^+$ in VB. Besides, the inserted Ag NPs created a surface plasmon resonance effect which increased the absorption of light. Because it has a lower Fermi level than CB of $MoS_2$, GO could provide a viable transfer channel with intriguing conductivity for the generated electrons.

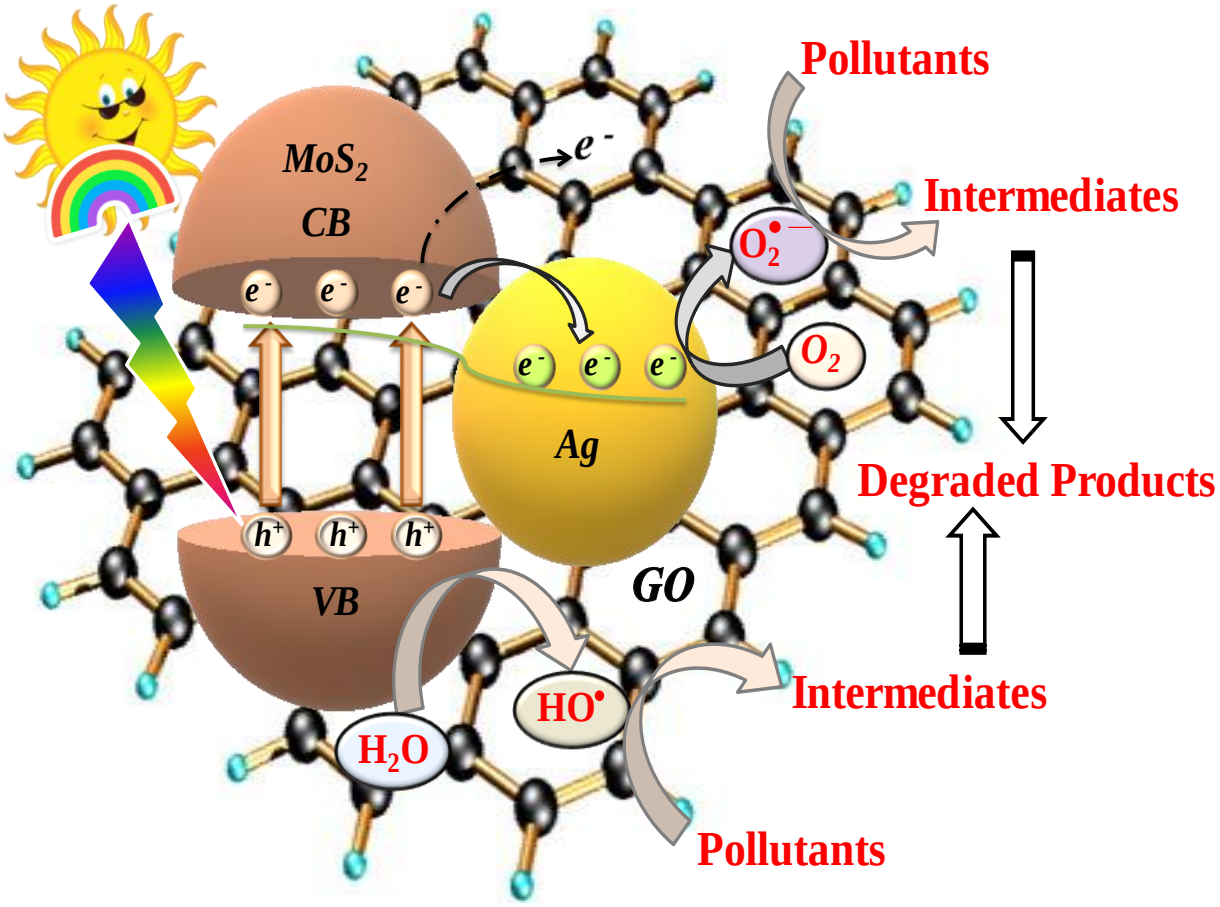


**Scheme 5.2.** A schematic depiction of the possible mechanism involved in the photodegradation of pollutants by MAG catalysts.

Furthermore, when $MoS_2$ and Ag NPs are joined to produce a composite material, a "Schottky barrier" is formed at their interfaces, implying the development of an effectual $e^-$ transfer pathway from $MoS_2$ to Ag.[35] These two effects of accelerating charge separation and transfer could fairly justify the excellent photocatalytic activity of $MoS_2$/Ag/GO ternary hybrids, which offers considerable potential for practical recyclable use. The CB's electrons are strong reductants, converting $O_2$ adsorbed on the surface of the catalyst to $O_2^{-\bullet}$ radicals. Furthermore, upon chemical reaction with water can produce more $^{\bullet}$OH radicals. Furthermore, the holes generated in the VB aid the breakdown of contaminants by interacting directly with them or via producing $^{\bullet}$OH which further react with the pollutant. The following are the possible steps in degradation reaction:

$MoS_2/Ag/GO + h\nu \longrightarrow e^- + h^+$

$H_2O + h^+ \longrightarrow H_2O^+ \longrightarrow OH^- + h^+$

$O_2 + e^- \longrightarrow O_2^{-\bullet} + h^+$

$H_2O^+ \longrightarrow OH^- + h^+$

$OH^- + h^+ \longrightarrow {}^{\bullet}OH$

${}^{\bullet}OH / O_2^{-\bullet} + TC/FIP \longrightarrow$ Degraded Products

## References


(1) Monga, D.; Sharma, S.; Basu, S. Advances in Transition Metal Dichalcogenide-Based Two-Dimensional Nanomaterials. *Mater. Today Chem.* **2021**, *19*, 100399. https://doi.org/10.1016/J.MTCHEM.2020.100399.

(2) Monga, D.; Basu, S. Enhanced Photocatalytic Degradation of Industrial Dye by G-$C_3N_4/TiO_2$ Nanocomposite: Role of Shape of $TiO_2$. *Adv. Powder Technol.* **2019**, *30* (5), 1089–1098. https://doi.org/10.1016/j.apt.2019.03.004.

(3) Sharma, S.; Basu, S. Highly Reusable Visible Light Active Hierarchical Porous $WO_3/SiO_2$ Monolith in Centimeter Length Scale for Enhanced Photocatalytic Degradation of Toxic Pollutants. *Sep. Purif. Technol.* **2020**, *231*, 115916. https://doi.org/10.1016/j.seppur.2019.115916.

(4) Garg, A.; Basu, S.; Shetti, N. P.; Reddy, K. R. 2D Materials and Its Heterostructured Photocatalysts: Synthesis, Properties, Functionalization and Applications in Environmental Remediation. *J. Environ. Chem. Eng.* **2021**, *9* (6), 106408. https://doi.org/10.1016/j.jece.2021.106408.

(5) Sharma, S.; Basu, S. Fabrication of Centimeter-Sized $Sb_2S_3/SiO_2$ Monolithic Mimosa Pudica Nanoflowers for Remediation of Hazardous Pollutants from Industrial Wastewater. *J. Clean. Prod.* **2021**, *280*, 124525. https://doi.org/10.1016/j.jclepro.2020.124525.

(6) Singla, S.; Sharma, S.; Basu, S.; Shetti, N. P.; Aminabhavi, T. M. Photocatalytic Water Splitting Hydrogen Production via Environmental Benign Carbon Based Nanomaterials.

*Int. J. Hydrogen Energy* **2021**, *46* (68), 33696–33717. https://doi.org/10.1016/j.ijhydene.2021.07.187.

(7) Monga, D.; Basu, S. Tuning the Photocatalytic/Electrocatalytic Properties of $MoS_2$/$MoSe_2$ Heterostructures by Varying the Weight Ratios for Enhanced Wastewater Treatment and Hydrogen Production. *RSC Adv.* **2021**, *11* (37), 22585–22597. https://doi.org/10.1039/D1RA01760H.

(8) Singla, S.; Sharma, S.; Basu, S. $MoS_2$/$WO_3$ Heterojunction with the Intensified Photocatalytic Performance for Decomposition of Organic Pollutants under the Broad Array of Solar Light. *J. Clean. Prod.* **2021**, *324* (6), 129290. https://doi.org/10.1016/j.jclepro.2021.129290.

(9) Aggarwal, M.; Basu, S.; Shetti, N. P.; Nadagouda, M. N.; Aminabhavi, T. M. Photocatalytic Conversion of $CO_2$ into Valuable Products Using Emerging Two-Dimensional Graphene-Based Nanomaterials: A Step towards Sustainability. *Chem. Eng. J.* **2021**, *425*, 131401. https://doi.org/10.1016/j.cej.2021.131401.

(10) Siddique, Z. B.; Basu, S.; Basak, P. Development of Graphene Oxide Dispersed Natural Ester Based Insulating Oil for Transformers. *IEEE Trans. Dielectr. Electr. Insul.* **2021**, *28* (4), 1326–1333. https://doi.org/10.1109/TDEI.2021.009445.

(11) Kaur, N.; Verma, A.; Thakur, I.; Basu, S. In-Situ Dual Effect of Ag-Fe-$TiO_2$ Composite for the Photocatalytic Degradation of Ciprofloxacin in Aqueous Solution. *Chemosphere* **2021**, *276*, 130180. https://doi.org/10.1016/j.chemosphere.2021.130180.

(12) Ikram, M.; Khan, M. I.; Raza, A.; Imran, M.; Ul-Hamid, A.; Ali, S. Outstanding Performance of Silver-Decorated $MoS_2$ Nanopetals Used as Nanocatalyst for Synthetic Dye Degradation. *Phys. E Low-Dimensional Syst. Nanostructures* **2020**. https://doi.org/10.1016/j.physe.2020.114246.

(13) Lu, D.; Wang, H.; Zhao, X.; Kondamareddy, K. K.; Ding, J.; Li, C.; Fang, P. Highly Efficient Visible-Light-Induced Photoactivity of Z-Scheme g-$C_3N_4$/Ag/$MoS_2$ Ternary Photocatalysts for Organic Pollutant Degradation and Production of Hydrogen. *ACS Sustain. Chem. Eng.* **2017**, *5* (2), 1436–1445. https://doi.org/10.1021/acssuschemeng.6b02010.

(14) Zhao, W.; Zhang, Z.; Zhang, J.; Wu, H.; Xi, L.; Ruan, C. Synthesis of Ag/$TiO_2$/Graphene and Its Photocatalytic Properties under Visible Light. *Mater. Lett.* **2016**.

https://doi.org/10.1016/j.matlet.2016.02.063.

(15) Mishra, A.; Mehta, A.; Sharma, M.; Basu, S. Impact of Ag Nanoparticles on Photomineralization of Chlorobenzene by $TiO_2$/Bentonite Nanocomposite. *J. Environ. Chem. Eng.* **2017**. https://doi.org/10.1016/j.jece.2016.12.042.

(16) Dimiev, A. M.; Tour, J. M. Mechanism of Graphene Oxide Formation. *ACS Nano* **2014**. https://doi.org/10.1021/nn500606a.

(17) Arthi G, P. B.; BD, L. A Simple Approach to Stepwise Synthesis of Graphene Oxide Nanomaterial. *J. Nanomed. Nanotechnol.* **2015**. https://doi.org/10.4172/2157-7439.1000253.

(18) Monga, D.; Ilager, D.; Shetti, N. P.; Basu, S.; Aminabhavi, T. M. 2D/2d Heterojunction of $MoS_2$/g-$C_3N_4$ Nanoflowers for Enhanced Visible-Light-Driven Photocatalytic and Electrochemical Degradation of Organic Pollutants. *J. Environ. Manage.* **2020**, *274*, 111208. https://doi.org/10.1016/j.jenvman.2020.111208.

(19) Qumar, U.; Hassan, J.; Naz, S.; Haider, A.; Raza, A.; Ul-Hamid, A.; Haider, J.; Shahzadi, I.; Ahmad, I.; Ikram, M. Silver Decorated 2D Nanosheets of GO and $MoS_2$ Serve as Nanocatalyst for Water Treatment and Antimicrobial Applications as Ascertained with Molecular Docking Evaluation. *Nanotechnology* **2021**, *32* (25), 255704. https://doi.org/10.1088/1361-6528/abe43c.

(20) Sharma, S.; Basu, S. Visible-Light-Driven Efficient Photocatalytic Abatement of Recalcitrant Pollutants by Centimeter-Length $MoO_3$/$SiO_2$ Monoliths with Long Service Life. *Appl. Mater. Today* **2021**. https://doi.org/10.1016/j.apmt.2021.101033.

(21) Sengupta, I.; Sharat Kumar, S. S. S.; Pal, S. K.; Chakraborty, S. Characterization of Structural Transformation of Graphene Oxide to Reduced Graphene Oxide during Thermal Annealing. *J. Mater. Res.* **2020**. https://doi.org/10.1557/jmr.2020.55.

(22) Pratheesya, T.; Harish, S.; Navaneethan, M.; Sohila, S.; Ramesh, R. Enhanced Antibacterial and Photocatalytic Activities of Silver Nanoparticles Anchored Reduced Graphene Oxide Nanostructure. *Mater. Res. Express* **2019**. https://doi.org/10.1088/2053-1591/ab1567.

(23) Wu, D.; Wang, X.; Wang, H.; Wang, F.; Wang, D.; Gao, Z.; Wang, X.; Xu, F.; Jiang, K. Ultrasonic-Assisted Synthesis of Two Dimensional BiOCl/$MoS_2$ with Tunable Band Gap and Fast Charge Separation for Enhanced Photocatalytic Performance under Visible Light.

*J. Colloid Interface Sci.* **2019**, *533*, 539–547. https://doi.org/10.1016/j.jcis.2018.08.084.

(24) Monga, D.; Basu, S. Single-Crystalline 2D BiOCl Nanorods Decorated with 2D $MoS_2$ Nanosheets for Visible Light-Driven Photocatalytic Detoxification of Organic and Inorganic Pollutants. *FlatChem* **2021**. https://doi.org/10.1016/j.flatc.2021.100267.

(25) Al-Gaashani, R.; Najjar, A.; Zakaria, Y.; Mansour, S.; Atieh, M. A. XPS and Structural Studies of High Quality Graphene Oxide and Reduced Graphene Oxide Prepared by Different Chemical Oxidation Methods. *Ceram. Int.* **2019**. https://doi.org/10.1016/j.ceramint.2019.04.165.

(26) Stobinski, L.; Lesiak, B.; Malolepszy, A.; Mazurkiewicz, M.; Mierzwa, B.; Zemek, J.; Jiricek, P.; Bieloshapka, I. Graphene Oxide and Reduced Graphene Oxide Studied by the XRD, TEM and Electron Spectroscopy Methods. *J. Electron Spectros. Relat. Phenomena* **2014**, *195*, 145–154. https://doi.org/10.1016/j.elspec.2014.07.003.

(27) Kundu, A.; Sharma, S.; Basu, S. Modulated BiOCl Nanoplates with Porous G-$C_3N_4$ Nanosheets for Photocatalytic Degradation of Color/Colorless Pollutants in Natural Sunlight. *J. Phys. Chem. Solids* **2021**, *154*, 110064. https://doi.org/10.1016/j.jpcs.2021.110064.

(28) Qiao, D.; Li, Z.; Duan, J.; He, X. Adsorption and Photocatalytic Degradation Mechanism of Magnetic Graphene Oxide/ZnO Nanocomposites for Tetracycline Contaminants. *Chem. Eng. J.* **2020**. https://doi.org/10.1016/j.cej.2020.125952.

(29) Haldorai, Y.; Kim, B.-K.; Jo, Y.-L.; Shim, J.-J. Ag@graphene Oxide Nanocomposite as an Efficient Visible-Light Plasmonic Photocatalyst for the Degradation of Organic Pollutants: A Facile Green Synthetic Approach. *Mater. Chem. Phys.* **2014**, *143* (3), 1452–1461. https://doi.org/10.1016/j.matchemphys.2013.11.065.

(30) Awasthi, G. P.; Adhikari, S. P.; Ko, S.; Kim, H. J.; Park, C. H.; Kim, C. S. Facile Synthesis of ZnO Flowers Modified Graphene like $MoS_2$ Sheets for Enhanced Visible-Light-Driven Photocatalytic Activity and Antibacterial Properties. *J. Alloys Compd.* **2016**. https://doi.org/10.1016/j.jallcom.2016.04.267.

(31) Guo, F.; Huang, X.; Chen, Z.; Ren, H.; Li, M.; Chen, L. $MoS_2$ Nanosheets Anchored on Porous $ZnSnO_3$ Cubes as an Efficient Visible-Light-Driven Composite Photocatalyst for the Degradation of Tetracycline and Mechanism Insight. *J. Hazard. Mater.* **2020**. https://doi.org/10.1016/j.jhazmat.2020.122158.

(32) Lin, X.; Wang, X.; Zhou, Q.; Wen, C.; Su, S.; Xiang, J.; Cheng, P.; Hu, X.; Li, Y.; Wang, X.; Gao, X.; Nözel, R.; Zhou, G.; Zhang, Z.; Liu, J. Magnetically Recyclable $MoS_2/Fe_3O_4$ Hybrid Composite as Visible Light Responsive Photocatalyst with Enhanced Photocatalytic Performance. *ACS Sustain. Chem. Eng.* **2019**. https://doi.org/10.1021/acssuschemeng.8b05440.

(33) Khan, M. H.; Bae, H.; Jung, J.-Y. Tetracycline Degradation by Ozonation in the Aqueous Phase: Proposed Degradation Intermediates and Pathway. *J. Hazard. Mater.* **2010**, *181* (1–3), 659–665. https://doi.org/10.1016/j.jhazmat.2010.05.063.

(34) Aanchal; Barman, S.; Basu, S. Complete Removal of Endocrine Disrupting Compound and Toxic Dye by Visible Light Active Porous G-$C_3N_4$/H-ZSM-5 Nanocomposite. *Chemosphere* **2020**, *241*, 124981. https://doi.org/10.1016/j.chemosphere.2019.124981.

(35) Chen, Y.; Liu, H.; Li, X.; Tang, S.; Gu, C.; Wei, G.; Jiang, T.; Zhou, X. Development of RGO@$MoS_2$@Ag Ternary Nanocomposites with Tunable Geometry Structure for Recyclable SERS Detection. *Sensors Actuators, B Chem.* **2021**. https://doi.org/10.1016/j.snb.2021.129856.

# *Conclusions and Future aspects*

**Chapter 1:**

Water pollution and energy requirement are the environmental challenges that pose a threat to our daily lives and long-term growth. Various unique technologies for environmental remediation have been successfully established at this time. AOPs are the techniques ensuring complete mineralization of hazardous organic pollutants into simple degraded products. Using bountlessly available sunlight energy, semiconductor photocatalysis can be the efficient method for treatment of wastewater. Hence, the researchers are now more focussed on the development of visible–light active photocatalysts as most of the commercial photocatalysts are only UV-light active. TMDCs have emerged as highly sought nanostructures as they are finding diverse electro and photocatalytic applications. This can be accredited to their exceptional physicochemical properties such as high surface-to-volume ratio, narrow bandgap, and excellent charge transfer capability in addition to good visible-light absorption tendency. The limitation of photogenerated charge carrier recombination can be easily overcome by combining TMDCs with other semiconductor materials. For the synthesis of these TMDCs, microwave assisted techniques are most potential methods as they are less-time consuming, more efficient, provide even localized heating. Although many efforts have been made in this area, but most of the techniques reported in literature requires much time as well as high temperature and pressure conditions also not much emphasis has been laid on the photo/electro catalytic applications of TMDCs based composites. Hence the research focuses on the preparation of various TMDCs based composites ($MoS_2$/g-$C_3N_4$, $MoS_2$/$MoSe_2$, BiOCl/$MoS_2$ and $MoS_2$/Ag/GO) via microwave assisted technique and evaluation of its photocatalytic performance for degradation of organic pollutants under different reaction parameters.

**Chapter 2:**

A rapid and convenient synthesis of flower-like $MoS_2$ and $MoS_2$/g-$C_3N_4$ nanocomposites was attempted by the microwave technique with variable weight ratios (1:1, 1:3, 3:1 and 5:1). The photocatalysts were employed further for photo-electrocatalytic degradation of methylene blue in different light (UV, visible and sunlight) irradiation. By changing the weight ratios of $MoS_2$ and

g-$C_3N_4$, one can modify the catalytic efficiency. From the present work, we suggest that the amount of $MoS_2$ and g-$C_3N_4$ has a high impact on photo-electrocatalytic degradation. The best degradation performance was observed with MSC (5:1) nanocomposite in sunlight. The degradation of colorless fipronil pesticide confirms indirect photocatalysis. The mechanism of degradation was also explained using scavengers. The electrochemical behavior of methylene blue was studied at $MoS_2$/g-$C_3N_4$ (5:1) modified GCE. Cyclic voltammetry was employed to determine the redox behavior of methylene blue. Based on the electrochemical experiments, we confirm that redox mechanism of methylene blue involved two protons and two electrons to yield colorless leucomethylene blue. The environment-friendly nature and high reusability efficiency of the developed photocatalysts/electrocatalysts make them suitable for sustainable wastewater treatment applications.

**Chapter 3:**

In summary, the 2D/2D heterojunction of $MoS_2$/$MoSe_2$ with different weight ratios was successfully prepared by the facile microwave technique which is less time taking and cost-effective. The prepared materials show high photocatalytic and electrocatalytic performance. Compared with the pure $MoS_2$ and $MoSe_2$, the photocatalytic efficiency of the composites was highly enhanced towards methylene blue dye and fipronil pesticide degradation. Due to their similar energy levels, the heterojunction formed between the two, assist the separation of charges which results in the better degradation activity of the composites. The degradation efficiency was remarkably affected by varying the amount of $MoS_2$ and $MoSe_2$ in the composite. The MSMSe (1:3) composite shows the best catalytic activity due to its higher surface area and lower recombination rate of charges as compared to other composites. Moreover, the pH of the solution, the amount of catalyst, and the exposed area has a high impact on the degradation efficiency of the present catalysts. The high removal of COD and TOC in the real wastewater confirms the as-prepared catalysts can be used in the physico-chemical treatment of real wastewater. Also, the recovery and reuse of the catalyst make it suitable for long-term application. In the acidic medium, the synthesized nanocomposites are highly efficient electrocatalysts for HER activity with a stable current density. The EDLC studies show that the MSMSe nanocomposites are potential electrode material with high capacitance retention for energy storage devices. The studies in this work can give a genuine guide for the fast and easy

synthesis of highly efficient; visible-light based stable catalysts for photocatalytic wastewater treatment and electrocatalytic hydrogen production.

**Chapter 4:**

The study comprises the successful preparation of 2D/2D BiOCl/$MoS_2$ heterostructures through fast, one-step microwave-assisted technique and the variation of their properties and photocatalytic activities with the composition of BiOCl and $MoS_2$. The prepared BiOCl/$MoS_2$ composites show single-crystalline nature with high surface area and low charge recombination. The interfacial contact of BiOCl and $MoS_2$ results in a high synergistic effect which enhances the degradation capability of the composites thus resulting in higher removal of organic and inorganic pollutants like methylene blue dye, fipronil pesticide, and Cr(VI) metal. The excellent practical efficiency of the catalyst was confirmed through high COD and TOC removal in textile industrial wastewater without any pretreatment. The optimization of different degradation parameters was done to determine the conditions for maximum degradation efficacy. The high reusability of the catalyst with ease of separation confirms the good photostability of catalyst for many degradation runs. The enhanced photocatalytic activity for both organic and inorganic pollutants as well as real industrial wastewater indicates that the catalyst is efficient for detoxification of water containing different types of pollutants.

**Chapter 5:**

Ternary composites of $MoS_2$ nanopetals and GO sheets with Ag NPs were prepared using the microwave-assisted technique. The introduction of GO provides a high surface area and also an electron transfer path for photogenerated electrons. The composites have a large surface area and superior optical characteristics, making them ideal for photocatalytic activity. The study of different reaction parameters revealed that the catalyst is highly effective for the degradation of TC and FIP at natural pH, even with a low catalyst dose. The predominant role of hydroxyl radicals and holes in the process of degradation was affirmed by trapping experiments. The catalyst's excellent practical performance was demonstrated by the significant removal of COD and TOC from industrial wastewater without any pretreatment.

**General Conclusion**

The core focus of this thesis is to develop visible-light active photocatalysts for efficient wastewater treatment. In this work, composites of $MoS_2$ with different semiconductors (g-$C_3N_4$,

$MoSe_2$, BiOCl, GO) were prepared which has been utilized for the degradation of recalcitrant pollutants. It has been enlightened that the photocatalytic efficiency of $MoS_2$ has been greatly improved by the formation of heterojunction due to tuning of its band gap and reduced recombination rate. All the composite materials prepared show excellent photocatalytic activity in the visible light. Considering all the factors (degradation efficiency, catalyst amount, reusability etc.) it has been observed that the composite BiOCl/$MoS_2$ (1:3) show remarkably excellent photocatalytic activity towards degradation of organic pollutants. This might be due to its lower energy band gap and reduced recombination rate attributed to heterojunction formation. Moreover, the morphology of the composite consists of both rod like BiOCl and nanosheets of $MoS_2$ which might provide higher active sites for the degradation of pollutants. This innovative and highly active photocatalyst is well suited for use in photocatalytic degradation and other applications, and it paves the door for the future fabrication of different highly effective heterojunction photocatalysts to address energy and environmental issues.

**Future aspects**

In this thesis, the main focus relies on photocatalysis by elucidating the physical characteristics of the catalyst rather than the electrochemical behaviour. Though people are currently concentrating on photoelectrocatalytic (PEC) degradation of organic pollutants with concomitant $H_2$ evolution, which has received a lot of attention due to the use of a minimal external potential to aid electron transmission. Shape of photocatalysts also imposed a significant impact on the properties and activities of materials, hence TMDCs with different morphology can also be explored for optimizing the variation in activity with shape. The tunable bandgap energy of TMDCs facilitates the formation of composites with other materials. In spite of the fact that TMDC nanostructured materials are magnificent substrates for various applications, there is a lot of space for logical exertion for the progression in the interdisciplinary region. There is much room for their exploration in biomedical fields for the detection and treatment of various diseases. There is also a huge scope to increase the selectivity and sensitivity in sensor area by the modification of TMDCs. Along these lines, more applications are yet to be expected to investigate the tunable properties of TMDC-based nanomaterials in the near future and advancements.

# *List of Publications*

## In Peer-Reviewed (SCI) Journals

1. **Divya Monga**, Davalasab Ilager, Nagaraj. P. Shetti, Soumen Basu, & Tejraj M Aminabhavi. 2D/2D heterojunction of $MoS_2$/g-$C_3N_4$ nanoflowers for enhanced visible-light-driven photocatalytic and electrochemical degradation of organic pollutants. *Journal of Environmental Management*, *274*, (2020) 111208. **(I.F. 6.789)**.
2. **Divya Monga**, & Soumen Basu. Tuning the photocatalytic/electrocatalytic properties of $MoS_2$/$MoSe_2$ heterostructures by varying the weight ratios for enhanced wastewater treatment and hydrogen production. *RSC Advances*, *11*(37), (2021), 22585-22597. (**I.F. 3.361**).
3. **Divya Monga**, & Soumen Basu. Single-Crystalline 2D BiOCl Nanorods Decorated with 2D $MoS_2$ Nanosheets for Visible Light-driven Photocatalytic Detoxification of Organic and Inorganic Pollutants. *FlatChem*, (2021), 100267. (**I.F. 5.227**)
4. **Divya Monga,** & Soumen Basu. Combination of $MoS_2$ nanopetals with Ag nanoparticles decorated graphene oxide for boosting photocatalytic abatement of recalcitrant pollutants under visible light irradiation. *Advanced Powder Technology*, (2022), 103555. **(I.F. 4.833)**
5. **Divya Monga**, Surbhi Sharma, Nagaraj. P. Shetti, Soumen Basu, Kakarla Raghava Reddy, & Tejraj M Aminabhavi. Advances in transition metal dichalcogenide-based two-dimensional nanomaterials. *Materials Today Chemistry*, *19*, (2021), 100399. **(I.F. 8.301)**.
6. **Divya Monga**, Nagaraj. P. Shetti, Soumen Basu, Kakarla Raghava Reddy, Michael Badawi, Adrián Bonilla-Petriciolet & Tejraj M. Aminabhavi. Engineered biochar: A way forward to attenuate water pollution and pollutants toxicity. *Fuel*, (2021), 122510. (**I.F. 6.609**).
7. **Divya Monga** & Soumen Basu. Enhanced photocatalytic degradation of industrial dye by g-$C_3N_4$/$TiO_2$ nanocomposite: Role of shape of $TiO_2$. *Advanced powder technology*, *30*(5), (2019), 1089-1098. **(I.F. 4.833)**.
8. Nagaraj. P. Shetti, Davalasab Ilager, Shweta J Malode, **Divya Monga**, Soumen Basu

& Kakarla Raghava Reddy (2020). Poly (eriochrome black T) modified electrode for electrosensing of methdilazine. *Materials Science in Semiconductor Processing*, *120*, 105261. **(I.F. 3.927)**.

9. **Divya Monga**, Nagaraj. P. Shetti, Soumen Basu, Kakarla Raghava Reddy, & Tejraj M. Aminabhavi. Research Status of Clean and Sustainable Hydrogen Production Technologies: A Review. (communicated)

# *Conferences and workshops attended*

1. *Attended a National Virtual Conference on "**Recent Advances Analytical Techniques-2020 (RAAT-2020)**" organize by Dept. of Chemistry, Shri Varshney College Aligarh, UP and CBMR, Lucknow, UP (16-17 August 2020).*
2. Presented poster at a National Conference, RTCES-2019 on the topic "**Synthesis of g-$C_3N_4$/$TiO_2$ Nanocomposite with variable shapes for photocatalytic degradation of Rhodamine B**" held at Punjabi University, Patiala on February 07-08, 2019.
3. International virtual conference conducted by U-SERC on the topic, "**Modern Instrumental and Characterization Techniques in Applied Sciences-2020**" (MICTAS-2020), attended at online mode on 5-6 July 2020.
4. Attended the "**DST & ACS VIRTUAL WORKSHOP** on **"MASTERING THE PUBLISHING PROCESS"** July 28, 2020.